# *STRATEGIES FOR OPTOGENETIC STIMULATION OF DEEP TISSUE PERIPHERAL NERVES*

**By**

**Benjamin E. Maimon**

**B.S. Biomedical and Mechanical Engineering**
**Duke University, 2012**

**SUBMITTED TO THE DIVISION OF HEALTH SCIENCES AND TECHNOLOGY IN PARTIAL FULFILLMENT OF THE REQUIREMENTS FOR THE DEGREE OF**

**Doctor of Philosophy**

**at the**

**Massachusetts Institute of Technology**

**June 2018**



Signature of Author: Signature redacted
Harvard-MIT Program in Health Sciences and Technology
February 20, 2018

Certified by: Signature redacted
Hugh M. Herr, PhD
Professor of Media Arts and Sciences
Thesis Supervisor

Accepted by: Signature redacted
Emery N. Brown, MD, PhD/Director
Harvard-MIT Program in Health Sciences and Technology
Professor of Computational Neuroscience and Health Sciences and Technology

# DECLARATION

This dissertation is the result of my own work and includes nothing, which is the outcome of work done in collaboration except where specifically indicated in the text. It has not been previously submitted, in part or whole, to any university of institution for any degree, diploma, or other qualification.

Signed: Signature redacted

Date: 3-30-18

Benjamin E. Maimon
Massachusetts Institute of Technology

# SUMMARY / ABSTRACT

Optogenetic technologies have been the subject of great excitement within the scientific community for their ability to demystify complex neurophysiological pathways in the central and peripheral nervous systems. Optogenetics refers to the transduction of mammalian cells with a light-sensitive transmembrane protein, called an opsin, such that illumination of the target tissue initiates depolarization; in the case of a neuron, illumination results in the firing of an action potential that can control downstream physiology. The excitement surrounding optogenetics has also extended to the clinic with a human trial using the opsin ChR2 in the treatment of retinitis pigmentosa currently underway and several more trials potentially planned for the near future. In this thesis, we focus on the use of viral techniques to transduce peripheral nerve tissue to be responsive to light. We characterize the properties of optogenetic peripheral nerve transduction, optimizing for variables such as expression strength, wavelength specificity, and time-course of expression. Within the scope of this thesis, three new methods for optogenetic peripheral nerve stimulation are described: (1) a method for optogenetic motor nerve control using transdermal illumination, (2) a method employing unique wavelengths to selectively target optogenetic subsets of motor nerves, and (3) a method for extending optogenetic expression strength and time-course. The work is important because it lays the foundation for future advancements in optogenetic peripheral nerve stimulation in both a scientific and clinical context.

# ACKNOWLEDGEMENTS

Thank you to Hugh Herr for inspiring my motivation for research in bionics, my parents for advising me to continue my doctoral work, my academic committee for donating their time and advice to help motivate new research directions, and the entire Harvard & MIT communities for being supportive and open with research tools and assistance. Thank you to my thesis committee chair Ed Boyden and my thesis committee member Elfar Adalsteinsson for dedicating the time to review my thesis.

Additionally, I would like to thank the following individuals for contributing ideas, time, or research support throughout the PhD process: Chris Towne, Amauche Emenari, Rhyse Bendell, Katherine Song, Kathleen Cormier, Charlene Condon, Mike Brown, Jennifer Haupt, Morgan Jamiel, Or Shemesh, Christopher Lee, Ron Riso, Stephanie Ku, Jean-Francois Duval, Lillian Chen, Matt Carty, Simon Talbot, Jeff Wyckoff, Ioannis Yannas, Alex Springer, Katharina Ross, Nathan Klapoetke, Kiryl Piatkevich, Emilie Revol, Peter Calvaresi, Claudia Varela, Ben Leaker, Shriya Srinivasan, Alex Harding, Mina Fahmi, Ho-Jun Suk, Demian Park, Maurizio Diaz, Alexis Schneider, Shiv Pillai, Matt Weber, Laurel Lee, Christopher Tugman, Anthony Zorzos, Kaitlyn Sparks, Lisa Freed, Abigail Schiff, Ellen Buckley Jordan, Carolyn Madden, Cameron Taylor, and Hyungeun Song.

I would also like to thank the following organizations: The Koch Histology Core, The Koch Microscopy Core, The Koch Live Animal Imaging Core, the DCM Pathology Laboratory, the Koch Biopolymers Core, the Synthetic Neurobiology Group, and The Broad Institute.

This work was funded by the MIT Media Lab Consortium.

.

# AUTHOR LIST

The following scientists contributed to Chapter 2: Katherine Song, Ron Riso, Anthony Zorzos, Rhyse Bendell, Hugh Herr

The following scientists contributed to Chapter 3: Shriya Srinivasan, Stephanie Ku

The following scientists contributed to Chapter 4: Alex Harding, Mina Fahmi, Anthony Zorzos, Rhyse Bendell, Peter Calvaresi, Shriya Srinivasan, Hugh Herr

The following scientists contributed to Chapter 5: Anthony Zorzos, Kaitlyn Sparks, Shriya Srinivasan, Maurizio Diaz, Hugh Herr

The following scientists contributed to Chapter 6: Maurizio Diaz, Emilie C. M. Revol, Alexis M. Schneider, Ben Leaker, Claudia E. Varela, Shriya Srinivasan, Hugh Herr

The following scientists contributed to Chapter 7: Mina Fahmi, Shriya Srinivasan, Hugh Herr

# CONTENTS

**1 INTRODUCTION ..... 14**

1.1 CURRENT STATE OF THE PERIPHERAL NERVE STIMULATION ..... 15

1.2 OPTOGENETICS FOR PERIPHERAL NERVE STIMULATION ..... 19

APPENDIX 1: PERIPHERAL NERVE STIMULATION DEVICES[12] ..... 22

**2 CHALLENGES IN HIGH-RESOLUTION SYNTHETIC PERIPHERAL INTERFACES ..... 24**

2.1 INTRODUCTION ..... 24

2.2 METHODS ..... 27

2.3 RESULTS ..... 34

2.4 DISCUSSION ..... 40

**3 PERIPHERAL NERVE OPTOGENETICS ..... 43**

3.1 BRIEF INTRODUCTION TO PERIPHERAL NERVE OPTOGENETICS ..... 43

3.2 FOS THEORY ..... 44

3.3 KEY VARIABLES AFFECTING FOS ..... 47

3.4 TIME VARIANCE OF OPSIN ..... 50

**4 TRANSDERMAL OPTOGENETIC PERIPHERAL NERVE STIMULATION 54**

4.1 INTRODUCTION ..... 55

4.2 METHODS ..... 56

4.3 RESULTS ..... 63

4.4 DISCUSSION ..... 72

**5 TWO COLOR OPTOGENETIC PERIPHERAL NERVE STIMULATION ..... 76**

5.1 INTRODUCTION ..... 77

5.2 METHODS ..... 81

5.3 RESULTS ..... 86

5.4 DISCUSSION ..... 100

APPENDIX 2: SUPPLEMENTAL FIGURES FOR CHAPTER 5 ..... 106

**6 PERIPHERAL OPTOGENETIC LONGEVITY ..... 116**

6.1 INTRODUCTION ..... 117

6.2 METHODS ..... 121

6.3 RESULTS ..... 129

6.4 DISCUSSION ..... 146

APPENDIX 3: SUPPLEMENTAL FIGURES FOR CHAPTER 6 ..... 152

**7 SCIENTIFIC AND CLINICAL IMPACT ..... 160**
7.1 CLINICAL OPTOGENETIC CHALLENGES ..... 161
7.2 KEY ADVANTAGES OF FOS BY APPLICATION ..... 166
7.3 WEARABLE DESIGNS FOR CLINICAL OPTOGENETICS ..... 170
**8 REFERENCES ..... 181**

# List of Tables

Table 3.1 Variables that influence success of optogenetic peripheral nerve stimulation ..... 47

Table 6.1 Potential causes for loss of optogenetic expression over time..... 120

Table 6.2 Contribution of factors to conclusion of ChR2-specific immunogenicity. ..... 146

Table 7.1 Nerve targets for clinical transdermal optogenetic peripheral nerve stimulation ..... 170

# LIST OF FIGURES

FIGURE 1.1 COMMON IMPLANTABLE PERIPHERAL NERVE STIMULATION PARADIGMS....16

FIGURE 1.2: STIMROUTER DEVICE – WIRELESS, PERCUTANEOUS CONTROL OF CHRONIC PAIN. ....18

FIGURE 2.1 MICROCHANNEL CONSTRUCTION ....30

FIGURE 2.2 COLLAGEN-EMBEDDED MICROCHANNEL ....31

FIGURE 2.3 ACTIVE MICROCHANNEL IMPLANT IN FERRETS ....34

FIGURE 2.4: ELECTROPHYSIOLOGICAL CONDUCTION OF EMG THROUGH MICROCHANNEL ....35

FIGURE 2.5: HISTOLOGICAL ASSESSMENT OF PASSIVE MICROCHANNEL....37

FIGURE 2.6: ACTIVE MICROCHANNEL FAILURES....39

FIGURE 3.1 OPTICAL PROPERTIES OF BIOLOGICAL TISSUES AS A FUNCTION OF WAVELENGTH FOR ABSORPTION COEFFICIENTS (LEFT)[73] AND SCATTERING COEFFICIENTS (RIGHT)[74] ....48

FIGURE 3.2 MODEL DESCRIBING FOS TIME-VARIANCE ....53

FIGURE 4.1 PROCEDURE FOR MEASURING FLUENCE RATE AND EMG ....58

FIGURE 4.2 FLUENCE RATE MODELING FOR NERVE DEPTHS ENCOUNTERED IN THIS STUDY ....62

FIGURE 4.3 THERMAL MODEL FOR 473 NM ILLUMINATION OF PERIPHERAL GEOMETRY....64

FIGURE 4.4: ELECTROPHYSIOLOGICAL FINDINGS FOR TRANSDERMAL FOS ....66

FIGURE 4.5: IMMUNOFLUORESCENCE ASSESSMENT OF CHR2-EYFP+ NEURAL TISSUE ....69

FIGURE 4.6 *IN VIVO* IMAGING OF TRANSDUCED C.P.N. ....72

FIGURE 5.1: PERIPHERAL NERVE OPSIN SCREEN ....87

FIGURE 5.2: IMMUNOFLUORESCENT OPSIN EVALUATION ....90

FIGURE 5.3 TWO COLOR INDEPENDENT OPTOGENETIC PERIPHERAL NERVE STIMULATION ....92

FIGURE 5.4 FLUENCE RATE MODELING FOR RED AND BLUE LIGHT ....95

FIGURE 5.5: LOSS OF EXPRESSION AND MUSCLE ATROPHY IS OPSIN-DEPENDENT ..... 97

FIGURE 5.6: JAWS INHIBITS MUSCLE TREMOR ..... 99

FIGURE 5.7: MUSCLE FORCE AND EMG ARE PROPORTIONAL ..... 106

FIGURE 5.8: BEAM PROFILER USED TO ANALYZE LASER SHAPE, SPREAD, AND CO-LOCALIZATION ..... 107

FIGURE 5.9: INJECTION LEAKAGE AND MUSCLE SPECIFICITY TESTING IN P2 RAT USING DYE. ..... 108

FIGURE 5.10 H&E IMAGE USED FOR COLLECTING GEOMETRY REQUIRED FOR FLUENCE RATE MODELING CALCULATIONS ..... 109

FIGURE 5.11: THERMAL MODEL FOR RED & BLUE LASERS IN STIMULATION AND INHIBITION ..... 110

FIGURE 5.12: CHRIMSONR EXPRESSES *IN VITRO*, BUT NOT IN PERIPHERAL NERVES *IN VIVO* ..... 111

FIGURE 5.13: IN VITRO OPSIN EXPRESSION ..... 112

FIGURE 5.14: RED VS. BLUE OPSIN ELECTROPHYSIOLOGY FINDINGS ..... 113

FIGURE 5.15 SPINAL CORD OPSIN EXPRESSION ..... 114

FIGURE 5.16 TRANSDERMAL TWO-COLOR EMG ..... 115

FIGURE 6.1: ALL BUT ONE RATS LOSE EXPRESSION OVER TIME, INDEPENDENT OF DOSE, AGE, OR LOCATION OF INJECTION ..... 130

FIGURE 6.2: HISTOLOGY REVEALS NEURONAL ATTACK IN ADAPTIVE IMMUNE RESPONSE ..... 132

FIGURE 6.3: RAG2$^{-/-}$ RATS SHOW PROLONGED TRANSDERMAL OPTOGENETIC EXPRESSION ..... 135

FIGURE 6.4: TACROLIMUS-TREATED RATS SHOW EXTENDED OPTOGENETIC EXPRESSION ..... 138

FIGURE 6.5: UNDER CAG PROMOTER, CHR2 EXPRESSES IN MYOCYTES, CAUSING INFLAMMATION ..... 142

FIGURE 6.6: WITHOUT EYFP REPORTER, CHR2 STILL ELICITS IMMUNE RESPONSE ..... 144

FIGURE 6.7: SANDWICH ELISA FOR DETECTION OF ANTI-CHR2-EYFP PLASMA ANTIBODIES ..... 152

FIGURE 6.8: IMMUNE RESPONSE IS SPECIFIC TO WT RATS ..... 153

FIGURE 6.9: IMMUNE RESPONSE LARGELY SPECIFIC TO PLACEBO RATS ..... 154

FIGURE 6.10: PS2 DID NOT PREVENT ANTI-CHR2 IMMUNE RESPONSE ..... 155

FIGURE 6.11: BIODISTRIBUTION AND ELISA FOR CAG PROMOTER ..... 156

FIGURE 6.12: EXCITOTOXICITY CONTROLS REVEAL NO DIFFERENCE FROM RATS WITH REGULAR STIMULATION ..... 157

FIGURE 6.13 CHR2-ONLY VIRUS STILL ELICITS IMMUNE RESPONSE ..... 159

FIGURE 7.1 GENERAL CONTROLLER ARCHITECTURE FOR CLOSED-LOOP OPTOGENETICS 171

FIGURE 7.2: WEARABLE DESIGNS AS A WRISTBAND (TOP) OR PATCH (BOTTOM) ..... 173

FIGURE 7.3 MOTOR CONTROL ARCHITECTURE FOR POSITION CONTROL USING OPTOGENETICS ..... 174

FIGURE 7.4: CLOSED LOOP POSITION CONTROL DIAGRAM OF MURINE ANKLE ..... 175

FIGURE 7.5: CLOSED-LOOP POSITION CONTROL OF MURINE ANKLE ..... 175

FIGURE 7.6 LED KNEE BRACE OR LEG PATCH FOR OPTOGENETIC CORRECTION OF FOOT-DROP ..... 177

FIGURE 7.7: MOTOR CONTROL ARCHITECTURE FOR FOOT-DROP CONTROL USING OPTOGENETICS ..... 177

FIGURE 7.8 WEARABLE PATCH FOR OPTOGENETIC VAGUS NERVE STIMULATION ..... 178

FIGURE 7.9: CONTROLLER ARCHITECTURE FOR OPTOGENETIC VNS TREATMENT OF DEPRESSION ..... 179

# List of Abbreviations and Acronyms

AAV: Adeno Associated Virus
AC: Anterior Compartment
ALS: Amyotrophic Lateral Sclerosis
ANOVA: Analysis of Variance
AP: Action Potential
BBB: Blood Brain Barrier
BF: Biceps Femoris Muscle
BSCB: Blood Spinal Cord Barrier
c.p.n.: Common Peroneal Nerve
CBC: Complete Blood Count
CHAT: Choline Acetyl Transferase
ChR2: ChR2(H134R)
CMAP: Compound Motor Action Potential
CNS: Central Nervous System
CTL: Cytotoxic T Lymphocytes
DAPI: 4',6-diamidino-2-phenylindole
DC: Duty Cycle
DTH: Delayed Type Hypersensitivity
EAE: Experimental Autoimmune Encephalomyelitis
ELISA: Enzyme-Linked Immunosorbent Assay
EMG: Electromyography
EMS: Electrical Muscle Stimulation
ET: Essential Tremor
FES: Functional Electrical Stimulation
FOS: Functional Optogenetic Stimulation
FSC: Forward Scatter
GN: Gastrocnemius Muscle
H&E: Haematoxylin and Eosin stain
Hb: Hemoglobin
HCT: Hematocrit
IF: Immunofluorescence
IM: Intramuscular
IMES: Implantable Myoelectric Sensor
LED: Light Emitting Diode
LIFE: Longitudinal Intrafascicular Electrode
LTMR: Low Threshold Mechanoreceptor
MC: Monte Carlo
MCH: Mean Corpuscular Hemoglobin
MCV: Mean Corpuscular Volume
MHC: Major Histocompatibility Complex
MOI: Multiplicity of Infection
MS: Multiple Sclerosis
MU: Motor Unit
NF200: Neurofilament 200
OPD: o-phenylenediamine
PBS: 0.1M Phosphate Buffered Saline 1X
PC: Posterior Compartment
PDMS: Polydimethylsiloxane
PFA: Paraformaldehyde
PNS: Peripheral Nervous System
PRR: Pattern Recognition Receptor
PW: Pulse Width
PWA: Persons with Amputation
$Rag2^{-/-}$: Rag2 knockout
RBC: Red Blood Cells
RDW: Red Blood Cell Distribution Width
ROS: Reactive Oxygen Species
s.n.: Sciatic Nerve
SCID: Severe Combined Immunodeficiency
SSC: Side Scatter
t.n.: Tibial Nerve
TA: Tibialis Anterior Muscle
TENS: Transcutaneous Electrical Nerve Stimulation
TIME: Transverse Intrasfascicular Multichannel Electrode
VNS: Vagus Nerve Stimulation
vp: viral particles
WBC: White Blood Cell
WT: wild-type

# List of Appendices

Appendix 1: Approved Peripheral Nerve Stimulation Devices[12] 22

Appendix 2: Supplemental Figures for Chapter 5 106

Appendix 3: Supplemental Figures For Chapter 6 152

# 1 INTRODUCTION

The ability to control peripheral nerve activity has been considered a key challenge in a wide diversity of medical sub-disciplines. Peripheral nerves are implicated in the majority of human physiology, ranging from autonomic regulation of cardiovascular, pulmonary, and gastric organ-systems to the somatic control of skeletal muscle and sensation of cutaneous, nociceptive, and proprioceptive fibers. As the body's key communication system, peripheral nerves function as a biological information superhighway, conveying complex signals at rapid speeds via electrical depolarization. Peripheral nerve stimulation has a profound effect in mitigating numerous pathologies associated with the peripheral nervous system (PNS). Somatic peripheral nerve stimulation, synonymous with functional electrical stimulation (FES), is commonly employed in chronic pain, but also has been used in paralysis, such as post-stroke drop foot, cerebral palsy, multiple sclerosis, and as of recently, in closed-loop amputation feedback[1]. Autonomic peripheral nerve stimulation has shown efficacy in depression and epilepsy via vagus nerve stimulators, in bladder and bowel control via sacral neuromodulation, and recent evidence suggesting opportunities in diabetes, obesity, and heart & lung function. In this chapter, the current state of the art of peripheral nerve stimulators are described. Additionally, we describe the rationale for the study of optogenetic peripheral nerve stimulation technologies for addressing some of the unique challenges of conventional electrical nerve stimulation technologies.

## 1.1 Current State of the Peripheral Nerve Stimulation

A great variety of technologies are currently employed for peripheral nerve stimulation. Many devices are on the market with FDA approvals as both 510(k)s and PMAs. Other devices are in investigational or research stages, at some level of human or animal models. Further, there are devices for peripheral nerve stimulation with applications that range from diagnosis to treatment. Electrodes affixed to a current source and recording system are employed clinically for nerve conduction tests in the diagnosis of entrapment and demyelination, with a diagnosis of carpal tunnel syndrome representing a very common application for the tool. On the treatment side, transdermal and implantable peripheral nerve stimulation devices have been employed in several different nerves for unique applications. Applications of transdermal FES of somatic sensory nerves, for example, commonly include the mitigation of chronic pain. Transdermal systems are generally divided into transcutaneous electrical nerve stimulation (TENS) or electrical muscle stimulation (EMS) devices based on their application. On the implantable side, devices include nerve cuff electrodes, book electrodes, Transverse Intrafasicular Multichannel Electrodes (TIMEs), Longitidual Intrafscicular Electrodes (LIFEs), paddle electrodes, and sieve or regenerative electrodes[2]. In addition, multichannel cylindrical electrodes, such as those commonly used in Spinal Cord Stimulation (SCS) are frequently used off-label to treat peripheral nerve pain[3–6]. Lastly, some systems are partially implanted. Percutaneous cylindrical multichannel electrodes have recently become the primary method of peripheral nerve stimulation in recent years[7]. Compared to transdermal devices, implantable devices can directly target individual nerves with fewer off-target effects.

### 1.1.1 Advantages of unique peripheral nerve interfaces

We highlight the key advantages and disadvantages to several peripheral nerve electrode interface designs (Fig 1.1). Cuff electrodes can vary significantly in size and shape, but the general form employs a flexible silicone or polyimide biocompatible membrane designed to wrap around a nerve, with stainless steel, platinum, iridium or tungsten electrodes built into the internal surface facing the superficial epineurial surface[8]. Key advantages of cuff electrodes include selective stimulation of fascicles by multiple electrode contact design,

minimal mechanical distortion of the electrodes during motion, and proximity of electrodes to the nerve[9]. However, cuff electrodes are disadvantaged in that high-resolution selective stimulation is not possible due to fascicular variability of each peripheral nerve both across patients and throughout the length of a single patient's nerve. A TIME can penetrate through both epineurium and perineurium, the fibrous tissue layers enveloping the nerve and its fascicles respectively. The drawback of a TIME is that it elicits a fibrosis response over time and cannot be used permanently for fear of tearing or damaging the nerve, or the risk of axonal loss[10]. Sieve electrodes and have been shown to demonstrate nerve efferent and afferent signaling in a nerve regeneration model; however, sieve electrodes are considered to be damaging to the nerve due to compressive forces applied by the rigid silicon during motion[11]. Each design represents a unique tradeoff between stimulation specificity and invasiveness. As the device becomes more invasive, it is associated with increased inflammation and axonal death due to mechanical stresses. Axonal death begins to occur as low as ~30 mm Hg at the nerve; within 1 hour, research has shown vascular changes in animal models and paraesthesia in human subjects[12]. Inflammation due to foreign body encapsulation can easily induce these elevated pressures at the nerve. In addition, drawbacks associated with implantable devices include mechanical failure, device tissue heating, a chronic foreign body inflammatory response.

**Figure 1.1 Common Implantable Peripheral Nerve Stimulation Paradigms**

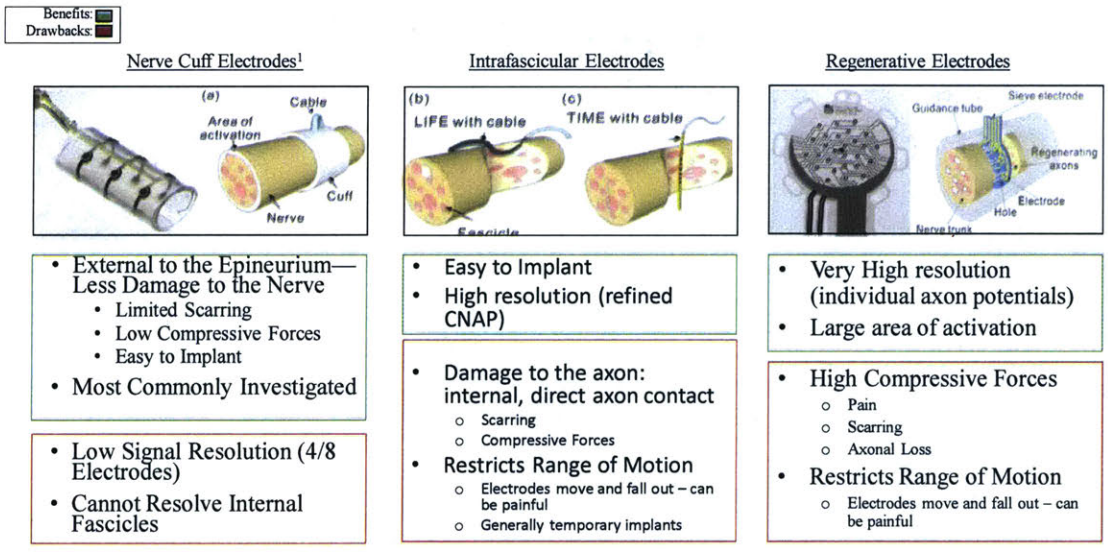

### 1.1.2 Applications of Peripheral Nerve Interfaces

Peripheral nerve interfaces have been employed previously for stimulation of phrenic nerves for diaphragmatic paralysis, somatic nerves in patients with hemiplegia and paraplegia, vagal nerves in patients with epilepsy and depression, autonomic nerves for urinary and gastrointestinal disorders, and peripheral nerves for control of neuropathic pain[13]. Within the neuropathic pain, the majority of indications are within the head and face for occipital neuralgia, cluster headache, trigeminal neuralgia. The somatic nerves for neuropathic pain have focused on median, ulnar, sciatic, ilioinguinal, and genito-femoral nerves[13]. Of the annually implanted neurostimulators, global market insights estimates that in 2018, roughly 15% are for sacral nerve stimulation and roughly 5% are for vagus nerve stimulation. About 60% of neurostimulators are implanted each year for spinal cord stimulation. However, within the United States, peripheral nerve stimulation for the treatment of chronic pain has been considered unapproved by the FDA until recently – as a result, a decent portion of these spinal cord stimulation devices have been used in an off-label for different regional pain syndromes.

### 1.1.3 Current Peripheral Nerve Stimulation Devices

A full list of devices approved (as of 2016) for peripheral nerve stimulation is given in Appendix 1[13]. For the treatment of chronic pain, the predominant clinical use has been the off-label use of Medtronic or St. Jude SCS devices such as the InterStim II. However, the field of peripheral nerve stimulation is rapidly growing. Two recently approved technologies have targeted peripheral nerve stimulation for the treatment of chronic pain directly. Bioness Inc.'s Stimrouter device was approved by the FDA in February 2015 for the treatment of chronic peripheral nerve pain (Figure 1.2). Stimwave's StimQ system was approved one year later for the same indication. Both devices are on-label.

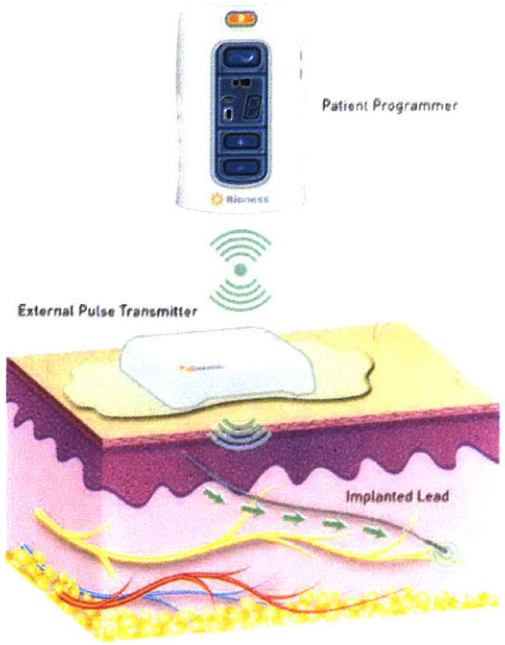


**Figure 1.2: StimRouter device – wireless, percutaneous control of chronic pain.**

For the treatment of paralysis, several transdermal and implanted systems have been employed in research and clinical applications. The NeuroControl Freehand system was the first FDA approved implantable FES system. The application was to restore function movement to upper limbs of tetraplegia patients with C5-C6 spinal cord injuries[14]. Although this device was taken off the market mainly due to financial constraints, several other devices employ peripheral nerve stimulation for restoration of motor functionality. The NESS H200 controls hand motor function for patients with C5 tetraplegia using surface electrodes and does not require implantation. The Parastep Ambulation System received premarket approval from the FDA in 2015 to market a full walking system for C6-T12 spinal cord injuries that restores gait in paraplegic patients, controlled by a finger switch. Lastly, there are a range of devices for treating foot drop using peripheral nerve stimulation. Common etiologies for the occurrence of foot-drop are cerebral palsy, MS, and stroke. Several TENS products are commercially available including the Bioness L300, Innovative Neurotronics Walkaide System, Ottobock's MyGait, Odstock's Dropped Foot Stimulator, and the XFT-2001. There are also implanted stimulators that are

commercially available including the Ottobock ActiGait in Europe. These products target the c.p.n. directly, with the goal of initiating dorsiflexion in a closed-loop fashion in response to detection of the swing phase of the gait cycle.

There are many challenges to today's electrical peripheral neurostimulation systems. Almost all systems have a certain risk of migration rate, ranging from 2-13% in peripheral nerve stimulation for chronic pain[15,16] to 16% for sacral nerve stimulation[17]. Additionally, pain is reported in up to 25% of sacral nerve devices over the lead or generator site[17]; this data is not available for peripheral nerve stimulation for pain, but the overall complication rate is reported to be 24%[15]. Systems for vagus nerve stimulation (VNS) have a number of common side effects including cough, hoarseness, dyspnea, and headache. Severe side effects include paralysis or cardiac arrest[18]. Systems for foot drop are suggested to have limited-to-no improvement over traditional ankle foot orthoses, only modest improvements in walking, and sometimes pain associated with undesired stimulation of properly innervated sensory subsets[12]. Further, FES for paralysis in general has been shown to result in high levels of energy consumption, as measured by heart rate and metabolic consumption with use[19]. All of the above challenges are limited to conventional electrical systems, which need to be directly adjacent to the target axons, cannot specify between molecularly distinct or anatomically unique efferent or afferent axons, and recruit motor units in a reverse order recruitment pattern.

## 1.2 Optogenetics for Peripheral Nerve Stimulation

The development and application of optogenetics to FES represents a new opportunity for the expansion of peripheral nerve stimulation. Some benefits of FOS over FES include natural order motor unit recruitment[20], ability to target molecularly defined nerve subtypes[21,22], and anatomical specificity via retrograde transport[23]. Further, FOS can selectively activate nerves from a distance, mitigating the high complication rates associated with pain and infection due to direct mechanical compression. FOS also has high-resolution specificity, which can target precise subsets of neurons based on the type of gene therapy vector employed. However, FOS is not without its own set of complications. Drawbacks of FOS include that it requires gene therapy, generally

performed today via AAV injections. Gene therapy within neurons of the central nervous system result in a permanent change to those cells, which has an inherent risk due to unknown effects of long-term transgenesis. Further, there are a range of known effects to address with optogenetic gene therapy itself, which is discussed in more detail in Chapters 3 & 7[24,25].

The potential for optogenetics to translate into a clinical tool hinges on a few key upcoming trials. In March 2016, Retrosense Therapeutics initiated the first-in-human gene therapy for optogenetics using ChR2 as a potential treatment for retinitis pigmentosa[26]. Additional companies such as Gensight have similar optogenetic clinical trials, which may potentially begin in the next few years[27,28]. If these trials demonstrate successful results, the clinical potential for FOS in paralysis treatment or the mitigation of chronic pain may be the next steps for optogenetic applications. Even further, optogenetic techniques have recently been applied to peripheral nerves for glucose-related pathologies[29], cardiac pacing, gastrointestinal motility, erectile dysfunction, and others. The range of possibilities for successful optogenetic implementation is very broad. However, for these clinical tools to become reality, studies optimizing optogenetic stimulation of nerves at depth, while concurrently evaluating time course, safety and efficacy are critical.

This thesis first seeks to discuss the underlying motivation for optogenetic peripheral nerve interfaces. In Chapter 2, an experiment assessing the challenges associated with high-resolution microchannel peripheral nerve interfaces is presented along with a discussion of how optogenetics can address some of the key challenges. Chapter 3 reviews the literature of peripheral nerve specific optogenetic experiments with a focus on modeling the variables that affect optogenetic activation of deep tissue peripheral nerve targets. In Chapter 4, a transdermal approach to optogenetic activation of peripheral nerves is presented. In Chapter 5, a method for targeting anatomically defined peripheral nerve susbsets from the same target peripheral nerve using optogenetics is presented. In Chapter 6, a mechanism for extending optogenetic longevity in peripheral nerves is presented.

Lastly, in Chapter 7, the findings are summarized, and the future work required for further development of clinical peripheral nerve optogenetic therapies is presented.

# APPENDIX 1: PERIPHERAL NERVE STIMULATION DEVICES[13]

| No. | Indication | Company | Device | USA (FDA) | Europe (CE mark) | Canada (Health Canada) | Notes |
|---|---|---|---|---|---|---|---|
| *Pain* | | | | | | | |
| 1 | Severe intractable pain | Medtronic | RF systems (X-Trel, Mattrix) with Resume II (3587A), Resume TL (3986A), and OnPoint (3987A) electrode | * | * | 05/2000 | True PNS system/RF systems only |
| 2 | Severe intractable pain | St. Jude Medical | RF system (Renew) with percutaneous leads (3143, 3146, 3153, 3156, 3183, 3186, 3066, 3161, 3163, 3166, 3169) | * | * | | True PNS system/RF systems only |
| 3 | Chronic intractable postsurgical back pain | Medtronic | RestoreUltra, RestoreAdvanced, RestoreSensor, and PrimeAdvanced with percutaneous leads | | 05/2011 | * | Subcutaneous nerve stimulation |
| 4 | Intractable chronic migraine | St. Jude Medical | Genesis system | | 09/2011 | | PNS of occipital nerves |
| 5 | Intractable chronic migraine | St. Jude Medical | Eon Mini system | | 09/2012 | | PNS of occipital nerves |
| 6 | Chronic intractable pain in the trunk | Boston Scientific | Precision Plus SCS system | | 08/2012 | | PNS |
| 7 | Pain due to diseases of peripheral nerves | Neurimpulse | Lightpulse 100, 100L, 102 systems | | 11/2010 | | Subcutaneous PNS |
| 8 | Chronic intractable pain | Spinal Modulation | Axium system | IDE, 08/2013 | 12/2011 | | Dorsal root ganglion stimulation |
| 9 | Acute pain of cluster headache | Autonomic Technologies | Pulsante SPG stimulation system | IDE, 07/2014 | 10/2012 | | Sphenopalatine ganglion stimulation |
| 10 | Chronic shoulder pain | SPR Therapeutics | Smartpatch PNS system | | 01/2013 | | Up to 30 days stimulation |
| 11 | Chronic migraine | CerboMed | t-VNS system | | 08/2012 | | Transcutaneous vagus nerve stimulation |
| 12 | Chronic migraine | Cephaly Technology | Cephaly TENS system | 04/2014 | * | 11/2010 | Transcutaneous trigeminal nerve stimulation |
| 13 | Chronic peripheral neuropathic pain | Algotec | Neurostimulator PENS therapy | | * | | PENS therapy – no implant involved |
| 14 | Chronic amputation pain | Neuros Medical | Altius implantable system | IDE, 09/2013 | | | High frequency nerve block |
| 15 | Chronic pain of peripheral nerve origin | Bioness | StimRouter neuromodulation system | IDE, 04/2012 | | | Implanted PNS device with external power source |
| 16 | Chronic low back pain | Mainstay Medical | ReActiv8 system | | | | Medial branch stimulation |
| *Motor dysfunction* | | | | | | | |
| 17 | Partial or complete respiratory insufficiency | Avery Biomedical | Mark IV breathing pacemaker | 03/1998 | *(1999) | | Phrenic nerve stimulation |
| 18 | Need in maintenance of artificial respiration | Atrotech | Atrostim PNS V2.0 system | | * | | Phrenic nerve stimulation |

| | | | | | | | |
|---|---|---|---|---|---|---|---|
| 19 | Respiratory failure due to SCI | Synapse Biomedical | NeuRx diaphragm pacing system | HDE, 06/2008 | 11/2007 | 03/2013 | Diaphragmal stimulation |
| 20 | Respiratory failure due to ALS | Synapse Biomedical | NeuRx diaphragm pacing system | HDE, 09/2011 | 11/2007 | | Diaphragmal stimulation |
| 21 | Obstructive sleep apnea | Inspire Medical | Inspire system | 04/2014 | 12/2010 | | Hypoglossal nerve stimulation |
| 22 | Obstructive sleep apnea | ImThera Medical | Aura 6000 system | IDE, 11/2014 | 03/2012 | | Hypoglossal nerve stimulation |
| 23 | Obstructive sleep apnea | Apnex Medical | HGNS system | IDE, 08/2011 | | | Hypoglossal nerve stimulation |
| *Epilepsy* | | | | | | | |
| 24 | Refractory epilepsy | Cyberonics | NCP/Demipulse/Aspire systems | *(1997) | *(1994) | 08/1998 | Implanted vagus nerve stimulation |
| 25 | Epilepsy | CerboMed | NEMOS system | | 03/2010 | | Transcutaneous vagus nerve stimulation |
| 26 | Epilepsy/ Lennox-Gastaut syndrome | NeuroSigma | Monarch eTNS system | HDE, 01/2015 | 09/2012 | 04/2013 | Transcutaneous trigeminal nerve stimulation |
| *Depression* | | | | | | | |
| 27 | Treatment-resistant depression | Cyberonics | VNS system | 07/2005 | 03/2001 | 04/2001 | Implanted vagus nerve stimulation |
| 28 | Depression | CerboMed | NEMOS system | | 03/2010 | | Transcutaneous vagus nerve stimulation |
| 29 | Depression | NeuroSigma | Monarch eTNS system | | 09/2012 | 04/2013 | Transcutaneous trigeminal nerve stimulation |
| *Urinary/gastrointestinal dysfunction* | | | | | | | |
| 30 | Urinary/fecal urge incontinence | Medtronic | InterStim (3023) and InterStim II (3058) neurostimulators | *(1997) | *(1994) | 12/1999 | Sacral nerve stimulation |
| 31 | Overactive bladder/urinary retention | Medtronic | InterStim II (3058) neurostimulator | 07/2006 | *(2006) | * | Sacral nerve stimulation |
| 32 | Overactive bladder | Axonics | Axonics system | | | | Sacral nerve stimulation |
| *Hypertension/heart failure* | | | | | | | |
| 33 | Resistant hypertension | CVRx | Rheos Baroflex/ Barostim neo hypertension therapy system | HDE, 10/2014 | 10/2007 | | Carotid sinus and nerve stimulation |
| 34 | Heart failure | CVRx | Barostim neo system | | 09/2014 | | Carotid sinus and nerve stimulation |
| *Obesity* | | | | | | | |
| 35 | Severe obesity | EnteroMedics | Maestro system | 01/2015 | 03/2009 | | Vagus nerve block |
| *Tinnitus* | | | | | | | |
| 36 | Tinnitus | Micro-Transponder | Serenity system | IDE, 10/2013 | | | Vagus nerve stimulation with paired impulses |

* Asterisk denotes existence of full regulatory approval when the date of approval is unknown or unconfirmed. HDE = Humanitarian device exemption; IDE = Investigational device exemption.

# 2 Challenges in High-Resolution Synthetic Peripheral Interfaces

Peripheral nerve interfaces for high-resolution recording and stimulation of nerve activity have significant potential, but also significant drawbacks. We describe the implementation of regenerative microchannels for peripheral nerve interfacing. In this work, we evaluate regeneration-based microchannel activity within peripheral nerves in a rat and ferret model. We describe significant challenges in their implementation that represent key limitations to future clinical potential. As a result of these challenges, we describe the opportunity for optogenetic peripheral nerve stimulation to address the full range of these challenges.

## 2.1 Introduction

As wearable robotics has advanced in design and miniaturization, a large variety of advanced upper and lower-extremity prostheses have been built to improve the quality of life for persons with amputation (PWA). The commercially available bebionic3 is a myoelectric-controlled robotic devices, capable of 14 different grip patterns that can enable

a handshake, pick up a key, control a computer mouse, and perform a range of other tasks. However, because efferent control in the bebionic3 and other upper-extremity limb prostheses is limited to skin surface electromyography (EMG) of only 1-2 independent muscle bodies, the user has to manually switch between different grip patterns with the press of a switch or a change of settings on the interface computer, limiting native intuitive control. New developments with implantable myoelectric sensors (IMES) have enabled recordings from a larger number of individual residual muscle bodies in both upper limb[30] and lower limb amputees[31]. However, residual muscle bodies vary from person to person – persons with transhumeral and transfermoral amputations lack the residual muscle bodies of the forearm and leg respectively, which control motion in the wrist, hand, ankle and foot. To provide a higher degree of control, direct recordings from the nerves may be able to recreate the independent muscle signals lost during amputation, consistent with evidence suggesting the somatotropic arrangement of peripheral nerves[32,33].

Recently, several groups have developed neuroprosthetic interface devices capable of providing long-term touch and vibration feedback for PWA using nerve cuffs and intrafascicular electrodes[1,34]. These devices have enabled moderate to long-term afferent feedback to PWA from "second skin" pressure sensors located on the fingertips of the prosthesis; however, the neuroprosthetic interfaces employed are anatomically limited. Nerve cuffs can only selectively stimulate the external surface of large nerves and they cannot selectively stimulate a small, targeted bundle of axons within the body of the nerve[2]. Book electrodes have increased spatial range by flattening the nerve, but, like cuff electrodes, they do not have high spatial resolution for groups of axons[2]. Intrafascicular electrodes have better spatial resolution in the body of the nerve, but they are limited to recording only a small fraction of nerve axons and may have long-term complications[2]. Lastly, implantable microarrays provide exquisite resolution, down to individual single-unit activity from individual sensory action potentionals[35]; however, they are associated with significant pathology to the nerve due to high mechanical stiffness[2]. Regenerative microchannel peripheral nerve interfaces may offer a highly selective, mechanically compliant alternative to conventional nerve interface technologies because of their unique

potential to provide increased biospatial resolution for both control of and sensory feedback from a prosthesis[2].

Previous attempts to develop microchannel peripheral nerve interfaces have been met with some success[36–39]. Musick et al. (2013) implemented a rat s.n. end-to-end repair model to demonstrate nerve regeneration within an uncoated poly di-methyl siloxane (PDMS) microchannel array[36]. The microchannel functioned to bridge the transected nerve, which regrew through the seventy 110 μm x 120 μm channels. Although regrowth was not present in all channels, each channel that exhibited regrowth contained blood vessels, myelinated nerves, and fibrous tissue. One key finding was that the total number of nerve fibers throughout all channels decreased significantly from 2067 ± 617 at 3 months postop to 442 ± 193 at 9 months postop. Possible explanations include a pruning of axonal sprouts, chronic inflammatory response or mechanical compression causing axonal "centering" towards the middle of each channel. To mitigate against both chronic inflammatory response and mechanical compression, the Musick et al. study supports the idea that geometry of the channel may be of critical importance; small channel size may be a limiting factor in the development of healthy nerve fibers, due to a 15 μm-50 μm thick contractile capsule guiding nerve regeneration and outgrowth[40].

In addition to cross-sectional area, microchannel length has been previously analyzed for optimal regeneration. Using PDMS channels, Lacour et al. (2009) determined that a 1 mm length was the best to encourage proliferation based on total axon counts at 4 weeks and 12 weeks post implant through the channels and that numbers dropped significantly when the channels were larger than 3 mm in length. Interestingly, the mean number of axons increased in the 1 mm length channel, from 171 at 1 month postop to 1,427 after 3 months postop, likely due to the additional sprouting in the 2 month period[37].

Recently, microchannels were implemented in a gait study that monitored long-term recordings from nerves over the gait cycle in awake moving animals[41]. Increased neural

signals were differentially associated with the plantarflexion portion of the gait cycle, as would be expected with direct recordings from motor neurons. However, an analysis of motor neuron distribution within the channels may have helped explain whether channels exhibiting weaker electroneurographic signals during plantarflexion were directly associated with majority large motor axons. The objective of this study is to evaluate nerve regeneration through three types of nerve arrays: passive, active, and active with collagen. The passive arrays we implant into the rat t.n. and the active and active with collagen we implant into ferret t.n. We employ electrophysiology and immunofluorescence to assess the extent of regeneration through these constructs, which enables the identification of unique populations of nerve subtypes by channels.

## 2.2 Methods

### 2.2.1 Passive Microchannel Fabrication

The passive microchannel array fabrication process utilized standard microfabrication and assembly techniques[37]. The final device design was a 4×4 array of 3 mm length, 200 μm wide square channels, with a pitch of 250 μm in both dimensions. The array was composed of layers of PDMS, an elastomer commonly used in implantable biomedical devices, and in previous microchannel designs[36]. First, an SU-8 mold was photolithographically defined on a 4" silicon wafer substrate. A 200 μm thick layer of PDMS (Sylgard 184, Dow Corning, 10:1 mixing ratio) was spin-coated onto the mold and thermally cured. The individual layers were manually cut from the substrate and released from the mold. The full array was formed by manually stacking, aligning, and bonding individual PDMS layers using oxygen plasma techniques[42].

### 2.2.2 Active Microchannel Electrode Array Fabrication

The active microchannel arrays were fabricated from an SU-8 substrate, a flexible photosensitive polymer commonly used in the microelectronics industry because of its versatility and potential for generating high aspect-ratio structures[43]. As a biocompatible polymer[43,44], SU-8 has been extensively explored and used as an implant material for biomedical devices[45]. It was employed to fabricate our microchannel arrays, balancing functionality, scalability, and ease-of-use. The final device design in this study was a 4×5

array of 3 mm long, 200 μm wide square channels, with a sidewall thickness of 10 μm in both dimensions (Fig 1a). Each channel was embedded with three electrodes, one in the center and the remaining two on the outermost regions in a standard tripolar layout configuration for recording peripheral nerves[46].

The array comprised stacked individual layers, assembled in a 3-dimensional format after planar fabrication was complete. First, a sacrificial release layer of aluminum was deposited onto a 6" silicon wafer. A 10 μm layer of SU-8 was photolithographically patterned on top of the aluminum, defining the device lower substrate. Then, titanium and platinum (10 nm and 50 nm, respectively) were patterned using a standard liftoff procedure[47], thereby defining the electrode sites, bond pads, and interconnects. A 2 μm thick SU-8 electrical insulation layer was patterned on top of the metal such that only the electrode sites and bond pads were exposed. The sidewalls of the microchannels were defined by patterning a 200 μm thick layer of SU-8. The sidewalls measured 10 μm wide and 3 mm long. Finally, the individual layers were released from the wafer by selectively etching the sacrificial aluminum layer. The full array was formed by manually stacking, aligning, and bonding individual device layers. This was accomplished by using SU-8 itself as an adhesion layer. Several microns were deposited on the underside of each layer, via aerosol (SU-8 MicroSpray, Microchem), and the layers were manually stacked, aligned, and bonded (Fig 2.1A). The bonding procedure was the same as standard SU-8 curing methods, utilizing UV-exposure and thermal treatment.

Each electrode in the array was electrically connected, via metallic traces integrated into a ribbon cable, to external recording and stimulating electronics. The ribbon cable was fabricated using standard flexible circuit board techniques, and was composed of a dual layer of copper traces embedded in polyimide, another commonly employed flexible biocompatible polymer[45]. Both terminals of the ribbon cable contained 2-dimensional arrays of through-holes designed to interface with both the microchannel array and a percutaneous port. The ribbon cable was twisted into a helical shape under mild heat to allow for stretchability along its length. This manipulation was performed as a strain relief

measure to provide relative movement buffer between the device and the percutaneous port to eliminate both buckling in the cable or transmission of mechanical force on the device.

The percutaneous port was composed of an electrical connector (NanoStrip, Omnetics Connector Corporation) embedded in a biocompatible shell. This shell was fabricated with a USP-VI biocompatible 3D printing resin (Duraform PA, 3D systems) and designed to allow for easy electrical docking and connection to skin tissue. The metallic tails of the electrical connector were connected to the through-holes of the ribbon cable using a biocompatible conductive epoxy (EP3HTSMed, Master Bond Inc). The interface was embedded in silicone. The microchannel array was connected to the ribbon cable using pin-grid array techniques[48]. Individual gold-coated pins were connected to the array of through-holes in the ribbon cable, and that array of pins subsequently connected to the microchannel array bond pads (Fig 2.1B). All connections were again made through the use of a biocompatible conductive epoxy and the interface was embedded in silicone. The final device measured ~20 cm long, but could be stretched more than 50% without significant force transmission (Fig 2.1C).

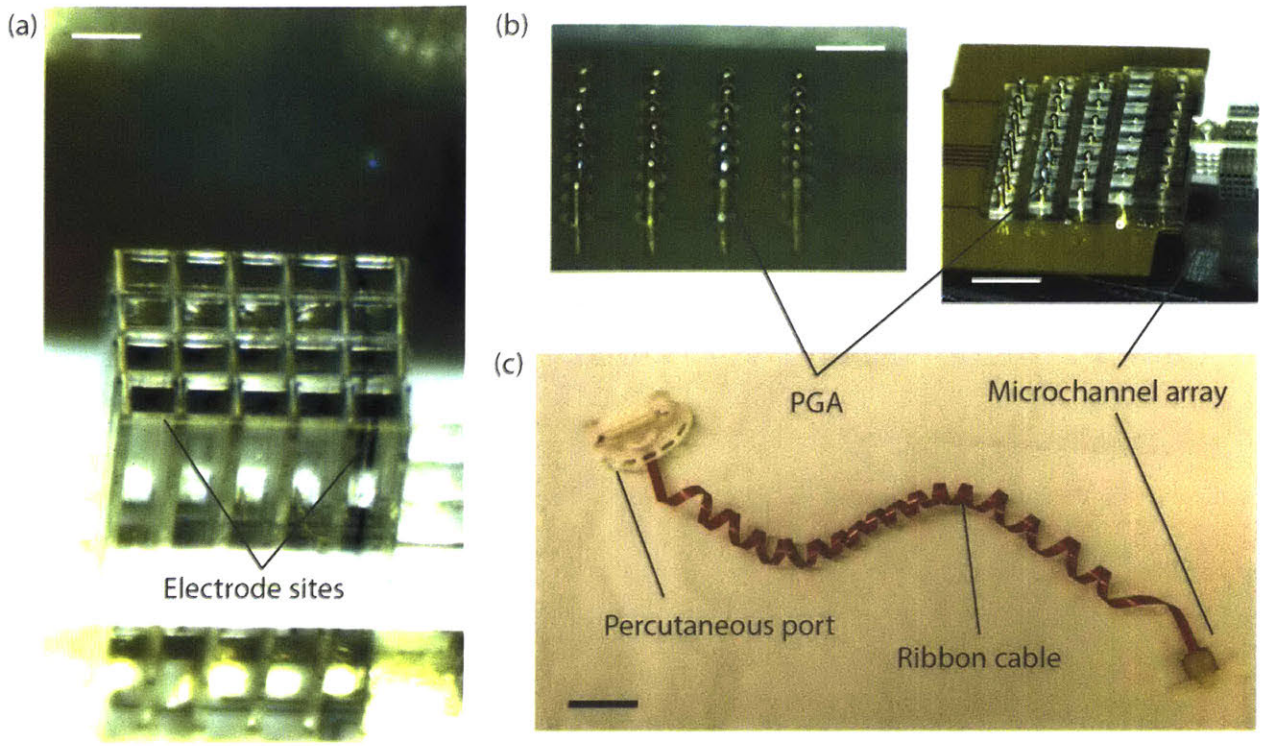


**Figure 2.1 Microchannel Construction**

*A) Assembled SU-8 microchannel array with visible Pt electrodes. Scale bar, 400 μm. B) PGA techniques are used to electrically connect the electrodes in the array to interconnects on a ribbon cable. Scale bar, 1 mm. C) The overall system is composed of three parts: the microchannel array, a ribbon cable interconnect, and a percutaneous port. Scale bar, 2.5 cm.*

## 2.2.3 Collagen Scaffold Array Fabrication

It was hypothesized that a porous collagen scaffold introduced within the microchannels may help enhance regenerated axon counts both in the short-term and long-term and help mitigate against the chronic foreign body response. To make the Collagen-GAG suspension for the channels, lyophilized bovine type 1 collagen (Advanced BioMatrix) was blended using a dispersing tool (IKA) with chondroitin 6-sulfate solution (C-4384, Sigma) in glacial acetic acid in a procedure previously described[49]. Each silicone tube end of the completed microchannel was sealed using cut micropipette tips, sealed by a custom-

fabricated elastomeric cylinder (Qure Medical). The blended collagen mixture was injected through the elastomer and into the microchannels using a 3mL syringe and a 22G needle. A 25G needle was placed through the elastomer on the opposite side of the channel to permit air to flow out of the sealed channels. The filled Collagen-GAG device was slowly lowered at 100 μm/s using a custom fabricated motor system into Slytherm XLT Heat Transfer Fluid (Chempoint) cooled to -100°C with liquid nitrogen to orient ice crystals longitudinally within the collagen[49]. Following the freezing, micropipette tips were quickly removed and the still-frozen device was rapidly transferred to a lyophilizer to be freeze-dried. Verification of the longitudinally oriented collagen matrix through the channels was performed with light microscopy (Fig 2a,b).

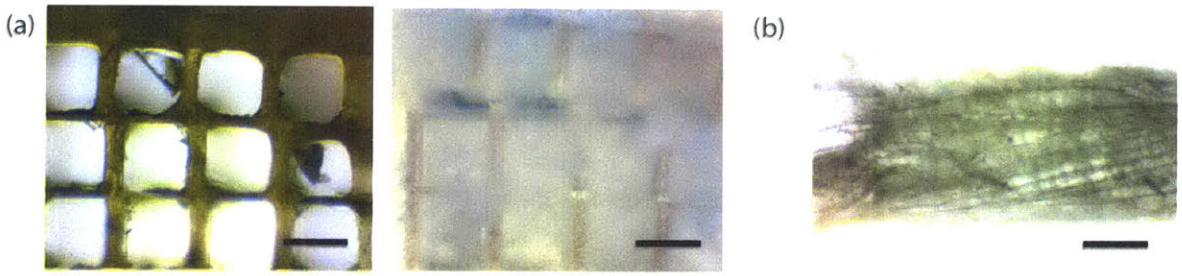


**Figure 2.2 Collagen-Embedded Microchannel**

*A) Micrograph of microchannel array cross section showing channels without (left) and with (right) an embedded collagen matrix. Scale bar, 200 μm. B) Micrograph of matrix removed from an individual channel showing axial orientation of porous collagen fibers. Scale bar, 40 μm.*

## 2.2.4 EMG and Histological Analysis of Passive Array in Rats

Experiments were conducted on four adult male Lewis rats under the supervision of the Committee on Animal Care at Massachusetts Institute of Technology. Under isoflurane anesthesia, a 1.5 cm skin incision was opened along the lateral aspect of the right hindlimb. The BF was identified and detached from its insertion at the proximal tibia and reflected dorsocaudally. The t.n. was identified electrically with a Checkpoint neurostimulator (Checkpoint Surgical) and transected 1 cm distal to the s.n. bifurcation. Careful attention was paid such that the sural n. was not cut. The microchannel was sterilized with ethylene

oxide for 24 hours prior to implantation. During implant, channels were sutured to the t.n. at both proximal and distal end plates with 9-0 nylon suture. The BF was reattached with 5-0 suture and the skin incision was closed with suture and wound glue.

Five months later, under isoflurane anesthesia, a 2 cm skin incision was made on the lateral aspect of the right hindlimb and the microchannel was identified in the same surgical method described above. The s.n. proximal to the channel was identified, and a hook electrode was carefully wrapped around the nerve to elevate it from the surrounding tissue. Stimulation current was ramped until supramaximal stimulation was achieved, as measured by EMG. The current pulses delivered to the sciatic nerve were 50 μs long and varied in amplitude from 0.01 mA to 1 mA. To record EMG, a 36AWG stainless steel multifilament wire was threaded through 25G needles; the distal 2 mm was stripped of insulation and bent over the edge of the needle. Two wires were placed in the TA and GN by inserting and then removing the needle from two locations in the muscle body, located roughly 1 cm apart longitudinally. EMG recordings were amplified (a fixed gain of 200) using the RHA2216 amplifier circuit (Intan Technologies), wired to a Raspberry Pi (Premier Farnell) with custom-built software for recording and processing EMG. Data analysis was performed using MATLAB (Mathworks).

Tissue specimens were fixed in 4% paraformaldehyde in 0.1M Phosphate Buffer Solution (PBS) at 4°C overnight and were transferred to 70% ethanol for dehydration before subsequent paraffin processing. Under a dissecting scope, PDMS layers and platinum traces were meticulously peeled away from the paraffin-processed tissue samples between layers using Number 5 forceps (Fine Science Tools) as it was discovered that the soft PDMS prevented proper tissue sectioning. The remaining tissue was embedded in paraffin blocks, and 10 μm sections were cut every ~100 μm in the tissue through the block. Gel-coated slides (Leica) with the tissue slices were heated at 100°C for 30 minutes to induce epitope retrieval. Slides were then processed for immunofluorescence using primary antibodies anti-Neurofilament 200 (NF200) (Millipore, MAB1623) and anti-Choline acetyl transferase (CHAT) (Millipore, AB144P); secondary antibodies included Alexa Fluor anti-

goat 568 nm (Life Technologies), Alexa Fluor anti-mouse 488 nm (Life Technologies), and DAPI. Slides were coverslipped in mounting medium (Dako) and images were captured with an Evos FL Auto microscope (Leica).

### 2.2.5 EMG and Histological Analysis of Active Array in Ferrets

Four adult ferrets (Charles River Labs) were anesthetized with intramuscular injections of ketamine/xylazine, followed by intubation and delivery of isoflurane anesthesia under supervision from the Committee on Animal Care at Massachusetts Institute of Technology. Ferrets were chosen for their large size, quadrupedal gait, and ability to withstand the large surgical procedure required. A 6 cm incision was made through the skin and connective fascia superficial to the distal femur, knee, and proximal tibia on the lateral aspect of the right lower limb. The BF muscle was identified, removed from its insertion at the proximal tibia, and reflected dorsocaudal to reveal the s.n., t.n., and c.p.n. (Fig 2.3A).

A second ~3 cm incision was made through the skin at the ferret's ipsilateral dorsal surface, superficial to the 8$^{th}$ rib roughly 15 cm from the first incision. Using a hemostat, the percutaneous port along with the coiled ribbon cable was tunneled through the subcutaneous fascia from the leg to the dorsal surface incision and was affixed at this incision using 5-0 nylon suture (Fig 2.3B,C). The sural n. was fascicularly dissected proximally from the t.n., and the two silicone tubes terminating the microchannel on each end were sutured to the epineurium of the proximal and distal ends of the transected t.n. using 9-0 Vicryl suture. Four ferrets were implanted with the synthetic SU-8 array: two with channels embedded with collagen and two without. The BF muscle was reattached distally over the channels, and the skin incision closed with suture and wound glue. One week post-op, x-rays were taken to verify position and orientation of the device (Fig 2.3D).

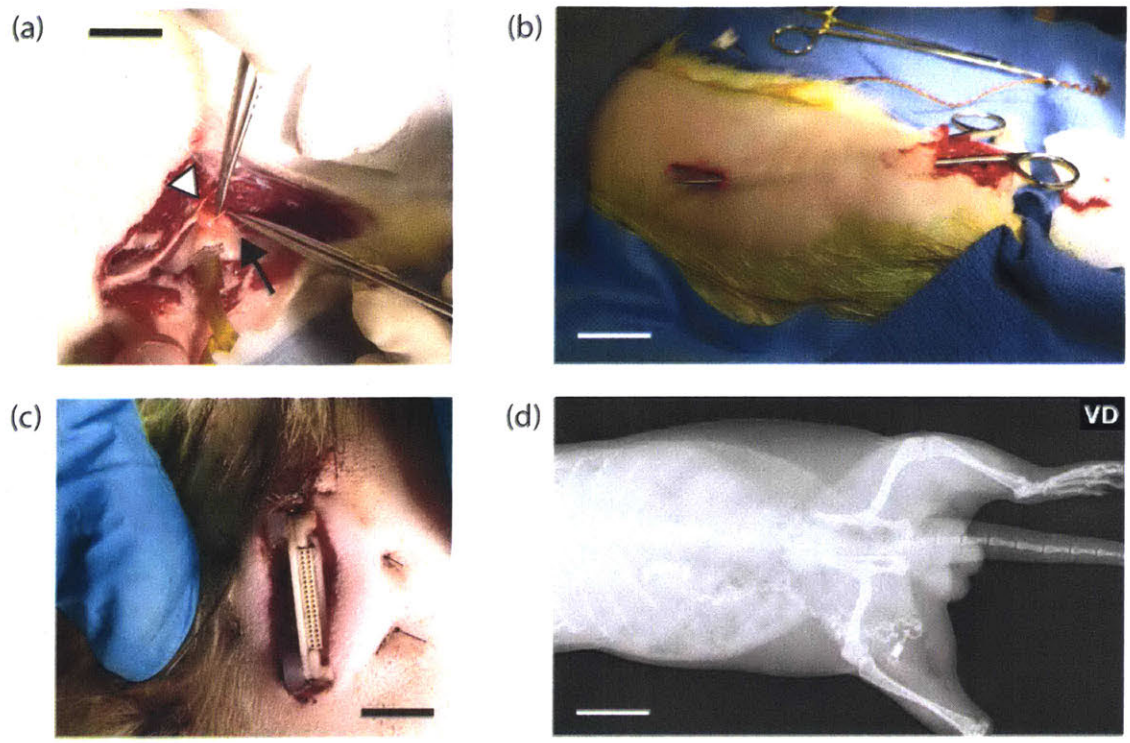


**Figure 2.3 Active Microchannel Implant in Ferrets**

*A) Distribution of s.n. branches in ferret with c.p.n. (arrowhead) and sural n. (arrow) dissected from t.n. as well as GN muscle (forceps). Scale bar: 6 mm. B) Subcutaneous tunneling from percutaneous port incision site (left) to microchannel implant site (right) with coiled ribbon cable in background. Scale bar: 3 cm. C) Percutaneous port with 40 pin connector sutured in subcutaneous space. Scale bar, 8 mm. D) Radiograph taken 1 week post-implant showing locations of channel adjacent to GN muscle and port adjacent to right caudal rib. Scale bar: 3 cm.*

## 2.3 Results

### 2.3.1 Passive Microchannel in Rats

*In vivo* regeneration was assessed 5 months after device implantation via wire EMG recordings from GN and TA muscles in the anesthetized rat (Fig 2.4A). Current-controlled single pulses or pulse trains were applied to the s.n. proximal to its bifurcation into the t.n. and c.p.n. using a custom-built hook electrode. Both EMG and ankle angular position were

recorded in the leg. Direct stimulation of the s.n. resulted in ankle dorsiflexion, with corresponding EMG activity in both the TA and the GN for both single pulses and pulse trains at maximum voltage of ~10 $mV_{pp}$ (Fig 2.4B). To verify electrophysiological regeneration through the microchannels, the c.p.n. and t.n. branches around the microchannel were transected, and stimulation was reapplied at the s.n.. Significant Compound Muscle Action Potential (CMAP) activity was recorded in the GN, indicating t.n. regeneration through the PDMS channels, but a sharp drop of EMG activity was observed at the TA because its innervation pathway was cut (Fig 2.4C). For both individual pulses and pulse trains, maximum CMAP amplitude decreased in the GN after the fibers around the microchannel were transected (P = .02, & .05 respectively by Student's t test), indicating that they too likely contributed to innervation of the GN. Mild plantarflexion was observed at the ankle, consistent with the GN+/TA- EMG response.

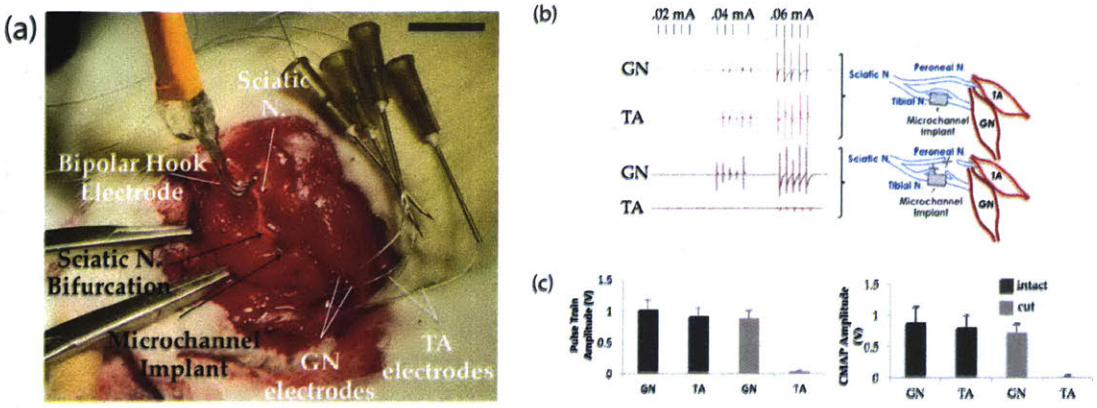


**Figure 2.4: Electrophysiological conduction of EMG through microchannel**

*(A) EMG recording equipment set-up for stimulating nerves and measuring downstream muscle activity. Scale bar: 1.5 cm. (B) EMG traces showing electrophysiological activity in the GN through the microchannel, whereas the TA has lost activity. (C) EMG amplitude in both GN and TA in response to stimulation of the t.n. and c.p.n. upstream of the microchannel.*

To assess for axon variation across individual channels by molecular subtype, double immunofluorescence of samples was conducted with anti-NF200 to stain for individual axons, anti-CHAT to stain for cholinergic motor axons[50,51], and DAPI to assess for fiber distribution by channel post-regeneration (Fig 2.5A). Certain channels exhibited predispositions to CHAT+ fibers (Fig 2.5B), CHAT- fibers (Fig 2.5C), or low axon counts altogether (Fig 2.5D). The significant variation in total axon counts by channel was identified by individual NF200+ fibers, ranging from a minimum of 13 axons per channel to a maximum of 236 axons per channel (Fig 2.5E). Significant variation in motor axon counts by channel was identified by CHAT+ fibers, ranging from a minimum of 3 axons per channel to a maximum of 142 axons per channel, represented as a percentage of total fibers (Fig 2.5F). Certain channels exhibited a predisposition to either motor or sensory axons, in accordance with the "like-fibers" travel together hypothesis. However, it is unclear what geometric or biochemical factors contributed to this phenomena as there does not seem to be a strong relationship between either channel location within the array (Fig 2.5F) or total axon count within a given channel and the percentage of CHAT+ fibers within that channel (Fig 2.5G).

In the PDMS device, 200 μm channels were implemented in the attempt to overcome the 15-35 μm thick layer of connective tissue encapsulation identified from previous research efforts regenerating axons through 110 μm channels[40]. Increasing the channel size in this study to 200 μm over previously published work of ~110μm channels[36] did not show a significant increase in axon counts either in individual channels (significant variation, but with maximum of ~250 axons) or total counts (2067 at 110 μm vs. 1906 at 200 μm). Nor did the larger channels prevent t.n. fibers from simultaneously regenerating around the device (Fig 2.5H). It was discovered that fibrous nerve encapsulation was thicker within the 200 μm regenerating microchannels presented here than the previously published work on ~100 μm channels[36], possibly indicating a geometry-independent process for chronic inflammatory changes of a foreign body response or mechanical pressure response (Fig 2.5I), which built up over the 5 month regeneration period. To confirm regeneration in the GN, muscle fibers were evaluated enzymatically for activity using an ATPase stain to identify Type 1 and Type 2 muscle fibers[52]; fibers exhibited the characteristic loss of

"checkerboard" pattern of Type 1 and Type 2 muscle fibers, as expected with nerve transection and regeneration (Fig 2.5J)[53].

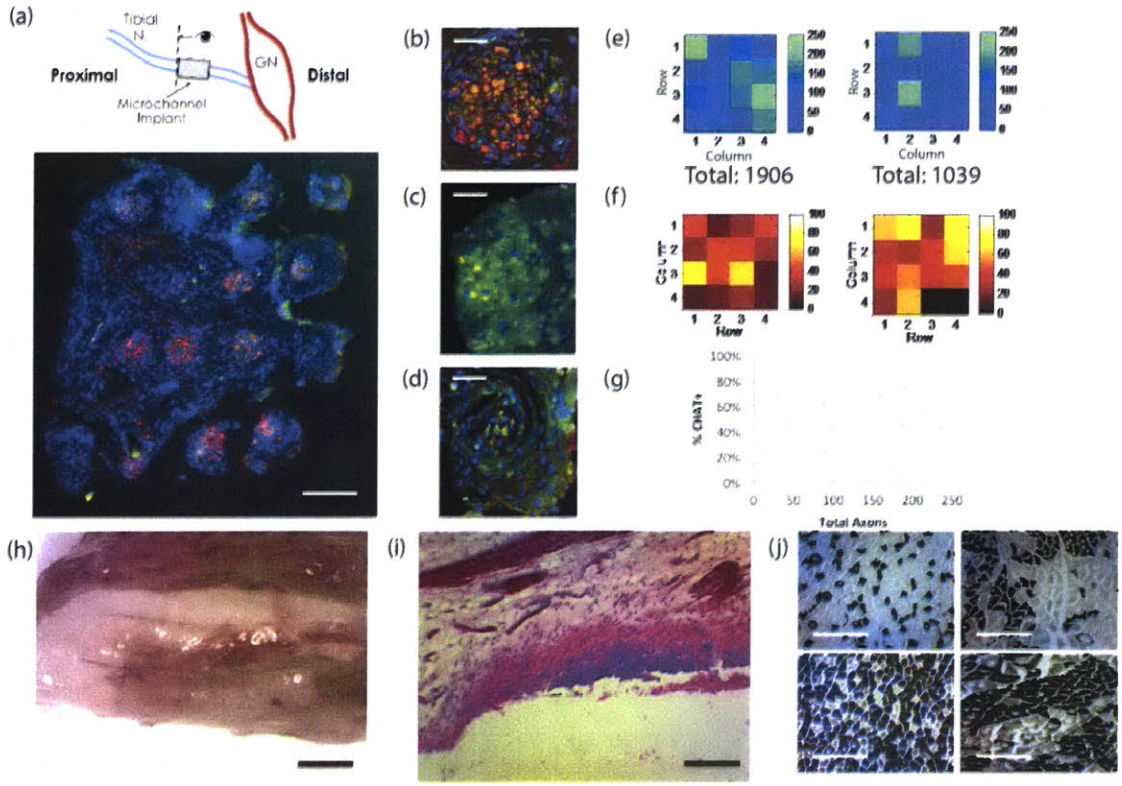


**Figure 2.5: Histological assessment of passive microchannel**

*A) Diagram depicting t.n. cross section as it enters the microchannel; Cells are stained for NF200 (green), CHAT (red) and DAPI (blue). Significant numbers of axons are present in 14/16 channels. Scale bar, 200 µm. B) Close up of sample 1 row 3 column 1, a channel that exhibits majority CHAT+ axons. Scale bar, 40 µm. C) Close up of sample 1 row 4 column 4, a channel that exhibits very few CHAT+ axons. Scale bar, 40 µm. D) Close up of sample 3 column 4, a channel that exhibits few axons. Scale bar, 40 µm. E) Total axon counts as determined by NF200+ staining in two rats, left corresponding to the sample 1 image in A. F) Percentage of NF200+ axons that are also CHAT+ within same channels as in E. G) Percentage of CHAT+ axons as a function of total axon count by channel. H) View of Microchannel with regenerated tibial n. fibers growing around device. Scale bar, 0.8 mm. I) Chronic foreign body inflammation at microchannel interface with H&E. Scale bar, 40 µm. J) Type 1 (dark, top; light, bottom) and Type 2 (light, top; dark bottom) muscle fiber staining of medial GN indicates loss of "checkerboard distribution" (right) compared*

*to healthy (left) following nerve transection and regeneration. Tissues were stained at a pH of 4.31 (top) and a pH of 10.20 (bottom). Scale bars, 125 μm.*

### 2.3.2 Active Microchannel Electrode Array in Ferrets

Four months after implantation, ferrets were anesthetized and the lower limb was exposed as described above. The t.n. was found to have regenerated in all of the ferrets, with stimulation of the proximal t.n. producing a plantarflexion response. To evaluate regeneration through the microchannel device, all branches of the t.n. which had regenerated around the microchannel, the s.n. and c.p.n. were transected, such that proximal FES was restricted to the device itself. In only two ferrets of the four (one of each the pure synthetic and hybrid-collagen designs), stimulation of the s.n. produced a plantarflexion response. In both of these ferrets, the nerve did not appear to be growing through the majority of the channels, in contrast to the aforementioned rat experiments. Instead, regeneration was limited to a few channels of the array (Fig 2.6A,B). In the other two ferrets, a significant neuroma formed at the proximal end of the microchannel and all regeneration from the neuroma bypassed the device (Fig 2.6C). Both stimulation and recordings through the percutaneous port were plagued by mechanical defects in the ribbon coil, likely caused by repeated animal movement resulting in loss of electrical connectivity; to compensate for this loss, the ribbon cables were carefully delaminated during surgery and electrical current was applied directly to the platinum traces with the stimulator (Fig 2.6D). This resulted in plantarflexion in the same two of four ferrets that exhibited regeneration through the channels, demonstrating some electrical connectivity to nerves growing through the device.

It was found that the regenerated nerve in both ferrets only grew through 1-2 of the channels (Fig 6E). The nerve tip exhibited the characteristic contraction closure response, indicating that regeneration had yet to be complete at 4 months; follow-up experiments in ferrets may require 6-12 months to restore full function. Cross-sections of the tissue were stained against NF200 and DAPI. The NF200+ neural tissue appeared to be growing in sparse and disorganized clumps with indiscernible individual axons (Fig 6f) possibly indicating immature neural tissue.

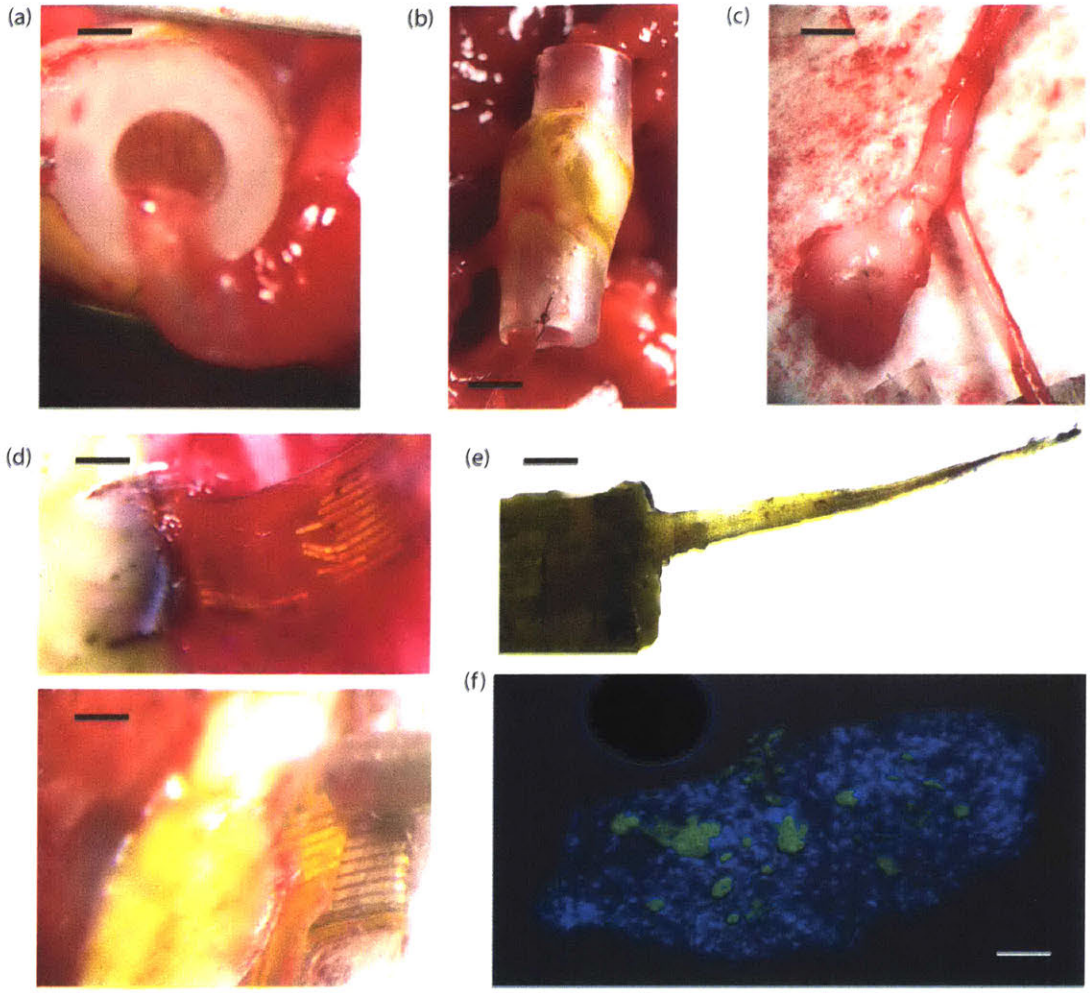


**Figure 2.6: Active Microchannel Failures**

*A) Axial view through proximal aspect of microchannel showing 5x4 grid array with neural tissue growing into device. Scale bar, 0.6 mm. B) Longitudinal view of regeneration through microchannel. Scale bar, 2 mm. C) Significant neuroma formation at proximal end of microchannel at transected t.n. (left) compared to c.p.n. (right). Scale bar, 1.5 mm. D) Ribbon cable at percutaneous port shows mechanical failure and trace breakage. Scale bar, 2 mm. Electrophysiological studies through device were instead conducted via direct stimulation of ribbon adjacent to channel. E) Micrograph depicting characteristic contraction closure of regenerating nerve from microchannel. Scale bar, 300 μm. F) IF against NF200 (green) and DAPI (blue) showing sparse and disorganized clumping of neural tissue. Scale bar, 35 μm.*

## 2.4 Discussion

### 2.4.1 Discoveries in Microchannel Implementation

In this work, we present a new geometry for a passive PDMS microchannel and a completely novel design for an active regenerative microchannel electrode with and without a porous collagen scaffold; we employ these devices in a rat and ferret animal models to analyze the extent of functional regeneration through the device by axon subtype. Despite robust EMG activity in both the GN and TA muscles, the strong dorsiflexion identified during electrical stimulation indicates a significantly weaker t.n. compared to the c.p.n.: in a healthy animal, supramaximal sciatic stimulation results in co-contraction with predominant plantarflexion[54]. The dorsiflexion we observe is attributable directly to the microchannel device. Possible explanations include the disorganized growth of fibers both outside of and within the different channels interfering with the timing of end plate depolarization, incomplete myelination of the alpha motor fibers at 20 months[55], decreased axon counts compared to the healthy t.n.[56] or small diameter, unhealthy fibers[55]. Although the GN was not visually or histologically atrophied, muscle denervation and repair, shown in the loss of checkerboard pattern distribution of Type 1 and Type 2 muscle fibers, is also independently associated with muscle weakness, especially in the early phases of regeneration[57]. Further work is needed to determine the precise cause of the weakened plantarflexor response noted through t.n. microchannels.

The mixed distribution of motor and sensory fibers by channel provides insight into the way in which nerve fibers regenerate through microchannels. Whereas in the native nerve, alpha motor neurons projecting to the same muscle tend to travel together and sensory fibers within the nerve tend to travel together, there appears to be a loss of organization within the regenerating channels[51,58]. Although there appears to be a relationship between larger axon diameters and CHAT+ fibers, there does not appear to be a relationship between larger number of fibers and type of fibers within each channel. Previous research has shown in the setting of transection and restricted growth, large motor neurons tend to regenerate more quickly than small, less-myelinated sensory fibers[59], although research is conflicted, suggesting equal regeneration times for large myelinated sensory fibers[60]. It is

possible that the differential speed of regeneration and subsequent pruning of the motor sprouts results in the predominance of mixed motor-sensory fibers within a channel at first; the sensory or motor fibers may be pruned at a later point in order to establish a greater segregation of axon subtype by channel in accordance with the normal physiological somatotropic and topographical distribution of healthy nerves[33]. Previous work suggests large alpha motor fibers may have more limited regeneration than large sensory fibers through a polyimide sieve[61]. Future work defining molecular subtypes and anatomic variation via retrograde tracers at multiple post-transection time points may help elucidate the precise mechanisms underlying subtype segregation within channels during regeneration.

### 2.4.2 Challenges of High-Resolution Synthetic Interfaces

Many challenges remain to future adoption of microchannel nerve interface. These broad categories include: 1) navigating both the wound contraction closure immune response as well as the chronic foreign body immune response, 2) electrically teasing nerve firings in microvolt range given a low signal-to-noise ratio for recording in awake, moving animals, and, 3) building a robust percutaneous system that addresses key areas for electrical and mechanical improvement in the device design.

The difficulty of mitigating the inflammatory changes of the immune system is exemplified by thick fibrous encapsulation of regenerating axons where they make contact with the device. Axons are pushed to the center of each channel and surrounded by a ring of fibrous tissue. Possible explanations for this thick fibrous layer include foreign body response, but also include the direct mechanical transmission of force directly onto the surface of the nerve, killing the new axonal sprouts. To mitigate both, soft biocompatible flexible interfaces have shown long-term advantages in peripheral nerve interfacing over rigid silicon-based sieve electrodes[62]; however, the mechanical compliance of PDMS is clearly not sufficient to mitigate force transmission or foreign body encapsulation from within a nerve. Future work developing heavily biomaterial-based nerve interfaces may be necessary before microchannel interfaces are robust enough to be used clinically. In all animals studied, a pathological neuroma formed at the proximal end of the transected t.n.

to some degree, indicating the nerve is still interpreting the microchannel as an obstructive mechanical impediment to regeneration. Like the lake that forms upstream of a dam, the neuroma forms proximal to the microchannel. As the fibers seek an alternate path the end organ and circle back on themselves, the neuroma grows in size, recruiting inflammatory cells and producing fibrosis. Like the low-pressure river which gets through the dam, only a small trickle of fibers manage to regrow through the channels on the distal end.

With the soft PDMS microchannel we employ, there is limited regeneration. The number of t.n. axons growing through the device is 10-20% of original, representing a major loss of neuronal activity. Further, the axons that did grow through the device were small – although they conducted with FES, it is unclear to what extent they were actually functional for voluntary contraction. In terms of biomaterial-assisted regeneration, collagen did not appear to have an influence in increasing the type or number of fibers that regenerated through the channels. A more detailed evaluation with higher sample sizes and different collagen pore sizes could help evaluate if there is potential for optimization.

In terms of the device itself, there are several challenges – axons die easily from the smallest amount of mechanical pressure. Further, axons are naturally encapsulated by fibrous tissue in order to be successfully insulated from external biological processes. A synthetic microchannel device inherently disrupts this natural process, forcing each subgrouping of axons to be encapsulated independently. High-resolution peripheral nerve stimulation with targeted end-organ selectivity on a localized anatomic scale cannot be functionally achieved with conventional electrical devices, which require direct contact with the target nerve fiber to initiate depolarization. A method for stimulation of subsets of peripheral nerve targets from a distance remains the holy grail of peripheral neuromodulation. It is a goal that cannot be accomplished with conventional methods of electrical interfacing, which requires the target axons to be directly adjacent to the source current in order for the axons to activate. To achieve this end, exploration of non-electrical methods is valuable next step.

# 3 PERIPHERAL NERVE OPTOGENETICS

This section describes techniques that are important for optogenetic stimulation of deep tissue peripheral nerves.

## 3.1 Brief Introduction to Peripheral Nerve Optogenetics

The use of single algal rhodopsins to depolarize neurons has been employed since 2005[63]. Variants on the original channelrhodopsin (ChR1) have been introduced that optimize several key properties of opsins. These include photocurrent, illumination sensitivity, on kinetics, off kinetics, expression levels, membrane trafficking, and others. Several promising opsins have been introduced from site directed mutagenesis. ReaChR, for example, is a highly sensitive opsin that was engineered from VChR1 with the N-terminus & L171I point mutations taken from ChIEF, and the F transmembrane domain taken from VChR2. These mutations increased photocurrent, wavelength, and membrane trafficking properties at the expense of a slow channel closure rate[64]. Unlike site-directed mutagenesis, identification of new, naturally occurring opsins have also increased the optogenetics toolbox. Chrimson was discovered as a naturally occurring opsin in the species Chlamydomonas noctigama. Although these opsins have great potential, their study has, to date, been restricted to the CNS.

The *in vivo* study of peripheral nerve optogenetics to date has employed either transgenic models or opsin delivery through viral, chemical or cell transplantation methods. Transgenic models have employed the opsins ChR2, NpHR, ArchT and bPAC. In addition to ChR2, NpHR, and ArchT, viral, cell transplant, and chemical optogenetic models in the peripheral nerve have employed a broader range of opsins including ChETA, Optovin, EROS, and Melanopsin. By far, the most common opsin employed is ChR2, used in 23 of 31 published studies for *in vivo* peripheral nerve optogenetics as of 2016. The majority of these studies focus on sensory activation, but as of 2016, there have been seven studies using channelrhodopsin for activating somatic motor tissue in the PNS, all of which employ ChR2. Three of these studies used viral methods for transduction, two of which used rats and one of which used mice. For the viral publications, the techniques employed include a DPSS laser coupled to a custom fiber nerve cuff implanted on the sciatic nerve[23], a DPSS laser coupled to a fiber on the exposed phrenic nerve[65], and an LED on the exposed sciatic nerve[66]. For the transgenic animals, illumination techniques include an LED nerve cuff[20], a DPSS laser coupled to a fiber adjacent to the spinal cord[67,68], and a DPSS laser coupled to a fiber external to the exposed sciatic nerve[69]. Within sensory studies, a transdermal optogenetic approach has been employed to inhibit and activate murine nociceptors and touch receptors[70]. These represent all of the preliminary peripheral nerve optogenetics stimulation studies of the past 10 years. All of them required surgical exposure or used implanted light sources for a short-term evaluation, leaving room for significant opportunities to advance the methods and technologies for targeting deep tissue nerves in a robust, long-term way.

## 3.2 FOS Theory

### 3.2.1 Optogenetic Induction of Motor Activity via Axonal Stimulation

The probability of eliciting an action potential (AP) at a specific axon optogenetically can be generally represented as a function of three variables: $N_{ch}$ represents the number of effective channels within the membrane in the illumination area, $I_{ch}$ represents the

individual photocurrent of a given opsin channel which can be derived from intrinsic opsin properties, and φ represents the optical fluence rate at the nodal membrane of the axon.

$$P_i(AP) = f(N_{ch,i}, I_{ch}, \phi_i)$$

Several factors may influence the number of effective opsin channels ($N_{ch}$) including concentration of injected AAV, total volume of AAV injected, efficiency of viral retrograde transport up to the neuron body, episomal transcription and translation rates, efficiency of anterograde opsin transport, affinity of the opsin for the cell-membrane, and evasion of intracellular pattern recognition receptors (PRRs) and ubiquitination machinery. Some of the intrinsic opsin properties, which may determine the spontaneous photocurrent of a channel, include the open and closed state-model and rate-constants, the on/off kinetics, and conformational-change pore diameter. The fluence rate at the membrane of an axon as a function of time is driven by optical variables including the power, shape, wavelength, frequency and duty cycle of illumination. If the first and second variables ($N_{ch,i}, I_{ch}$) are optimized, it may be possible to change the fluence without compromising $P_i$(AP); one can optimize to such an extent that the low fluence stimulation of deep tissue nerves with transdermal illumination is possible. This adds anatomical variables as contributors to fluence rate, including the distance between the nerve and the skin surface, the axon's relative position within the cross-section of the nerve, and the optical absorption and scattering properties of the tissues between the nerve and the skin surface. This thesis seeks to show that the depth to nerve from the skin surface can be significantly increased by: chapter 4) increasing viral particles delivered, chapter 5) increasing opsin photocurrents & decreasing absorption and scattering coefficients, and chapter 6) increasing efficiency of viral transduction through targeted immunosuppression.

To evaluate whether these strategies can improve FOS of deep tissue nerves, the CMAP corresponding to the targeted nerve is measured in response to transdermal nerve illumination of a specific laser power. The total CMAP can be modeled by the following formula, where $MU_i$ is the EMG voltage produced by a single activated axon firing its innervated myocytes, and $N_{ax}$ is the total number of opsin+ axons in the nerve.

$$CMAP = \sum_{i}^{N_{ax}} MU_i * P_i(AP)$$

Since CMAP can be measured easily with EMG electrodes and even estimated visually by the strength of ankle plantar/dorsiflexion, there is a very direct way to study how manipulations of certain FOS input variables affect the caliber of the optogenetic response. One metric for nerve depth of optogenetic stimulation is the minimum fluence rate required to elicit an EMG response. Other metrics include the slope and offset of the linearized EMG vs. illumination power curve. Similar to the minimum fluence, the offset represents the minimal power necessary to activate the highest $P_i(AP)$ axons. The slope represents the illumination cost of recruiting both deeper and lower $P_i(AP)$ axons. The trade-off with increasing illumination power is the risk of tissue heating and phototoxic damage, although these risks are partially offset by using low DCs, as described in Chapters 4 and 5.

### 3.2.2 Modeling FOS in the peripheral nerve

Previous work into optogenetic transfection of the PNS has provided some key insights into the protein dynamics and rates of expression. Llewellyn et al. define a minimum fluence rate required to activate ChR2 channels in the sciatic nerve of a tg-ChR2 mouse of 1 $mW/mm^2$ [20]. The minimum fluence rate applied at the surface of the nerve is 6 $mW/mm^2$, modeled using the Kubelka-Munk theory of light propagation through brain tissue outlined by Aravanis et al[71]. Because they use a transgenic mouse, expression levels of ChR2 are more homogenous than with the use of viral methods, where viral aggregation and anisotropy of fluid diffusion may enable a wider variation in MOI and subsequently opsin density per axon. Although AAVs have been employed in freely moving WT rats and mice[23,70,72], all FOS of peripheral nerves has heretofore required implantable devices, which have some similar drawbacks as implantable FES devices listed in Chapter 1.

Applying an optogenetic model to a multi-compartment, double cable, myelinated axon model, Arlow et al. modeled variability in what they define threshold source irradiance for optogenetic excitation, ranging from several hundred $\mu W/mm^2$ to several hundred $mW/mm^2$ [73]. Key factors, which influence the simulated irradiances, include the distribution of the illumination, the pulse duration, axon diameter, intermodal spacing, and source-to-axon distance. However, the authors do not assess the contribution of ChR2 density, instead deriving the value by a combining minimum fluence and individual opsin photocurrent from the Llewellyn et al. paper.

## 3.3 Key variables affecting FOS

Several key variables influence the likelihood of a given motor unit to activate upon illumination. These variables can be categorized in three broad descriptions: (1) factors that affect the fluence rate or the amount of light that hits the optogenetic nerve target, (2) properties that are intrinsic to the opsin itself, and (3) factors that affect the amount of opsin present on the nerve. These are summarized in Table 3.1.

**Table 3.1 Variables that influence success of optogenetic peripheral nerve stimulation**

| Fluence Rate ($\phi(t)$) | Channel Current ($I_{ch}$) | Number of Channels ($N_{ch}$) |
|---|---|---|
| <u>t-independent</u><br>Illumination power<br>Wavelength<br>Beam shape and size<br>Axon depth<br>Scattering + Absorption Coef.<br><br><u>t-dependent</u><br>Frequency<br>DC | Intrinsic property of opsin<br>Channel State Map & Rate Constants (e.g., Open State 1, Closed State 1, Open State 2, Closed State 2, etc.) | [AAV]<br>Volume AAV<br>Retrograde Efficiency<br>Transcription/Translation Rate<br>Anterograde Efficiency<br>Membrane Trafficking<br>Evasion of PRR and immune response |

Fluence rate is a function of several variables that are both independent and dependent on time. In terms of time-independent processes, fluence rate on the nerve or muscle target of interest is a direct function of illumination power. Wavelength of illumination affects the scattering, absorption, and anisotropy coefficients, which in turn affect the fluence rate at certain depths in biological tissues. These coefficients vary as a function of molecular composition of the target tissue; for example, heavily vascularized tissues such as muscle are likely to have greater hemoglobin levels, which in turn heavily increases the absorption for shorter wavelengths (Figure 3.1). Beam shape and size also influence fluence rate, with narrow beams resulting in higher fluence rates for the same illumination power. However, this difference becomes less pronounced as the target organ becomes deeper due to scattering. Further, narrow beams are more likely to cause heating and phototoxicity because absorption is directly proportional to fluence rate. As a time-variant process, FOS is dependent upon the exact opsin conformation, which may vary in conductance throughout the microsecond-millisecond process of conformational state change. Further, the photons which directly strike an opsin operate in a stochastic process – the more light, and more time that light has an opportunity to strike an opsin, the greater the chance that an individual opsin will open. Cumulatively, this increases the chance that the axonal nodal transmembrane voltage will reach the -55 mV threshold for depolarization. As a result, illumination PW, a function of both DC and frequency, is critical – insufficient PW ceases to recruit enough opsin to drive the transmembrane current required to induce nerve depolarization.

**Figure 3.1 Optical properties of biological tissues as a function of wavelength for absorption coefficients (left)[74] and scattering coefficients (right)[75]**

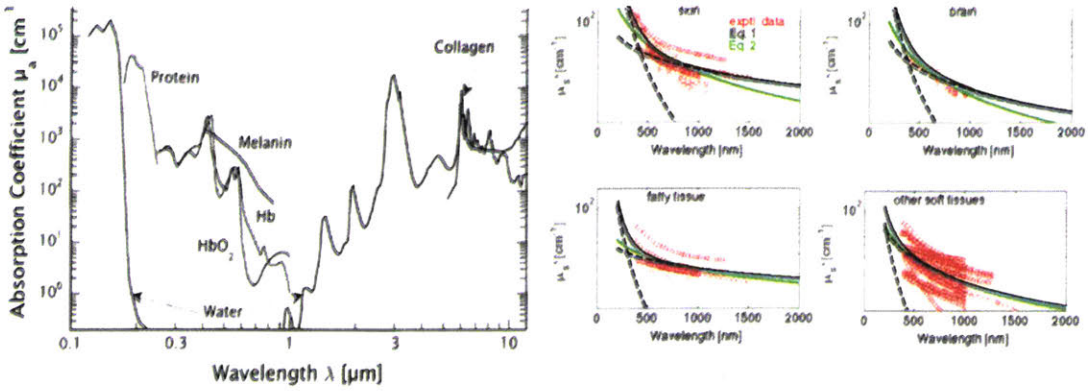


Intrinsic properties of the opsin also play a role in affecting the likelihood of depolarization. An opsin's photocurrent is directly proportional to its channel conductance. For a given expression level, higher photocurrent per opsin cumulatively increases the transmembrane current, resulting in an increased likelihood of a depolarization event. Further, an opsin's off-kinetics affects the likelihood of the opsin to be re-triggered. Opsins with very slow kinetics remain in a closed state for a time, decreasing the frequency of stimulation and preventing tetanic activation.

Lastly, the number of opsin channels within the membrane is a key metric for determining whether an opsin will depolarize in response to illumination. Increasing the density of opsin channels increases the net transmembrane current, which directly increases likelihood of reaching the -55 mV AP threshold. In chapter 4, we assess the result of increasing the [AAV] and total volume of AAV on channel density. Other works have studied the effect of AAV serotype and capsid engineering on retrograde transport[76,77] and BSCB crossing[78], concluding that capsid itself is a critical factor in improving gene delivery of peripheral nerve targets. Following episomal DNA delivery, gene transcription and translation rates are critical, as well as protein folding properties, membrane trafficking, and anterograde transport from the CNS soma to the axonal membrane. Additionally, avoiding any potential deleterious effects of the opsin within the biological system is critical, including immunogenicity, cytotoxicity, and any other process that influences axonal expression levels.

## 3.4 Time Variance of Opsin

We mention above how time dependent processes affect cumulative fluence rate and therefore probability of a photon stochastically striking an opsin and changing its state. However, the state map of the opsin also operates in a time-dependent process. We define three temporal regimes for optogenetic stimulation: activation, inactivation, and regeneration. Upon initial photon strike, the opsin pore opens at once, resulting in a strong increase in the channel conductance driving inward current via the passage of cations into the cell. Simultaneous opening of all channels results in the highest probability of a depolarization event because of the large, synchronized inward current, which increases the likelihood that an axon will reach the -55 mV depolarization required to initiate an AP. Researchers modeling the dynamics of ChR2 have identified a four state model for the protein (Fig 3.2C). Upon initial depolarization, the opsin shape changes from C1 to O1, encompassing the largest diameter transmembrane pore and high-conductance passage of cations. If illumination ceases while the opsin is in O1 state, the channel closes back to C1. If illumination continues, the opsin transitions to O2, which contains a smaller diameter pore corresponding to roughly 20-30% of the conductance of O1 for ChR2[79]. If illumination ceases in the O2 state, the opsin closes to C2, and may spontaneously revert to C1 driven by much slower cellular kinetics. A repeat illumination event while the opsin is in C2 decreases the overall change in conductance upon re-illumination, driven by the following equation

$$i_{transmembrane} = N_{Ch,O1} * i_{O1} + N_{Ch,O2} * i_{O2}$$

Assuming conductance of O2 is roughly one fifth of the conductance of O1, we can rearrange the transmembrane current as the following.

$$i_{transmembrane} = i_{O1} * (N_{Ch,O1} + \frac{N_{Ch,O2}}{5}) = i_{O1} * [Effective\ ChR2]/axon$$

We define the number of opsin molecules in each state multiplied by their relative, normalized transmembrane currents as the Effective ChR2 concentration per axon. After illumination ceases on the initial depolarization event, the majority of the ChR2 is in O2 and is driven to C2. This results in a state of inactivation upon continued illumination because, for certain axons, all opsin channels operating purely in O2 is insufficient to reach

the threshold required for depolarization. As the opsin spontaneously reverts to C1 over time, certain axons that were subthreshold to fire can now reach the voltage threshold for initiation of an action potential. These kinetics are depicted visually in Figure 3.2. In the activation phase, illumination is sufficient to reach the desired angle. In the inactivation phase, illumination maxes out and cannot maintain the desired angle. In the regeneration phase, sufficient axons have reached an equilibrium between O1 and O2 states that continued stimulation results in maintenance of the desired angle (Figure 3.2A). This is further reflected in the kinetics of a closed-loop position controller. Initial tracking of a sinusoidal position input is perfect, followed by inactivation ~5 seconds into the stimulation, in which even higher fluence rates cannot compensate for the lack of motor activation. The nerve slowly recovers, and ~30 seconds later, the position controller has regenerated (Fig 3.2B).

On an axonal scale, we represent these three phases based on axons that exist on a binary scale: either they depolarize or not, based on membrane concentration of effective ChR2 (Figure 3.2C). Certain axons are close to illumination thresholds, and after firing once, they no longer receive sufficient illumination to continue to fire, because previously superthreshold O1 opsins have decayed to O2 and are now subthreshold. These axons are represented in green. As time continues, the proportion of O1 axons increases again, eventually reaching a steady state. For some axons, this steady-state is now sufficient to induce depolarization again – these axons are represented in orange. Other axons remain substhreshold and are represented in green. This model also demonstrates the effect of fluence rate. Certain axons have low sensitivities due to low expression likely a consequence of low MOI – for these axons, fluence rates need to be significantly increased in order to depolarize. However, fluence rate cannot compensate for the lowest expressing axons; they will never depolarize even at the highest fluence rates. This agrees with our finding that the transdermal illumination CMAP is always equal to or less than the exposed nerve illumination CMAP for all optogenetics studies. We define the likelihood of eliciting an action potential as being directly proportional to the cumulative transmembrane current of all opsins.

$$P_i(AP) = f\left(N_{ch,i}, I_{ch}, \phi_i\right) \propto i_{transmembrane}$$

If we define the function g(i) as the contribution of cumulative transmembrane current on the intracellular voltage, and the corresponding intracellular voltage's subsequent effect on the likelihood of reaching a depolarization event, we can rearrange the CMAP equation such that we directly relate EMG activity to opsin concentration.

$$CMAP = \sum_{i}^{N_{ax}} MU_i * \mathrm{g}(i_{O1} * [Effective\ ChR2]_i)$$

In subsequent chapters, we explore strategies to increase the concentration of effective opsin as well as the open state photocurrent by varying the opsin.

**Figure 3.2 Model describing FOS time-variance**

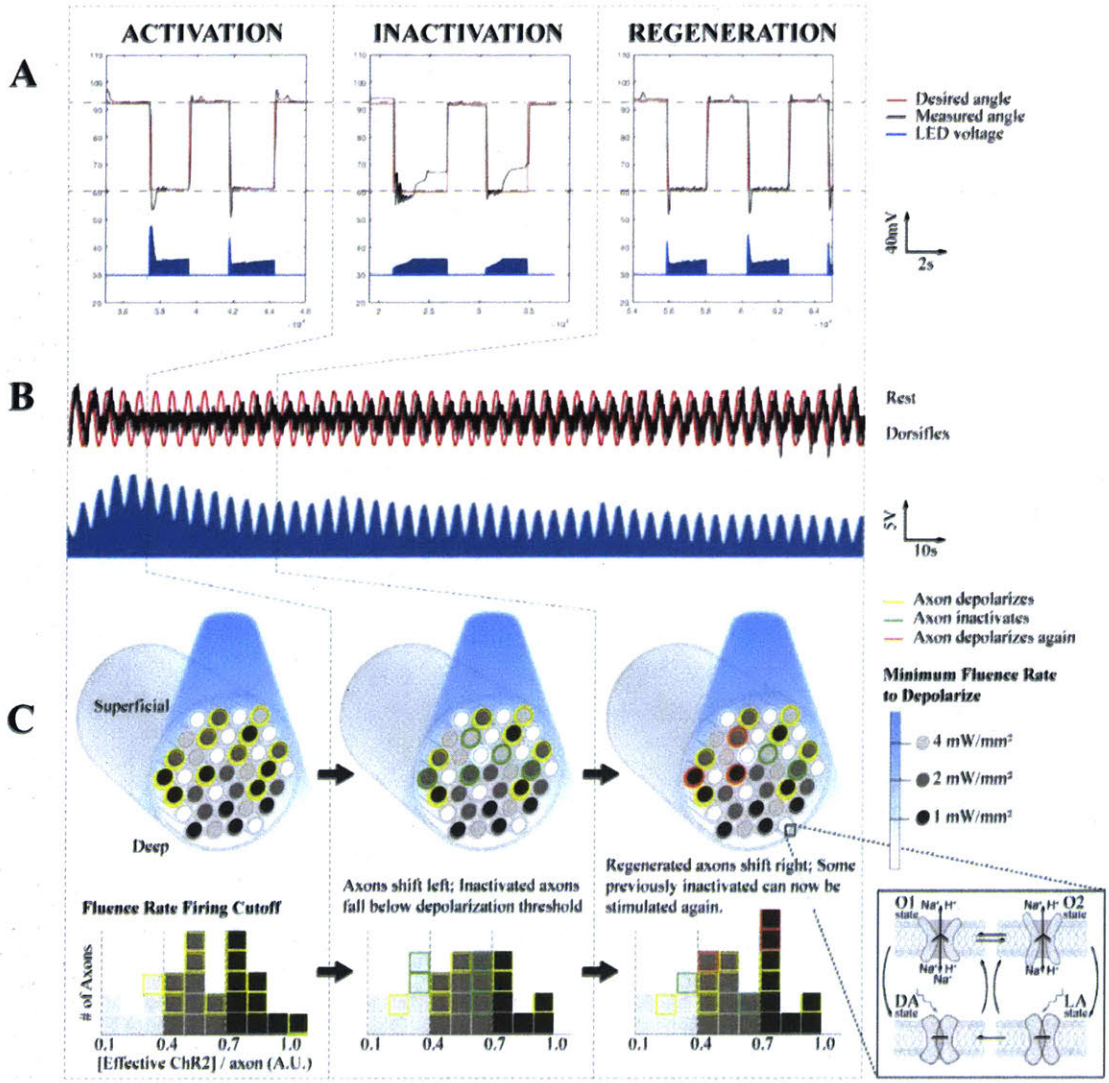

# 4 TRANSDERMAL OPTOGENETIC PERIPHERAL NERVE STIMULATION

A fundamental limitation in both the scientific utility and clinical translation of peripheral nerve optogenetic technologies is the optical inaccessibility of the target nerve due to the significant scattering and absorption of light in biological tissues. To date, illuminating deep nerve targets has required implantable optical sources, including fiber-optic and LED-based systems, both of which have significant drawbacks. Here we report an alternative approach involving transdermal illumination. Utilizing an intramuscular injection of ultra-high concentration AAV6-hSyn-ChR2-EYFP in rats, we demonstrate transdermal stimulation of motor nerves at 4.4 mm and 1.9 mm depth with an incident laser power of 160 mW and 10 mW, respectively. Furthermore, we employ this technique to accurately control ankle position by modulating laser power or position on the skin surface. These results have the potential to enable future scientific optogenetic studies of pathologies implicated in the peripheral nervous system for awake, freely-moving animals, as well as a basis for future clinical studies.

## 4.1 Introduction

The retrograde transfection of AAV6-hSyn-ChR2-YFP, injected intramuscularly, has been shown to result in a repeatable muscle activation in response to *direct* optical stimulation of the peroneal and tibial nerves[23]. Direct illumination was accomplished using several different invasive techniques: the exposed nerve illuminated with a free-space optical source[23], an LED-based optical nerve cuff[20], and a fiber-optic-based optical nerve cuff[23]. These invasive methods were relied upon to provide a sufficiently high fluence rate to activate the target opsins expressed in the nerves. A *transdermal* illumination approach was successfully pursued for suppressing pain receptors in mice via stimulation of superficial cutaneous nociceptors[70]. Transdermal illumination has been postulated to target pain and touch fibers due to their superficial nature; deep-tissue targets were previously considered optically inaccessible because of the significant attenuation of blue light in biological tissue[75,80]. Transdermal stimulation of sensory axons in the sciatic nerve of transgenic mice has been previously linked to cortical recordings, yet it is unclear the extent to which cutaneous co-activation affected the measurements[81].

There have been several optogenetics studies leveraging non-invasive illumination in the brain. Both trans-cortical optical stimulation of ChR2-expressing neurons[82] and trans-cortical neural silencing using the red-shifted opsin Jaws[83] could reliably activate and inhibit neural populations respectively. The latter may have been due to the improved penetration of red light in tissue. Both experiments, however, required a fiber implant beneath the skin. Recent work in the vibrissa motor cortex of an awake, head-fixed mouse demonstrated optogenetic stimulation through bone and skin using both the red-light opsin ReaChR and ChR2, although the degree of movement was superior with ReaChR, which could produce reliable vibrissa motions up to 10 mm from the skin surface[64]. Direct transdermal optogenetic control of smooth muscle in rats[84] and skeletal muscle in transgenic mice[85] has been demonstrated. However, nerve targets are smaller and deeper than muscle targets, and represent a greater challenge to the transdermal approach. Infrared neural stimulation has also been presented as a promising optogenetics alternative that may produce anatomically selective, transdermal stimulation without genetic modification of

target tissue. However, major concerns include heating-induced tissue damage, non-selective co-stimulation of sensory and motor fibers, and difficulty localizing the target nerves[86].

The ability to control peripheral nerves situated under deep tissue structures with transdermal, optical signals would be of enormous benefit, integrating all of the advantages conferred by optogenetics while averting the drawbacks associated with implantable devices, such as mechanical failure, device tissue heating, and a chronic foreign body response. However, the aforementioned issue remains: peripheral nerves are located deeply beneath several tissue types, including skin, blood vessels, adipose tissue, and muscle. These tissues strongly attenuate visible light, preventing the majority of delivered light from reaching the target nerve. We hypothesized that by injecting a higher overall number of viral particles, more viral DNA would hone to the motor neuron nucleus increasing the multiplicity of infection (MOI), translating to a higher density of ChR2 channels in the axon and sufficiently high optical sensitivity such that transdermal, optogenetic control of nerves is possible. We evaluate this hypothesis by analyzing opsin expression levels and muscle response as a function of injected viral particles (vp) and fluence rate in a rat model.

## 4.2 Methods

### 4.2.1 Evaluation of Peripheral Nerve Depths

To measure the thickness and type of tissue between the skin surface and target nerve, a critical factor in determining how much light reaches the different nerve depths, the right hindlimbs of four 5-week old and four 8-week old Fischer 344 rats were extracted, postfixed for 48 hours in 4% paraformaledehyde (PFA), decalcified 36 hours in acetic acid, paraffin processed, embedded, sectioned at 25 μm thickness every ~250 μm, and stained with H&E. The sciatic nerve (s.n.) was traced to its division into the common peroneal nerve (c.p.n.) and tibial nerve (t.n.), which were followed distally, slice by slice, to their end plates at the tibialis anterior muscle (TA) and gastrocnemius muscle (GN), respectively. The c.p.n and t.n. depth, relative to skin, was measured on each slice; the slice

with the minimum distance between nerve and skin surface was conservatively used for gathering the tissue geometry required for modeling. A Monte Carlo (MC) simulation was created for estimating fluence rate distribution in the rat c.p.n. and t.n. Key inputs to the model included tissue geometry, attenuation coefficients for scattering ($\mu_s$) and absorption ($\mu_a$), and anisotropy factors in skin, muscle, connective tissue, epineurium and nerve, which were gathered from previous studies[87–91].

### 4.2.2 Fluence Model Validation

To validate the fluence rate simulation and its applicability to other geometries, a direct measurement of fluence rate was pursued. A method previously used to measure fluence rate in a directionally isometric and minimally invasive manner involves a small ruby sphere directly coupled to a fiber-optic cable[92]. The measured intensity of the ruby's emission at its spectral peak of ~694 nm is directly dependent on fluence rate. The device was constructed by attaching a 400 μm diameter ruby sphere (Edmund Optics) to the polished edge of a multimode fiber optic cable with 400 μm core and 25 μm cladding (ThorLabs) with UV-curing epoxy (ThorLabs). The other end of the fiber optic cable was connected to a spectrometer (ThorLabs). The system was calibrated by illuminating the ruby sphere at known fluence rates with a DPSS 473 nm laser (OptoEngine) and measuring the spectrometer intensity at 694 nm. To measure direct fluence rate in vivo, a 5 mm skin incision was made at the lateral femur in two female, 200 g Fischer 344 rats. The isometric probe was inserted at the incision and routed distally into three separate regions of interest: 1) the subcutaneous space at the mid-tibia, 2) the c.p.n at its most superficial location, and 3) the t.n. at its most superficial location. Spectrometer intensity at 694 nm was measured with transdermal, 473 nm illumination for a range of powers, and translated to fluence rate using the calibration described above (Fig 4.1A).

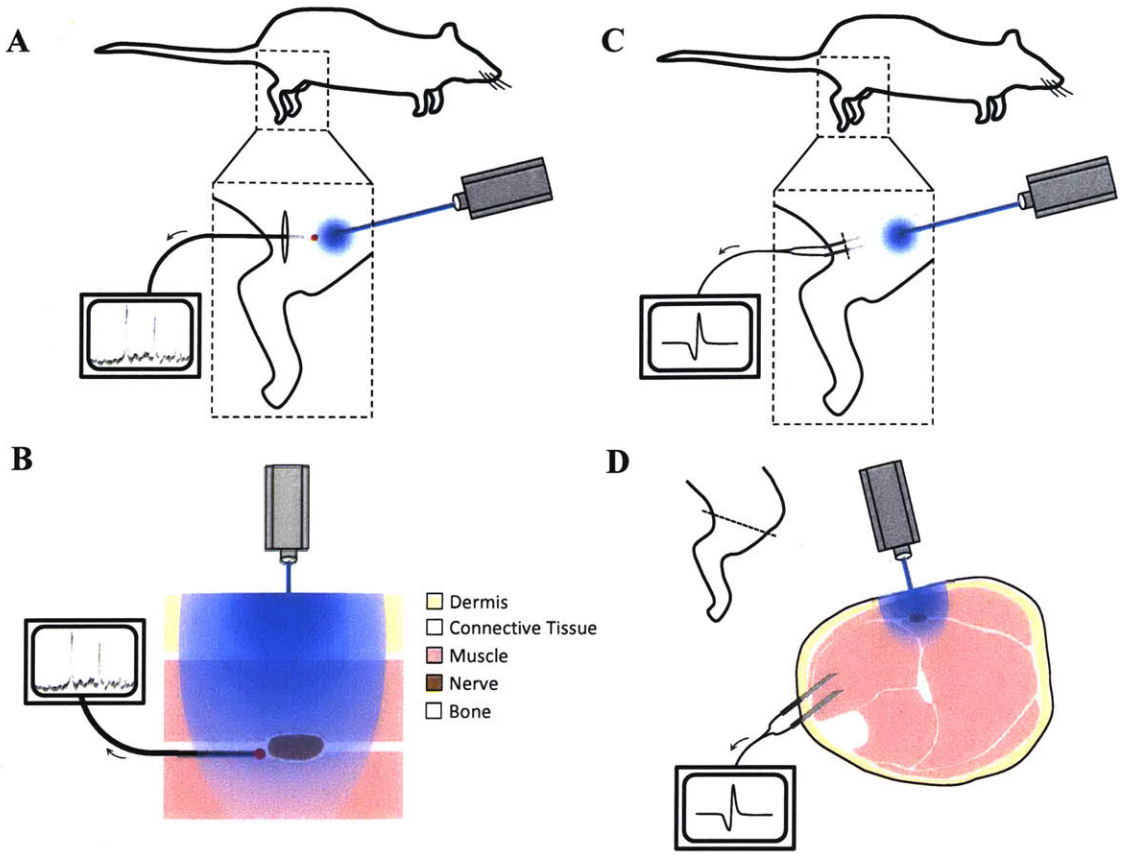


**Figure 4.1 Procedure for measuring fluence rate and EMG**

*(A) A small ruby sphere connected to a fiber optic is implanted into the rat hind limb via an incision made 1-2 cm proximal to the target measurement location. A 473 nm free-space laser illuminated the ruby sphere through transdermal illumination of the hind limb. Fluorescent emissions from the ruby sphere were collected by a spectrometer via a fiber optic and used to quantify fluence rate. (B) A cross-section of the target measurement location shows the ruby sphere in proximity to the representative common peroneal nerve. (C) Bipolar recording needle electrodes were inserted into the target musculature to record muscle activity in response to transdermal illumination of the nerve. (D) A schematic cross-section of the hind limb depicting connective tissue, musculature, bone, common peroneal nerve, and dermis anatomy. Biopolar recording needle electrodes were used to record muscle activity of both the TA (shown) and GN (not shown) in response to transdermal illumination. Tissue type legend refers to both (B) and (D) cross-sections.*

### 4.2.3 Viral Vectors and Injection

Viral vectors were produced in two batches. In the 8 week adult Fischer 344 rats, 4 dosages were tested: low (n=1), medium (n=1), high (n=1), and highest (n=2). In the neonate Fischer 344 rats, 2 dosages were tested: low (n=5) and high (n=10) (Fig 4.4B). Low- and medium-dose AAV6-hSyn-ChR2(H134R)-EYFP viral vectors were produced from the Vector Core facility at the University of North Carolina Chapel Hill, provided in a concentrated dosage of $1.4\times10^{13}$ vp/mL. The hSyn promoter was employed to restrict optogenetic activation to nerve tissue, which was validated by directly illuminating the injected muscles and noting the lack of response. At the time of surgery, the thawed vector was diluted with 0.9% sterile saline to $3\times10^{12}$ vp/mL and $9\times10^{12}$ vp/mL for injection into the low-dose and med-dose adult Fischer 344 rats respectively. The low-dose neonates were injected 2 days postpartum (P2) with $1.4\times10^{13}$ vp/mL virus as received. Ultra-high concentration AAV6-hSyn-ChR2(H134R)-EYFP viral vector was procured from Virovek Inc., at a titer of $1.2\times10^{14}$ vp/mL, and injected undiluted into the high- and highest-dose adult and high-dose P2 neonates.

Twenty rats (Charles River Laboratories) were housed under a 12:12 light:dark cycle in a temperature-controlled environment with food and water ad libitum. To deliver AAV for adult rats (n=5), a 0.5-1 cm skin incision was made over the tibia in the anesthetized rats and the biceps femoris (BF) muscle was reflected from its proximal insertion at the tibia to reveal the c.p.n.'s synaptic junction at the TA end plate. 75 μL of virus was intramuscularly injected in 3 regions of TA muscle within 1 cm of the end plate at a speed of 5 μL/min with an additional 5 μL of virus directly injected into the c.p.n. at the end plate at a speed of 1 μL/min, totaling $2\times10^{11}$ vp and $7\times10^{11}$ vp for the low- and medium-dose adults respectively (n=1 each). For the high- and highest-dose adults, a total of 20 μL and 35 μL was injected at 5 μL/min into the TA with an additional 5 μL of virus injected at 1 μL/min directly into the c.p.n. at the end plate, totaling $3\times10^{12}$ vp (n=1) and $5\times10^{12}$ vp (n=2) respectively. In the low-dose P2 neonate rats (n=5), 2 μL was injected through the skin into the TA at 1 μL/min totaling $3\times10^{10}$ vp, a dosage identical to a previous study[23]. For the high-dose P2 neonate rats (n=10), 5 μL was injected through the skin into the TA

at 1 μL/min; two weeks following, the right hindlimbs of the same animals were opened in the same method as the adults and 4 μL was injected directly into the TA with an additional 1 μL into the c.p.n. at the endplate at a speed of 1 μL/min totaling $1\times10^{12}$ vp. Following all open injections, the BF was sutured with 5-0 vicryl, and the skin was closed with wound clips and tissue glue.

### 4.2.4 Electrophysiological Recordings

For each rat, a twitch response to 473 nm transdermal illumination was tested at 2, 5 and 8 weeks post-injection. At 8 weeks, direct optical stimulation of the nerve was also tested for 15/20 animals. The remaining 5 were the highest dose neonates; both transdermal and direct optical stimulation of the nerve was tested at 11 weeks instead (Fig 4.4B). To measure the strength of nerve responses, four 30G monopolar electromyography (EMG) needles (Natus Medical) were directly inserted through the skin into the GN and TA for bipolar recording; a ground electrode was placed subcutaneously at the back. Careful needle placement limited acute inflammation at the illumination site. Needles were connected to a 20 kS/s multi-channel amplifier with a fixed 200x gain (IntanTech). A 473 nm laser (OptoEngine) was secured above the anesthetized animal to a stage assembly allowing for six degrees of freedom (Fig 4.1B). The laser beam had a Gaussian cross-sectional profile and 3 mm diameter ($1/e^2$), corresponding to a peak irradiance at the surface of the skin of 45 $mW/mm^2$ at a measured output power of 160 mW. Electrical signals controlling the laser amplitude, pulse width, and frequency were simultaneously recorded by the amplifier, enabling temporal synchronization of laser pulses and EMG. Data analysis was performed in MATLAB.

### 4.2.5 Euthanasia and histological evaluation

For 15 rats, the endpoint was 8 weeks; to assess for levels of ChR2 expression longer-term, 5 of the high-dose neonate rats were euthanized at 11 weeks. In the terminal surgery, the c.p.n., t.n., GN, and TA were exposed and directly illuminated to assess nerve activation and verify lack of muscle response to direct illumination. Following exposed nerve illumination, rats were anesthetized and transcardially perfused with 60 mL PBS followed by 60 mL 4% PFA in PBS. Spinal cord, TA, and s.n. were dissected, post-fixed for 12

hours, paraffin processed, embedded, and sectioned at 10 μm. EYFP expression was amplified with Rb pAb anti-GFP (ab290, Abcam) at 1:200 (unless specified) with Alexa Fluor 568 (Fisher); s.n. was labeled with gt anti-CHAT (AB144P, Millipore) at 1:100 and Alexa Fluor 488 (Fisher), all in 1% w/v BSA in PBS-T. Immunofluorescence images were taken on an Evos FL Auto (Fisher) epifluorescence microscope at 10x or 20x and processed with ImageJ.

### 4.2.6 Fluence Rate Modeling

The measured tissues between the skin surface and nerve comprised skin, connective tissue, muscle, and epineurium (Fig 4.2A), with total depth ranging from 1.4 mm for the c.p.n. in the 5-week rat to 5.3 mm for the t.n. in the 8-week rat (Fig 4.2B). For human comparison, the distance from skin surface to the median and ulnar nerves at the wrist measure 2.1 mm and 3.2 mm respectively[93] (Fig 4.2B). For a 200 g rat, the fluence rate along the centerline below the incident laser as a function of distance shows ~2 orders of magnitude and ~3.5 orders of magnitude declines for the c.p.n. and the t.n. respectively (Fig 4.2C).

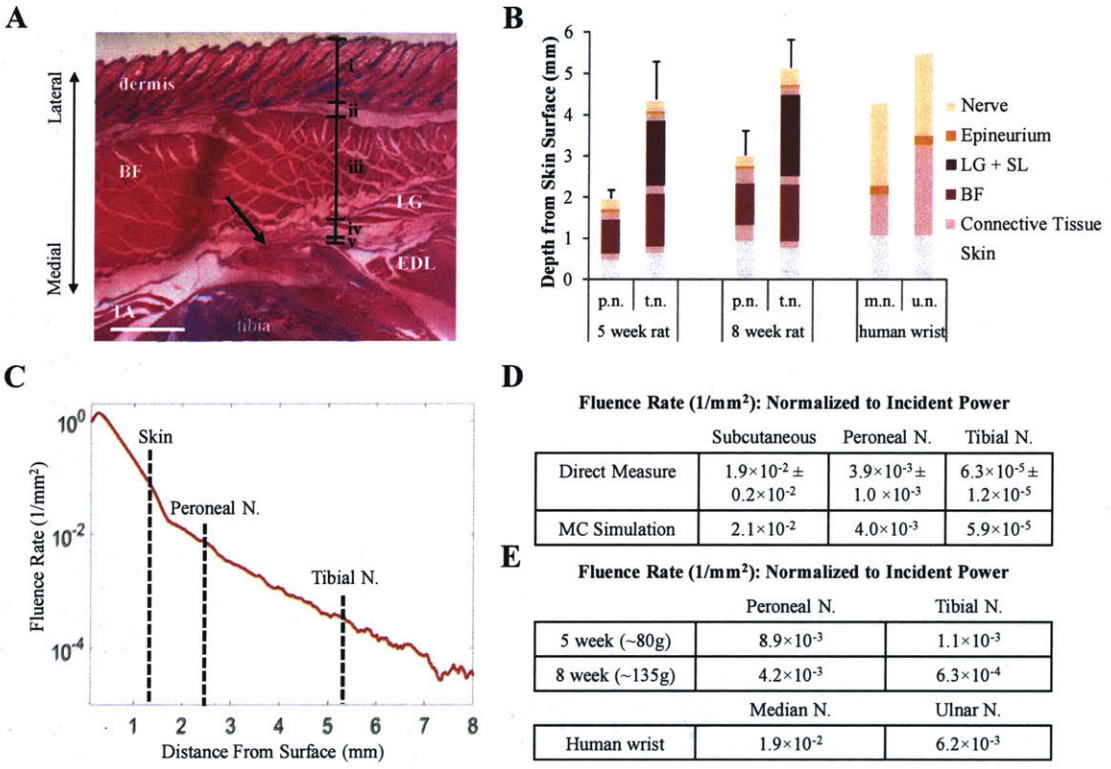


| | Subcutaneous | Peroneal N. | Tibial N. |
|---|---|---|---|
| Direct Measure | $1.9\times10^{-2}\pm 0.2\times10^{-2}$ | $3.9\times10^{-3}\pm 1.0\times10^{-3}$ | $6.3\times10^{-5}\pm 1.2\times10^{-5}$ |
| MC Simulation | $2.1\times10^{-2}$ | $4.0\times10^{-3}$ | $5.9\times10^{-5}$ |

| | Peroneal N. | Tibial N. |
|---|---|---|
| 5 week (~80g) | $8.9\times10^{-3}$ | $1.1\times10^{-3}$ |
| 8 week (~135g) | $4.2\times10^{-3}$ | $6.3\times10^{-4}$ |
| | Median N. | Ulnar N. |
| Human wrist | $1.9\times10^{-2}$ | $6.2\times10^{-3}$ |

**Figure 4.2 Fluence rate modeling for nerve depths encountered in this study**

*(A) H&E cross-section to measure tissue depth in 8-week female rat showing peroneal nerve (arrow) adjacent to proximal tibia at most superficial location of the nerve with i. skin, ii. connective tissue, iii. muscle, iv. connective tissue, v. epineurium (LG = Lateral GN, EDL = Extensor Digitorum Longus), scale bar = 1 mm. (B) Common peroneal nerve (c.p.n.) and tibial nerve (t.n.) depths by tissue type by rat age compared to human median nerve (m.n.) and ulnar nerve (u.n.) depths at adult wrist. (C) Monte Carlo (MC) estimated normalized fluence rate as a function of distance from skin normalized to incident power for a 200 g rat. (D) Comparison of direct fluence rate measurements and MC simulation results. The relative standard deviation for all MC simulations was between 3% and 5% (n=5). (E) Normalized fluence rate for 5-week and 8-week rats at the c.p.n. and t.n., as well as for the m.n. and u.n. at the human wrist.*

Direct fluence rate measurements are shown alongside the MC simulation results (Fig 4.2D), showing good agreement with a maximum deviation of 12%. The normalized

fluence rate was found to be $3.9\times10^{-3}$ $mm^{-2}$ at the peroneal nerve for the 8-week rat and $1.1\times10^{-3}$ $mm^{-2}$ at the tibial nerve of a 5-week old rat (Fig 4.2E). As such, the 160 mW, 473 nm laser source, transdermally incident, yields fluence rates of 624 $\mu W/mm^2$ and 176 $\mu W/mm^2$ at each of the respective nerves. The estimates for normalized fluence rate at the surface of the median nerve and ulnar nerve in the human wrist show comparable magnitudes to the rat, with 160 mW incident light providing 3 $mW/mm^2$ and 992 $\mu W/mm^2$ respectively.

## 4.3 Results

### 4.3.1 Light induced stimulation is optogenetic, not thermal

To assess whether stimulation of the nerve was optogenetic in nature and not driven by optically-induced heating of the nerve, an optical model of the Pennes bioheat equation provided in the Matlab package by Stujenske et al. was adapted for the peripheral nerve anatomy and tissue properties[94,95]. In addition to the MC output and tissue-specific $\mu_a$, other inputs to the thermal model included tissue density, heat capacity, thermal conductivity, perfusion rate, and metabolic generation for rat tissue gathered from the literature (Fig 4.3C)[96–100]. While the mechanism behind thermally induced spontaneous nerve fiber firing is not entirely clear, some research suggests that heating may activate the TRPV1 transmembrane channel directly[101].

In addition to driving spontaneous nerve fiber depolarization activation, light-induced heating of biological tissues has been shown to drive phototoxic effects. Phototoxicity has been shown in both retinal[102] and cortical tissues[103], where cellular damage is elicited by the high illumination intensities required to depolarize opsins. In an opsin-independent manner, the mechanism may be thermal[104], although fluorescent reporters are known to generate reactive oxygen species (ROS) directly in response to illumination, which can elicit structural and DNA damage, and at high levels, initiate apoptosis[105]. Within the tissues of interest, phototoxicity may drive nerve fiber death and Wallerian degeneration. Despite potential regeneration after this process, the viability of distal tissues in response to repeated light-induced thermal injury would have devastating long-term consequences

and impede clinical application of optogenetic technologies. As a result, understanding how to deliver light safely to biological tissue without compromising the integrity of the target is of crucial importance.

A conservative thermal analysis using incident 473 nm irradiation at 160 mW incident power, 10 ms pulse width (PW) and 40 Hz for 5 s suggested a max temperature rise of 0.11 °C at the c.p.n. and a max of 1.34 °C within the dermis; the max dermal temperature decreased by ~35% within 0.5 s of ending stimulation (Fig 4.4A,B). Optical excitation of nerves has been shown to be primarily dependent on a threshold nerve temperature of 42-45 °C, suggesting that the 0.11 °C change could not contribute to excitation itself[106].

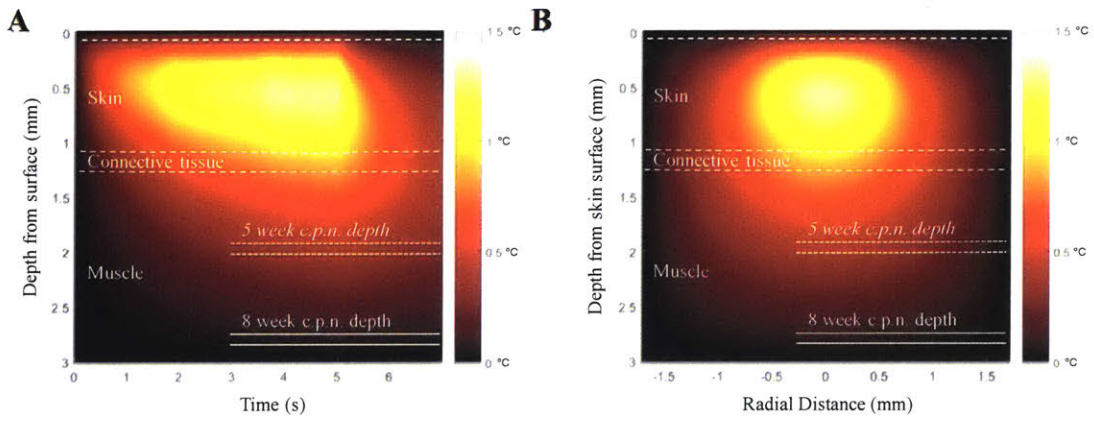


C

| Tissue Type | $\mu_a$ ($mm^{-1}$) | $\rho$ ($kg/mm^3$) | $C_p$ ($mJ/kg°C$) | $k_{th}$ ($mW/mm°C$) | $\omega_b$ (1/s) | $\dot{q}_m$ ($mW/mm^3$) |
|---|---|---|---|---|---|---|
| Skin | .090 [15] | 1.05e-6 [26] | 3.39e6 [23] | .372 [23] | 1.97e-3 [23] | 1.83e-3 [23] |
| Connective Tissue | .107 [#,*,16] | 1.03e-6 [23] | 2.37e6 [23] | .395 [23] | 6.36e-4 [23] | 5.91e-4 [23] |
| Muscle | .117 [#,16] | 1.05e-6 [22] | 3.42e6 [23] | .518 [23] | 8.3e-3 [24] | 6.50e-4 [24] |
| Epineurium | .107 [#,*,16] | 1.03e-6 [23] | 2.37e6 [23] | .395 [23] | 6.36e-4 [23] | 5.91e-4 [23] |
| Nerve | .090 [^,19] | 1.08e-6 [23] | 3.61e6 [23] | .490 [23] | 2.87e-3 [23] | 2.67e-3 [23] |
| ***Value in model*** | ***All*** | ***1.05e-6*** [22] | ***2.37e6*** [23] | ***.518*** [23] | ***8.3e-3*** [24] | ***6.50e-4*** [24] |

| | $T_i$ (°C) | $T_a$ (°C) | $C_{p,b}$ ($mJ/kg°C$) | $\rho_b$ ($kg/mm^3$) |
|---|---|---|---|---|
| ***Value in model*** | ***37*** [20] | ***36.7*** | ***3.60e6*** [20] | ***1.06e-6*** [20] |

**Figure 4.3 Thermal model for 473 nm illumination of peripheral geometry**

*(A) Simulated tissue temperature rise vs. time at beam center modeled with adapted Pennes Bioheat Equation. Matlab package provided by Stujenske et. al[19] adapted for 8 week p.n. tissue geometry identified histologically (Fig 4.2A,B) and optical absorption properties. Key inputs to model include transdermal 473 nm irradiation at 160 mW*

*incident power (corresponding to max irradiation of 142 mW/mm$^2$ at beam center) with a 1/e$^2$ Gaussian beam profile of 3 mm diameter, 10 ms PW, and 40 Hz frequency for 5 s duration. 5 week p.n. depth shown for comparison. (B) Spatial temperature distribution after 5 s stimulation with same parameters showing max temperature elevation above 1 °C constrained to skin ~1 mm within beam center. (C) Table of tissue properties used as inputs for bioheat simulation. Nomenclature defined as $\mu_a$ = Absorption Coefficient, $\rho$ = Tissue Density, $C_p$ = Specific Heat, $k_{th}$ = Thermal Conductivity, $\omega_b$ = Blood Perfusion Rate, $\dot{q}_m$ = Metabolic Heat Generation Rate, $T_i$ = Initial Temperature, $T_a$ = Arterial Temperature calculated from $T_a = T_i - \dot{q}_m / (\omega_b * C_{p,b} * \rho_b)$, $C_{p,b}$ = Specific Heat of Blood, and $\rho_b$ = Density Blood. Values directly sourced from citations listed, using rat properties where available and human properties where not available. Model was found to be robust to full range of tissue heat properties with a ~40% max dermis temperature change in response to change of properties from most liberal to most conservative combination. #473 nm coefficients extrapolated by linear interpolation between 400 nm / 450 nm and 500 nm when possible or 500 nm when not possible, *Adipose tissue conservatively used in place of connective tissue and epineurium, ^Brain tissue used in place of nerve tissue.*

### 4.3.2 Electrophysiological Findings

The presence of transdermal optical stimulation was defined by repeatable, temporally synchronized EMG twitches of characteristic triphasic or biphasic pattern (Fig 4.4A). Transdermal illumination produced twitches in 12 of the 20 tested animals at 5 weeks post-injection, with a 13$^{th}$ responding at 8 weeks post-injection (Fig 4.4B). The presence of low-dose animals that did not respond to identical transdermal illumination served as both a negative control against heating-induced optical nerve stimulation and demonstrated that higher dosages increased the likelihood of transdermal stimulation (Fig 4.4C). In addition, the lack of response of the low dose animals to direct illumination of the exposed nerve at 8 weeks, a fluence rate ~2 orders of magnitude greater than the transdermal fluence at the same nerve, serves to reinforce that the response is optogenetic and dose-dependent in nature as opposed to purely thermal or optical. Several control animals not injected with ChR2 virus were tested both with transdermal and direct nerve illumination with the same

parameters and found to have no EMG response (data not shown), further clarifying the response seen as optogenetic and not thermal.

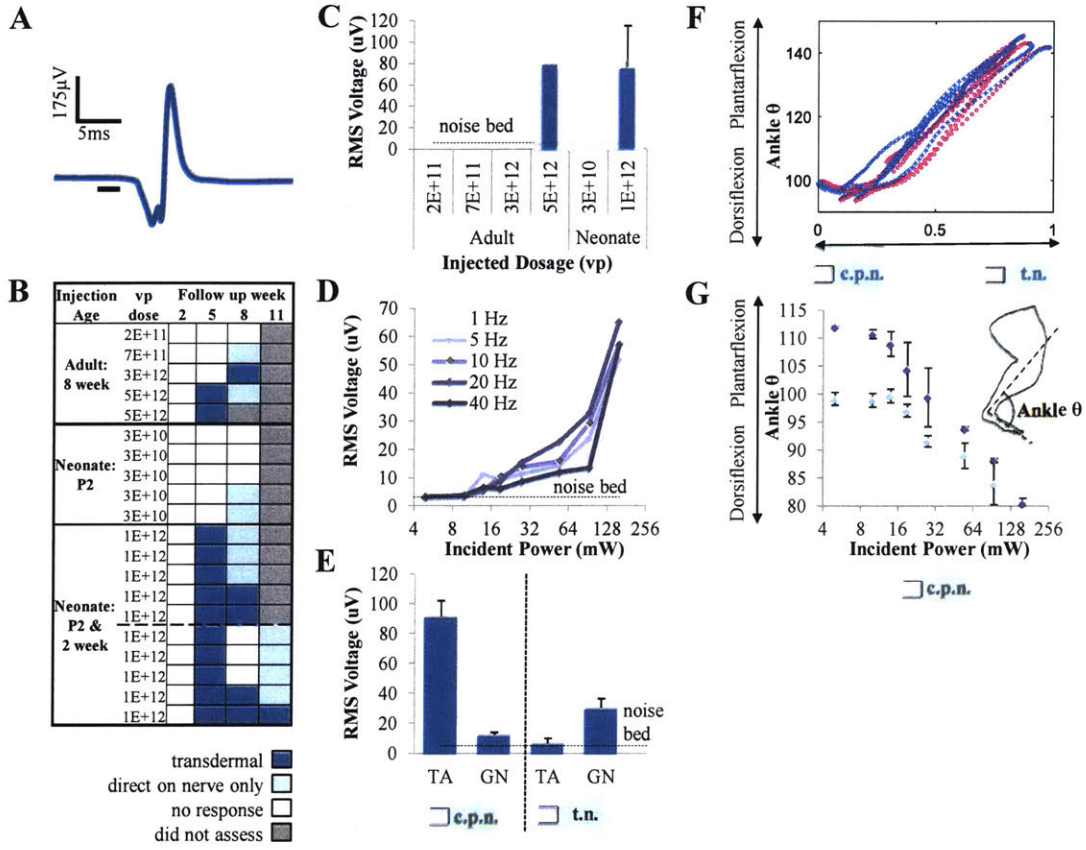


**Figure 4.4: Electrophysiological findings for transdermal FOS**

*(A) Biphasic EMG twitch waveform generated by the TA in response to transdermal illumination of the proximal tibia (160 mW laser power). (B) Variation in transdermal (2, 5, 8, 11 weeks) and direct-nerve (8 or 11 weeks) optical response as a function of dosage and age. (C) Calculated RMS EMG in TA at 5 weeks post-injection for 5 s transdermal stimulation: n=5 (5 Hz, 10 ms PW, 160 mW skin surface power). (D) Calculated RMS EMG in TA as a function of incident power and frequency for 5 s transdermal stimulation for P2 neonate at 5 weeks post-injection: n=1 (10 ms PW). (E) RMS voltage showing preferential stimulation of TA over GN in response to transdermal illumination at proximal tibia corresponding to common peroneal nerve (c.p.n.) and preferential stimulation of GN muscle over TA in response to transdermal illumination at mid-calf*

*corresponding to tibial nerve (t.n.): n=1 (5 Hz, 4 s duration, 3 trials, 10 ms PW, 160 mW skin surface power). (F) Ankle angle as a function of light position as laser was moved between proximal tibia and mid-calf. Horizontal axis normalized over ~8 mm distance between illumination regions; position data smoothed with 30 point moving average filter: n=1. (G) Ankle angle as laser power at proximal tibia ramped up from 5 mW to 160 mW (violet) and back down to 5 mW (blue): n=2.*

The stability of the transdermal response is uncertain. At 8 weeks post-injection, 6/10 of the original P2 neonates and 1/2 of the highest dose adults previously showing a transdermal response lost the response. For five of the animals, these nerves remained optogenetically excitable with direct nerve illumination at 8 weeks. The other five were kept 3 additional weeks to verify that extra time does not lead to overexpression. At 11 weeks, only 1 of these 5 animals responded to transdermal illumination; similar to the 8 week animals, direct nerve illumination resulted in twitches in all of the animals tested, although the response was significantly weaker than those animals euthanized at 8 weeks.

The transdermal RMS voltage was found to increase as a function of laser power; twitch responses were seen with as low as 10 mW incident power, which corresponds to a MC simulated fluence rate at the surface of the nerve of 89 $\mu W/mm^2$ (Fig 4.4D). In addition, it was found that the transdermal response could target muscles highly specific to laser position on the skin surface (Fig 4.4E). Illumination of the skin at the proximal tibia, superficial to the insertion of the c.p.n. in the TA, resulted in dorsiflexion and stimulation at mid-calf, superficial to the insertion of the t.n. in the GN, resulted in plantarflexion (Fig 4.4F). Alternating laser position could accurately produce a desired ankle position with little hysteresis or fatigue. In addition, incident power could be modulated to affect ankle position—with the laser targeting the skin superficial to the c.p.n. ramped from 10 mW to 160 mW, the ankle slowly dorsiflexed. A subsequent decrease in power resulted in the return to plantarflexion, although baseline not achieved, likely due to resting tension.

### 4.3.3 Immunofluorescence reveals strong axonal ChR2 expression

Evaluation of s.n. cross-sections showed strong ChR2+ fluorescence in both c.p.n and t.n. divisions (Fig 4.5A). Non-targeted t.n. shows strongest ChR2+ expression in the fascicles directly adjacent to the c.p.n, possibly indicating perineurial crossing of AAV at the level of the s.n. during injection or retrograde transport. Despite the goal of exclusive motor fiber transfection, only 40% and 35% of c.p.n. and t.n. ChR2+ axons co-express CHAT, a marker of motor neurons[107]. Fluorescence and diameter were measured for each ChR2+/CHAT- fiber to identify if the sensory fibers exclusively comprised the large diameter muscle spindle fibers, but no strong relationship between fluorescence and diameter was found. Histological cross-sections of the spinal cord show strongest expression within the several bright ChR2-EYFP+ motor neurons in the ventral horn of the high-dosed animals (Fig 4B). Sensory fiber transfection is also seen in spinal cord sections with ChR2+ dorsal horn expression appearing strongest in the nucleus proprius, dorsal nucleus of Clarke, and first order fibers of the ipsilateral gracile fasciculus, all of which indicate proprioceptive and touch sensors from the lower limbs (Fig 4.5B). Faint ChR2+ expression is seen in lamina I of the dorsal horn, indicating few ChR2+ Aδ or C fibers, possibly consistent with a protective "foot-tucking" response seen during transdermal foot stimulation of the awake, freely-moving rat.

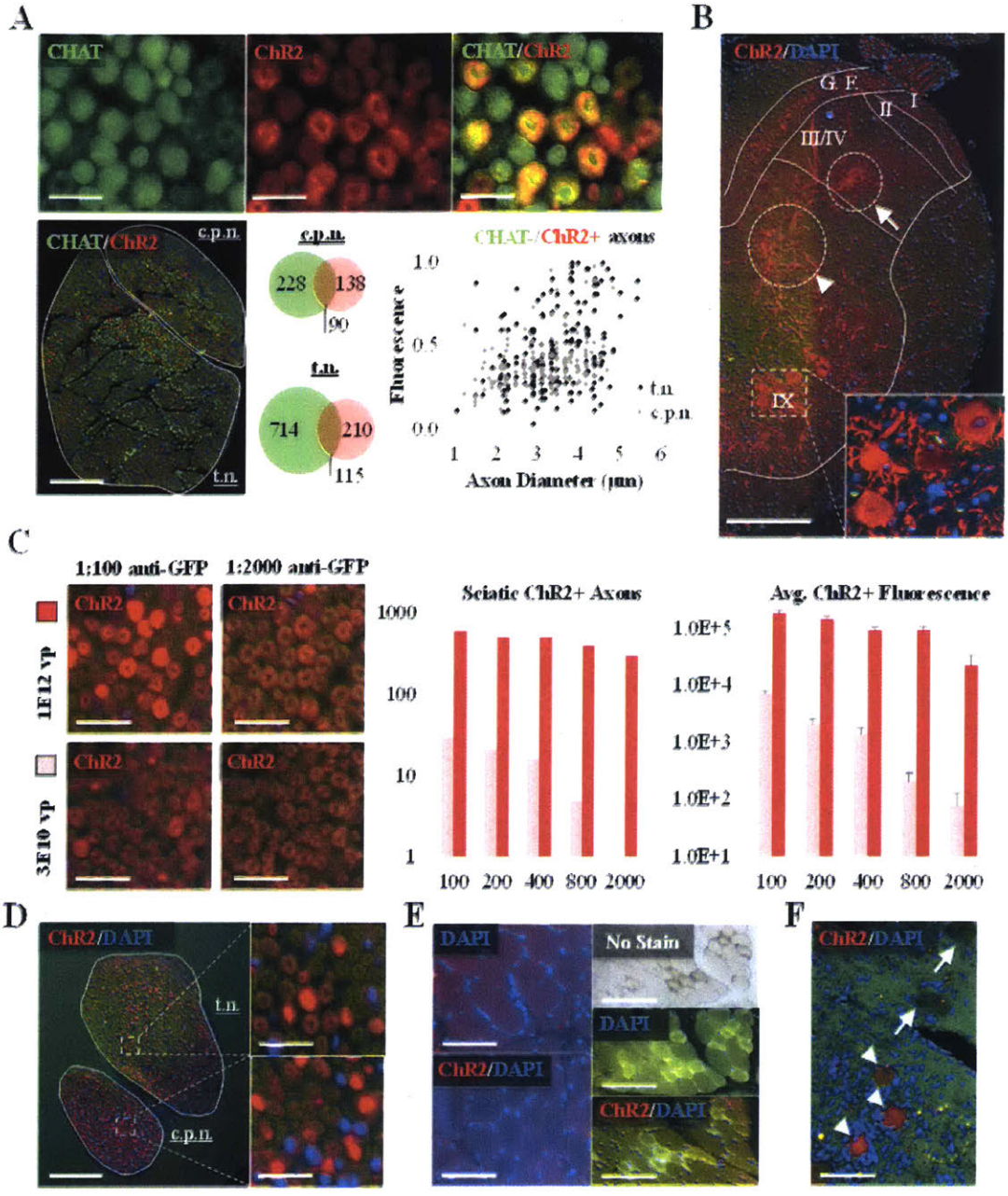


**Figure 4.5: Immunofluorescence assessment of ChR2-EYFP+ neural tissue**

*(A) 8-week post neonate injection sciatic nerve (s.n.) labeled for CHAT (green) and ChR2 (red) with corresponding counts in both the common peroneal nerve (c.p.n.) (targeted) and tibial nerve (t.n.) (non-targeted): scale bar 12.5 μm (top) and 150 μm (bottom). (B) Half-section of right spinal cord of 8-week post neonate injection between L3 and S1 labeled for ChR2 (red) and DAPI (blue). Within white matter, laminae I-IV & IX are outlined and likely nucleus proprius (arrow) and dorsal nucleus of Clarke (arrowhead). Within grey*

*matter, gracile fasciculus (G.F.) outlined: scale bar 325 μm. (C) Serial dilution of anti-GFP primary antibody to evaluate relative opsin density between low-dose and high-dose P2 neonate injections, with 1:100 and 1:2000 dilutions shown: scale bar 17.5 μm; comparison of transduction efficiency vs. primary antibody concentration shown in both total ChR2+ axon count and summed fluorescence of all ChR2+ axons for both doses. (D) representative 11-week post neonate injection s.n. labeled for ChR2 (red) with c.p.n. and t.n. outlined: scale bar 200 μm (left), 25 μm (right top) and 25 μm (right bottom). (E) TA labeled for both ChR2 (red) (bottom, left + right) along with negative controls (top left, right middle) indicating no difference in illumination of individual myocytes. Green autofluorescence of certain fibers (right) may indicate darker or hypercontracted fibers muscle fibers (no stain) as opposed to opsin present in the muscle tissue: scale bar 80 μm (left top and left bottom), 125 μm (right top, middle, bottom). (F) Spinal cord segment showing peri-neuronal inflammatory infiltrate surrounding ChR2+ neurons (arrowhead) compared to ChR2 negative neurons (arrow): scale bar 100 μm.*

To compare relative opsin density between dosages, both ChR2+ axon counts and summed average fluorescence was measured within the s.n. for several concentrations of primary antibody (Fig 4.5C). The serial dilution shows an order of magnitude difference between high-dose and low-dose rats in both axon counts and total fluorescence. This difference increases to ~2 orders of magnitude for the axons and ~3 orders of magnitude for the fluorescence as the concentration of primary in blocking solution decreases from 1:100 to 1:800. The relative drop in fluorescence as antibody concentration decreases suggests a weaker density of opsin channels within ChR2+ axons in the low-dose animal, due to non-specific binding out-competing the few ChR2+ antigen sites present within the axons. This histological evidence suggests a higher average opsin channel density per axon in the high-dose animal, providing a mechanistic rationale for the lower fluence required at the axon surface for transdermal stimulation in the high-dose rats.

Expression of opsin over time as measured by ChR2+ axon density in the s.n. revealed qualitative similarities between the 8-week post-injection rats and the 11-week post-

injection rats both in the c.p.n. and the t.n. (Fig 4.5D). To verify muscle tissue was not responsible for transdermal peripheral nerve stimulation, TA cross-sections were stained against opsin (Fig 4.5E). Fluorescence of the muscle samples with the antibody was indistinguishable from autofluorescence of the negative control, suggesting lack of ChR2 within myocytes. Some myocytes were found to autofluoresce at higher levels than others; this was caused by the darker pigmentation of the same myocytes, perhaps a function of the heterogenous population of muscle fibers or caused by hypercontracted fibers of yet unknown etiology. Lastly, one spinal cord section revealed a large number of DAPI+ nuclei selectively surrounding ChR2+ ventral horn neurons, indicative of a peri-neuronal inflammatory response (Fig 4.5F). However, this finding was not repeatable in other animals.

### 4.3.4 Whole Animal Imaging

Use of IVIS imaging machine revealed fluorescence was weak and limited to the c.p.n. at the time of euthanasia. No EYFP fluorescence could be seen transdermal through the skin (Fig 4.6). Further, after removing the lateral skin on the hindlimb and surgically exposing the BF muscle, no fluorescence activity was detected. This further confirms that hSyn is properly restricting optogenetic activity to neuronal targets and not muscle targets. However, upon surgical exposure of the sciatic nerve and its bifurcation into the tibial and peroneal branches, fluorescence activity was identified predominately on the c.p.n. branch. This is to be expected given that the density of ChR2+ axons in the c.p.n. is higher than that of the t.n..

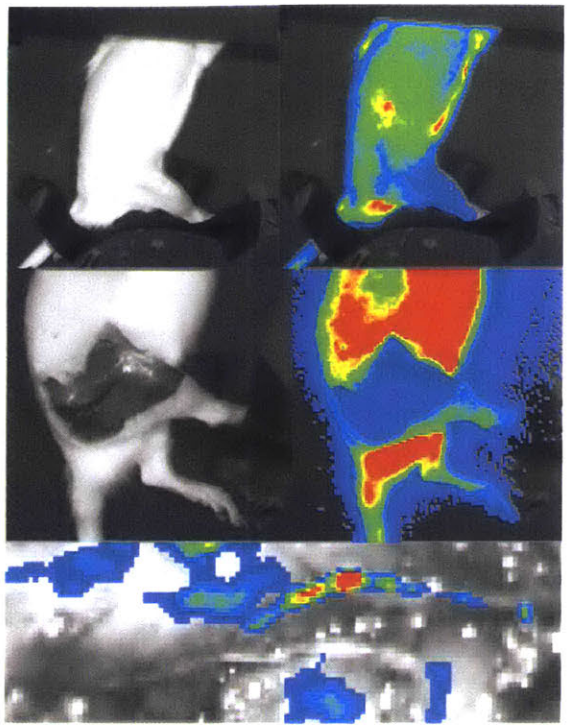

**Figure 4.6 *In Vivo* imaging of transduced c.p.n.**

*In vivo imaging reveals limited fluorescence activity to the c.p.n (bottom) as opposed to transdermal (top) or through the muscle (middle).*

## 4.4 Discussion

In this experiment, we hypothesized that transdermal illumination of peripheral nerve targets could be achieved by utilizing ultra-high virus concentration to inject more viral particles and therefore more transgene copies in the motor neuron genome, translating to a higher density of ChR2 channels in the axon, and a lower fluence rate required for depolarization. The data presented in this study support this hypothesis. In the neonates, we first saw transdermal EMG spikes for illumination of the 5-week c.p.n. and t.n. at 10 mW and 160 mW incident power respectively. When these powers are input to the normalized MC model for the 5-week animals, they translate to an estimated fluence rate at the surface of the c.p.n. of 89 $\mu W/mm^2$ and the t.n. of 176 $\mu W/mm^2$. When the animals were tested again at 8 weeks, we saw transdermal EMG spikes with illumination as low as 55 mW on the surface of the c.p.n.; however, we did not see any EMG spikes when

illuminating the surface of the t.n. of the 8-week animals. When input to the MC model, the estimated minimum fluence rate at the c.p.n. to produce EMG spikes was 215 $\mu W/mm^2$. A nerve surface fluence rate threshold in this range (89 – 215 $\mu W/mm^2$) represents roughly an order of magnitude decrease from previously published experimental thresholds on fluence rates required for peripheral axonal ChR2(H134R) activation[20,73], although neurons in the Central Nervous System have seen activations in this range in culture, brain slices, and awake, moving animals[108–110]. Increasing the total number of AAV particles delivered can therefore significantly improve the sensitivity of optogenetically active axons to illumination.

There has been significant interest in the topic of long-wavelength opsins and their potential utility for improving optogenetic activation of deep tissue targets by making the illumination more robust, safe, and practical. The absorption and scattering coefficients of red light (600 – 700 nm) in most biological tissues are significantly lower than those of blue-green light (400 – 500 nm), enabling activation of deeper targets with the same illumination intensity[75]. Additionally, transdermal optogenetic nerve activation of the same depths modeled here may be achievable with either a lower fluence rate or a lower AAV dosage. The decreased fluence rate implies that illumination power can be reduced, protecting against thermally induced tissue alterations or burns. The decreased dosage may further help protect against anti-AAV immune activity. Two variants have been identified as promising in red-light activation: ReaChR and Chrimson, both known to respond in the 600 – 700 nm wavelength region[64,111]. Future work studying the properties of red-shifted opsins in the peripheral nervous system will likely yield further scientific and clinical insights for transdermal optogenetics.

Although motor axons were targeted in this experiment, complete specificity measured by CHAT co-labeling and selective ventral horn expression was not achieved, indicating combining intramuscular and intra-nerve at end-plate injections may not be ideal for selective motor stimulation. Previous work indicates some dorsal horn expression is expected due to spindle fiber co-transfection[23]. The ChR2 distribution in the spinal cord

suggests proprioceptors are activated, but it is unclear how many touch or pain fibers are also being expressed as evidenced by ChR2+ expression in the smaller axons. A future experiment utilizing a transgenic CHAT-cre mouse and a flexed-AAV6 could help determine if virally induced CHAT-restricted ChR2 expression could selectively drive motor axons. This may enable fundamentally improved studies in optogenetic experimentation in awake, moving animals, a subset that likely is experiencing an undesirable sensory co-stimulation.

The stability and time course of ChR2 expression is a critically important component of peripheral nerve opotogenetics experiments[112]. In this paper, we evaluate the stability of transdermal stimulation from 5 weeks to 8 weeks, and notice a loss in optogenetic responsiveness in several animals. Anatomically, as the rat ages, the size of the muscles and skin, which separate the nerve from the laser source increases, decreasing the fluence rate at the nerve. However, aging does not account for a stronger transdermal response at the highest dose adult rats 5 weeks post-injection compared to the ~40% smaller P2 neonates at 8 weeks. In addition, the minimum fluence rate required for depolarization appears to increase over the 3-week period, indicating a potential decrease in optogenetic sensitivity. Another explanation could be that highly expressing ChR2 animals may elicit a stronger toxicity or immune response[112]; dose-dependent immune and inflammatory responses have been reported in previous AAV-mediated gene therapy, including recent human clinical trials[25,113]. Cellular ChR2 decreases over time have also been previously reported as a shutdown of transgene expression, independent to externally manifested capsid-specific immunogenicity[114]. Prior work suggests transgene shutdown to occur between 4 weeks and 12 weeks for DRG-injected AAV6, although other serotypes show superior stability[70,76]. In this study, the spinal cord section, which demonstrates a selective peri-neuronal inflammatory response, may hint at an immunogenic etiology to the loss of opsin expression over time. AAV titre-dependent inflammation has been previously reported in intra-spinal dorsal horn microinjections[115]; perhaps retrograde transport of AAV capsid from the muscle is also sufficient to elicit an immunogenic response in the spinal cord. Future work studying the mechanistic nature of the decrease of optogenetic expression as a function of dosage is critical.

# 5 Two Color Optogenetic Peripheral Nerve Stimulation

Peripheral nerve stimulation technologies have conventionally relied upon anatomic placement of electrodes adjacent to subsets of sensory or motor fibers for selective end organ targeting. Here, we use optogenetics to target the end effector's innervating fibers directly, relying on retrograde transfection of AAV6 to restrict axonal opsin expression to the desired fiber targets. We perform an *in vivo* screen in the murine model and identify the first channelrhodopsins and halorhodopsin responding to red light in the peripheral nerve. We then combine two channelrhodopsins with spectrally distinct activation profiles to drive opposing muscle activity via two-color illumination of the same mixed nerve. Lastly, we show halorhodopsin-mediated reductions in electrically evoked muscle tremor spectrally optimized for deep peripheral nerves. Together, these results demonstrate the first completely non-invasive peripheral neurostimulator with targeted multi-fascicle resolution. The findings broadly unveil new avenues of scientific and clinical exploration including motor control in paralysis, biomimetic sensation feedback for amputees, and targeted inhibition of muscle tremor, among others.

## 5.1 Introduction

A method for selective stimulation of independent nerve fiber populations within the same nerve remains a long sought goal of neural engineers in the PNS. Peripheral nerves are composed of heterogeneous populations of sensory and motor fibers, intermingled within fascicles, encoding stimuli for both unique anatomical coordinates and functional subgroups of sensory and motor fibers. Nerve fibers that produce the sensation of touch from one side of a finger may travel adjacent to nerve fibers responsible for motor control of a forearm muscle or stretch sensors from a hand muscle. The magnitude of the peripheral nerve (up to 100,000 individual fibers in a single nerve) combined with the difficulty of stimulating individual fibers selectively represents a key impediment to the development and implementation of neural interface technologies for paralysis, pain, amputation, human augmentation, and other conditions. Producing a peripheral neural interfacing technology that can selectively and consistently stimulate individual fiber targets with specificity and precision remains an elusive goal.

To date, all techniques employed to tackle this challenge have relied upon anatomic targeting of the nerve fibers within fascicles due to their somatotopic organization. Nerve cuff electrodes route current from electrode contact points to the immediately adjacent fibers for spatially distinct stimulation[9]. Longitudinal and transverse intrafascicular electrodes (LIFEs, TIMEs) stimulate nerve fiber sub-populations from within the nerve[9,34,116]. Microchannel and sieve electrodes divide the nerve into distinct regenerated groups, and then stimulate these independently[36]. While great strides have been made in the development and implementation of these technologies, significant challenges remain. Fascicles buried within the nerve are beyond the reach of external multichannel nerve cuff electrical contact points, resulting in inadvertent stimulation of non-targeted fascicles[9]. Both LIFEs and TIMEs are not meant for long-term use due to risk of mechanical damage and inflammatory responses within the nerve itself; additionally both can only target the few fiber groups directly adjacent to the electrode contact points[9]. Regenerated fibers through sieve electrodes do not recapitulate all of the features of healthy nerves including number and caliber of fibers, functional somatotopic organization, and grouping of fiber

types within a regenerated channel[117]. Because all of these electrical techniques rely purely on spatial orientation of nerve fibers, they can be difficult to implement consistently in nerves such as the recurrent laryngeal, which has significant mixing of nerve fibers throughout the length of the nerve[118,119]. Additionally, all of the techniques above are invasive, requiring implants, which can increase risk of nerve damage. To mitigate the risk of implants, infrared neural stimulation (INS) has been employed to target individual nerves at a distance, which can theoretically achieve high spatial resolution via targeting of unique nerves[120]. However, INS has not been able to stimulate nerve fascicles selectively from a distance, although selectivity was shown invasively using a nerve cuff fixed to an extraneural optical fiber[121]. This is because the INS excitation mechanism is largely thermal, which increases the difficulty of selective activation of nerve fiber subsets from a distance.

More recently, optogenetic stimulation of peripheral nerve system has been shown with the translatable goal of mitigating the pathophysiology of several disease states including chronic pain[70], muscle fatigue[20], and others. One key benefit of the optogenetic approach lies in the selectivity imposed by the viral transfection methodology. Retrograde transfection from a specific injected end effector (e.g., muscle, skin) can enable selective stimulation of the nerve fibers that innervate only that specific injection area. Previous efforts have validated end organ selectivity within muscle tissue by exploring the spatially distinct populations of transfected ventral horn motoneurons within the lumbar spinal cord[23]. Anatomically selective transfection is a powerful tool, if applied for the management of chronic pain, paralysis, or amputation feedback. However, a method to stimulate two subpopulations independently within the same peripheral nerve distinguished by end effector using optogenetics has proven elusive.

One property of the algal channelrhodopsins and halorhodopsins employed for optogenetics lies in the spectrally distinct nature of each opsin. Neuroscientists have sought high-performing red opsins due to the higher transmissivity of red light in biological tissues[122]. Red light can reach neural targets located deeper from the skin surface or

through thick neural tissue, which can theoretically activate optogenetic targets with lower surface intensities and attenuate concerns of light-mediated thermal damage[94,123]. Two variants have been identified as exceptionally promising in red-light activation: ReaChR and Chrimson, both known to respond in the 600 – 700 nm wavelengths[64,111]. ReaChR was engineered by replacing the VChR1 red-shifted channelrhodopsin with the N-terminus & L171I point mutation from ChIEF, and the F transmembrane domain from VChR2; the mutations increased photocurrent, wavelength, and membrane trafficking properties, but ReaChR was reported to still suffer from slow channel closure rate $\tau_{1/e}$ = 137 ms[64]. Chrimson was discovered as a naturally occurring opsin in the species Chlamydomonas noctigama. Using mutagenesis, Chrimson was engineered into ChrimsonR through the K176R mutation, which further red-shifted the opsin's spectrum and shortened $\tau_{1/e}$ from 21.4 ms to 15.8 ms. Whereas ReaChR has previously shown efficacy in mammals *in vivo*, exploration of Chrimson and ChrimsonR has been limited to brain slices, *in vitro* neurons, and Drosophila melanogaster within the published literature[64]. Other red-shifted variants including VChR1 and C1V1 have spectral domains that are only slightly shifted from ChR2 with peak excitation wavelengths in the 500-550 nm range[124,125].

When choosing an opsin for peripheral nerve experimentation, wavelength is only one consideration. Other key properties include temporal kinetics to drive tetanic frequencies, photocurrents to decrease depolarization threshold, and membrane targeting to drive efficiency of expression. In exploring the diversity of naturally occurring opsins, two other variants are particularly promising: CoChR, a powerful blue opsin with 470 nm photocurrents 4-5x that of ChR2(H134R)[126], and CsChR, an opsin with great membrane trafficking[111]. By taking advantage of the latter's membrane-trafficking properties, CsChrimson was created from the 74 N-terminus amino acids of CsChR and the 271 transmembrane domain amino acids of Chrimson[111]. CsChrimson has been employed in drosophila, but has not yet been tested in mammals[111]. Spectrally distinct inactivation in peripheral nerve applications is also of significant interest. JAWS, an engineered halorhodopsin with red-shifted inactivation peak at ~600 nm, has been shown functionally in the central nervous system, but deep tissue inhibition of peripheral nerve fibers has yet to be explored[83].

Independent two color neuronal stimulation was shown in brain slices following in utero electroporation with both ChrimsonR and CoChR[111]. However, when applying the best potential opsin candidates within the optogenetics toolbox to the peripheral nervous system, several system-specific challenges arise. First, the efficacy of viral transfection is significantly lower in the peripheral nervous system compared to the central nervous system due to the low efficiency of retrograde viral transfection of AAV[76]. Second, the peripheral nervous system is not immune-protected like much of the central nervous system. Immune responses to intramuscular injections have been shown for AAV injections in several mammalian species including humans for a variety of AAV-mediated gene transfection applications[24,25]. Third, expression of opsin protein localized to the cell body of the neuron is not sufficient to induce optogenetic responses to peripheral nerve illumination. Murine peripheral nerves can extend ~20 cm in length, compared to the ~30 μm neuronal cell diameter. Previous mapping of CNS neurons in transgenic mice has suggested that direct illumination of the axon itself may not be sufficient to induce an action potential, as compared to direct illumination of the cell body[109]. Successful nerve transfection implies sufficient opsin expression within the entire length of the axon membrane such that illumination anywhere along the nerve produces an action potential. These challenges significantly increase the difficulty of peripheral nerve optogenetics implementations compared to those of the CNS.

The creation of a peripheral nerve specific opsin toolbox would confer an enormous benefit to future scientific studies as well as a framework for future translatable systems for optogenetic disease treatment. We hypothesize that the intramuscular injection of AAV6 coding for a red opsin and a blue opsin in opposing muscle pairs would enable selective transfection of the nerve fibers corresponding to each muscle via spectrally distinct illumination of the same mixed nerve. We evaluate this hypothesis by screening several opsins with unique properties in the peripheral nervous system, and then applying the most promising, spectrally distinct candidates together in a rat hindlimb *in vivo* as a function of both modeled and applied fluence rate.

## 5.2 Methods

All animal experiments were conducted on Fischer 344 rats under the supervision of the Committee on Animal Care at the Massachusetts Institute of Technology.

### 5.2.1 Opsin Injection

The choice of opsins was based on both a literature search as well as conversations with experts in the field highlighting opsins with promising characteristics in both the red and blue spectra. The construct format was AAV6-hSyn-*Opsin-Reporter*-WPRE. The use of hSyn restricted expression to neural tissue. Virus was produced by Virovek, Inc from plasmids at a titer of $1\times10^{14}$ vg/mL. The opsin – fluorescent reporter combinations included ChR2(H134R)-EYFP[23], CoChR-GFP, Chrimson-GFP, ChrimsonR-tdtomato[111], csChrimson-tdtomato[111], ReaChR-Citrine[64], and JAWS-KGC-GFP-ER2[83]. Plasmids for CoChR, Chrimson, ReaChR, and JAWS were purchased from AddGene. The CsChrimson plasmid was synthesized by Genscript. Under isoflurane anesthesia, neonatal Fischer 344 rats 2 days postpartum (P2) (Charles River Labs) were injected IM transdermally with 15 μL virus targeting the AC (Fig 5.1A, 5.6A). The injection was delivered through a 34G needle (WPI) affixed to an intraocular kit (WPI), Silflex tubing (WPI), and a 10 μL nanofil syringe (WPI) on the UMP3 syringe pump (WPI) with injection rate set to 75 nL/s. In between each unique virus, the full system was flushed with $dH_2O$ followed by 2% w/v NaOH in $dH_2O$ followed by $dH_2O$ to prevent inter-viral contamination. All thirty-five rats were housed under a 12:12 light:dark cycle in a temperature-controlled environment with food and water ad libitum and euthanized at 8 weeks post injection.

### 5.2.2 Channelrhodopsin electrophysiology measurements

For each channelrhodopsin, a twitch response to both a 473 nm DPSS laser (OptoEngine) and a 635 nm diode laser (OptoEngine) was assessed via transdermal illumination of the lateral right hindlimb of the anesthetized rat at 2, 4, 6, and 8 weeks post-injection (Fig 5.1B). Laser pulses were controlled using a myDAQ (National Instruments) controlled by the NI Elvis Function Generator and custom software written in Matlab. Transdermal illumination targeted two specific locations on the surface of each animal: near the knee for the peroneal nerve, near the mid-calf for the t.n.. At 4 and 8 weeks post-injection, direct

optogenetic stimulation of the exposed s.n. was also tested for all animals. To stimulate the s.n. directly, a 0.5 cm incision was made on the right lateral hindlimb adjacent to the femur. The knee flexors and extensors were separated via blunt dissection along muscle planes, exposing the s.n. The presence of a foot twitch in response to illumination was evaluated both electrophysiologically and visually. To measure the strength of the electrophysiological response, four 30G monopolar electromyography (EMG) needles (Natus Medical) were directly inserted through the skin into the GN and TA of each rat for bipolar recording as described previously[123]. Needles were connected to a 20 kS/s multi-channel amplifier with a fixed 200x gain (IntanTech). Both the 473 nm laser and the 635 nm laser were secured above the anesthetized animal to an assembly allowing for six degrees of freedom. If a twitch was seen visually or electrophysiologically, EMG for each animal was recorded as a function of illumination intensity, frequency, pulse width, and molecular fatigue in response to a prolonged stimulation train. Force and EMG were recorded for select trials simultaneously using a force sensor (Shimpo FGV-0.5XY) affixed to the rat foot with suture (Fig 5.7A). Both laser beams had a Gaussian cross-sectional profile and 3 mm diameter ($1/e^2$), corresponding to a peak irradiance at the surface of the skin of 45 $mW/mm^2$ at a measured output power of 160 mW. The lasers were verified with a -40 dB CCD and beam profiler software (Thorlabs) to verify the laser beam size, shape, and strength were equivalent (Fig 5.8). Electrical signals controlling the laser amplitude, pulse width, and frequency were simultaneously recorded by the amplifier, enabling temporal synchronization of laser pulses and EMG. Two XLamp LEDs (XP-E2, Cree, Inc.) of 625 nm and 475 nm wavelength were used for transdermal stimulation. LEDs were powered from a current source (T-Cube, ThorLabs) at 1.2 A, 1-5 Hz with 5% DC to limit heating.

### 5.2.3 Halorhodopsin electrophysiology measurements

For the JAWS rats, the sciatic nerve was exposed at 2, 4, 6, and 8 weeks post-injection as described above. A custom bipolar hook electrode elevated the proximal sciatic nerve. Current pulses (50 μs, 17 Hz, 0.1 – 4 mA, 5-15 s) stimulated the nerve through the hook electrode while 0.2 – 1 s (17-45 $mW/mm^2$, 20-40% DC) of 473 nm or 635 nm illumination targeted the exposed sciatic nerve, the proximal tibia (transdermal), and the mid-calf

(transdermal). During trials, EMG was measured via needle electrodes as described above in both TA and GN channels (Fig 5.6B). In a terminal procedure 8 weeks post-injection, the sciatic nerve of the contralateral limb of the 5 rats was exposed and the experiment was repeated as above for the non-injected limb.

### 5.2.4 Two Opsin Injection

To assess selectivity of P2 injections, one P2 pup was injected intramuscularly at 75 nL/s with 15 μL dye containing Fast Green FCF (Sigma) in PBS, targeting the hindlimb anterior compartment on one side and the posterior compartment on the other side. Immediately following the injection, the pup was euthanized with CO2 and decapitation; the hindlimb muscles were dissected and photographed (Fig 5.9). For the two opsin viral injections, nine rats were housed under a 12:12 light:dark cycle in a temperature-controlled environment with food and water ad libitum. At P2, six pups were injected intramuscularly with 15 μL AAV6-hSyn-CsChrimson-tdtomato targeting the anterior compartment and 15 μL AAV6-hSyn-ChR2(H134R)-EYFP, targeting the posterior compartment. The remaining three pups were injected at P14 under isoflurane anesthesia. In this procedure, a 0.5 cm incision was made lateral to the mid-tibia. The peroneal nerve was exposed from underneath the biceps femoris and 12 μL of AAV6-hSyn-csChrimson-tdtomato was injected into the exposed TA adjacent to the peroneal nerve endplate at a rate of 75 nL/s, and 3 uL was injected directly into the peroneal nerve at the endplate at a rate of 50 nL/s. The injection system was flushed as described previously and the tibial nerve was exposed. 12 μL of AAV6-hSyn-ChR2(H134R)-EYFP was injected into the exposed GN adjacent the tibial nerve endplate at a rate of 75 nL/s and 3 μL was injected into the tibial nerve at the endplate at a rate of 50 nL/s. The skin incisions were closed with wound clips and wound glue. After 4 weeks and 8 weeks the P2 ratss were tested for responsiveness to both transdermal illumination and direct illumination of the exposed sciatic nerve using both the 473 and 635 nm lasers and the LEDs: three rats were euthanized at each timepoint. During terminal procedures, the peroneal and tibial nerves were exposed by caudal reflection of the biceps femoris muscle and illuminated with both red and blue lasers at varying illumination intensities.

### 5.2.5 Tissue processing and analysis

Following EMG recordings during terminal procedures, rats were euthanized via intra-peritoneal sodium barbital followed by transcardial perfusion with 60 mL PBS followed by 60 mL 4% PFA in PBS. Both dorsiflexor and plantarflexor muscle groups on ipsilateral and contralateral hindlimbs were carefully dissected, cut from their origin and insertion points, and weighed. Spinal cord, TA, and sciatic nerve were dissected, fixed for 12-24 hours, paraffin processed, embedded, and cross-sectioned at 10 μm. For the two opsin animals, spinal cord sections were embedded either longitudinally or in cross-section and sectioned at 10 μm thickness. Expression of EYFP, GFP, and Citrine was amplified with Rb pAb anti-GFP (ab290, Abcam) at 1:200 or Gt pAb anti-GFP (ab5450, Abcam) at 1:100 with anti-Rb Alexa Fluor 488 (Fisher). Expression of tdtomato was amplified with pre-adsorbed Rb pAb anti-RFP (600-401-379, Rockland) at 1:25 with anti-Rb Alexa Fluor 568 (Fisher). All antibodies were diluted in 1% w/v BSA in PBS-T. Immunofluorescence images were taken on an Evos FL Auto epifluorescence microscope (Fisher) at 10x (spinal cord) or 20x (s.n.). Using ImageJ, opsin$^{+}$ axons and neurons were counted manually whereas total axon counts were estimated from representative counts of subsets of the nerve.

### 5.2.6 Fluence Model

To model the fluence rate of red and blue illumination through the rat limb to the nerve, a procedure was used as described previously[123]. Briefly, the right hindlimbs of four 2-week old and four 4-week old Fischer 344 rats were extracted, fixed, and sectioned at 10 μm thickness every ~250-500 μm, and stained with H&E. The sciatic nerve was traced to its division into the common peroneal nerve and tibial nerve, which were followed distally to their end plates. The c.p.n and t.n. depth, relative to skin, was measured on each slice; the slice with the minimum distance between nerve and skin surface was conservatively used for gathering the tissue geometry required for modeling (Fig 5.10). A MC simulation was created in Matlab for estimating fluence rate distribution in the rat peroneal and tibial

nerves using code previously provided[123]. Key inputs to the model included tissue geometry, attenuation coefficients for scattering ($\mu_s$) and absorption ($\mu_a$), and anisotropy factors in skin, muscle, connective tissue, epineurium and nerve, which were gathered from previous studies[87–91]. The model simulated ~$10^6$ photons, which was sufficient to maintain confidence interval within 5% of fluence estimates using ~$10^7$ photons. To assess whether stimulation of the nerve was optogenetic in nature and not driven by optically-induced heating of the nerve, an optical model of the Pennes bioheat equation provided by Stujenske et al. was adapted for the peripheral nerve anatomy and tissue properties as described previously[94,95]. In addition to the MC output and tissue-specific $\mu_a$, other inputs to the thermal model included tissue density, heat capacity, thermal conductivity, perfusion rate, and metabolic generation for rat tissue gathered from the literature (Fig 5.11)[96–100].

### 5.2.7 Cell Culture

Hippocampal cells from Swiss-Webster mice were obtained and cultured as previously published[63]. Cells were incubated with 0.4 mL media containing AAV6 coding for opsin (concentration: $5x10^{-19}$ mg/mL) for 72 hours. Expression was measured by imaging the fluorescent reporters for each opsin on a confocal fluorescent microscope at 10x magnification. CellProfiler built-in functions were used to determine the intensity and distribution of expressed opsins within each cell and its axonal projections. Patching of hippocampal cells was performed as described previously[111].

### 5.2.8 Statistical Analysis

Statistical significance was calculated in Microsoft Excel with the data analysis toolbox. For comparisons of individual groups, student's two-tailed t-tests with unequal variance were performed. For comparisons of multiple groups, a single factor ANOVA was performed for significance followed by post-hoc two-tailed Fishers Least Significant Difference tests for individual groups. All data represent the mean ± s.d. of at least three independent experiments unless otherwise specified; the number of trials is reported in the data provided.

## 5.3 Results

### 5.3.1 Optogenetic Peripheral Nerve Expression is Opsin-Dependent

Of the six channelrhodopsins evaluated, four (ReaChR, CoChR, CsChrimson, and ChR2) resulted in successful electrophysiological muscle expression in response to illumination of the nerve. As expected, all four opsins exhibited EMG spikes in response to 473 nm illumination, but only ReaChR and CsChrimson exhibited spikes to 635 nm illumination (Fig 5.1C). Unexpectedly, the strength of the EMG response to 473 nm illumination was greatest in ChR2 as measured in both the TA and GN channels, despite the higher photocurrents of CoChR[111] (Fig 5.1D). Within the red channel, we found that the strength of the CsChrimson EMG in response to 635 nm illumination greatly exceeded that of ReaChR (Fig 5.1D). Despite multiple attempts, transdermal or direct illumination of the exposed sciatic nerve of animals injected with either Chrimson or ChrimsonR at 473 nm or 635 nm did not result in any electrophysiological spiking at any time during the course of the experiment (Fig 5.1C). Additional *in vivo* ChrimsonR experiments varying virus source, dosage, age of injection, serotype and injection volume surprisingly did not produce any electrophysiological twitches at any time (Fig 5.12A), despite verified *in vitro* expression of the opsin measured both with fluorescence (Fig 5.13G) and with patching (Fig 5.12B,C). Force and EMG were found to be linearly related within the range of EMG and force measurements produced by optogenetic activity (Fig 5.1B), in line with previous findings[127].

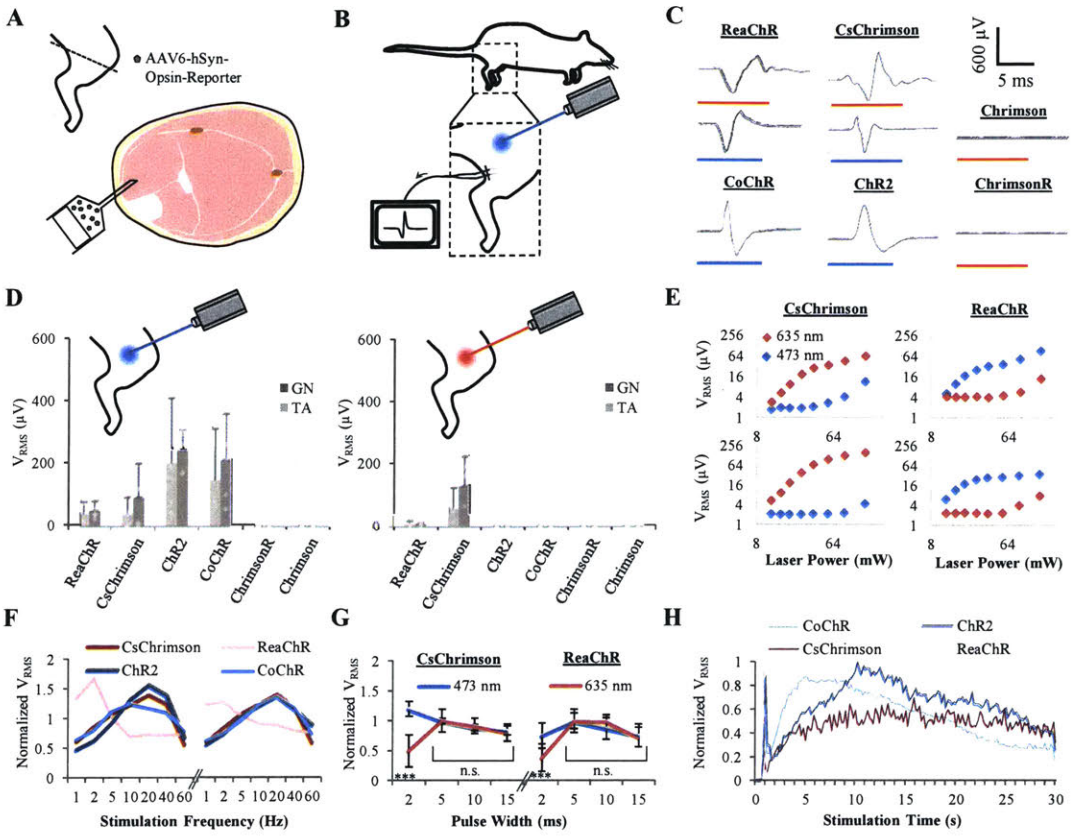


**Figure 5.1: Peripheral nerve opsin screen**

*(A) 15uL AAV6-hSyn-Opsin-Reporter injected into TA Fischer 344 rats 2 days postpartum. (B) At 2, 4, 6, and 8 weeks post-injection, 473 nm laser (shown) or 635 nm laser (not shown) illuminated surface of animal while EMG was recorded. (C) Select EMG spikes from optogenetic activation with either 473 nm pulses (blue) or 635 nm pulses (red). (D) Average RMS voltage calculated from EMG for 45 mW/mm$^2$ illumination of exposed sciatic nerve at 4 weeks post-injection for 473 nm illumination (left) and 635 nm illumination (right) recorded from TA and GN (PW = 10 ms, f = 5 Hz) for ReaChR: n=4, CsChrimson: n=4, ChR2: n=5, CoChR: n=5, ChrimsonR: n=5, Chrimson: n=5. (E) Direct illumination of the sciatic nerve induced GN RMS voltage calculated against illumination power for 635 nm 473 nm lasers for two CsChrimson (left) and two ReaChR (right) rats 4 weeks post-injection. (F) Normalized $V_{RMS}$ as a function of stimulation frequency for 473 nm illumination of the exposed sciatic nerve 4 weeks post-injection for both GN (left) and TA (right): (157 mW, 10 ms PW); CsChrimson (n=2), ReaChR (n=4 for GN, n=3 for TA),*

*ChR2 (n=5), CoChR (n=5). (G) Normalized $V_{RMS}$ as a function of stimulation PW for 473 nm and 635 nm illumination of both exposed nerve and transdermal (157 mW, 5 Hz). $V_{RMS}$ calculated for each trial with min threshold set to 3.25 μV to exclude noise, normalizing across all PWs for each animal and then averaging all trials for 473 nm CsChrimson (n=7), 635 nm CsChrimson (n=40), 473 nm ReaChR (n=34), and 635 nm ReaChR (n=11). Comparison was performed using student's one tailed t test unequal variance (***P<0.001; n.s. = not significant). (H) Rolling average $V_{RMS}$ from each animal at 4 weeks in response to direct illumination of the nerve with 473 nm light (CoChR, ReaChR, ChR2) or 635 nm light (CsChrimson) for 30 s at 40 Hz and 10 ms PW, normalized to maximum EMG over 30 s.*

We identified a key differential in the optical sensitivity for both CsChrimson and ReaChR as a function of illumination intensity (Fig 5.1E). At low illumination intensities (2.8 $mW/mm^2$), 635 nm illumination produced strong CsChrimson EMG comprising many distinct motor units. However, 635 nm illumination could not elicit ReaChR EMG until the illumination intensity exceeded 25 $mW/mm^2$. Conversely, 473 nm illumination resulted in ReaChR EMG at low illumination intensities (2.8 $mW/mm^2$), but CsChrimson required at least 16 $mW/mm^2$ for weak stimulation. Despite robust stimulation of ReaChR at a range of wavelengths, CsChrimson remained the only opsin identified to have higher sensitivity to red light compared to blue light, making it a prime candidate for two color peripheral nerve optogenetics.

The frequency response of each opsin in the peripheral nerve was found in agreement with previously reported literature's *in vitro* characterizations[64,111]. ReaChR was not able to sustain high frequency firings over 5 Hz. The frequency producing the maximum $V_{RMS}$ ($f_{max}$) was identified for CsChrimson, ChR2, and CoChR to be 20 Hz. For ReaChR, $f_{max}$ = 2 Hz (Fig 5.1F). CsChrimson was also found to have a slight peak shift with 635 nm illumination to $f_{max}$ = 10 Hz compared to 473 nm illumination (Fig 5.14A). Unlike the frequency response, the pulse width response was found to be similar for all four opsins for 473 nm stimulation (Fig 5.14B). Although the strength of the response appeared to

decrease with increasing pulse width, this was likely indicative of low recovery time between stimulation trains and was not indicative of a physiologic phenomenon. However, for both CsChrimson and ReaChR, the strength of the EMG in response to a 2 ms pulse width of 635 nm illumination was significantly lower than in response to a 2 ms pulse of 473 nm illumination ($P<10^{-6}$) (Fig 5.1G), indicating that opsin on-kinetics are wavelength dependent. This dependence must be biomolecular, because 635 nm illumination of the same intensity must have a greater photon density and therefore likelihood of opsin strike because of both the Planck-Einstein relation and the lower absorption of red light in tissue.

To evaluate each opsin's response to a prolonged stimulation train, a 30 s step response to 40 Hz stimulation was measured. Normalized $V_{RMS}$ showed nonlinearity for all opsins (Fig 5.1H). A rapid, strong peak corresponding to the onset of illumination was followed by a ~2 s refractory period where muscle activity dropped sharply. A 2-10 s $V_{RMS}$ recovery generally followed until a slow, steady decline of muscle activity due to fatigue until stimulation ended. Due to its slow off-kinetics, ReaChR was constrained to a strong initial peak followed by a dearth of follow up activity. The approximate shape of the step response was bucketed for each opsin and trial, revealing that ChR2 and CoChR were consistently activated throughout the full illumination duration as compared to CsChrimson and ReaChR, which showed weaker activity following the initial pulse (Fig 5.14C).

### 5.3.2 High EMG Efficiency Suggests ChR2 is Most Robust Opsin for Peripheral Nerve Stimulation

The electrophysiological results align well with histological findings. Sciatic nerve cross-sections of each opsin reveal strong expression for ReaChR, CsChrimson, ChR2, and CoChR as compared to Chrimson and ChrimsonR (Fig 5.2A). ReaChR animals 2 & 3 showed robust axon immunofluorescence and CsChrimson animals 1 & 5 showed moderate immunofluorescence compared to other animals in those same groups, aligning identically with the presence of EMG from direct sciatic nerve illumination of those same animals just prior to euthanasia (Fig 5.2B,5.5A). For each electrophysiologically active

opsin, an EMG efficiency was calculated from the ratio of $V_{RMS}$ to total opsin+ axon counts (Fig 5.2C). Although ReaChR had high axonal expression, it produced weak action potentials, resulting in low opsin efficiency. CsChrimson, despite having low axon counts, produced reasonable EMG signals resulting in a stronger efficiency. Despite the high photocurrents of CoChR, ChR2 had the highest efficiency, producing very high EMG signals compared to its histological fluorescence counts.

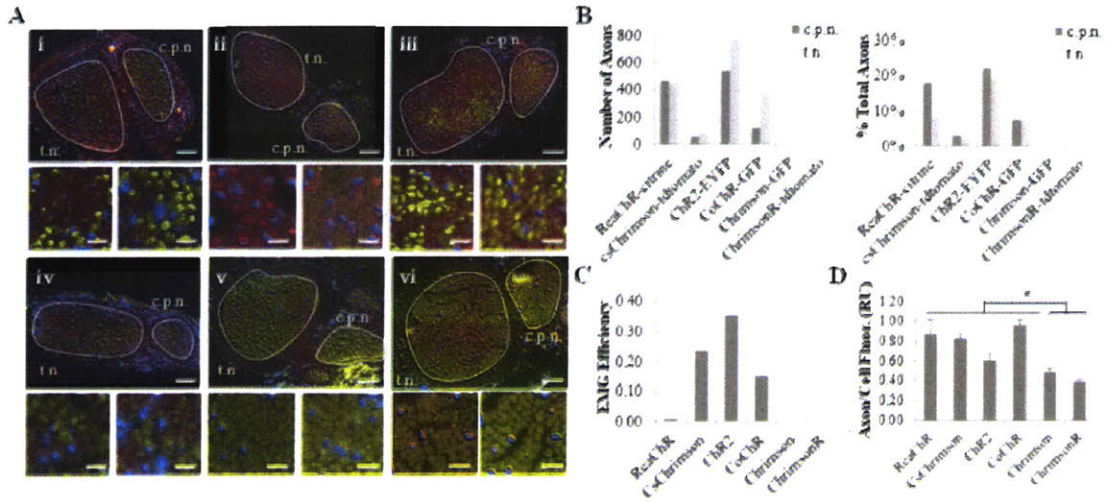


**Figure 5.2: Immunofluorescent opsin evaluation**

*(A) Sciatic nerve stained for GFP, EYFP, or citrine (green), tdtomato (red), and DAPI (blue) with outlined divisions for common peroneal nerve (c.p.n.) and tibial nerve (t.n.) (top) (scale bar: 150 μm). Representative zoom in sections of t.n. (bottom, left), and c.p.n. (bottom, right) (scale bar: 15 μm) for: (i) ReaChR, (ii) CsChrimson, (iii) ChR2, (iv) CoChr, (v) Chrimson, (vi) ChrimsonR. (B) Number of opsin$^+$ axons in representative sciatic nerve sections (left) and as percentage of total counts (right). (C) EMG efficiency calculated as GN $V_{RMS}$ of 8 week rat to 473 nm illumination (ReaChR, ChR2, CoChR) or 635 nm illumination (CsChrimson) on exposed sciatic nerve, divided by number of opsin$^+$ axons for the same animal (160 mW, 5 Hz, 10 ms). (D) Ratio of in vitro fluorescence of axon to cell body for ChR2: n=6, CoChR: n=10, JAWS: n=10, CsChrimson: n=7, ReaChR: n=4, ChrimsonR: n=4, and Chrimson: n=7.*

Despite lack of *in vivo* s.n. immunofluorescent or electrophysiological responses for Chrimson and ChrimsonR, we discovered *in vitro* fluorescence in all opsins in hippocampal cultures (Fig 5.13). Expression in the cell body was much higher than in the axonal projections for each opsin. The ratio of axonal expression to cell body expression was calculated, normalized, and compared across opsins (Fig 5.2D). Notably, ChrimsonR and Chrimson demonstrated ratios (<0.5) which were significantly smaller than the other opsins ($p < .045$), suggesting expression was more concentrated in the cell body for these opsins. Spinal cord immunofluorescence revealed clear, ipsilateral opsin$^+$ expression in ventral horn neurons for all opsins except for Chrimson and ChrimsonR, which may have had some very weak expression in comparison to the contralateral side (Fig 5.15A). These results together suggest that the lack of Chrimson and ChrimsonR expression within motor axons may be related to both overall low levels of cytoplasmic protein as well as poor axonal membrane trafficking.

### 5.3.3 CsChrimson and ChR2 Drive Two Color Independent Stimulation of Subsets of Sciatic Nerve

After characterizing the individual opsins, three P14 rats and six P2 rats were injected with AAV6 carefully targeting the TA for CsChrimson and the GN for ChR2 (Fig 5.3A). For the P2 rats, transdermal illumination 4 weeks post-injection provided both dorsiflexion & TA spikes in response to red light compared to plantarflexion & GN spikes in response to blue light; these movements and electrical recordings were repeatable even when the light source position on the surface of the skin was reversed, demonstrating source-agnostic control of peripheral nerve subsets. At 8 weeks post-injection, the sciatic, peroneal, and tibial nerves were exposed. Illumination of the peroneal nerve exclusively revealed EMG spikes in the TA EMG channel. 635 nm illumination elicited a very strong $V_{RMS}$ response as low as 10 mW (2.8 mW/mm$^2$), whereas 473 nm illumination could only produce spikes at 160 mW (45 mW/mm$^2$) (Fig 5.3D), consistent with the illumination intensity recruitment curve for CsChrimson (Fig 5.1E). Conversely, illumination of the tibial nerve exclusively revealed EMG spikes in the GN channel only, and only in response to 473 nm

illumination (Fig 5.3D), consistent with the illumination intensity recruitment curve for ChR2[123].

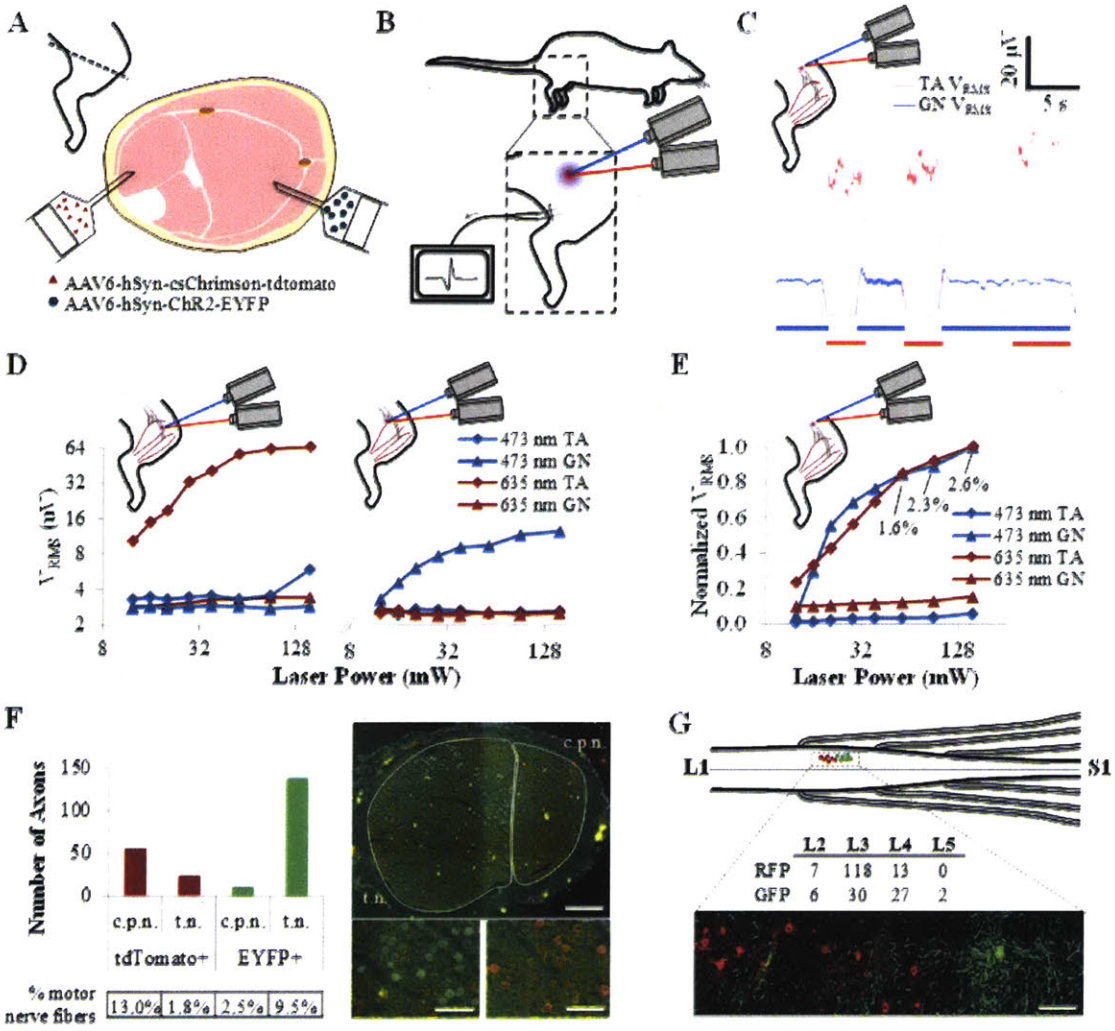


**Figure 5.3 Two color independent optogenetic peripheral nerve stimulation**

*(A) 15uL AAV6-hSyn-csChrimson-tdtomato injected into TA and 15 μL AAV6-hSyn-ChR2-EYFP injected into GN of P2 or P14 Fischer 344 rat. (B) After 8 weeks, each laser illuminated the exposed nerves while EMG was recorded. (C) $V_{RMS}$ calculated from EMG elicited by co-localized 635 nm laser (red) and 473 nm laser (blue) directly illuminating sciatic nerve. Lasers differentially activate TA electrodes (red) and GN electrodes (blue) (5 Hz, 3 ms PW, $P_{635nm}$= 157 mW, $P_{473nm}$= 90 mW; RMS calculated every 0.1 s with 0.5 s window). (D) With both lasers co-localized on the peroneal nerve (c.p.n., left) and tibial nerve (t.n., right), 473 nm laser followed by 635 nm laser was ramped in a power sweep*

*from 12 to 160 mW while TA and GN EMG were recorded (5 Hz, 10 ms PW, 4 s each). (E) With both lasers co-localized on the sciatic nerve, 473 nm laser and 635 nm laser was ramped in a power sweep from 12 to 160 mW while TA and GN EMG were recorded (5 Hz, 10 ms PW, 4 s each). For the sciatic nerve, EMG was normalized to max $V_{RMS}$ for each wavelength. Force is also shown as a percentage of body weight, at the illumination intensities where force exceeded the recordable threshold. (F) Immunolabeling reveals spatially distinct opsin within t.n. and c.p.n. fascicles of the mixed sciatic nerve in both absolute and relative quantities. Representative histological sections of sciatic nerve with c.p.n. and t.n. fascicles outlined stained for both tdtomato (red) and EYFP (green): scale bar = 10 μm. (G) Spinal cord histological section showing tdtomato+ neurons (csChrimson) and EYFP+ neurons (ChR2+) generally in distinct groups, corresponding to their relative ventral horn locations.*

Direct illumination of the exposed sciatic nerve with blue and red light produced EMG specific to the injected muscle (Fig 5.3C & 5.3E). Co-stimulation of both muscles with blue and red illumination produced co-contraction. The TA channel EMG increased slightly with co-stimulation compared to red illumination alone, indicating that blue illumination recruited additional CsChrimson motor units, which were subthreshold with red illumination. However, red illumination did not influence the strength of GN channel, consistent with ChR2's inability to be activated by red illumination (Fig 5.3C). Independent two color EMG was also seen via transdermal illumination of the sciatic nerve using high-powered LEDs (Fig 5.16). Electrophysiological findings are consistent with histologic evaluation of the mixed sciatic nerve's tibial and peroneal fascicles, which contained 7x more $ChR2^+$ axons and 6x more $CsChrimson^+$ axons respectively (Fig 5.3F). The overall percentage of myelinated axons transduced remained low at ~5% for the peroneal nerve (16% of peroneal motor axons) and ~2.5% for the tibial nerve (12% of tibial motor axons), consistent with histology for CsChrimson alone[56]. Longitudinal slices of the spinal cord showed spatial distinction of the predominately cranially located $CsChrimson^+$ neurons compared to caudally located $ChR2^+$ neurons (Fig 5.3G), consistent with rat studies of spinal anatomy[128,129]. Axial spinal cord cross-sections revealed distinct groupings of $CsChrimson^+$ and $ChR2^+$ neurons within the ipsilateral ventral horn (Fig

5.15B). Taken with the electrophysiological results, these histological findings validate independent optogenetic stimulation of subsets of peripheral nerve targets.

### 5.3.4 635 nm Illumination Achieves Four-fold Higher Fluence Rate for Deep Nerves

To evaluate how much farther red light can penetrate in deep tissue peripheral nerve targets, a MC model was constructed for the full range of tissue geometries analyzed in this study. Tissue cross-sections revealed a nerve depth ranging from 0.8 mm for the 2 week old peroneal nerve to 5.0 mm for the 8 week old t.n. (Fig 5.4A) with the majority of the intermediate tissue represented by skin and muscle (Fig 5.10). The MC model showed the fluence rates from 635 nm illumination well exceeded fluence rates from 473 nm illumination for all nerves modeled. Whereas the $\log_{10}$ reduction of normalized blue light fluence rate is constrained to the first ~1 mm of tissue, the equivalent red light permeated approximately ~2 mm, within range of the 2 week t.n. (Fig 5.4B). The MC model showed that at depth, blue light was more targeted than red light, consistent with transdermal findings; whereas red illumination of the mid-calf targeting the tibial nerve elicited both strong GN and TA responses, blue illumination excited more GN activity (Fig 5.14D). A centerline plot showing fluence rate as a function of tissue depth revealed that blue fluence rate exceeded red fluence within the first ~300 μm of tissue, consistent with the increased anisotropy of the scattering of red light compared to blue light (Fig 5.4C). After the crossing point, red fluence gradually increased relative to blue fluence, reaching ~4x greater by a 4 mm depth.

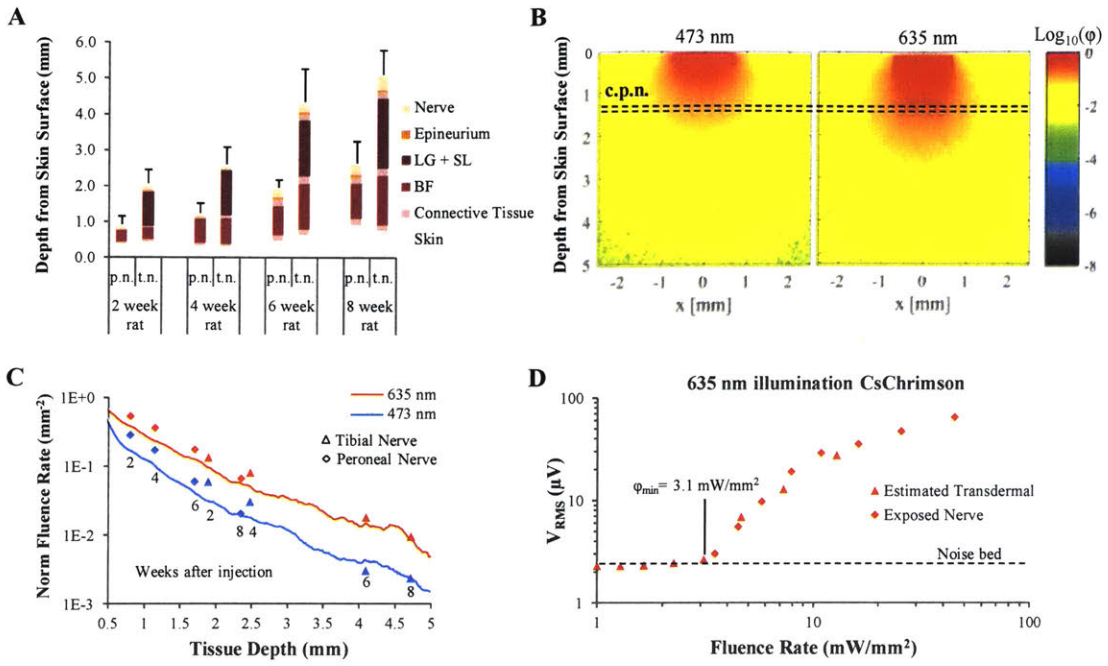


**Figure 5.4 Fluence rate modeling for red and blue light**

*(A) Tissue depth estimates for distance to nerve by tissue for peroneal nerve (p.n.) and tibial nerve (t.n.) at smallest distance to skin surface. (B) 2D representation of 473 nm and 635 nm MC output with common peroneal nerve (c.p.n.) location shown for 4 week p.n. geometry with z = tissue depth and x = radial distance from beam center. (C) Monte Carlo (MC) output with fluence rate along centerline for modeled 8-week t.n. for both 635 nm and 473 nm illumination along with independently modeled MC for peroneal nerve and tibial nerves for 2, 4, 6, and 8 week c.p.n. and t.n.. (D) Measured GN EMG as a function of fluence rate for both transdermal illumination of t.n. (estimated fluence rate from MC Model) and direct stimulation of exposed sciatic nerve (known fluence rate) of same CsChrimson+ nerve at 4 weeks post-injection.*

The normalized fluence rate to 635 nm illumination was found to be $6.8\times10^{-2}$ $mm^{-2}$ at the peroneal nerve for the 8-week rat and $9.7\times10^{-3}$ $mm^{-2}$ at the tibial nerve of the 8-week old rat (Fig 5.4C). As such, the 160 mW, 635 nm laser source, transdermally incident, yields fluence rates of 10.9 $mW/mm^2$ and 1.6 $mW/mm^2$ at each of the respective nerves. Comparatively, the normalized fluence rate to 473 nm illumination was found to be

$2.1\times10^{-2}$ $mm^{-2}$ at the peroneal nerve and $2.5\times10^{-3}$ $mm^{-2}$ at the tibial nerve, showing a 3-4x difference. An EMG vs. fluence rate comparison between transdermal illumination (subject to the MC results) and direct illumination of the exposed nerve showed $V_{RMS}$ agreement within the overlap range, suggesting the MC model accurately predicted fluence rate at the nerve (Fig 5.4D). A thermal analysis using with incident irradiation showed a max temperature rise of 1.16 °C for 473 nm and 1.05 °C for 635 nm at the two week peroneal nerve (Fig 5.11A,B). For both wavelengths, the heat dissipated by ~35% within 0.5 s of ending stimulation. The model was found to reach steady-state at ~7s (Fig 5.11C), suggesting that pulsed 30 s illumination, even directly on the exposed nerve would be subthreshold for heating-induced optical nerve activity, which is primarily dependent on a threshold nerve temperature of 42-45 °C[106].

### 5.3.5 ChR2 Outperformed CoChR, ReaChR, and CsChrimson Despite Elevated Red Fluence Rates at Depth

When comparing all opsins, peak optogenetic excitability was found 4 weeks after injection as measured by number of animals responding to illumination (Fig 5.5A), consistent with our previously reported loss of optogenetic responsiveness from 5 weeks to 8 weeks post-injection for ChR2[123]. At 4 weeks, 5/5 ReaChR and 5/5 CsChrimson animals responded to 160 mW transdermal illumination of blue and red light, corresponding to MC-modeled fluence rates of 1.9 $mW/mm^2$ and 3.8 $mW/mm^2$ at the peroneal nerve surface respectively. At 8 weeks, however 0/5 ReaChR and 0/4 CsChrimson animals responded to transdermal illumination of either wavelength. Direct illumination of the exposed nerve activated 2/5 ReaChR and 2/4 CsChrimson animals respectively at minimum fluence rates of 16 $mW/mm^2$, strongly suggesting loss-of-expression over time. CoChR and ChR2 animals fared slightly better with 2/4 and 2/5 animals respectively maintaining responsiveness to transdermal blue illumination at 8 weeks. Additionally, all of the ChR2 and CoChR animals maintained optogenetic excitability to direct stimulation of the sciatic nerve at 8 weeks, although this EMG response was weak for certain animals.

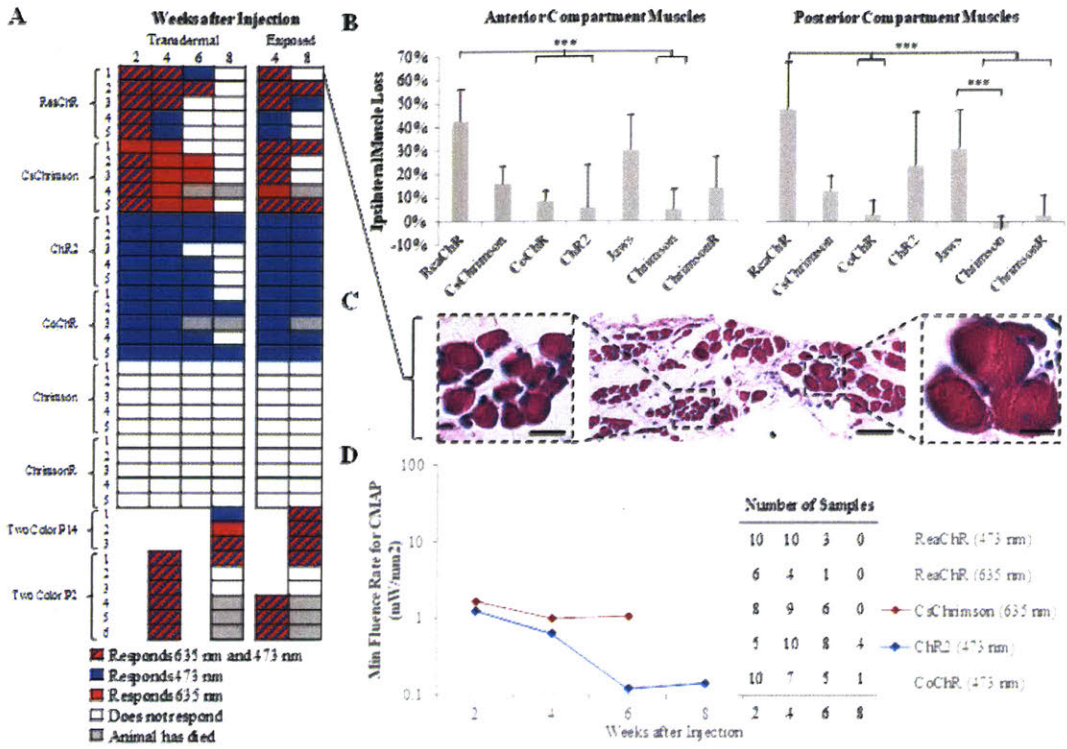


**Figure 5.5: Loss of expression and muscle atrophy is opsin-dependent**

*(A) Excitability to blue and red illumination in both transdermal (left) and exposed nerve (right) as a function of weeks post-injection for each animal tested. (B) AC muscle atrophy as a percentage decrease from contralateral side (left); PC muscle atrophy as a percentage decrease from contralateral side (right). ReaChR/csChrimson/CoChR (n=4), ChR2/Jaws/Chrimson/ChrimsonR (n=5); (*** $P < 0.001$; ** $P < 0.01$ and n.s. not shown; $P_{ANOVA,\ Anterior}$ = 9e-4; $P_{ANOVA,\ Posterior}$ = 9e-5). (C) H&E cross-section of TA of ReaChR animal (center; scale bar = 80 μm) with breakout (left/right; scale bar = 20 μm). (D) Minimum fluence rate for CMAP calculated by multiplying minimum illumination power to produce each animal's transdermal EMG spike by the estimated fluence rate for that animal and wavelength from Fig 5.4D. Sample sizes for each group shown.*

We noticed ipsilateral muscle mass reductions in most opsin expressing groups; loss of optogenetic responsiveness appeared to correlate to muscle atrophy by opsin group (Fig 5.5B). The ReaChR animals exhibited the most significant 40-50% reductions in muscle mass for both anterior and posterior compartments, significantly greater than CoChR and

Chrimson groups. JAWS animals also had muscle mass reductions in both anterior and posterior compartments of ~30%. CsChrimson and ChR2 had moderate muscle mass losses ranging from 10-25% for both groups. Chrimson and ChrimsonR never expressed optogenetically, so the lack of ipsilateral muscle loss correlated with lack of expression. CoChR, which still expressed fairly well at 8 weeks, had negligible muscle loss as well. H&E cross-sections of the TA revealed shrunken myocytes (Fig 5.5C, left) interspersed within fibrous tissue and healthy myocytes (Fig 5.5C, right), characteristic of denervation atrophy. Despite the atrophy, there were no obvious signs of immune cells or inflammatory infiltrates directly within the muscle. However, coronal H&E sections of spinal cord suggest increased presence of inflammatory cells adjacent to transduced neurons (Fig 5.15C), in agreement with previously reported elevated cellularity[123]. A further evaluation shows VH neuronal losses in ipsilateral coronal L3 and L4 spinal cord sections, following the same pattern as the muscle atrophy by opsin. Together, these findings may suggest neuronal loss of opsin expressing neurons.

The minimum transdermal illumination for spike induction was mapped via the MC estimated fluence rates to provide a minimum nerve fluence rate capable of eliciting action potentials for each opsin (Fig 5.5D); these numbers account for both the increased fluence of red light at depth as well as each rat's growth over the experimental period. For all opsins, the minimum fluence rate was found between 4 and 6 weeks after injection, consistent with previously reported loss of excitability of the best expressing axons over time. Of all opsins, ChR2 required the lowest overall fluence to initiate action potentials of 122 $\mu W/mm^2$, roughly 4x smaller than CoChR's minimum of 502 $\mu W/mm^2$. Comparatively, CsChrimson (635 nm) and ReaChR (473 nm) had higher minimum fluence rates of 984 $\mu W/mm^2$ and 636 $\mu W/mm^2$ respectively, both at 4 weeks after injection. ReaChR's responsiveness to 635 nm illumination as measured by minimum fluence was 3x-10x greater than its responsiveness to 473 nm illumination at measured ages, aligning with the ReaChR's higher $V_{RMS}$ sensitivity to 473 nm illumination.

### 5.3.6 JAWS Inhibits Muscle Tremor in Wavelength-Dependent Manner

To assess motor inhibition using JAWS, supramaximal current was delivered directly to the sciatic nerve via a hook electrode at 17 Hz and 50 μs PW (Fig 5.6B). 635 nm illumination (160 mW, 1 Hz, 20% DC) on the exposed sciatic nerve resulted in consistent attenuation in the measured EMG at the downstream muscles (Fig 5.6Ci). 473 nm illumination of the same nerve had little to no effect on the measured EMG (Fig 5.6Cii), consistent with both the higher scattering of blue light and the higher relative sensitivity of JAWS to red illumination[83]. Two strategies verified that the tremor reduction during illumination was optogenetic and not thermal. First, 635 nm illumination of the contralateral sciatic nerve with identical FES produced no measureable changes in EMG (Fig 5.6Ciii). Second, a temperature model found that limiting the duty cycle to 20% limited max temperature rise in the tissue to 0.82 °C following 10 s of stimulation, well below the temperature limit for thermally-mediated nerve firing effects[106] (Fig 5.11D).

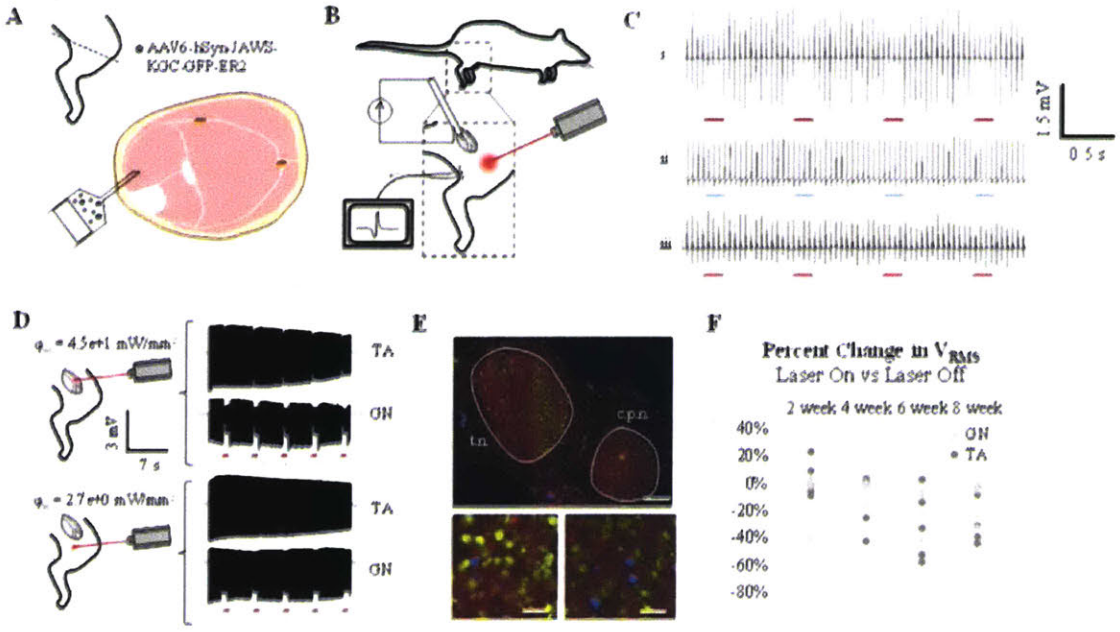


**Figure 5.6: JAWS inhibits muscle tremor**

*(A) 15uL AAV6-hSyn-JAWS-KGC-GFP-ER2 injected into AC of Fischer 344 rats 2 days postpartum. (B) At 2, 4, 6, and 8 weeks post-injection, sciatic nerve was exposed and current-controlled hook electrode was placed around nerve as 635 nm laser*

*simultaneously illuminated either the TA motor point (shown), the GN motor point or the sciatic nerve directly. (C) GN EMG traces from 17 Hz, 50 μs supramaximal electrical stimulation of sciatic nerve of 8 week old animal with i. 635 nm laser illuminating ipsilateral sciatic nerve (n=5), ii. 473 nm laser illuminating ipsilateral sciatic nerve (n=2), and iii, 635 nm laser illuminating contralateral sciatic nerve (n=5). (D) Comparison of optogenetic-induced $V_{pp}$ reductions in 2 week old animal with direct illumination of exposed sciatic nerve (top) and transdermal illumination of tibial nerve (bottom). Estimated max nerve surface fluence rates shown (n=2). (E) Sciatic nerve cross-section showing JAWS expression in both tibial nerve (t.n.) and common peroneal nerve (c.p.n.) (n=5). (F) Percent reduction in $V_{RMS}$ calculated by ($V_{RMS,LaserOn}$ - $V_{RMS,LaserOff}$) / $V_{RMS,LaserOff}$ (n=5 GN and n=5 TA).*

JAWS motor inhibition was not limited to direct illumination of the exposed sciatic nerve. Notably, ~15% EMG reduction was achieved with transdermal illumination targeting the tibial nerve, compared to ~50% EMG reduction with 1 s of 635 nm pulses directly on the sciatic nerve (Fig 5.6D) consistent with the modeled reduction in nerve surface fluence rates. Additionally, the small TA EMG reductions associated with stimulation of the sciatic nerve directly disappeared completely with illumination targeting the tibial nerve, suggesting spatial selectivity of transdermal inhibition. Histological evaluation of JAWS sciatic nerve cross-sections revealed similar findings as channelrhodopsins, with consistent expression in ~15% axons (Fig 5.6E). Not all animals resulted in a strong reduction in FES-induced tremor. Maximum tremor reduction as measured by $V_{RMS}$ was -60%, achieved at 6 and 8 weeks post-injection (Fig 5.6F).

## 5.4 Discussion

In this experiment, we hypothesize that the intramuscular injection of a red opsin and a blue opsin in opposing muscle pairs enables selective transfection of the nerve fibers corresponding to each compartment such that opposing movements can be produced by changing the illumination wavelength on the mixed nerve. The data presented in this study support this hypothesis. To identify red opsins in the peripheral nervous system, we test a range of promising opsins shown to work *in vitro* and characterize *in vivo* peripheral nerve

properties and expression longevity. We use ChR2 and CsChrimson to show that spectrally-distinct illumination produces opposing muscle movements and electrophysiological recordings specific to the targeted muscle of each opsin. We further explore an optogenetic candidate for spectrally distinct inhibition for the treatment of muscle tremor in peripheral nerves.

We show the first known direct cross-comparison of promising opsins in the peripheral nervous system and report that opsin expression in the peripheral nerve is dependent on intrinsic properties of the opsin. Previous experiments have shown AAV-mediated gene expression in the peripheral nerve is serotype-[76], dose-[123], and promoter-[130] dependent. After controlling for the above, in addition to age of injection and viral concentration, we find that neither Chrimson nor ChrimsonR expresses in the peripheral nervous system as measured histologically or electrophysiologically. We further test ChrimsonR under a varying range of serotypes, dosages, viral sources, and injection ages *in vivo* and find no expression. Prior work has suggested the N-terminus of an ion channel contains a golgi export signal[131], although modification of this signal in a previous opsin did not yield a change in surface expression[132]. The complete lack of Chrimson expression juxtaposed with the moderate CsChrimson expression therefore implicates the crucial role of this N-terminus in virally-mediated peripheral nerve optogenetics. We conclude that N-terminus interaction dynamics with cell trafficking vesicles are critical to peripheral axonal transport and functional axonal expression.

For the opsins that respond within the peripheral nerve, we find that ReaChR is not ideal as judged by lack of wavelength specificity, poor kinetics, low EMG efficiency, and short-lived time course of expression. Compared to ReaChR, CsChrimson is found to have greater specificity to red light, higher amplitude EMG responses, superior high-frequency response and superior time-course of expression. However, when evaluating blue light opsins in the peripheral nerve, both CoChR and ChR2(H134R) outperformed ReaChR and CsChrimson as measured by strength of response and sensitivity. Previous studies have used 100 Hz for tetanized optogenetic contractions[20]. ReaChR is unable to sustain high

frequency stimulation above 5 Hz, which is required for conveying many afferent and efferent biological signals. CsChrimson, however, is able to sustain up to 40 Hz firings, although not consistently. Future work includes the evaluation of CsChrimsonR created by CsChrimson with a K171R mutation; CsChrimsonR combines the membrane targeting N-terminus of CsChrimson with the improved kinetics and red-shifted activation of ChrimsonR.

Due to its increased transmittance in biological tissues, the shift from blue to red opsins has been suggested as a critical leap to next stage adoption of optogenetic technologies. The MC model suggests that red light reaches 2-4x higher fluence rates than blue light at the nerve depths studied within this experiment (1 mm – 5 mm). The finding that the sensitivity, defined as the minimum nerve fluence rate to initiate an AP, of CsChrimson in response to transdermal illumination with red light did not outperform the sensitivity of ChR2 in response to transdermal illumination with blue light, even at low illumination intensities, implies that biological processes are a critically important factor in opsin choice and may outweigh benefits conferred by wavelength-dependent absorption and scattering differences. The minimum fluence required to depolarize ChR2 was 4x smaller than CoChR, suggesting that the number of functional ChR2 molecules within the axonal membrane must be at least 16x greater than the best-expressing CoChR animal, due to CoChR's ~4x greater photocurrent and more favorable off kinetics. Histologically, neither CoChR nor CsChrimson expressed as well as ChR2 as measured by overall axon counts. However, total counts are not indicative of illumination sensitivity, which reflects the number of functional opsins per axon. A qualitative assessment shows that the ChR2 axons appear brighter than both CoChR and CsChrimson, which would be consistent with higher opsin concentration per axon. Previous research suggests that the red light photocurrent of CsChrimson is roughly equal to the blue light photocurrent of ChR2(H134R) *in vitro*[111]. However, because of the difference in minimum fluence required for EMG, we can estimate that CsChrimson must functionally express at ~8x lower concentrations within the axonal membrane compared to ChR2.

We report the first case of muscle atrophy induced by optogenetic transfection of peripheral nerves and discover that atrophy appears correlated to the loss of optogenetic expression. One explanation for muscle mass reduction is due to direct neuronal toxicity of overexpressed opsin molecules resulting in neurogenic apoptosis. Neurogenic apoptosis would result in axonal loss, potentially explaining the low transfection rates seen in nerve cross-sections during histology. As neurons and their corresponding axons die, the previously innervated myocytes will shrink until axonal sprouting results in re-innervation. To rule out direct apoptosis of myocytes, we identified no evidence of inflammation or myocyte death within TA H&E sections. We have previously tested myocytes for ChR2 expression both electrophysiologically (looking for wide spikes) and immunohistochemically, and have found neither, indicating that hSyn appears to be properly restricting expression to the neuronal tissue, which may be limiting direct myocyte death[123].

In this experiment, we identified muscle atrophy is highest in the opsins that have been the most engineered. The opsins studied here found directly in nature (Chrimson, CoChR) and those with single amino acid substitutions (ChR2(H134R) and ChrimsonR) had the least atrophy. CsChrimson, which combined two naturally occurring opsins, had moderate atrophy. The opsins, which were heavily engineered (ReaChR and JAWS) had the most atrophy. The engineering of proteins could confer domains that enable higher leakage currents or ion imbalances triggering a neuronal apoptosis-mediated pathway. Another explanation for atrophy is neuronal cell death due to viral or opsin immunogenicity recruiting an adaptive immune response. AAV capsid has been previously shown to result in recruitment of an immune response in a dose-dependent fashion in both previous scientific experiments and human clinical trials[24,25]. However, since AAV serotype and dosage is identical across opsins, it is highly unlikely that AAV immunogenicity alone contributed to atrophy. Because opsins originate from algae, their DNA may contain CpG motifs that trigger a TLR9-mediated innate immune response; alternatively, the protein itself can trigger an adaptive immune response via MHCI presentation. We present evidence of ipsilateral inflammation in spinal cord H&E sections, suggesting an immune process may be occurring. However, further work is required to validate this mechanism.

Clinically, researchers aiming to deploy optogenetic technologies in human peripheral nerves should proceed extremely cautiously. Researchers looking to treat chronic pain and other peripheral nerve conditions must characterize optogenetic side effects in detail, and offer strategies to combat them.

To test the ability of red light to inhibit deep nerve activity in a spectrally distinct manner, we use JAWS to drive wavelength-dependent inhibition. We show a consistent 40-60% reduction in the magnitude of the muscle electrical activity using JAWS with direct illumination of the nerve. We believe, given high transmittance of red light in tissue, that this level of reduction can be also achieved in a transdermal approach with the use of high power LEDs operating at low duty cycles to limit heating. The $V_{RMS}$ reduction identified has significant implications for the direct treatment of Essential Tremor (ET), Parkinson's and MS-induced muscle tremor and spasticity. Frequency analyses of both Parkinson's and MS-induced tremor have identified 3-8 Hz as the range of tremor encompassing both goal directed movement and postural activity[133,134]. Here, we show efficacious tremor reduction at 16 Hz, equivalent to harmaline-induced mouse models of ET[135]. Use of spectrally distinct inhibitory opsins would play a significant role during goal-directed movement by enabling alternation of agonist-antagonist muscle inhibition. In the gait cycle, for example, one could inhibit dorsiflexion tremor with red light during toe-off and then inhibit plantarflexion tremor with blue light during terminal swing, both without interfering with voluntary muscle activity. Further, given FES-induced neuroplasticity in paralysis[136], the study of optogenetic tremor inhibition's effect on remodeling motor circuits in the spinal cord and dopaminergic circuits in the brain is of significant scientific interest. Although further work is needed to better understand the time-course of tremor-reduction, the simplicity and lack of invasiveness of the technique is appealing: one can imagine a targeted muscle injection followed by a small, transdermal LED patch that can be directly controlled by a patient or operated through a feedback loop.

This study proposes a non-invasive wavelength-dependent neurostimulator, which can stimulate nerve fascicles directly by end organ targeting. We believe that future studies of

paralysis, pain, tremor, and amputation research may benefit from this work. New studies can employ promoters to restrict spectrally distinct optogenetic transfection to molecularly defined subtypes as opposed to anatomically defined subtypes. Arcourt et al. describe the use of $Npy2r^{ChR2}$;$MafA^{ChR2}$ mice to identify how concurrent low threshold mechanoreceptor (LTMR) activation alleviates A-fiber mechanonociceptor-evoked pain in a mechanistic study of gate-control pain theory[137]. Chang et al. and Williams et al. describe how vagal afferent subtypes projecting to the lungs and GI tract have been differentially identified to activate respiratory behavior and the sensation of satiety respectively[21,22]. Using a viral construct with conditional expression, one could restrict spectrally distinct opsin to cutaneous or vagal subsets independently. Use of red and blue illumination to study how activation of one axonal subtype alleviates or enhances activation of another would be of significant scientific value for better understanding pain, touch, respiration, satiety, and other complex behaviors governed by molecularly-distinct opposing subsets of fibers. Stimulation of independent fibers within the same nerve of the same animal alleviates the need for time-intensive development and validation of transgenic strains and allays fears regarding inherent inter-strain variability in physiology experiments. Clinically, the translation of optogenetics in the treatment of human disease is alluring, given the powerful nature of the tool and the extremely high incidence of diseases implicated by peripheral nerves. The use of spectrally distinct opsins to stimulate fascicular and fiber groupings of peripheral nerves may play a significant role in the adoption of clinical optogenetic therapies.

# APPENDIX 2: SUPPLEMENTAL FIGURES FOR CHAPTER 5

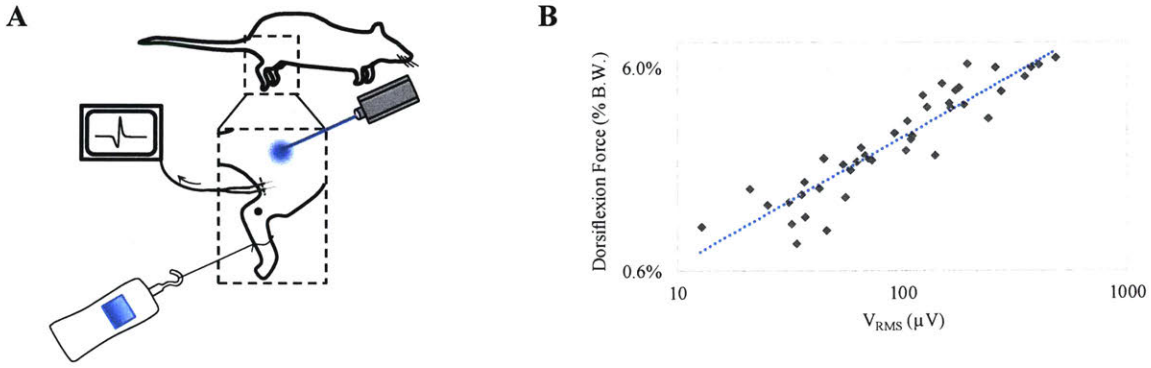


**Figure 5.7: Muscle Force and EMG are proportional**

*(A) Diagram of experiment used to collect Force/EMG relationship. Ankle is fixed in place at Achilles Tendon using towel clamps, which are fixed to helping hands (not shown). Force sensor is attached to foot using size 0 suture and placed for zero resting tension. Needles are simultaneously recording anterior compartment (not shown) and posterior compartment EMG. (B) Max dorsiflexion force as a percentage of the animal's body weight vs. calculated $V_{RMS}$ for a range of animals (n=9) and a range of input illumination intensities on the surface of the skin.*

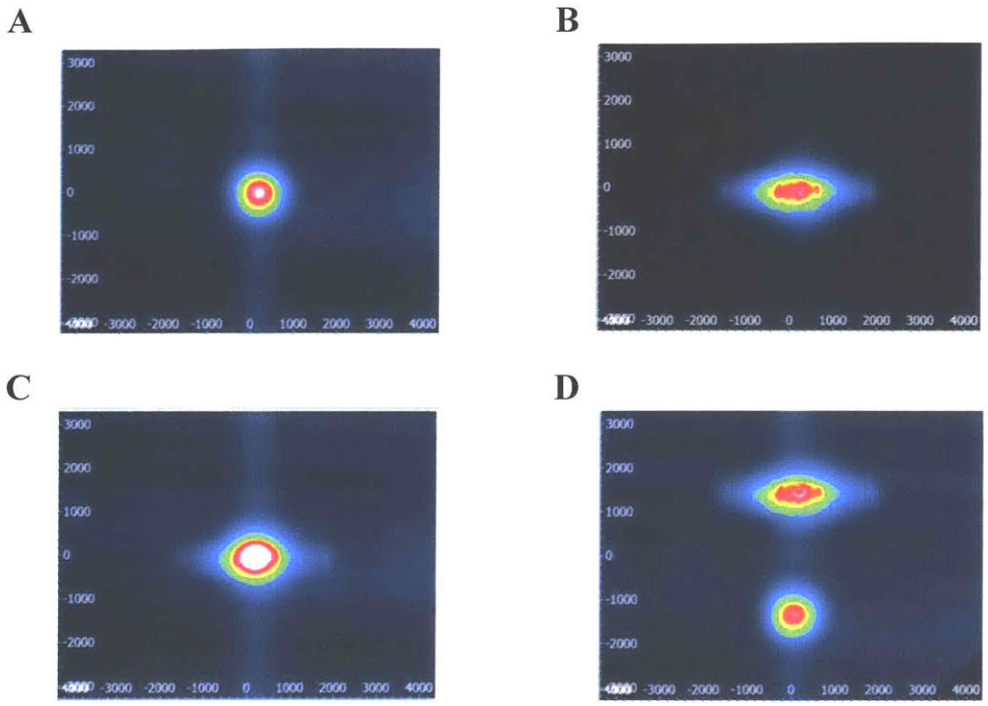


**Figure 5.8: Beam profiler used to analyze laser shape, spread, and co-localization**

*Vertical and horizontal axes in μm (A) Beam profile of 473 nm blue DPSS laser at 160 mW power (45 mW/mm$^2$ at beam center). (B) Beam profile of 635 nm red diode laser at 160 mW power (45 mW/mm$^2$ at beam center). (C) Superimposed blue and red lasers showing good co-localization at 160 mW power each. (D) Blue and red lasers shown adjacent to demonstrate same magnitude at 160 mW power each.*

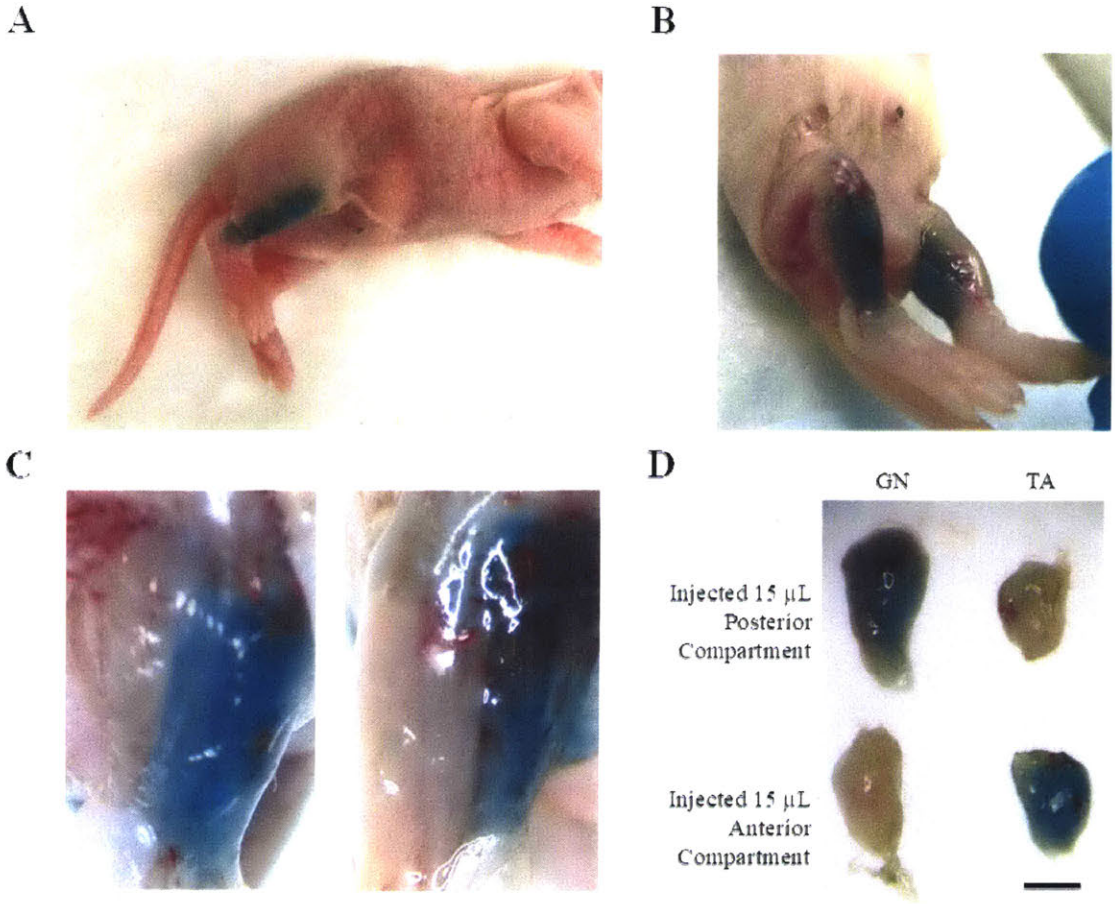


**Figure 5.9: Injection leakage and muscle specificity testing in P2 rat using dye.**

*(A) 15 µL injected IM and transdermally into anterior compartment of P2 rat. (B) 15 µL dye injected into right anterior compartment and 15 µL dye injected into left posterior compartment (intramuscularly and transdermally) of P2 rat. Following euthanasia, skin and BF removed from hindlimbs. (C) Left: zoom-in section of right limb with AC stained green and PC with no staining. Right: zoom-in section of left limb with PC stained green and AC unstained. (D) Dissection of PC and AC reveals specificity of injection method in targeting muscle group of interest, scale bar = 2 mm.*

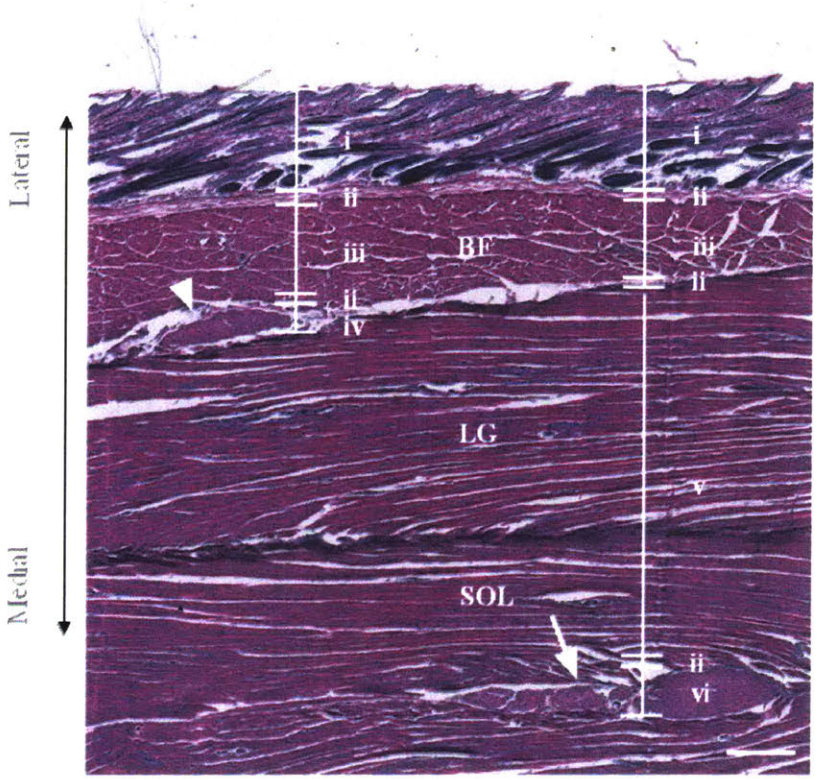


**Figure 5.10 H&E image used for collecting geometry required for fluence rate modeling calculations**

*Two week old rat showing peroneal nerve (arrowhead) and tibial nerve (arrow) along with muscles Biceps Femoris (BF), Lateral GN (LG), Soleus (SOL): i = dermis, ii = connective tissue, iii = BF muscle, iv = peroneal nerve, v = LG + SOL, vi = tibial nerve.*

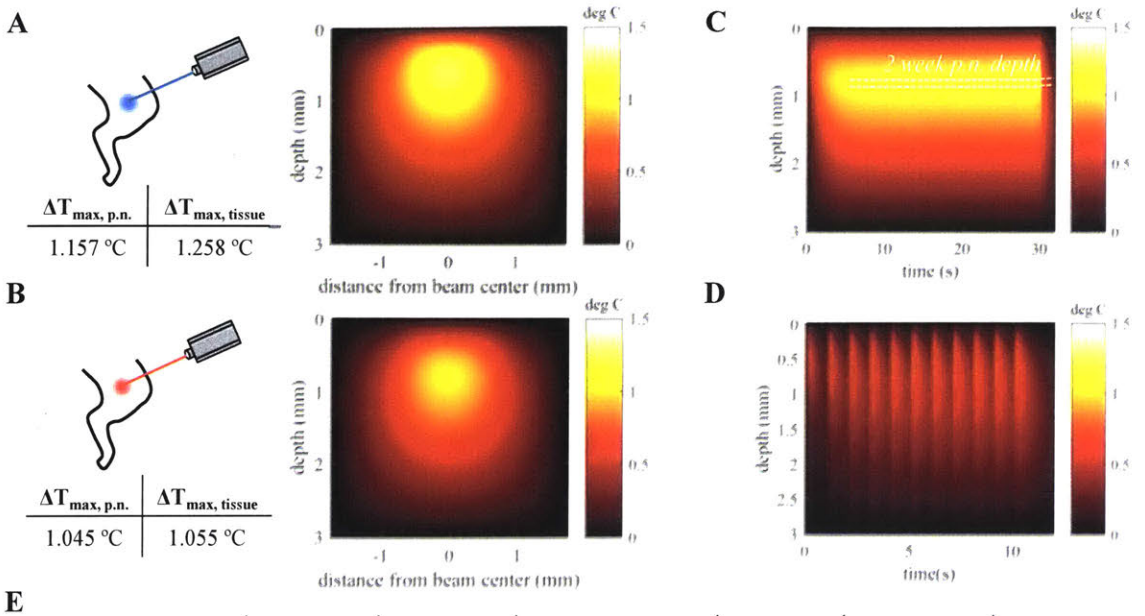


**E**

| Tissue Type | Air | Skin | Conn. Tissue | Muscle | Epineurium | Nerve |
|---|---|---|---|---|---|---|
| $\mu_{a,\,473\,nm}$ ($mm^{-1}$) | 1e-4 | .090 [15] | .107 [#,*,16] | .117 [#,16] | .107 [#,*,16] | .090 [^,19] |
| $\mu_{a,\,635\,nm}$ ($mm^{-1}$) | 1e-4 | .050 [15] | .107 [#,*,16] | .068 [#,16] | .107 [#,*,16] | .090 [^,19] |

**Figure 5.11: Thermal model for red & blue lasers in stimulation and inhibition**

*Simulated tissue temperature rise in space after 5 s stimulation with adapted Pennes Bioheat Equation for (A) 473 nm illumination and (B) 635 nm illumination along with max temperature changes within peroneal nerve (p.n.) and in full tissue modeled. Matlab package provided by Stujenske et al. adapted for 2 week p.n. geometry. Key inputs to model include transdermal irradiation at 160 mW incident power (45 mW/mm$^2$ at beam center) with a 1/e$^2$ Gaussian beam profile 3 mm diameter, 10 ms PW, and 40 Hz. (C) Simulated tissue temperature rise after 30 s of 635 nm illumination of same parameters as in (B) showing steady state at ~ 7s. (D) 635 nm JAWS direct nerve stimulation with 0.2 s PW, 1 Hz for 10 s. (E) Table of absorption properties used as inputs for bioheat simulation. All other inputs can be found in Maimon et al. $\mu_a$ = absorption coefficient with values directly sourced from citations listed, using same values if no wavelength-dependent values could be found. #473 nm and 635 nm coefficients extrapolated by linear interpolation between when possible, *Adipose tissue conservatively used in place of connective tissue and epineurium, ^Brain white matter tissue used in place of nerve tissue. Model was found to be robust to full range of tissue heat properties with a ~40% max*

*dermis temperature change in response to change of properties from most liberal to most conservative combination.*

A

| Injection Location | Age at injection | Virus Source | AAV Serotype | Concentration (vg/mL) | Vol Inj (uL) | Total VP injected |
|---|---|---|---|---|---|---|
| TA | 8 w eek | UNC | 1 | 1.40E+12 | 25 | 3.50E+10 |
| TA | 8 w eek | UNC | 2 | 1.40E+12 | 25 | 3.50E+10 |
| TA | 8 w eek | UNC | 5 | 1.40E+12 | 25 | 3.50E+10 |
| TA | 8 w eek | UNC | 6 | 1.40E+12 | 25 | 3.50E+10 |
| TA | 8 w eek | UNC | 8 | 1.40E+12 | 25 | 3.50E+10 |
| TA | 8 w eek | UNC | 9 | 1.40E+12 | 25 | 3.50E+10 |
| TA | 8 w eek | UNC | 1 | 1.40E+12 | 25 | 3.50E+10 |
| TA | 8 w eek | UNC | 2 | 1.40E+12 | 25 | 3.50E+10 |
| TA | 8 w eek | UNC | 5 | 1.40E+12 | 25 | 3.50E+10 |
| TA | 8 w eek | UNC | 6 | 1.40E+12 | 25 | 3.50E+10 |
| TA | 8 w eek | UNC | 8 | 1.40E+12 | 25 | 3.50E+10 |
| TA | 8 w eek | UNC | 9 | 1.40E+12 | 25 | 3.50E+10 |
| TA | 8 w eek | UNC | 6 | 9.10E+12 | 80 | 7.28E+11 |
| TA | 8 w eek | UNC | 6 | 1.82E+12 | 80 | 1.46E+11 |
| TA (P2), TA+s.p.n (2w'k) | P2-2 w eek (5ul each) | Virovek | 6 | 1.20E+14 | 10 | 1.20E+12 |
| TA (P2), TA+s.p.n (2w'k) | P2-2 w eek (5ul each) | Virovek | 6 | 1.20E+14 | 10 | 1.20E+12 |
| TA (P2), TA+s.p.n (2w'k) | P2-2 w eek (5ul each) | Virovek | 6 | 1.20E+14 | 10 | 1.20E+12 |
| TA (P2), TA+s.p.n (2w'k) | P2-2 w eek (5ul each) | Virovek | 6 | 1.20E+14 | 10 | 1.20E+12 |
| TA (P2), TA+s.p.n (2w'k) | P2-2 w eek (5ul each) | Virovek | 6 | 1.20E+14 | 10 | 1.20E+12 |
| TA+s.p.n | 8 w eek | Virovek | 6 | 1.20E+14 | 25 | 3.00E+12 |
| TA+s.p.n | 8 w eek | Virovek | 6 | 1.20E+14 | 25 | 3.00E+12 |
| TA+s.p.n | 8 w eek | Virovek | 6 | 1.20E+14 | 25 | 3.00E+12 |
| TA+s.p.n | 8 w eek | Virovek | 6 | 1.20E+14 | 25 | 3.00E+12 |
| TA | P2 | Virovek | 6 | 1.20E+14 | 15 | 1.80E+12 |
| TA | P2 | Virovek | 6 | 1.20E+14 | 15 | 1.80E+12 |
| TA | P2 | Virovek | 6 | 1.20E+14 | 15 | 1.80E+12 |
| TA | P2 | Virovek | 6 | 1.20E+14 | 15 | 1.80E+12 |
| TA | P2 | Virovek | 6 | 1.20E+14 | 15 | 1.80E+12 |

B

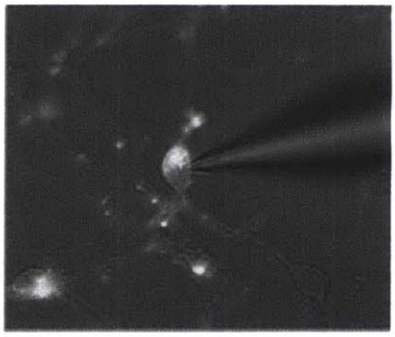

C

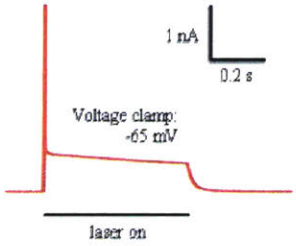


**Figure 5.12: ChrimsonR expresses *in vitro*, but not in peripheral nerves *in vivo***

*(A) 28 rats injected with ChrimsonR at varying dosages, serotypes, sources, ages, and injection volumes over course of experiment. None of these combinations provided any electrophysiological or visual twitch responses to either blue or red illumination of the nerve at any time tested. (B) Superimposed image of fluorescence and patching of cultured hippocampal cells from neonatal Swiss Webster mice treated with AAV6-hSyn-ChrimsonR-tdtomato. (C) Whole-cell voltage clamp patch with 635 nm illumination of transduced hippocampal cell.*

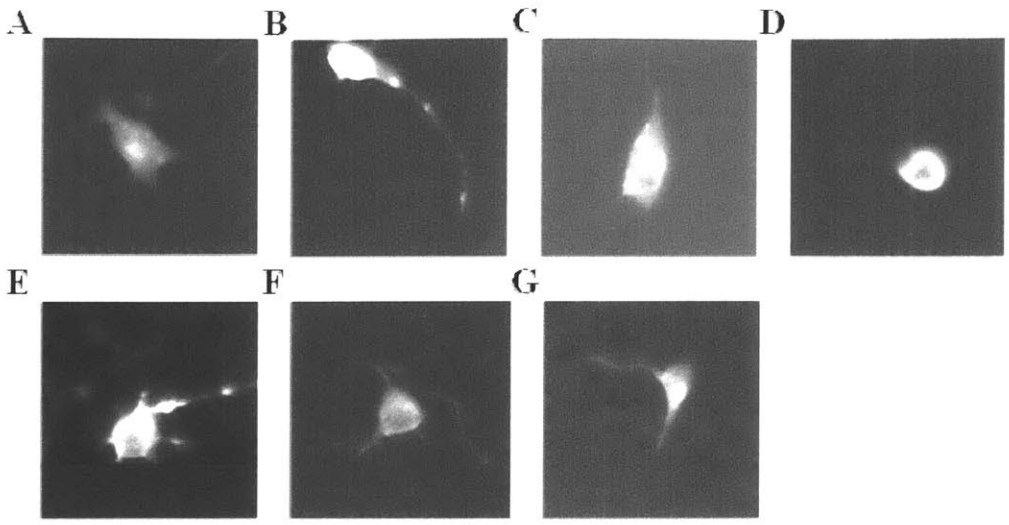


**Figure 5.13: In vitro opsin expression**

*In vitro expression from neonatal Swiss Webster mice hippocampal cells treated with AAV for the following opsins: (A) ChR2, (B) CoChR, (C) JAWS, (D) Chrimson, (E) CsChrimson, (F) ReaChR, and (G) ChrimsonR.*

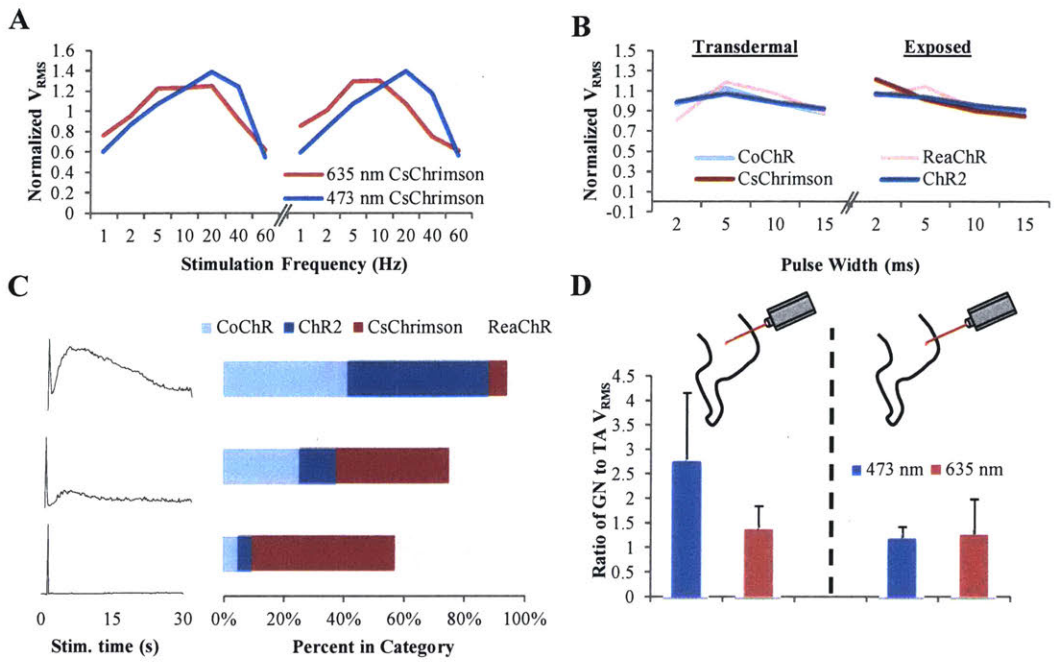


**Figure 5.14: Red vs. blue opsin electrophysiology findings**

*(A) Normalized CsChrimson frequency response with minimum $V_{RMS}$ cutoff at 7.25 μV comparing 635 nm and 473 nm stimulation of the exposed sciatic nerve for GN (left) and TA (right) with incident power of 160 mW and 10 ms pulse width (PW) for 473 nm TA (n=2), 635 nm TA (n=2), 473 nm GN (n=2), and 635 nm GN (n=5). (B) Normalized 473 nm PW response with $V_{RMS}$ cutoff at 3.25 μV calculated from averaging all trials of transdermal (left) and exposed (right) stimulation for CoChR ($n_{Trans.}$=18, $n_{Exp.}$=10), ReaChR ($n_{Trans.}$=24, $n_{Exp.}$=10), CsChrimson ($n_{Trans.}$=0, $n_{Exp.}$=7), ChR2 ($n_{Trans.}$=27, $n_{Exp.}$=10). No CsChrimson animals responded to transdermal 473 nm illumination at 4 weeks of age. (C) 30 s direct illumination of exposed sciatic nerve yielded moving average $V_{RMS}$ plots with 3 distinct shapes, which were manually categorized by appearance. Animals were 4 weeks after injection and stimulation employed either 473 nm illumination (all opsins) or 635 nm illumination (CsChrimson, ReaChR) with incident power of 157 mW, 10 ms PW, and 40 Hz frequency for CoChR (n=10), ChR2 (n=10), CsChrimson (n=14), and ReaChR (n=12). (D) Ratio of activation of GN fibers to TA fibers as measured by EMG needles. Transdermal blue (n=2) and red (n=3) illumination were compared at two sites on the 2 week rat skin surface (160 mW, 5 Hz, 10 ms PW). Illumination of the*

*mid-calf (left) preferentially targets the tibial nerve branch and the proximal tibia (right) preferentially targets the peroneal nerve branch.*

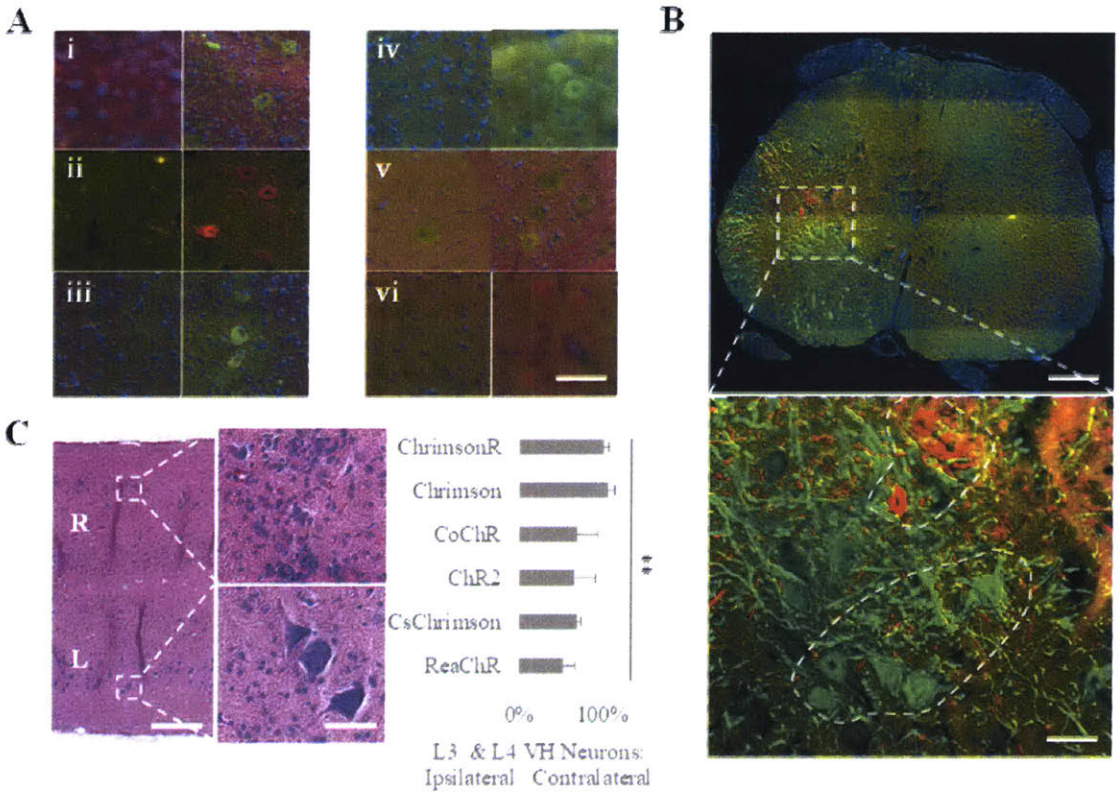


**Figure 5.15 Spinal cord opsin expression**

*(A) Coronal lumbar spinal cord sections focused on ventral horn neurons for contralateral (left) and ipsilateral (right) for i) ReaChR, ii) CsChrimson, iii) ChR2, iv) CoChR, v) Chrimson, and vi) ChrimsonR: scale bar = 80 μm. (B) L3 axial spinal cord section presented in radiological convention for two color animal injected with CsChrimson-tdtomato in AC and ChR2-EYFP in PC showing distinct grouping of neurons within ventral horn. For immunofluorescence images, red represents tdtomato, green represents YFP, and blue represents DAPI. Scale Bar = 50 μm. (C) Coronal lumbar H&E spinal cord section for ChR2 animal with ipsilateral inflammation present. Scale bar = 80 μm.*

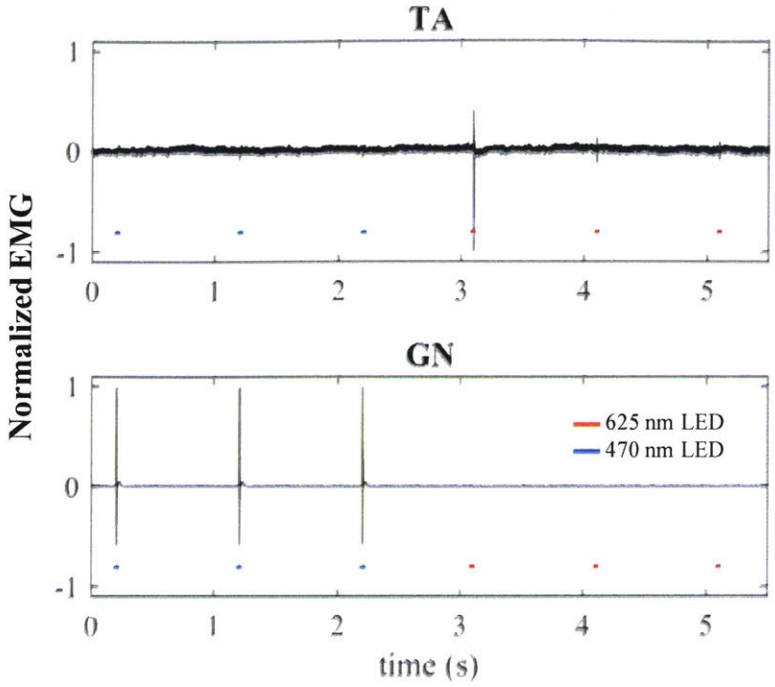


**Figure 5.16 Transdermal two-color EMG**

*Normalized Raw EMG from TA and GN recordings in response to transdermal illumination of the lateral hindlimb above the sciatic nerve with both blue (470 nm) and red (625 nm) LEDs with* $i_{LED}$*=1.2 A, f=1 Hz, PW=15 ms for 8 week post-injection rat.*

# 6 PERIPHERAL OPTOGENETIC LONGEVITY

Optogenetic technologies have been the subject of great excitement within the scientific community for their ability to demystify complex neurophysiological pathways in the CNS and PNS. The excitement surrounding optogenetics has also extended to the clinic with a human trial for ChR2 in the treatment of retinitis pigmentosa currently underway and trials planned for the near future. In this work, we attempt to identify the cause of optogenetic loss-of-expression within the ventral horn motor neurons following an AC injection with AAV6-hSyn-ChR2(H134R) with and without fluorescent reporter. Using a Sprague Dawley $Rag2^{-/-}$ rat, we discover optogenetic loss-of-expression is chiefly elicited by ChR2-mediated immunogenicity in the spinal cord, resulting in both CNS motor neuron death and ipsilateral muscle atrophy in both low and high Adeno-Associated Virus (AAV) dosages. We further employ pharmacological immunosuppression using a slow-release tacrolimus pellet to demonstrate sustained transdermal optogenetic expression up to 12 weeks. These results are significant because they suggest that all dosages of AAV-mediated optogenetic expression within the PNS are potentially unsafe. Clinical optogenetics for both PNS and CNS applications should take extreme caution when employing opsins to treat disease and may require concurrent immunosuppression. Future work in optogenetics should focus on designing opsins with lesser immunogenicity.

## 6.1 Introduction

The clinical excitement surrounding optogenetics is eminently justified – a single, precise injection transforms a patient's genome, making an anatomically targeted subset of neurons responsive to external control. Unlike electrical stimulation, the molecular specificity associated with unique promoters can limit off-target effects. Opsin engineering has conferred a toolbox of choices, each with its own favorable characteristics – photocurrent, wavelength, kinetics, and illumination sensitivity can be tuned to an application's needs[111,138]. Lastly, an opsin's DNA sequence is relatively short allowing it to be easily packaged within an AAV for stable delivery.

Using optogenetics to treat retinitis pigmentosa became the first clinical application, with chronic pain, cardiac pacing, and other PNS applications currently under investigation. In March 2016, Retrosense Therapeutics (now Allergan) delivered the first in-human optogenetic therapy using AAV-ChR2 as part of an investigational new drug study. Gensight and Circuit Therapeutics are also working on optogenetic clinical models with potential in-human applications in the near future. These companies have largely been operating in the footsteps of Spark Therapeutics, which received FDA approval to market their RPE65 rAAV for retinal dystrophy in December 2017. Despite these rapid developments in rAAV and optogenetic deployment, academic research in the time-course, safety, and systemic tolerance of rAAV-administered optogenetic therapies within both PNS and CNS has lagged behind.

A limited number of previous studies describe optogenetic abnormalities and cytotoxicity; only a few discuss optogenetic expression time course[23,123]. Axonal blebbing or puncta have been shown in response to both AAV and lentiviral delivered ChR2[139] or NpHR[140] under the αCaMKII promoter in the cortex *in vivo* and in acute brain slices from transgenic Thy1-NpHR mice[141]. While these abnormalities are associated with only a slight loss of function, they are directly attributed to high opsin production, ER retention, and a membrane trafficking defect. Other reports have focused on the opsin's toxic effect on the

membrane. High opsin expression has been shown to increase membrane capacitance[142] and can lead to a loss of membrane integrity[143].

In addition to cytotoxicity, phototoxicity has been shown in both retinal[102] and cortical tissues[103], where cellular damage is elicited by the high illumination intensities required to depolarize opsins. In an opsin-independent manner, the mechanism may be thermal[104], although fluorescent reporters are known to generate reactive oxygen species (ROS) directly in response to illumination, which can elicit structural and DNA damage, and at high levels initiate apoptosis[105]. Unlike phototoxicity, optogenetic excitotoxicity is directly related to light-induced opsin activation. The mechanism underlying excitotoxicity has been described as a process of undesirable intracellular acidification due to selective proton permeability[144] and/or mitochondria-mediated apoptosis[145]. In the study proposing the latter, chronic blue light activation was employed to eliminate completely a notoriously resilient line of human melanoma cells selectively expressing ChR2(D156A)[145].

Unlike ChR2 toxicity, AAV specific immunogenicity has been described in numerous studies. These studies range from the presence of anti-AAV neutralizing antibodies in human clinical trials to titer-specific inflammatory responses to AAV spinal cord microinjections in mice[25,113,115,138]. Multiple strategies have been proposed to combat the immune response in AAV-mediated gene therapy including pharmacological intervention, dosing management, capsid decoys, and biomolecular engineering of AAV capsids[24,25]. In addition to cellular AAV responses, GFP cytotoxicity and immunogenicity have been described *in vivo* and *in vitro*[146,147], although evidence suggests YFP is less cytotoxic than GFP[148].

In terms of optogenetic immunogenicity, Doroudchi et al. describe an "in depth" safety profile consisting of biodistribution, ocular toxicity, systemic immunity, and complete blood count (CBC) tests for rAAV8-ChR2-heGFP intravitreal and subretinal injections[149]. Outside of the eye, their biodistribution study identified no transgene expression, despite

several DNA sequences in the liver, heart, skin, spleen, and muscle, which the authors attribute to cross-contamination or nonspecific binding of their SYBR tag. The ocular toxicity study does not identify any morphological changes in retinae using both H&E and CD45 immunohistochemistry. Lastly, systemic immunity found no toxicity in response to a delayed-type hypersensitivity (DTH) test as well as no abnormalities in CBC panels. From these preclinical tests, the authors conclude that AAV-ChR2 appears to be a safe method for restoration of vision in multiple mouse models of blindness.

However, several challenges arise in their analysis. First, the AAV's mGRM6 regulatory sequence specifically targets ON bipolar cells, which is likely responsible for the lack of transgene expression during biodistribution. The presence of ChR2 DNA >3X the threshold in skin, muscle, and liver in absence of transgene should not be assumed as nonspecific cross-contamination, especially given that liver and muscle are two of the highest concentration tropisms for AAV8 in intravenous delivery[77] and that the liver is a key organ for adenovirus clearance[150]. Additionally, the lack of local inflammation in the DTH ear test does not rule out systemic immune activity against the ChR2 transgene itself. Because the mGRM6 enhancer prevents ChR2 expression in the ear, the authors can only note a low inflammatory response to the AAV capsid itself. Lastly, systemic CBC levels are unlikely to change measurably in response to a small, targeted immune response in the eye. Measurements of subsets of white blood cells (WBCs) involved in transgene rejection such as activated macrophages or cytotoxic T lymphocytes (CTLs) identified with flow cytometry could have further strengthened the hematological assertion of safety.

As the rat ages, the distance separating the surface of the skin and the nerve increases; in transdermal experiments, light scattering within tissue could prevent sufficient light fluence from reaching the target nerve resulting in the false appearance of a loss-of-expression[123]. Further, since loss-of-expression may be multifactorial, several of the above mechanisms may be co-contributing to the findings. For example, cytotoxicity may result in neuronal death, which could release some AAV capsid proteins and activate an adaptive immune response.

From the above studies, the precise mechanism behind optogenetic loss of expression over time remains unclear. Is the opsin downregulated or degraded over time in an intracellular process? Does this occur at the episomal DNA level, the mRNA level, or the protein level? Does high multiplicity of infection (MOI) and membrane blebbing lead to neuronal apoptosis? Does excessive illumination cause acidification-induced cell death? Is there an immune response? If so, is it humoral or cell-mediated, innate or adaptive? Is it directed against the AAV capsid, the opsin or the fluorescent reporter?

To date, there have been no studies exhaustively analyzing the precise mechanism behind optogenetic peripheral nerve loss of expression. A mechanistic understanding *in vivo* could both confer enormous benefit to clinical trials that employ optogenetics to treat disease and enable previously unfeasible scientific studies that require stable, virally delivered optogenetics for a prolonged time-course. We summarize a list of mechanisms in Table I. These mechanisms can be categorized within five groups: direct nerve damage, cytotoxicity, immunogenicity, protein downregulation, and anatomical changes. Of the above potential mechanisms, we hypothesize that ChR2 immunogenicity is the chief cause of the loss of optogenetic expression. Further, we hypothesize that the use of pharmacological immunosuppression can extend optogenetic expression longevity. We evaluate this hypothesis by comparing optogenetic expression time-course of several AAV6 vectors within $Rag2^{-/-}$ rats, wild-type (WT) rats treated with tacrolimus, and WT rats, while performing bloodwork, histology, and gross anatomical observations to support the analysis.

**Table 6.1 Potential causes for loss of optogenetic expression over time**

| Potential Causes | Description | Likely Singular Physical Manifestation | Evidence in Literature |
|---|---|---|---|
| Phototoxicity | Light-induced thermal damage | Axonal death + Wallerian Degeneration | Khan et al.[104], Chen et al.[151] |
| Excitotoxicity | Optogenetic pore-induced electrostatic damage | Neuronal death via apoptosis | Beppu et al.[144],Perny et al.[145], Lignani et al.[152], Feldbauer et al.[153] |

| | | | |
|---|---|---|---|
| ChR2 toxicity | Toxicity of opsin build-up & aggregation | Neuronal death via apoptosis | Zimmerman et al.[142], Gradinaru et al.[143], Miyashita et al.[139], Li et al.[154] |
| EYFP toxicity | Toxicity of reporter build-up & aggregation | Neuronal death via apoptosis | Ansari et al.[146], Taghizadeh et al.[148] |
| AAV immunogenicity | Adaptive immune response to virus | Neuronal + muscular death via CTL | Montgomery et al.[138], Mingozzi et al.[25], Sack et al.[114], Kohro et al.[115] |
| ChR2 immunogenicity | Adaptive immune response to opsin | Neuronal death via CTL | None [#] |
| EYFP immunogenicity | Adaptive immune response to reporter | Neuronal death via CTL | Ansari et al.[146], Stripecke et al.[147] Kohro et al.[115] |
| Episomal DNA loss | rAAV DNA broken down or lost during division | Neuron likely healthy, no longer expresses | McCarty et al[155]., Fisher et al.[156] |
| Epigenetic silencing | rAAV DNA silenced/methylated (no longer transcribed) | Neuron likely healthy, no longer expresses | Robertson et al.[157], Okada et al.[158], Migliaccio et al.[159] |
| Transgene protein degradation or mRNA lysis | rAAV protein ubiquitinated and discarded via proteosome or no longer translated | Neuron likely healthy, no longer expresses | Jennings et al., Kong et al.[160] |
| Anatomical | More scattering in thick tissue | Neuron healthy, still expresses | Jacques et al.[75], Maimon et al.[123] |

[#]non-opsin transgene immunogenicity has been seen in AAV-mediated human gene therapy[25]

☐ Direct Nerve Damage ☐ Cytotoxicity ☐ Immunogenicity ☐ Protein downregulation ▨ Anatomical

## 6.2 Methods

All animal experiments were conducted on Fischer 344 or Sprague Dawley rats under the supervision of the Committee on Animal Care at the Massachusetts Institute of Technology.

### 6.2.1 Opsin Injection

Sprague Dawley (Horizon Discovery) or Fischer 344 (Charles River Labs) rats were injected at P2 (unless otherwise specified) with 15 µL AAV6-hSyn-ChR2(H134R)-EYFP-WPRE (unless otherwise specified). The use of hSyn restricted expression to neural tissue[123]. All virus was produced by Virovek, Inc from plasmids at a titer of $1\times10^{14}$ vp/mL. Under isoflurane anesthesia, rats were injected through a 34G needle (WPI) attached to an intraocular kit (WPI), Silflex tubing (WPI), and a 10 µL nanofil syringe (WPI) on the UMP3 syringe pump (WPI) with injection rate set to 75 nL/s. Rats were housed under a 12:12 light:dark cycle in a temperature-controlled environment with food and water ad libitum, and euthanized at either 8 or 12 weeks of age (unless otherwise specified). Each

rat was tested for expression either weekly or bi-weekly via transdermal illumination to a 105 $mW/mm^2$ (unless otherwise specified) 473 nm DPSS laser (OptoEngine) at varying laser intensities and/or a transdermal 0.6 W 475 nm LED (XP-E2, Cree, Inc.). Both laser and LED were set to 5 Hz and 5% DC (unless otherwise specified), illuminating the skin at the proximal tibia transdermal to the peroneal nerve (unless otherwise specified).

### 6.2.2 Dosing, Anatomy and Timing Groups

54 Fischer 344 neonatal rats were split into several groups to test the effect of different viral dosages, different locations of injection and different timing of injection. To test for effect of dosage on expression levels, six groups of three P2 neonates were injected into the right lower limb – both AC and posterior compartment (PC) – with 15 μL of AAV6-hSyn-ChR2(H134R)-EYFP-WPRE at the following dosages in vp/mL: 3E11, 1E12, 3E12, 1E13, 3E13, 1E14. Two weeks later, the TA on these animals was surgically exposed and rats were injected with another 12 μL directly into the TA and 3 μL directly into the peroneal nerve at the end plate at the same viral concentration, reaching the following total vp injected: (1) 1E10, (2) 3E10, (3) 1E11, (4) 3E11, (5) 1E12, (6) 3E12. To test the effect of injecting in the nerve vs. the muscle, four groups of four rats each were injected with the same virus at 1E14 vp/mL in the following groups: (1) 10 μL in the TA at 2 weeks postpartum; (2) 8 μL in the TA and 2 μL in the peroneal nerve at 2 weeks postpartum; (3) 5 μL in the TA at P2 and 5 μL in the surgically exposed TA 2 weeks later; (4) 5 μL in the TA at P2, 4 μL in the surgically exposed TA and 1 μL in the peroneal nerve at 2 weeks later. To test for the effect of injecting in different ages, four groups of five rats each were injected with the same virus at 1E14 vp/mL in the following groups: (1) 10 μL in the TA at P2; (2) 5 μL in the TA at P2 and 4 μL in the exposed TA & 1 μL in the exposed peroneal nerve at 2 weeks; (3) 2.5 μL in the TA at P2, P6, P10, and P14; (4) 2.5 μL each in the TA at P2 & 1 week postpartum, and 2.0 μL in the exposed TA & 0.5 μL in the exposed peroneal nerve each at 2 weeks postpartum and 3 weeks postpartum. Rats were also exposed at 4 and 6 weeks to direct illumination of the surgically exposed sciatic nerve. Rats were euthanized when transdermal illumination no longer produced any electrophysiological spikes, at a minimum of 8 weeks. This represented 8-12 weeks for all

animals with the exception of one animal, which still expressed transdermal up to 72 weeks post-injection (Fig 6.1A, 6.1B, 6.1D).

### 6.2.3 $Rag2^{-/-}$ and WT Groups

28 Sprague Dawley neonates were divided into 6 groups. 9 WT and 9 $Rag2^{-/-}$ P2 neonates received injections of 15 µL virus. Of these rats, (1) four WT and (2) four $Rag2^{-/-}$ rats comprised the excitotoxicity control groups. These animals did not receive any light stimulation over the course of the 12 weeks except during terminal procedures. The remaining (3) five WT and (4) five $Rag2^{-/-}$ rats comprised the high-dose group. Lastly, (5) five WT and (6) five $Rag2^{-/-}$ P2 neonates received injections of 1.5 µL virus comprising the low dose group. $Rag2^{-/-}$ rats were housed in SCID caging; liberal use of bleach and quatricide prevented infection during testing procedures. Further, all testing was transdermal in these groups, eliminating the need for surgery.

### 6.2.4 Drug Screen Groups

Thirty Sprague Dawley neonates were divided into three groups of 10 neonates each based on the slow-release pellet (Innovative Research of America) employed: Placebo, Tacrolimus (Sigma), and PS2 (Bio-X-Cell). Dosages were sourced from the literature: Tacrolimus: 5.0 mg/kg/day = 30 mg/pellet[161], and PS2: 0.95 mg/kg/day = 5.5 mg/pellet[162,163]. PS2 was lyophilized using isopropanol in dry ice to freeze liquid followed by 48 hour vacuum to sublimate ice crystals. All drug pellets were produced from powders, manufactured to release drug evenly over a 60-day period based on 100 g animal body weight per pellet using a proprietary matrix (Innovative Research of America). Each group of rats was housed separately. At P2, neonates were injected with 15 µL virus. When rats reached 50 g at roughly 2 weeks of age, a 2-4 mm incision was made ~5 mm caudal to the right ear and each rat was implanted with a single pellet. At ~5 weeks of age, when male rats reached 175 g, and when female rats reached 125 g, an incision was made ~5 mm caudal to the left ear; each male rat was given two additional slow release pellets while each female rat was given only one additional slow release pellet. This accounted for the female weight being ~33% less than the male weight from 5 week up through the point of euthanasia to maintain consistent dosing within a group.

### 6.2.5 CAG and No Reporter Groups

Five Fischer 344 rats were injected with 15 μL AAV6-hSyn-ChR2(H134R)-EYFP-WPRE and five Fisher 344 rats were injected with 15 μL AAV6-CAG-ChR2(H134R)-EYFP-WPRE, at the same 1E14 vp/mL dosage. These animals were tested every two weeks but additionally had one surgery as described previously[164] at week 4 post-injection to check for expression directly on the sciatic nerve. These rats were euthanized at 8 weeks as opposed to 12 weeks. Lastly, for the no reporter group, 10 Sprague Dawley rats were injected with 15 μL AAV6-hSyn-ChR2(H134R)-WPRE, eliminating the EYFP construct. Five of these rats were randomly selected to be euthanized at 8 weeks and five of these rats were selected to be euthanized at 12 weeks to increase the chance of catching expression within the nerve for immunofluorescence analysis.

### 6.2.6 Channelrhodopsin electrophysiology measurement

Laser and LED pulses were controlled using a myDAQ (National Instruments) controlled by the NI Elvis Function Generator and custom software written in MATLAB as described previously[164]. The presence of a foot twitch in response to illumination was evaluated both electrophysiologically and visually. To evaluate the presence of a twitch response electrophysiologically and subsequently measure the strength of that response, four 30G monopolar electromyography (EMG) needles (Natus Medical) were directly inserted through the skin into the gastrocnemius (GN) and tibialis anterior (TA) muscles of each rat for bipolar recording as described previously[123]. Needles were connected to a 20 kS/s multi-channel amplifier with a fixed 200x gain (IntanTech). The laser and LED were secured above the anesthetized animal to an assembly allowing for six degrees of freedom. The laser (OptoEngine) employed a beam of Gaussian cross-sectional profile and 3 mm diameter ($1/e^2$), corresponding to a peak irradiance at the surface of the skin of 105 $mW/mm^2$ at a measured output power of 375 mW. Electrical signals controlling the laser amplitude, pulse width, and frequency were simultaneously recorded by the amplifier, enabling temporal synchronization of laser pulses and EMG. EMG data was processed in MATLAB.

### 6.2.7 Lysate Production and ChR2-EYFP ELISA

To obtain ChR2-EYFP protein, hippocampal cells from Swiss-Webster mice were cultured in DMEM (D6171, Sigma) containing 1% L-glutamine, 1% Pen-Strep, and 10% Fetal Bovine Serum in a 24 well plate. Cells were transduced with 2 μL AAV6-hSyn-ChR2(H134R)-EYFP-WPRE (Western Blot and ELISA) or 2 μL AAV6-hSyn-ChR2(H134R)-WPRE (Western Blot only) at 1E14 vp/mL (Virovek). After 72-96 hours, EYFP production was assessed with fluorescence microscopy. Wells of successfully expressing plates were washed with 500 μL of sterile ice-cold PBS and incubated with 300 μL of trypsin for 2-4 min at 37 °C. 700 μL of culturing media were added to deactivate the trypsin. Resultant solution was transferred to a conical tube and centrifuged at low speed (650 g) for 5 min at 4 °C. Supernatant was decanted and cell pellet was gently resuspended in 1 ml of ice cold PBS. Solution was centrifuged at low speed (650 g) for 5 min at 4 °C and supernatant was decanted. Cell pellet was resuspended in 400 μL cell lysis buffer (ThermoFisher Scientific) with 40 μL protease inhibitor cocktail (P8340, Sigma), incubated for 30 min on ice, and then centrifuged for 10 min at 12000 RPM at 4 °C. The supernatant was decanted and frozen at -80 °C until use. Western blot was used to verify presence of EYFP (ab290, Abcam) and ChR2 (anti-ChR2, American Research Products) within lysate samples via co-localized bands at ~62 kDa (Supp. Fig 6.1A).

To measure serum IgG to ChR2-EYFP, a sandwich capture ELISA was developed on 96 well polystyrene plates (Nunc MaxiSorp, ThermoFisher Scientific). 100 μL/well pAb rabbit anti-GFP (ab290, abcam) at a 1:500 dilution in PBS was used as the capture Ab and incubated overnight at 4 °C, followed by blocking with 5% skim milk in PBS-T for 1 hour at room temperature in a rocking platform. 40 μL lysate containing ChR2-EYFP was incubated per well for 3 hours at room temperature in a rocking platform. ELISA validation was performed at 1:3 lysate dilution in PBS whereas most sample measurements were performed at 1:20 dilution in PBS. A standard curve of absorbance for a variety of samples at 1:3 and 1:20 lysate dilution showed a linear trend with $R^2 = 0.97$ (Supp. Fig. 6.1B). All reported values in this manuscript have been scaled to the predicted 1:3 lysate dilution.

40 µL detection antibody was added to each well for 2 hours, consisting of either mAb mouse anti-ChR2 (American Research Products, Inc.) diluted at 1:10 in blocking solution for positive controls or rat plasma samples. To identify optimal plasma dilution, samples were tested undiluted, at 1:30, and at 1:900 dilution in PBS suggesting that no dilution gave the greatest sensitivity between test groups (Supp. Fig 6.1D). 100 µL HRP-conjugated goat anti-rat or anti-mouse secondary antibodies (ThermoFisher Scientific) diluted at 1:2500 in PBS was incubated per well for 1 hour. Lastly, 100uL of 0.5 mg/mL OPD (ThermoFisher Scientific) in 90% deionized water and 10% stable peroxide substrate buffer (ThermoFisher Scientific) was added to each well. In between each step, wells were washed 3X for 5 minutes each with 100 µL PBS-T, except for the step prior to OPD, which required 5X washes. Absorbance at 450 nm was measured 15 minutes following the addition of OPD using a SpectraMax M5e plate reader (Molecular Devices). To account for inter-plate variability, each plate was linearly scaled relative to a negative serum control (serum from a non-transduced rat) and a repeated high-expressing serum sample from the same animal.

### 6.2.8 Biodistribution

Tissues for the biodistribution study were sourced from the Fischer 344 rats in the 3E12 and 3E10 dosage groups (n = 3 each) as well as the CAG group (n = 2). The tissues investigated included brain, heart, liver, kidney, cervical spinal cord, lungs, ipsilateral axillary lymph node, spleen, gastrocnemius, sciatic nerve, contralateral gastrocnemius, and contralateral sciatic nerve. All tissues were harvested at 8 weeks, snap-frozen and stored in microcentrifuge tubes at -80 °C. 5 mg of tissue was sampled from each collected specimen and DNA extraction from the various organs was performed using DNeasy Tissue Kit (Qiagen) with the addition of RNase to obtain pure DNA. DNA yields were quantified using Qubit Fluorometric Quantitation (ThermoFisher Scientific). Viral DNA was assessed by quantitative PCR (employing an absolute quantification method with a standard curve) on the DNA extract. After primer screening, two sets specific for ChR2 coding sequence were employed: Primer I (HPLC purified): (F) 5'- CAATGTTACTGTGCCGGATG-3', (R) 5'-ATTTCAATGGCGCACACATA-3', Primer II: (F) 5'-

GCCTACCAAACCTGGAAATCTA-3', (R) 5'- CTGTGGCAAGGTAGAGCATAG-3'). Samples were retained and used in parallel to analyze both 5 ng (once) and 15 ng (twice) of DNA in triplicates from each tissue. The standard curve was prepared with viral DNA, extracted from the viral particles themselves and purified using the same DNA extraction kit, with 5 mg GN tissue from non-injected control rat for purpose of tissue sample mimicry. Negative controls comprised control (non-injected) rat genomic DNA from the same set of tissues. 40 cycles were run on Roche Light Cycler 480 using SYBR Green I dye chemistry from KAPA SYBR Fast qPCR Master Mix (KAPA BIOSYSTEMS), followed by a melting curve for specificity analysis. The threshold was defined as 66 ChR2 copies per ng of tissue DNA, based on the limit of the dynamic range of the standard curves from all 3 runs. This level is similar to the previously mentioned biodistribution study[165], which set a threshold of 20 copies of beta actin for every viral copy as a threshold, which corresponds to roughly 20 copies/ng DNA in our study, below the confidence of the standard curve.

### 6.2.9 Tissue and sample processing, histology, immunohistochemistry, flow cytometry, and analysis

Blood collection at 6 weeks was done via tail vein draw of ~0.5 mL. Following EMG recordings during terminal procedures, ~0.5 mL blood was collected from rats via cardiac puncture. K3EDTA was used for anticoagulation (Minicollect, Greiner Bio-One). Rats were euthanized via intra-peritoneal sodium barbital followed by transcardial perfusion with 60 mL PBS followed by 60 mL 4% PFA in PBS. Both AC and PC muscle groups on ipsilateral and contralateral legs were carefully dissected, cut from their origin and insertion points, and weighed. Spinal cord, ipsilateral TA, and ipsilateral sciatic nerve were dissected, fixed for 24 hours, paraffin processed, embedded, and cross-sectioned at 10 μm. Spinal cord was sectioned in either axial or coronal orientation.

Complete blood counts (CBCs) were performed with automated differential (Hemavet 950SS, Drew Scientific). For flow cytometery samples, blood was diluted by 1X in PBS and then spun down (650 g, 15 min) over Lymphoprep (Stem Cell Technologies). White blood cells were collected from phase layer, spun down again in PBS (650 g, 5 min).

Supernatant was decanted and 500 µL PBS containing 1% BSA was added to resuspend cells followed by 1.25 µL PE-conjugated Ms mAb to CD3 (ab95509, Abcam) or 1.6 µL isotype control (ab172730, Abcam). After a 30-minute incubation at 4° C, samples were spun once again, supernatant was discarded, and 100 µL PBS containing 1% BSA was added to each sample followed by resuspension. Samples were incubated overnight at 4° C prior to flow analysis. For non-flow cytometry samples, blood was spun down (650 g, 15 min), plasma was collected and frozen at -80 °C.

For immunofluorescence, EYFP expression was amplified with Rb pAb anti-GFP (ab290, Abcam) at 1:200 or Gt pAb anti-GFP (ab6673, Abcam) at 1:100 with either anti-Rb or anti-Gt Alexa Fluor 488 (Fisher) or anti-Rb or anti-Gt AP (Biocare) and Vulcan Fast Red (Biocare). Expression of ChR2 was amplified with Ms anti-ChR2 at 1:50 (American Research Products, Inc.) and anti-Ms Alexa Fluor 488 (Fisher). Immunohistochemistry and immunofluorescence of inflammatory infiltrates employed Ms mAb anti-CD8α (ab33786, Abcam) or Ms mAb anti-CD68 (ab31630, Abcam) with either anti-Ms Alexa Fluor 568 (Fisher) or Goat anti-Ms HRP (GHP516, Biocare) with DAB (DB801, Biocare). All antibodies were diluted in 1% w/v BSA in PBS-T. Immunofluorescence images were taken on an Evos FL Auto epifluorescence microscope (Fisher) at 10x (spinal cord) or 20x (sciatic nerve). H&E and immunohistochemistry images were taken on a digital slide scanner (Aperio AT2, Leica) at 20X. Using ImageJ, opsin$^{+}$ axons were counted manually whereas total axon counts were estimated from representative counts of subsets of the nerve. Assessment of spinal cord inflammation was performed on ImageJ 10X DAPI+ sections using the freehand selection tool to choose equivalent areas of ventral horn gray matter on left and right coronal lumbar sections. The ImageJ process employed inversion, thresholding, conversion to masks, watershedding, and the "analyze particles" function with size limits set to 30-250 square pixels per cell. The number of total particles (corresponding roughly to the number of cells) was scaled to the total measured area of each selection.

### 6.2.10 Statistical Analysis

Statistical significance was calculated in Microsoft Excel with the data analysis toolbox. For comparisons of individual groups, student's two-tailed t-tests with unequal variance were performed. For comparisons of multiple groups, a single factor analysis of variance (ANOVA) was performed followed by post hoc Fisher's Least Significant Difference (LSD) test for significance. All data represent the mean ± s.d. of at least three independent experiments unless otherwise specified; the number of trials is reported in the data provided.

## 6.3 Results

### 6.3.1 Expression time-course not a function of dosage, rat age, or injection location

We first evaluated the injection dosage, the location of the injection, and the rat age during the injection to see if these variables affected the strength and time course of transdermal optogenetic expression levels (Fig 6.1A). In line with previous results[123], we found expression levels to be heavily dose-dependent, with transdermal expression beginning at dosages of 3E10 vp and increasing in strength through 3E12 vp (Fig 6.1B). Injecting rats at different ages did not affect time course of expression despite slightly weaker expression in the rats injected over the first 4 weeks, likely due to synaptic pruning at the neuromuscular junction, which occurs rapidly in the first two weeks of murine development[166]. This is particularly apparent in the rats injected at 2 weeks as opposed to P2. Loss of transdermal response occurred faster in the rats injected in the TA-only vs. the TA & nerve at 2 weeks. However, no matter the dosing, timing or location of the injection, all of the rats with the exception of one had lost transdermal expression by 10 weeks post-injection (Fig 6.1B). This one rat maintained transdermal expression up to 72 weeks post-injection with the laser source (Fig 6.1D) when it was euthanized for unrelated reasons. In the terminal procedure, this rat maintained strong levels of expression even with direct stimulation of the sciatic and peroneal nerves with different illumination sources (Fig 6.1D). Despite this

one animal, we could not sustain a long-term optogenetic response consistently with any specific dosing or injection scheme.

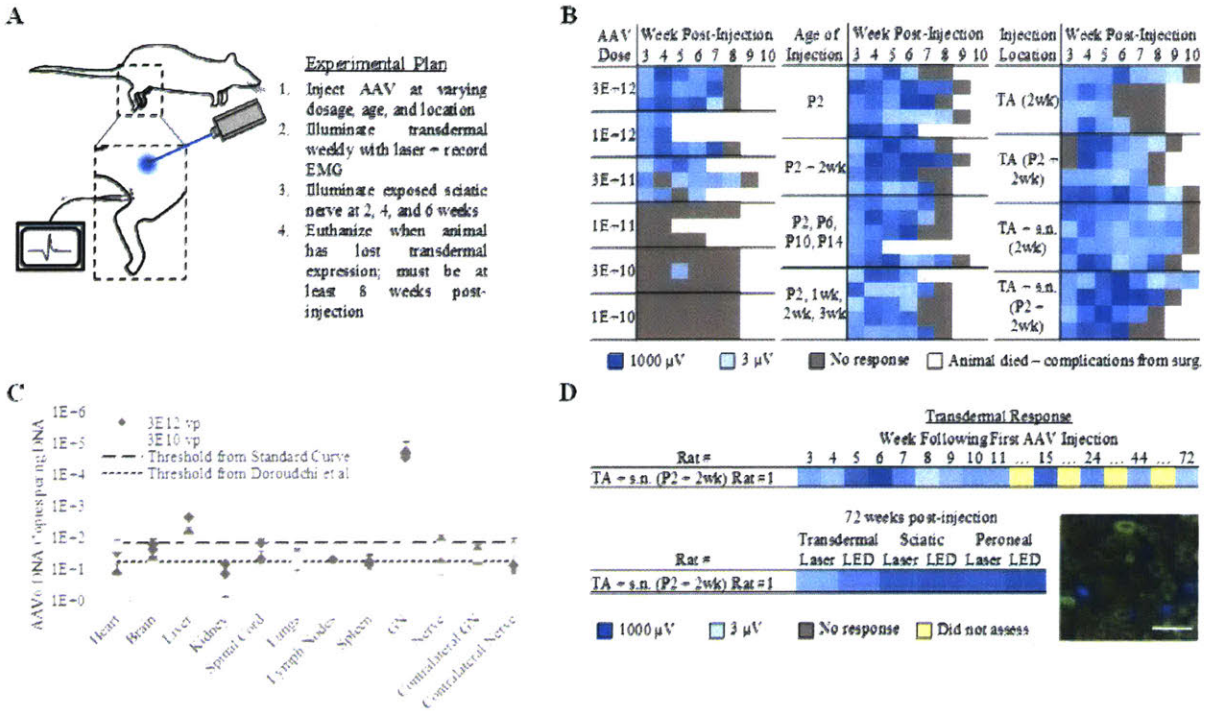


**Figure 6.1: All but one rats lose expression over time, independent of dose, age, or location of injection**

*(A) Experimental plan for dosage, timing, and location of injection animals. (B) Logarithmic $V_{RMS}$ amplitude of Tibialis Anterior (TA) motor activity in response to 473 nm, 45 mW/mm$^2$ transdermal illumination of the proximal tibia for 4 s at 5 Hz and 10 ms PW for different groups. (C) Biodistribution results for 3E12 vp and 3E10 vp injected animals. (GN = Gastrocnemius Muscle, Nerve = Sciatic Nerve). (D) Time-course for Rat #1 in group TA + s.n. P2 & 2 wk. This animal did not lose transdermal expression up through 72 weeks post-injection, when rat was euthanized. Expression on sciatic and peroneal at time of euthanasia with different illumination sources shown, as well as sciatic nerve cross-section showing ChR2+ axons (green) and DAPI (blue): scale bar = 30 µm.*

### 6.3.2 Biodistribution suggests viral expression predominately in muscle tissue

The analysis of viral vector spread by quantitative PCR on DNA extract from various organs revealed only minor off-target dissemination (Fig 6.1C). Viral DNA was found in high levels in the GN at the side of the injection for both concentrated and dilute injection groups, but in ~100x higher amounts for the concentrated injection group. Elevated levels in the liver were found to be consistent with standard bioclearance mechanisms[150]. The spinal cord showed the presence of viral DNA above the threshold in only one animal. Because the cervical spinal cord was sampled for biodistribution, and because AAV6 is likely to transverse retrograde only one synapse to the lumbar spinal cord, we expected, and identified no significant levels of DNA in the spinal cord. The sciatic nerve, targeted during the injection, also showed little to no viral DNA. This finding indicates that viral particles must travel in a retrograde fashion up the nerve via an intracellular pathway and that Schwann cells adjacent to each axon may be less susceptible to AAV gene delivery.

### 6.3.3 Activated immune cells target ChR2-EYFP+ neurons in spinal cord

We previously reported increased cell density within spinal cord samples of AAV6 transduced optogenetic rats as measured by DAPI+ fluorescence[123]. Here, we first evaluated H&E cross-sections of ChR2+ spinal cord samples, which showed ipsilateral inflammatory infiltrate predominately comprised of cells of lymphocytic origin (Fig 6.2A). We stained for CD8+ cytotoxic T lymphocytes (CTL) and discovered these CTLs appear to home to ChR2-EYFP transduced neurons directly (Fig 6.2B); the ChR2+ neurons are surrounded by CTLs that otherwise are not present significantly within the gray matter of the spinal cord. To assess for further inflammation, we stained for CD68+ activated macrophages, and discovered an aggressive inflammatory infiltrate comprising many immune cells adjacent to the location of transduced ventral horn motor neurons (Fig 6.2C). These results strongly suggested the presence of an adaptive immune process in the near vicinity of the optogenetically transduced neurons.

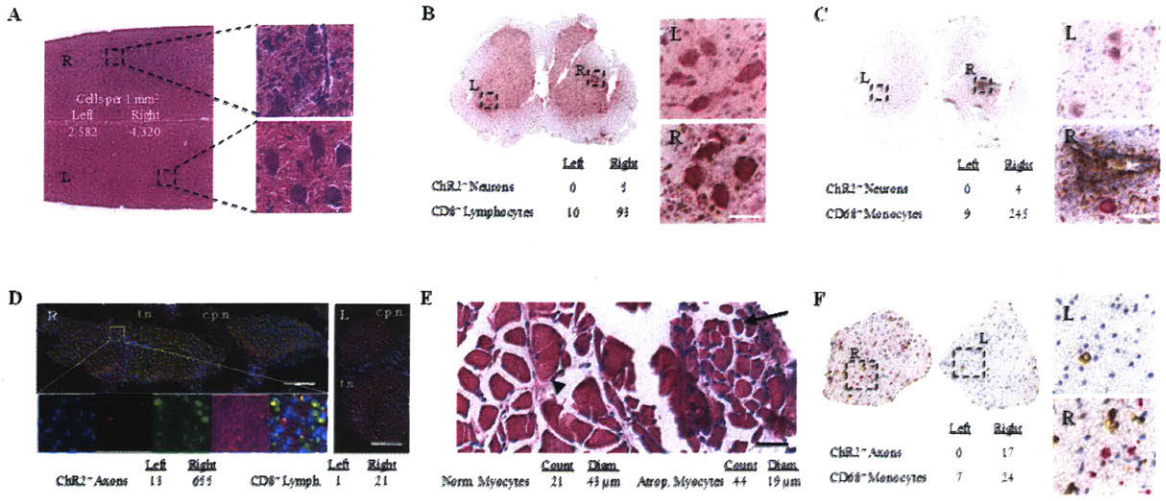


**Figure 6.2: Histology reveals neuronal attack in adaptive immune response**

*(A) Coronal lumbar H&E spinal cord section for ChR2-EYFP rat with ipsilateral inflammation present. Scale bar = 80 µm. (B) Lumbar spinal cord cross-section immunohistochemistry for ChR2-EYFP (red), CD8 (brown), and hematoxylin (blue). Scale bar = 60 µm. (C) Lumbar spinal cord cross-section immunohistochemistry for ChR2-EYFP (red), CD68 (brown), and hematoxylin (blue). Scale bar = 60 µm. (D) Sciatic nerve (R) and contralateral sciatic nerve (L) stained for ChR2-EYFP (green), CD8 (red), DAPI (blue), and background axons (magenta) with tibial (t.n.) and peroneal (c.p.n.) nerve divisions labeled. Scale bar (R) = 250 µm; Scale bar (L) = 500 µm. (E) Tibialis Anterior (TA) cross-section of ChR2 animal showing myocytes which are healthy (arrowhead) and those with denervation atrophy (arrow): Scale bar = 60 µm. (F) Ventral root cross-section immunohistochemistry for ChR2-EYFP (red), CD68 (brown), and hematoxylin (blue). Scale bar = 20 µm.*

We then explored sciatic nerve sections directly for evidence of immune cells (Fig 6.2D). Although there was no significant evidence of increased cellularity, immunofluorescence for CD8+ lymphocytes revealed the presence of 21 CTLs scattered throughout the ipsilateral sciatic nerve expressing ChR2-EYFP compared to only one CTL on the contralateral sciatic nerve. Both the CTLs and the ChR2-EYFP were found to be scattered throughout the peroneal and tibial nerve divisions so it is unclear whether the CD8+

lymphocytes targeted the nerve itself or specifically the ChR2-EYFP axons. Within the injected muscle, there is distinctive evidence of denervation atrophy (Fig 6.2E). Normal, healthy myocytes averaging 43 μm in diameter are adjacent to distinctively shrunken myocytes averaging 19 μm in diameter. Comparatively, the contralateral TA does not show any evidence of shrunken myocytes (not shown). There is no evidence of inflammatory infiltrate within ipsilateral TA H&E sections, indicating that the muscle tissue itself does not appear to be an immune target. Lastly, ventral root sections show increased presence of activated macrophages within roots containing ChR2-EYFP$^{+}$ axons, as opposed to contralateral roots (Fig 6.2F). Together, these results strongly suggest that ventral horn motor neurons and ChR2-EYFP transduced axons are being attacked by components of the adaptive immune system, resulting in neuron death and denervation atrophy in the muscle tissue.

### 6.3.4 ELISA shows ChR2-EYFP specific serum antibodies

Given the inflammatory infiltrate within spinal cord samples, it was theorized that the adaptive immune system was recognizing specific components of either the AAV6 capsid or the ChR2-EYFP fusion protein within the transduced neurons, which generally are co-localized. The ELISA to identify rat serum antibodies against ChR2-EYFP protein showed a strong AAV injection dose dependency (Supp. Fig 1B, 2C). The antibody levels of the rats injected with 3E12 vp was significantly higher (P = 7E-4) at roughly 0.4 compared to 0.1 in the rats injected with 3E10 vp and 1E10 vp, suggesting the rats were developing an antibody response to the ChR2-EYFP fusion protein in a dose-dependent fashion.

Despite the high antibody titer, we could not yet conclude that adaptive immune response was actually causing a loss of optogenetic expression in the rats. After all, the ventral horn neurons being transduced by AAV6 are in the spinal cord, and the CNS is notoriously considered immune protected via the blood-spinal cord barrier (BSCB). Further, the one animal that maintained transdermal optogenetic expression up to 72 weeks post-injection (Fig 6.1D) was found to have elevated antibody levels as measured by a serum ELISA

reading of 0.45, in line with other rats in his treatment group. If high antibody titer was causing loss-of-expression, we would expect prolonged expression to correlate with generally low IgG readings. Lastly, we noticed that no matter the intervention for muscle vs. muscle and nerve injections or different timing of injections, there was no significant effect on the overall ELISA antibody levels ($P_{ANOVA}$ = 0.34) (Fig 6.7). Together, these results suggest an immune response had occurred but further experiments were required to identify conclusively if this immune response was causing loss-of-optogenetic expression or merely clearing dead neurons following cytotoxic or excitotoxic-mediated apoptosis.

### 6.3.5 Rag2$^{-/-}$ rats maintain optogenetic expression, implicating adaptive immunogenicity as key mechanism underlying loss of expression

To identify causality, Rag2$^{-/-}$ rats were first phenotypically assessed to verify adaptive immune deficiency. Tail vein blood from WT and Rag2$^{-/-}$ Sprague Dawley rats at 6 weeks of age showed a significant difference in total white blood counts (WBC), driven predominately by lymphocyte deficiency in the Rag2$^{-/-}$ group (Fig 6.8A). Since Rag2 deficiencies do not affect innate immune lymphocyte populations, we employed flow cytometry and determined the remaining Rag2$^{-/-}$ lymphocytes were CD3$^{-}$, suggesting the lack of mature T cells (Supp. Fig 2B). We then transduced ventral motor neurons of Rag2$^{-/-}$ and WT rats and found that at 4 weeks post-injection, both groups expressed similarly. EMG responses were present in 5/5 animals of similar average magnitude (P = 0.31). However, by 12 weeks post-injection, 4/5 of the WT rats had lost twitch responses to transdermal illumination compared to 0/5 of the Rag2$^{-/-}$ rats (Fig 6.3A). Further, the minimum illumination power required to activate the targeted peroneal nerve stayed relatively constant in the Rag2$^{-/-}$ rats, as compared to the WT rats, which stopped responding to maximum illumination power (Fig 3B). This effectively ruled out anatomical changes alone, because the fluence change is not sufficient to prevent effective transdermal illumination of the nerve for Rag2$^{-/-}$ animals, the males of which are much larger than their WT female counterparts, all of whom had lost expression. The EMG results correlated well with the immunofluorescence findings which show significantly

greater ChR2-EYFP+ axons in the sciatic nerves of Rag2$^{-/-}$ rats compared to the WT rats (Fig 3E,F), as well as CD8+ lymphocytic inflammation only in the spinal cords of WT rats (Supp. Fig 6.8D,E).

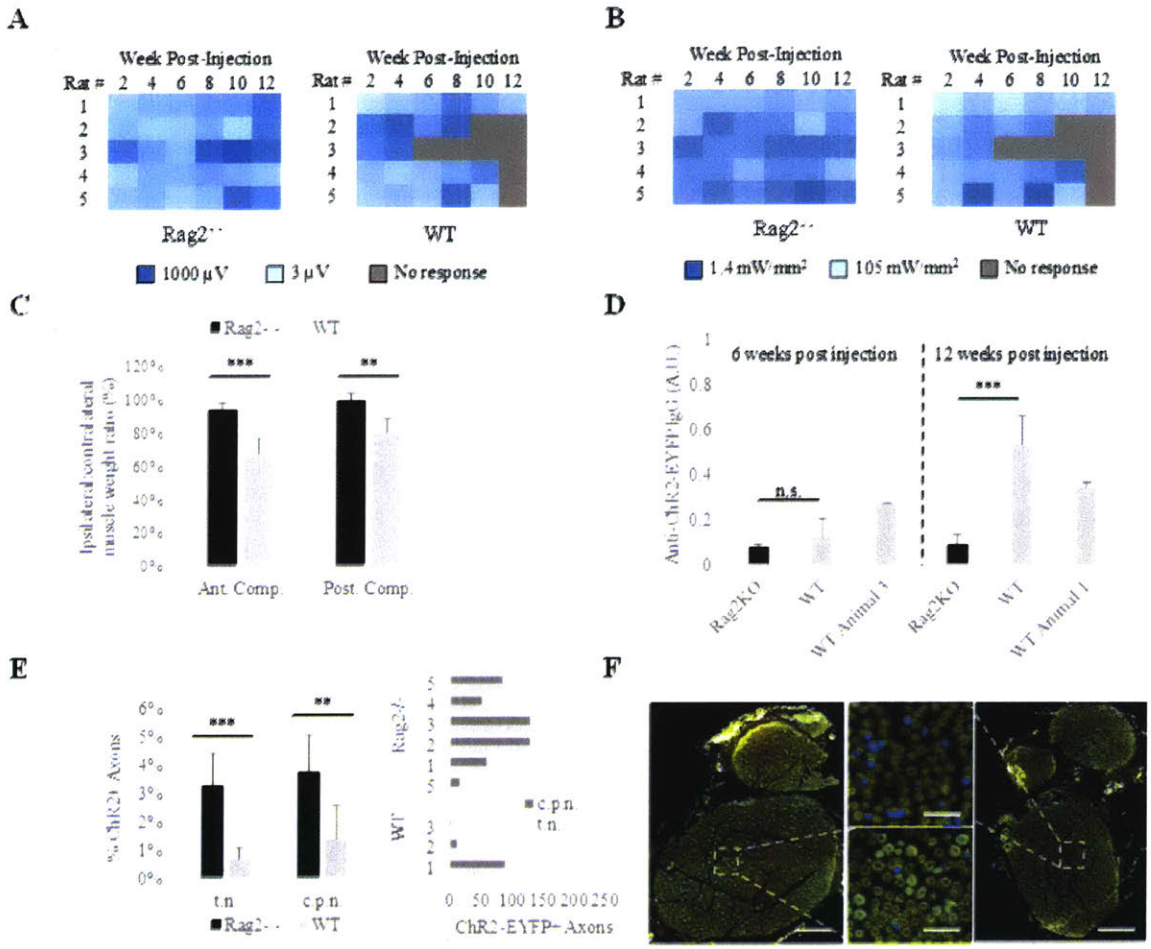


**Figure 6.3: Rag2$^{-/-}$ rats show prolonged transdermal optogenetic expression**

*(A) Logarithmic $V_{RMS}$ amplitude of Tibialis Anterior (TA) motor activity in response to 473 nm, 105 mW/mm$^2$ transdermal illumination of the proximal tibia for 4 s at 5 Hz and 10 ms PW for Rag2$^{-/-}$ and WT rats treated with high dose AAV6. (B) Logarithmic minimum transdermal illumination power needed to elicit transdermal EMG spikes from TA: $V_{RMS}$ spike threshold set to 2.45 µV, which was empirically determined to be the max noise level of recordings. (C) Ipsilateral to contralateral side of injection muscle weight ratio at the*

*time of euthanasia between high dose Rag2$^{-/-}$ and WT rats for both the anterior and posterior compartment muscle groups, representing primarily the Tibialis Anterior and Gastrocnemius muscles respectively (n=5 per group). P = 1E-3 for Ant. Comp. and P = 3E-3 for Post. Comp. (D) Normalized ELISA comparing plasma antibodies against ChR2(H134R)-EYFP for Rag2KO and WT rats at 6 weeks post injection (n = 2 for Rag2KO, n = 5 for WT) and 12 weeks post injection (n = 5 for both groups). P = 8E-4 for 12 week. WT Animal 3 was the only rat which lost transdermal optogenetic expression at week 6. WT Animal 1 was the only rat which maintained expression at week 12. In addition to being included in their respective groups, these animals are also shown separately. (E) ChR2-EYFP+ axon counts as percentage of total axons (left) and as absolutes (right) in tibial nerve (t.n.) and peroneal nerve (c.p.n.) divisions of sciatic nerve of WT and Rag2$^{-/-}$ rats ($n_{Rag2-/-} = 8$, $n_{WT} = 7$): $P_{left} = 2E\text{-}4$. $P_{right} = 3E\text{-}3$. Rats from excitotoxicity control group also included. (F) Sciatic nerve cross sections of representative Rag2$^{-/-}$ rat (left) and WT rat (right) labeled for ChR2-EYFP (green) and DAPI (blue). Scale bar$_{left,right}$ = 120 μm, Scale bar$_{center}$ = 20 μm..*

In agreement with the loss-of-expression findings, ipsilateral muscle atrophy was also found to be restricted to the WT rats (Fig 6.3C). Ipsilateral muscles were 33 ± 9% reduced and 19 ± 8% reduced compared to contralateral muscle weights in the anterior and posterior compartments respectively for WT rats. Comparatively, Rag2$^{-/-}$ rats had muscle reductions of 6 ± 5% and 1 ± 5% for the same compartments respectively. Anterior compartment muscle mass reductions ranged from a high of 47% for WT Rat #3 to a low of 23% for WT Rat #1, which correlates precisely with their optogenetic expression profiles. WT Rat #3 was the first rat to lose expression and therefore had the strongest immune response; WT Rat #1 had yet to lose expression at the time of euthanasia and thus the weakest immune response. These individual differences were also reflected in the ChR2-EYFP ELISA. At 6 weeks post-injection the plasma antibodies against ChR2-EYFP were slightly, but not significantly larger in the WT group compared to the Rag2$^{-/-}$ group (P = 0.29) (Fig 6.3D). However, the highly immunogenic WT Rat #3 was the outlier, with more than 2X the WT group's overall ChR2-EYFP specific plasma antibody levels at that time. By 12 weeks post-injection, the serum antibodies in the WT group increased

significantly, reaching 6X the $Rag2^{-/-}$ group (P = 8E-4). At this time, WT Rat #1 was the outlier with roughly half of the antibody expression of the group as a whole, in line with the lower atrophy and maintained immunofluorescent axonal expression in this rat (Fig 6.8F).

To rule out excitotoxicity as a contributing factor to loss of expression, we found the WT excitotoxicity controls showed similar results to the WT stimulated rats during terminal procedures. 4/4 WT rats showed no response to any transdermal illumination during terminal procedures compared to 0/4 of the $Rag2^{-/-}$ excitotoxicity controls (Fig 6.12A). Further, no significant muscle atrophy, nerve expression, or ELISA differences were found between stimulation and no-stimulation groups (Fig 6.12B,C,D). This suggests that the stimulation used in this experiment is insufficient to cause any excitotoxicity mediated neuronal death. Together, these data show conclusively that the adaptive immune system is a necessary condition for the loss of optogenetic expression and that a component of the AAV6-ChR2-EYFP immunogen is directly causing loss of expression.

### 6.3.6 Tacrolimus extends longevity of optogenetic expression in WT rats

To identify pharmacological candidates for extending the life of virally delivered optogenetic expression in a WT animal, two broad categories of FDA-approved drugs were evaluated: a monoclonal antibody against CD49d (PS2), also known as VLA-4 or α4 integrin, and a general immunosuppressant. As the murine analog of natalizumab, a treatment for Multiple Sclerosis (MS), PS2 was chosen for its anti-inflammatory effects in experimental autoimmune encephalomyelitis (EAE)[40]. However, PS2 was not found to have any effect maintaining long-term expression levels as compared to the placebo group (Supp. Fig 6.4A). Additionally, PS2 did not appear to have any effect on WBC or differentials. Further, PS2 animals developed non-specific anti-antibody neutralizing antibodies, which may have prevented drug efficacy (Fig 6.10C). Conversely, the general immunosuppressant tacrolimus was found to increase significantly the longevity of transdermal optogenetic expression in WT rats (Fig 6.4A).

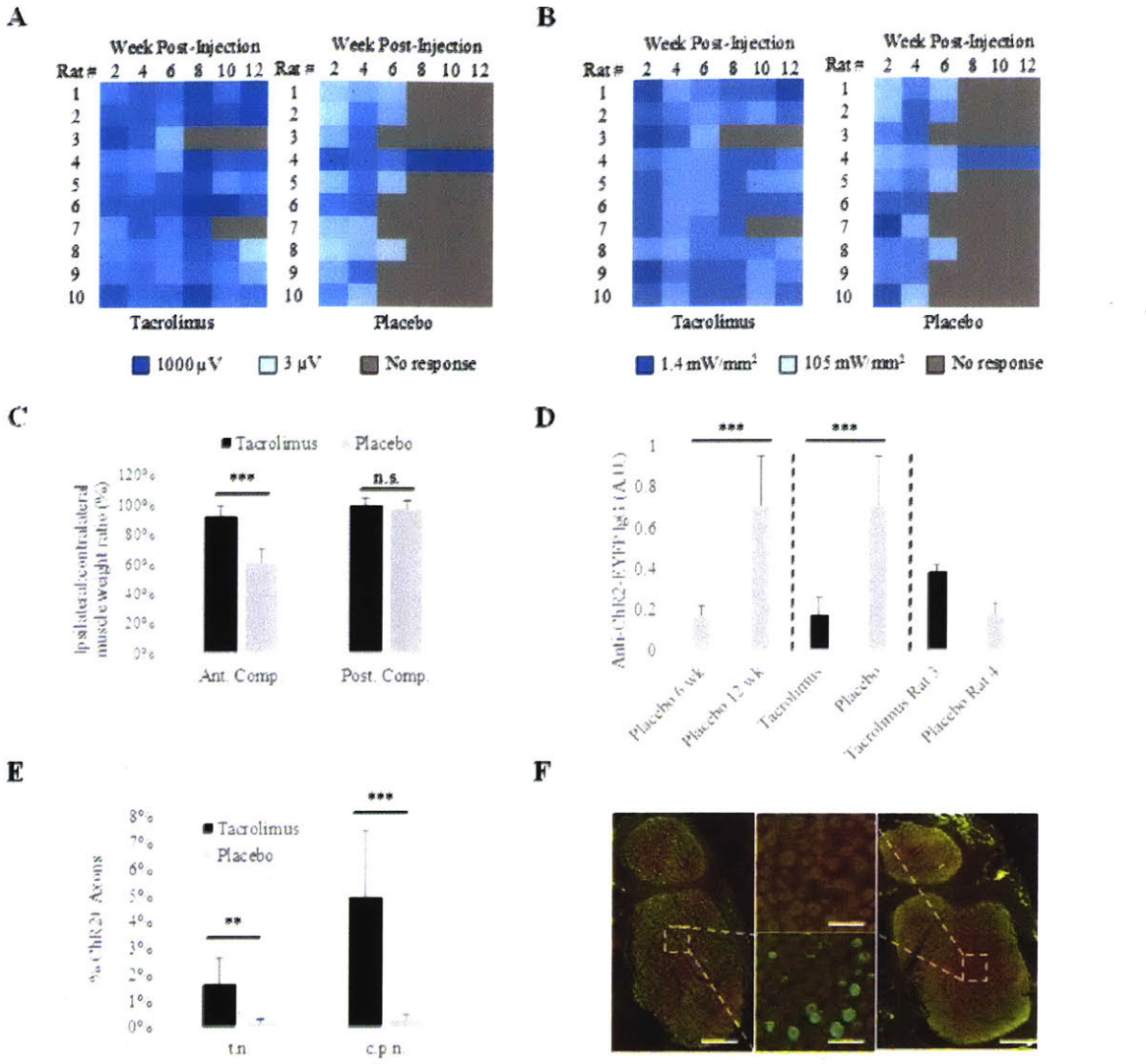


**Figure 6.4: Tacrolimus-treated rats show extended optogenetic expression**

*(A) Logarithmic $V_{RMS}$ amplitude of TA motor activity in response to 473 nm, 105 mW/mm$^2$ transdermal illumination of the proximal tibia for 4 s at 5 Hz and 10 ms PW for rats treated with slow release tacrolimus pellet vs. those with placebo pellet. (B) Logarithmic minimum transdermal illumination power needed to elicit transdermal EMG spikes from TA for tacrolimus-treated and placebo-treated rats: $V_{RMS}$ spike threshold set to 2.45 μV, which was empirically determined to be the max noise level of recordings. (C) Ipsilateral to contralateral side of injection muscle weight ratio at the time of euthanasia between tacrolimus and placebo rats for both the anterior and posterior compartment muscle groups, representing primarily the TA and GN muscles respectively (n=8 for tacrolimus, 9*

*for placebo group). Tacrolimus rats #3 and #7 (which had lost expression at time of euthanasia), and placebo rat #4 (which maintained expression at time of euthanasia) were excluded, as shown in Fig 6.9. P = 3E-6 for anterior compartment and P = .23 for posterior compartment. (D) Normalized ELISA comparing plasma antibodies against ChR2(H134R)-EYFP for WT rats at 6 weeks post injection (n = 10) and 12 weeks post injection (all others, n = 10). P = 5E-5 for 6 vs 12 week comparison. P = 3E-5 for tacrolimus vs. placebo comparison. In addition to being included in their respective groups, rat #3 in tacrolimus group and rat #4 in placebo group are also shown separately as they are outliers in their respective groups. (E) ChR2-EYFP+ axon counts as percentage of total axons in tibial nerve (t.n.) and peroneal nerve (c.p.n.) of tacrolimus and placebo rats ($n_{Tacrolimus}$ = 8, $n_{Placebo}$ = 9): $P_{t.n.}$ = 5E-3; $P_{c.p.n.}$ = 1E-3. Tacrolimus rats #3 and #7 (which had lost expression at time of euthanasia), and placebo rat #4 (which maintained expression at time of euthanasia) were excluded. (F) Sciatic nerve cross sections of representative Rag2$^{-/-}$ rat (left) and WT rat (right) labeled for ChR2-EYFP (green) and DAPI (blue). Scale bar$_{left,right}$ = 120 μm, Scale bar$_{center}$ = 20 μm.*

Similar to the Rag2$^{-/-}$ rats, all rats treated with tacrolimus or placebo responded well to transdermal illumination at 4 weeks post-injection (Fig 6.4A). However, at 6 weeks, only 5/10 of the placebo rats responded to transdermal illumination compared to 10/10 of the tacrolimus rats. By 8 weeks, that difference was extended to 1/10 placebo rats compared to 9/10 of the tacrolimus rats. This one outlier placebo rat continued to increase in expression strength until 12 weeks, whereas two of the tacrolimus rats (#3, #7) lost transdermal expression by 12 weeks. The minimum fluence rate to elicit electrophysiological spikes similarly showed increasing sensitivity of placebo rat #4 and maintained sensitivities of all tacrolimus rats except #3 and #7 (Fig 6.4B).

As with the WT rats, there was significant muscle atrophy within the anterior compartment of the placebo group of 38% as compared to 9% in the tacrolimus group (P = 3E-6) (Fig 6.4C). The atrophy ranged from a high of 57% to a low of 28% for the placebo rats and a high of 23% to a low of -6% for the tacrolimus rats, when omitting the three outliers:

tacrolimus rats #3 and #7 & placebo rat #4, which had atrophy of 58%, 43%, and 6% respectively (Fig 6.9C). Unlike the WT rats, the posterior compartments in both tacrolimus and placebo groups did not show any atrophy at all (3% and 1%), possibly indicating better targeting of the anterior compartment during the injection. Similar to the WT rats, the ELISA results support the findings of ChR2-EYFP immune responses (Fig 6.4D). At 6 weeks, the measured anti ChR2-EYFP plasma antibodies of the placebo group is small, increasing significantly by 12 weeks (P = 5E-5). At 12 weeks, the tacrolimus group maintained low plasma antibodies as compared to the placebo group (P = 3E-5) with tacrolimus rat #3 and placebo rat #4 as exceptions, in line with muscle atrophy and loss-of-expression profiles. These data strongly suggest that tacrolimus can be used to increase significantly the length of optogenetic expression.

It is unclear exactly what precipitated the lack of immune response for outlier placebo rat #4. Of note, at 6 weeks post-injection, this rat was found to be very anemic, with red blood cells (RBC), hemoglobin (Hb), and hematocrit (HCT) levels all 8 standard deviations below the average from the other 9 placebo animals (Fig 6.9D). Interestingly, the only other rat which maintained expression at week 12 (WT rat #1) was also anemic at 6 weeks. This rat's RBC, Hb, and HCT levels were found to be 5 standard deviations below the other 4 WT rats in its group. However, the white counts (including differentials) and platelet counts for these two outliers were not significantly different from that of their respective groups. In addition, we noticed that tacrolimus had an effect on the hematological properties of RBC. Within the tacrolimus group, RDW was significantly elevated (P = 1E-3) along with a corresponding reduction in MCV (P = 9E-4) and MCH (P = 4E-3) compared to the placebo group (Fig 6.10F). However, no significant anemia was present between the two groups ($P_{Hct,Hb} = 0.7$), even when excluding outlier placebo rat #4. We can therefore conclude that tacrolimus is causing a reduction in the average erythrocyte size. Since this is occurring when tacrolimus concentration hits peak levels around 4 weeks of age, and knowing that the rat erythrocyte life is roughly 60 days[45], we can conclude that the high RDW and low MCV may be explained by the combination of large erythrocytes prior to and small erythrocytes following the administration of tacrolimus therapy.

### 6.3.7 CAG promoter rules out AAV capsid as primary cause of immune response

To identify the role of AAV capsid in precipitating an immune response, we evaluated the ChR2-EYFP injected under the CAG promoter. Unlike hSyn, CAG does not restrict ChR2 expression to neural tissue, which was shown by the unique spiking behavior following transdermal illumination of these rats (Fig 6.5A). Whereas hSyn spikes are narrow and return to baseline within ~4 ms of activation, CAG spikes are wide and return to baseline ~20 ms following activation. The narrow coordinated spike at the beginning of an optogenetically activated CAG waveform represents direct neural firing – all myocytes are time-synced to depolarize at once. This is followed by wider-band activity from direct myocyte firing. This distinction is in agreement with our previous findings showing no motor activity following direct illumination of muscle in hSyn rats[3] compared to CAG rats, which showed exquisite motor control as would be expected with direct myocyte activation.

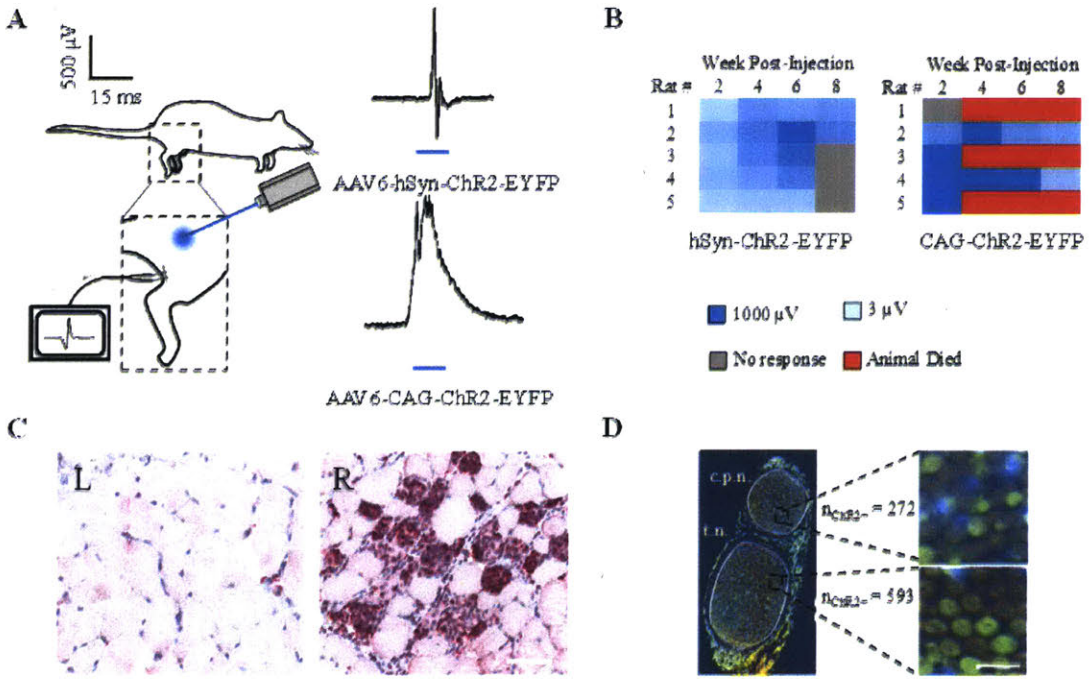

**Figure 6.5: Under CAG promoter, ChR2 expresses in myocytes, causing inflammation**

*(A) TA EMG recordings in response to 473 nm transdermal illumination of proximal tibia in rats treated with ChR2 restricted by either hSyn or CAG promoter. (B) Logarithmic minimum transdermal illumination power needed to elicit transdermal EMG spikes from TA for hSyn and CAG promoters: $V_{RMS}$ spike threshold set to 2.45 μV, which was empirically determined to be the max noise level of recordings. (C) TA muscle cross-section of CAG animal 8 weeks post-injection showing healthy myocytes devoid of inflammation on contralateral limb (left) and inflamed myocytes stained with vulcan red against ChR2-EYFP transfected myocytes (red, right): scale bar = 40 μm. (D) Immunofluorescence for ChR2+ axons in CAG-ChR2-EYFP sciatic nerve sections along with counts in peroneal (c.p.n.) and tibial (t.n.) sections: scale bar = 20 μm.*

Unlike the hSyn animals, the CAG rats exhibited excessive mortality of 60% (Fig 6.5B). Although necropsies did not reveal any specific cause of death, these animals overall had a lower weight than the WT rats and exhibited more hunching and eye staining. In terms of EMG levels, the two surviving CAG rats lost strength of the EMG signal from week 4 to week 8, similar to the hSyn controls. Unlike the hSyn promoter, an immunohistochemical analysis of the CAG TA showed significant ChR2+ myocytes. Not only were these myocytes spread throughout the section, there was lymphocytic inflammation specifically co-localized to the transduced myocytes (Fig 6.5C). The biodistribution for CAG animals revealed levels of ChR2-EYFP DNA within both the CAG and hSyn muscle were very similar at ~1E5 copies per ng DNA (Fig 6.10A). Therefore, given the identical AAV6 dosage and injection, and similar biodistribution results between the hSyn and CAG groups, the findings of high mortality and ChR2-EYFP specific myocyte inflammation in exclusively the CAG rats must indicate that the immune response is directly targeting ChR2-EYFP and not the AAV capsid. Both promoters result in similar levels of AAV capsid fragment expression on myocytic MHCI, but only the CAG rats result in myocytic immune attack suggesting ChR2-EYFP specific immunogenicity.

### 6.3.8 ChR2-only and ChR2-EYFP rats show equivalent immune activity, suggesting immune response is ChR2-specific

After determining the primary immunogen is ChR2-EYFP, we injected a last set of 10 rats with AAV6-hSyn-ChR2 lacking the fluorescent reporter. Interestingly, these animals at 4 weeks expressed at significantly weaker levels than those containing the fluorescent reporter ($P = .05$) (Fig 6.6A). Further, the movement was qualitatively weaker, although the minimum fluence rates needed to activate the nerves at 4 weeks was similar (Fig 6.6B). Because of this, it is likely that fewer axons expressed ChR2 at 4 weeks of age in absence of reporter, although 12 week counts were insignificantly different (Fig 6.6E, Supp Fig 6.13A). Without reporters, fluorescent activity for all sciatic nerves ranged between 0-2% of total axons with the exception of rats #2 and #7, which had peroneal transduction rates of 4% and 9% of all axons respectively. This agrees with electrophysiological findings. Rat #7 still expressed, responding well to transdermal stimulation at the time of euthanasia. One possibility is that without EYFP, the ChR2 protein can form dimers that are less excitable to optogenetic activation. Unlike with ChR2-EYFP, western blots from a ChR2-only lysate revealed a light band located at ~68 kDa, roughly double the size of the 34 kDa ChR2 protein (Fig 6.13D).

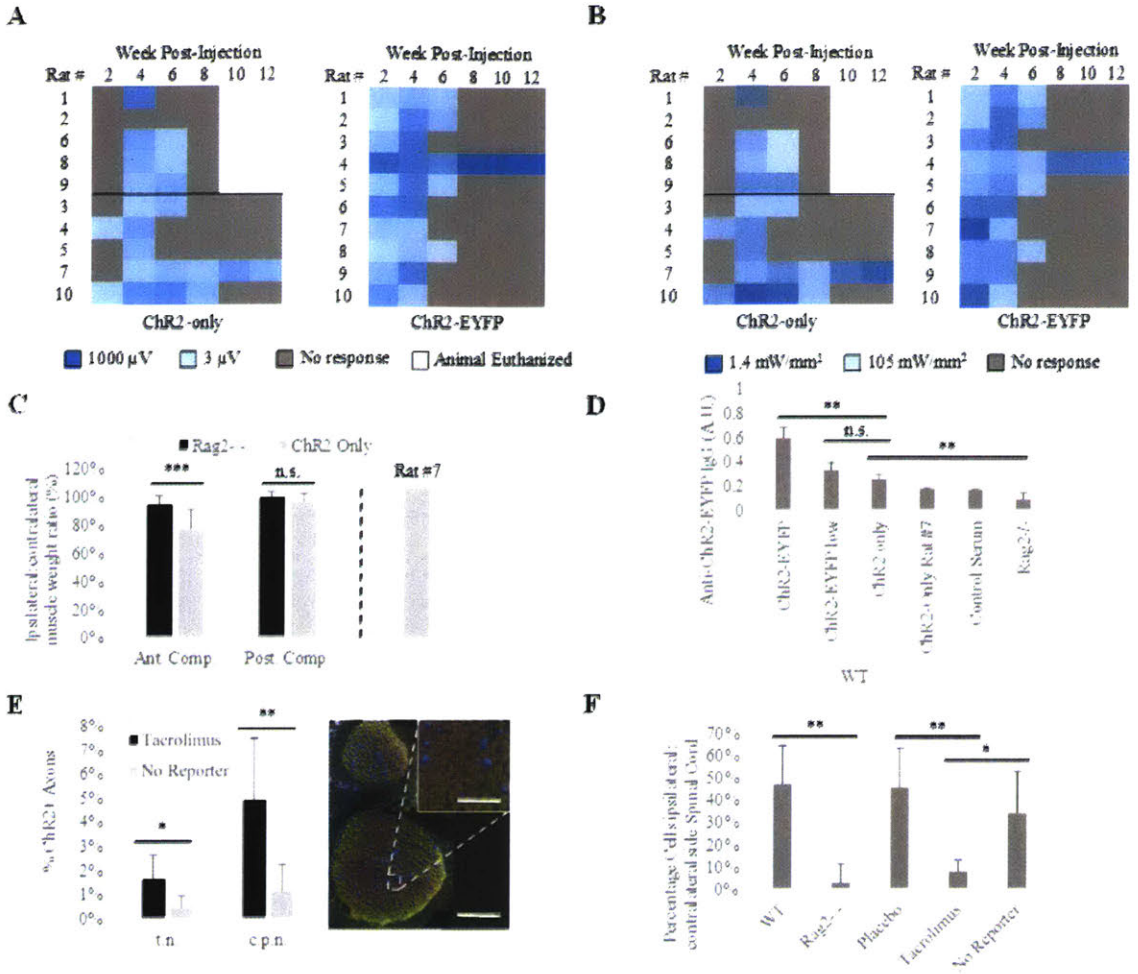


**Figure 6.6: Without EYFP reporter, ChR2 still elicits immune response**

*(A) Logarithmic $V_{RMS}$ amplitude of TA motor activity in response to 473 nm, 105 mW/mm$^2$ transdermal illumination of the proximal tibia for 4 s at 5 Hz and 10 ms PW for rats injected with ChR2-only vs. those with ChR2-EYFP. (B) Logarithmic minimum transdermal illumination power needed to elicit transdermal EMG spikes from TA for ChR2-only and ChR2-EYFP rats: $V_{RMS}$ spike threshold set to 2.45 µV, which was empirically determined to be the max noise level of recordings. (C) Ipsilateral to contralateral side of injection muscle weight ratio at the time of euthanasia between Rag2$^{-/-}$ and ChR2-only rats for both the anterior and posterior compartment muscle groups, representing primarily the TA and GN muscles respectively (n=9 for Rag2$^{-/-}$, n=9 for ChR2 only). ChR2-only rat #7 (which had maintained expression at time of euthanasia) was also shown separately and excluded from significance test (P = 7E-5 for Ant. Comp. and P =*

*.06 for Post. Comp.). (D) Normalized ELISA comparing plasma antibodies against ChR2(H134R)-EYFP for WT rats at normal and low dose, Rag2$^{-/-}$ rats at normal dose, and ChR2(H134R) WT rats without reporter ($n_{ChR2\text{-}EYFP}$ = 4, $n_{ChR2\text{-}EYFP\ low}$ = 4, $n_{ChR2\ only}$ = 3, $n_{Rag2\text{-}/\text{-}}$ = 5). Only ChR2-only rats who had lost all transdermal and subcutaneous expression at the time of blood collection were included. $P_{left}$ = .002; $P_{center}$ = .12; $P_{right}$ = .006. (E) ChR2-EYFP+ axon counts as percentage of total axons in tibial nerve (t.n.) and peroneal nerve (c.p.n.) of tacrolimus and no reporter rats ($n_{Tacrolimus}$ = 8, $n_{NoReporter}$ = 9): $P_{t.n.}$ = .02; $P_{c.p.n.}$ = 4E-3. Tacrolimus rats #3 and #7 (which had lost expression at time of euthanasia), and no reporter rat #7 (which maintained expression at time of euthanasia) were excluded. Sciatic nerve cross sections of representative no reporter rat labeled for ChR2 (green) and DAPI (blue). Scale $bar_{bottom}$ = 200 μm, Scale $bar_{top}$ = 30 μm. (F) Number of DAPI+ cells on ipsilateral side compared to contralateral side of spinal cord expressed as a percentage increase for WT (n=3), Rag2$^{-/-}$ (n=3), placebo (n=3), tacrolimus (n=3), and no reporter rats (n=5). $P_{ANOVA}$ = 8E-3. Can reject the null using Fisher's LSD at α = .01 for ** and α = .05 for *.*

As with the previous WT rats, ChR2-only rats revealed ipsilateral muscle loss in the anterior compartment averaging 22% (Fig 6.6C). Among the rats that lost expression in this group, muscle weight loss ranged from 35% Rat #1 to -5% in Rat #7, reflecting a drop in the number of transduced motor neurons compared to the WT and placebo groups of same dosage. To verify this AAV did not contain EYFP, immunofluorescence using antibodies against EYFP revealed no axons, whereas using antibodies against ChR2 yielded transduced axons (Fig 6.13B,C). To verify immunogenicity as opposed to toxicity in the ChR2 only group, immunohistochemistry on axial spinal cord sections revealed both a high number of CD8+ lymphocytes on the injection side as compared to the contralateral side (Fig 6.13E) and generally high cell densities on the ipsilateral side (Fig 6.13F). Further, the ELISA against ChR2-EYFP revealed a slight elevation of serum antibody as compared to the Rag2$^{-/-}$ rats and non-injected control samples; however, these antibodies were significantly lower than those of the same dose ChR2-EYFP injections (Fig 6.6D). Levels were insignificantly different from the antibody levels of the low-dose ChR2-EYFP injections in the WT rats. No reporter rat #7, which maintained expression at the time of

euthanasia, had lower levels of serum antibodies, in line with the non-injected sample. When high cell densities in the spinal cord are evaluated as a percentage increase over the contralateral side, placebo, WT, and no reporter rats all have significant inflammation compared to $Rag2^{-/-}$ and Tacrolimus treated groups: $P_{ANOVA}$ = 8E-3 (Fig 6.6F). Together, these results definitively implicate the ChR2 transgene protein as being highly immunogenic, eliciting a strong CTL-mediated PNS and CNS immune response resulting in motor neuron death, muscle atrophy, and immune activation.

## 6.4 Discussion

The contribution of each experiment to the conclusive establishment of immunogenic cause is outlined in Table II. Although other factors are not conclusively ruled out as contributing to loss-of-expression, the results show that ChR2 immunogenicity is definitely occurring and is a prime concern for optogenetic time-course.

**Table 6.2 Contribution of factors to conclusion of ChR2-specific immunogenicity.**

| Potential causes | hSyn-TA Histology | hSyn-SC Histology | hSyn-s.n. Histology | CAG-TA Histo.+ Biodist. | CAG Morbid | ChR2-EYFP ELISA | Excitotox Controls | Rag2$^{-/-}$ rat study | Drug Study | ChR2-only study |
|---|---|---|---|---|---|---|---|---|---|---|
| Phototoxicity | + | | - | | | | | | | |
| Excitotoxicity | + | | | | | | - | | | |
| ChR2 toxicity | + | - | | | + | | | | | |
| EYFP toxicity | + | - | | | + | | | | | |
| AAV immunogenicity | + | + | | - | - | | | | | |
| ChR2 immunogenicity | + | + | | + | + | + | | + | + | + |
| EYFP immunogenicity | + | + | | + | + | + | | + | + | |
| Episomal DNA loss | - | - | | | - | | | | | |
| Epigenetic silencing | - | - | | | - | | | | | |
| Upregulation of transgene degradation or mRNA lysis | - | - | | | - | | | | | |
| Anatomical | - | - | | | | | | - | | |

In this experiment, we hypothesize that ChR2 immunogenicity is causing the loss-of-expression over time in Sprague Dawley and Fischer 344 rats. The data presented in this study support this hypothesis. To identify ChR2-specific immunogenicity, we employ $Rag2^{-/-}$ rats and identify sustained levels of transdermal optogenetic expression over time. Further, we use a slow-release tacrolimus to extend expression levels in a WT animal. We then explore the immunogenic effect of AAV-ChR2 upon removal of the fluorescent reporter, and identify all the same signs of immunogenicity, suggesting ChR2 alone is still immunogenic.

In this work, we develop a comprehensive set of four tests that can identify whether an immune response is occurring for peripheral nerve optogenetics. First, we develop a novel ELISA that identifies serum antibodies against ChR2-EYFP. We validate this ELISA using serum from our AAV dosage curve to show that lower injection dosages result in reduced anti-ChR2-EYFP antibodies. The ELISA properly identifies group outliers, suggesting it is an optimal way of assessing immune response to optogenetic proteins. Second, we evaluate muscle atrophy and identify that reduced ipsilateral muscle weight is correlated with loss of expression. Further, we can estimate the number of previously transduced motor nerve fibers specific to a given muscle based on the amount of muscle mass reduction. This arguably provides a more reliable estimate of transduction efficiency than using nerve cross-sections, because nerve cross-sections may be biased by variability in branching of cutaneous, autonomic, or non-target muscle efferent nerve fibers. Third, we perform immunofluorescent observations of nerve fibers and spinal cord sections and identify elevated CD8+ lymphocytes and CD68+ macrophages co-localized to ChR2+ neurons and axons. Lastly, we perform DAPI+ cell counts of contralateral and ipsilateral spinal cord sections with an automated image processing algorithm and identify an increase of ipsilateral cell density. Together, these four tests comprehensively constitute a peripheral optogenetic-specific immune panel, which can be employed as a benchmark in future scientific and clinical optogenetic studies.

We present 13 potential mechanisms describing the loss of peripheral nerve optogenetic expression divided into five independent categories by mechanism of action: phototoxicity, cytotoxicity, immunogenicity, protein downregulation, and anatomy. While each of these mechanisms may play some role in loss-of-expression, our experiments suggest that ChR2 immunogenicity is the key contributor. To reach this conclusion, we first identify inflammation in spinal cord samples in certain WT rats. However, cellular apoptosis can also send damage signals and recruit inflammatory cells – spinal cord inflammation is not alone sufficient to rule out phototoxic, excitotoxic or cytotoxic mechanisms. The presence of CTLs and activated macrophages co-localized to ChR2+ neurons strongly suggests an adaptive immune process is occurring directly related to the AAV capsid or viral transgene. However, to prove this causatively, we employ $Rag2^{-/-}$ rats and find transdermal optogenetic expression is maintained at similar levels in all $Rag2^{-/-}$ rats at all time points. To extend time course of optogenetic expression in WT rats, we employ a subcutaneous tacrolimus pellet and identify transdermal expression in 8/10 tacrolimus vs 1/10 placebo rats at 12 weeks post-injection. To rule out AAV capsid immunogenicity, we inject two WT groups with identical AAV dosage, using CAG and hSyn promoters to modulate tissue specificity. Not only does the CAG promoter result in significant mortality, but it also results in immune infiltrates co-localized with ChR2+ myocytes. Myocytic inflammation does not occur with the hSyn promoter, despite the identical presence of AAV capsid within myocytes as shown by the biodistribution, enabling us to conclude that the adaptive immune system is targeting ChR2-EYFP and not AAV capsid. Lastly, we perform AAV-ChR2 injections without the EYFP reporter. We discover the same loss-of-expression time-course as with the EYFP reporter, allowing us to conclude, based on anatomical, hematological, and histological tests, that ChR2 itself is causing an immunogenic reaction.

In addition to the group effects defined by the above, we present outliers to the groups. One rat in the dosing, timing, and anatomy study maintained transdermal peripheral nerve expression for 72 weeks post-injection. This represents the longest-ever virally induced peripheral nerve optogenetic response to our knowledge, indicating that highly expressing long-term optogenetic stability is possible, even in the case of elevated levels of serum anti ChR2-EYFP antibodies. To understand why this might have been the case, we analyze

hematological abnormalities of WT rat #1 and placebo rat #4, both of which maintain transdermal expression when the other rats in their respective groups lose expression by week 12. It is interesting to note that both of these rats were significantly anemic at 6 weeks of age compared to other rats in their groups (P: ~1E-18 and ~1E-7), despite no difference in WBC or thrombocyte counts. At this age, only a few rats had lost transdermal optogenetic expression, so the early anemia may be a predictive way of screening rats for their future expression time-course. A low HCT has been previously associated with a complete elimination of the symptoms of experimental autoimmune encephalomyelitis (EAE), the murine analog of MS[168]. To date, EAE is one of the most representative conditions of optogenetic spinal cord inflammation. The authors propose that iron deficiency may impair CD4+ T cell maturity, which is also suggested in another study showing human subjects with low iron levels were less responsive to an influenza vaccine[169]. Further, the authors identified that their mice with a low HCT also had significantly elevated levels of IL-2, which helps promote development of CD25+ regulatory T cells. These regulatory cells may help temper the effects of the CD4+ and CD8+ T lymphocytes, preventing the spinal cord inflammation in the first place. It is unclear why these two rats are anemic to begin with; we do not believe that it has anything to do with the intervention itself, but instead it is just caused by natural variation. It is possible that iron deficiency and/or HCT may be used clinically to help screen patients for better outcomes in future CNS gene therapy studies, but a better mechanistic understanding of the relationship is critical.

Conversely, tacrolimus rats #3 and #7 both lost expression compared to the other rats in their group. We show that these two rats had normal levels of RDW at 6 weeks compared to the placebo group (P = 0.3), but not compared with the other rats in their own group (P = 4E-3). Previous research has shown a correlation between tacrolimus concentrations and RDW in blood samples from anemic transplant recipients[170,171]. This correlation was identified as important for proper titration of tacrolimus dosage in transplant recipients. The authors propose that RDW could be used to adjust tacrolimus dosage to the patient because "anisocytosis may affect the apparent plasma clearance of tacrolimus". Our findings suggest the opposite, that tacrolimus is in fact causing the anisocytosis, in which

case measures of RDW to predict tacrolimus dosage response may not be appropriate. Rats #3 and #7 may not have absorbed as much tacrolimus as evidenced by a positive immune panel (+ELISA, muscle atrophy, no nerve expression, and spinal cord cell infiltrate) as well as their normal RDW readings. Conversely, it is also possible that independent haematological abnormalities could still be affecting tacrolimus clearance, resulting in lower immunosuppressive efficacy in these two rats. Mechanistically, further study of the cause-effect relationships of immunosuppressants and hematological abnormalities is warranted, and may help improve outcomes for both organ transplant and perhaps future optogenetic therapy recipients.

In this study, we propose a pharmacological mechanism to extend optogenetic longevity for peripheral nerves. However, it is unclear to what extent are the findings in this study are specific to peripheral nerves. Like the blood brain barrier (BBB), the spinal cord is generally protected from immune attack by the BSCB, which can become dysfunctional in autoimmune conditions like MS[173]. However, we note inflammatory infiltrates directly within the spinal cord that resulted in the irreversible destruction of spinal motor neurons, leading to a permanent unilateral paralysis in the optogenetic treated rats. If we were to inject the virus directly into the spinal cord, would we still identify the same immunogenicity? Given that hSyn properly restricts ChR2 expression to neural tissue and that spinal cord ventral motor neurons project out into the peripheral nervous system, we postulate that immunogenicity is more a function of dosage and cell type than injection location. Using components of the immune panel we developed specifically to screen for optogenetic immunogenicity in this study, we encourage researchers to evaluate presence of serum anti-ChR2 antibodies in response to optogenetic transduction directly within the brain and retina to determine whether our results are truly peripheral nerve specific.

Future work should focus on mitigating the immune attack by designing opsins to evade immune recognition. One strategy to approach this may be first to identify peptide fragments that are most immunogenic and then alter these regions checking for immunogenicity. Other strategies could focus on the host, identifying if there is a causative

link between anemia and optogenetic immunogenicity and employing hematological strategies to evade immune recognition. While this study represents an important discovery in optogenetics and neuroimmunology, it is also a humbling one – it underscores the importance of exhaustive academic safety and validation testing of new technologies prior to their clinical and commercial implementations.

# APPENDIX 3: SUPPLEMENTAL FIGURES FOR CHAPTER 6

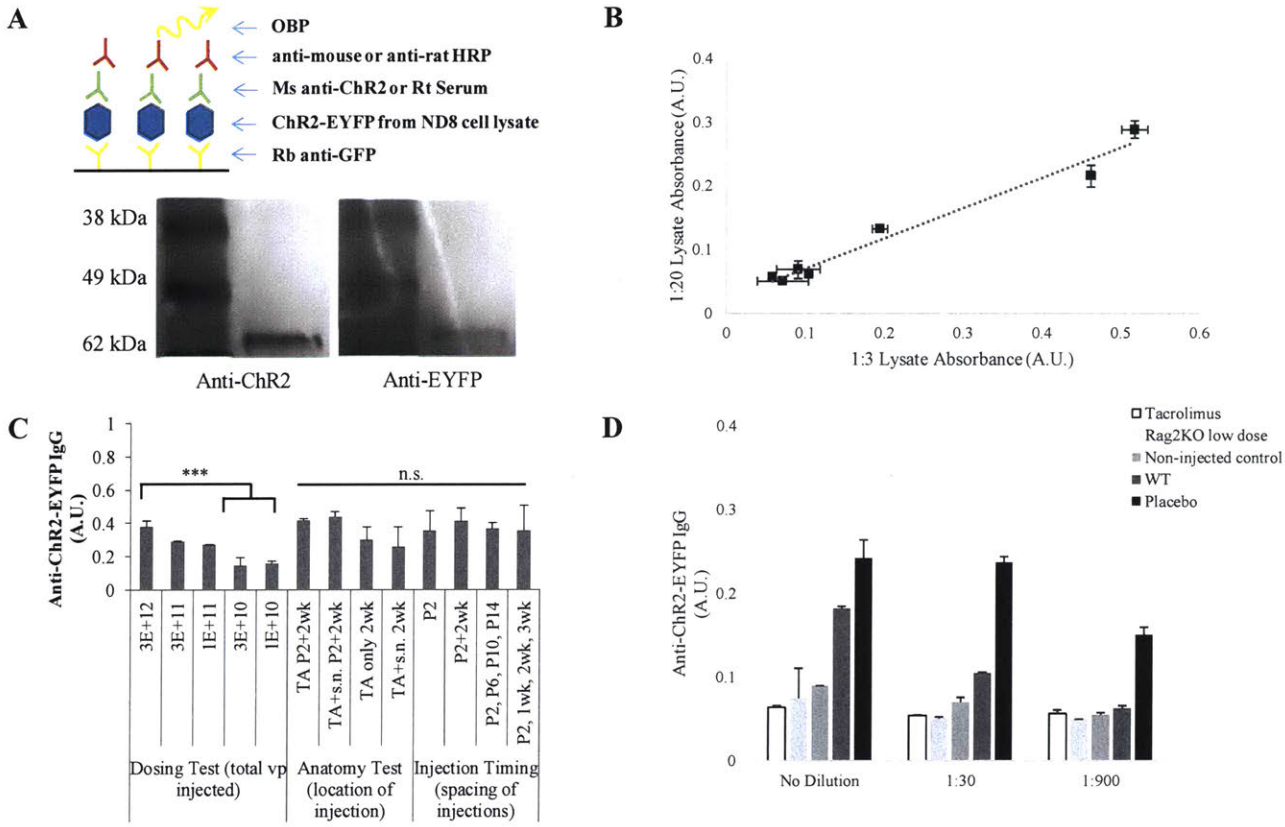


**Figure 6.7: Sandwich ELISA for detection of anti-ChR2-EYFP plasma antibodies**

*(A) Sandwich ELISA plan for detection of plasma antibodies to ChR2-EYFP. (B) Lysate dilution validation test for the ELISA protocol. There is a linear relationship between absorbance measured with lysate diluted 1:3 in PBS and lysate diluted 1:20 in PBS (R2 = 0.97). This result was used to scale all ELISA measurements to the expected value at 1:3 lysate dilution. (C) Terminal ELISA results for the dosage, anatomy, and timing rats showing a significant difference in anti-ChR2-EYFP antibody production between the E12 and E10 AAV dosage groups (P = 7E-4). No significant difference within the anatomy and timing groups by One-Factor ANOVA (P = .34). (D) Serum dilution validation test for the ELISA protocol. Serums were tested at no dilution, 1:30 dilution in PBS, and 1:900 dilution in PBS (n=2). The greatest sensitivity to distinguish between different serum samples was at no dilution.*

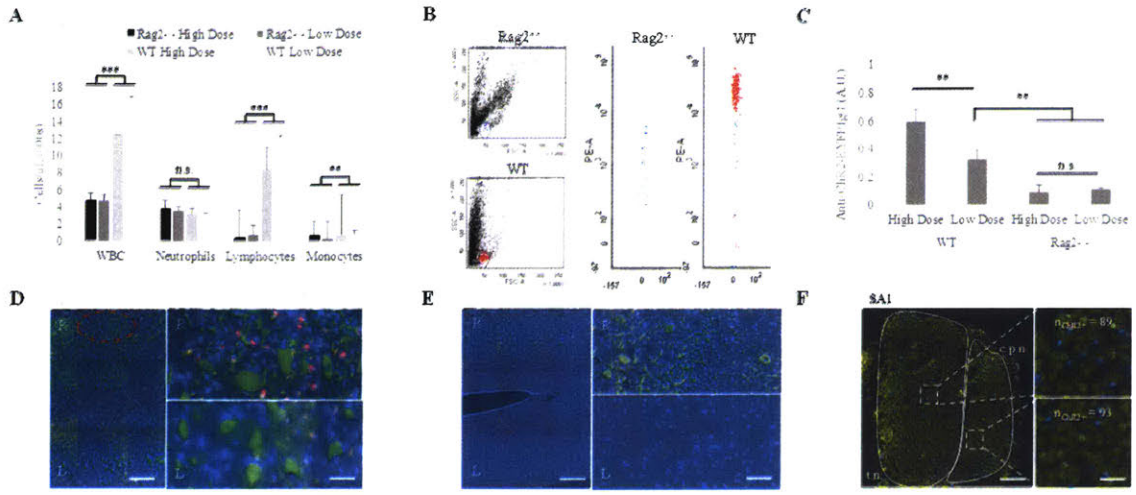


**Figure 6.8: Immune response is specific to WT rats**

*(A) White blood count (WBC) results for Rag2$^{-/-}$ and WT rats at low and high AAV6 injection doses 6 weeks post-injection with auto-differential ($n_{Rag2\text{-}/\text{-}\ High\ Dose}$ = 3, $n_{Rag2\text{-}/\text{-}\ Low\ Dose}$ = 4, $n_{WT\ High\ Dose}$ = 5, $n_{WT\ Low\ Dose}$ = 2). $P_{WBC}$ = 2E-4, $P_{Neutrophils}$ = 0.2, $P_{Lymphocytes}$ = 2E-4, $P_{Monocytes}$ = 8E-2. (B) Flow cytometry for CD3-Phycoerythrin (PE-A) from K3EDTA-treated whole blood samples comparing Rag2$^{-/-}$ and WT rat lymphocytes. Lymphocytes distinguished from whole blood by Forward Scatter (FSC) and Side Scatter (SSC) profiles shown. (C) Normalized ELISA comparing plasma antibodies against ChR2(H134R)-EYFP for Rag2KO (n=5 each) and WT (n=4 each) rats at high vp dose (1.5E12 vp) and low vp dose (1.5E11 vp) at 12 weeks post injection ($P_{left}$ = .003, $P_{right}$ = .003). The one WT high-dose animal which still expressed transdermal at 12 weeks was excluded. (D) Coronal spinal cord section from WT rat stained for nuclei (DAPI, blue), neurons (green), and CD8 (red). Red oval circles neuron-poor region containing many CD8+ cells (right): Scale bar (left) = 500 μm. Scale bar (right) = 70 μm. (E) Coronal spinal cord section from Rag2$^{-/-}$ rat stained for nuclei (DAPI, blue), ChR2-EYFP (green), and CD8 (red). Scale bar (left) = 500 μm. Scale bar (right) = 100 μm. (F) Nerve cross-section from WT rat #1 which maintained expression along with ChR2+ axon counts in tibial nerve (t.n.) division and common peroneal nerve (c.p.n.): Scale bar (left) = 120 μm. Scale bar (right) = 20 μm.*

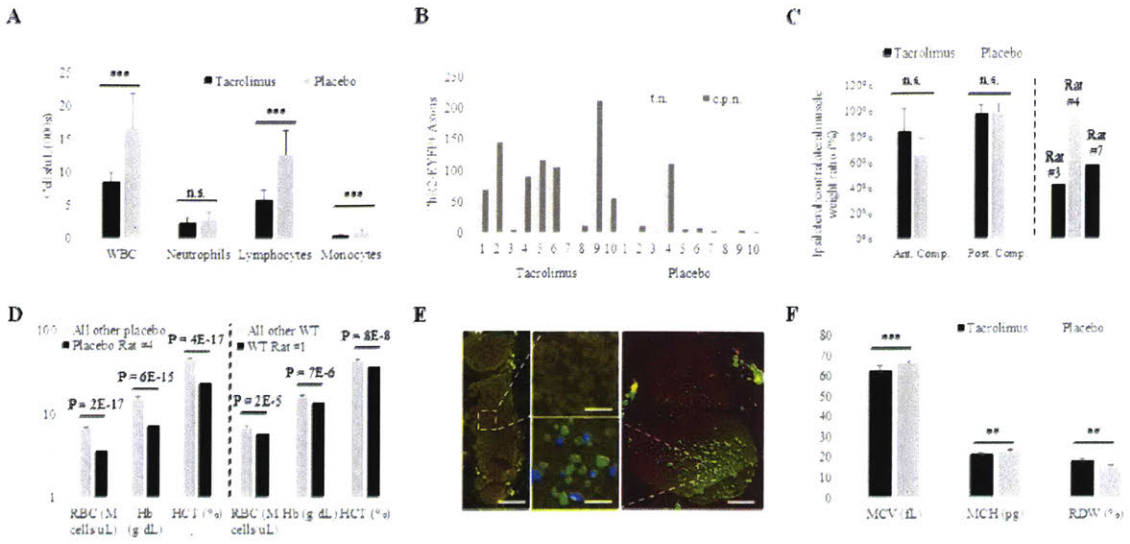


**Figure 6.9: Immune response largely specific to placebo rats**

*(A) White blood count (WBC) results for Tacrolimus and Placebo rats at 6 weeks post-injection with auto-differential ($n_{Tacrolimus}$ = 10, $n_{Placebo}$ = 10). $P_{WBC}$ = 7E-4, $P_{Neutrophils}$ = 0.2, $P_{Lymphocytes}$ = 1E-4, $P_{Monocytes}$ = 2E-4. (B) Complete counts of ChR2+ axons in tibial nerve (t.n.) and peroneal nerve (c.p.n.) for tacrolimus and placebo groups. (C) Ipsilateral to contralateral side of injection muscle weight ratio at the time of euthanasia between tacrolimus and placebo treated rats for both AC and PC muscle groups (n=10 per group). P = .09 for Ant. Comp. and P = .37 for Post. Comp. The AC ratio for individual rats #3 and #7 in the tacrolimus group, which had lost expression at week 12, and individual rat #4 in the placebo group, which maintained expression at week 12, are shown separately as well as included in the totals. (D) Red Blood Cell (RBC), hemoglobin (Hb), and hematocrit (HCT) counts for both placebo and wild-type (WT) rats along with outliers, which maintained long-term expression shown separately. (E) Immunofluorescence from outlier tacrolimus rat #3 (left) and placebo rat #4 (right) with zoom-in sections for each. Scale bar = 200 μm (left, right). Scale bar = 20 μm (center). (F) Mean Corpuscular Volume (MCV), Mean Corpuscular Hemoglobin (MCH), and Red Blood Cell Distribution Width (RDW) for tacrolimus and placebo treated animals suggesting tacrolimus-induced iron deficiency anemia (low MCV and high RDW). $P_{MCV}$ = 9E-4, $P_{MCH}$ = 4E-3, $P_{RDW}$ = 1E-3.*

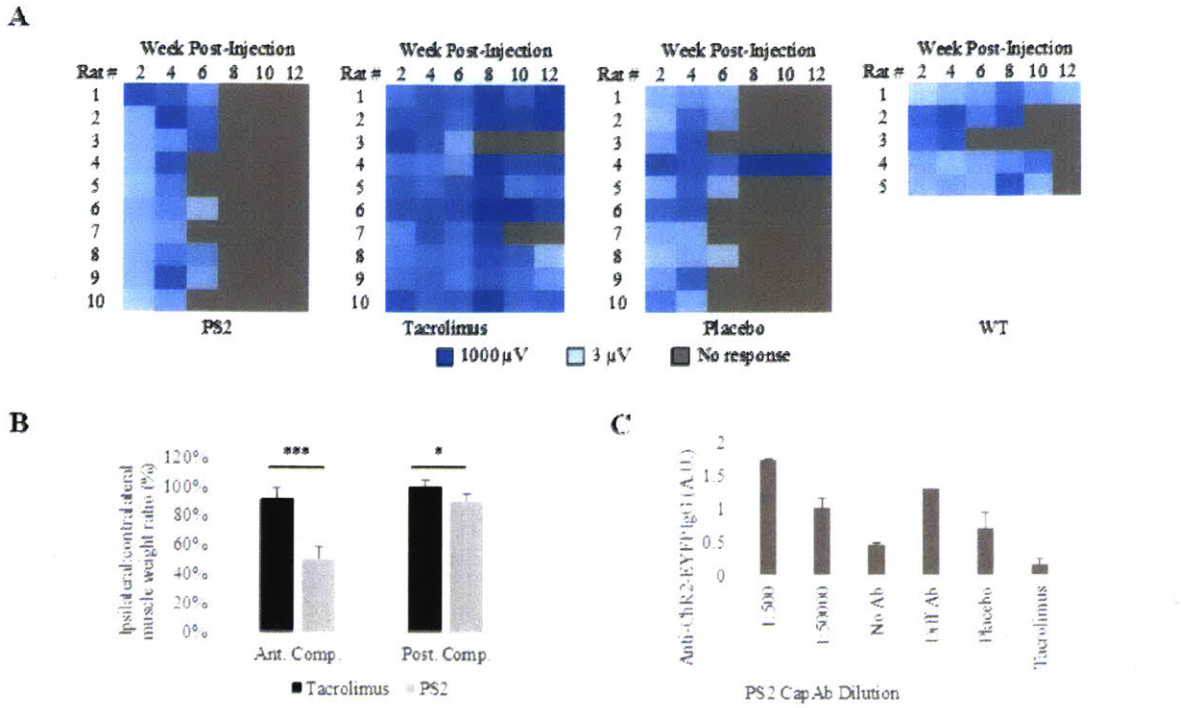


**Figure 6.10: PS2 did not prevent anti-ChR2 immune response**

*(A) Logarithmic $V_{RMS}$ amplitude of TA motor activity in response to 473 nm, 105 mW/mm$^2$ transdermal illumination of the proximal tibia for 4 s at 5 Hz and 10 ms PW for rats treated with PS2, tacrolimus, placebo, and nothing (WT). (B) Ipsilateral to contralateral side of injection muscle weight ratio at the time of euthanasia between PS2 and Tacrolimus rats for both the anterior and posterior compartment muscle groups ($n_{PS2}$=10, $n_{Tacrolimus}$=8). Tacrolimus rats #3 and #7 (which had lost expression at time of euthanasia) were excluded. $P_{AntComp.}$ = 4E-7 and $P_{PostComp}$ = .02. (C) Normalized ELISA showing development of neutralizing rat anti-antibody antibodies in PS2 population. Plasma antibodies against for PS2 rat treated with unique concentrations of capture antibody as well as same rat with a Rb anti-GAP43 antibody without any lysate (Diff Ab) along with placebo and tacrolimus are shown for comparison. Signal is much higher for PS2 rats in absence of lysate compared to placebo and tacrolimus rats indicating non-specific binding of rat antibodies to any capture antibody on the ELISA plate.*

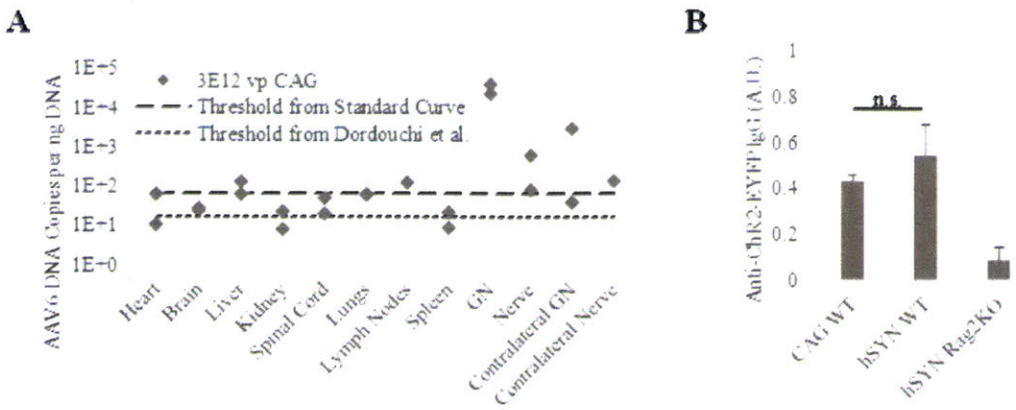


**Figure 6.11: Biodistribution and ELISA for CAG promoter**

*(A) Biodistribution results for 3E12 vp AAV6-CAG-ChR2-EYFP injected rats. Nerve = s.n. (n = 2). (B) Normalized ELISA comparing plasma antibodies against ChR2(H134R)-EYFP for transduction using CAG promoter and hSyn promoter 12 weeks post injection (n = 2 for CAG WT, n = 5 for hSyn WT, n = 5 for hSyn Rag2$^{-/-}$).*

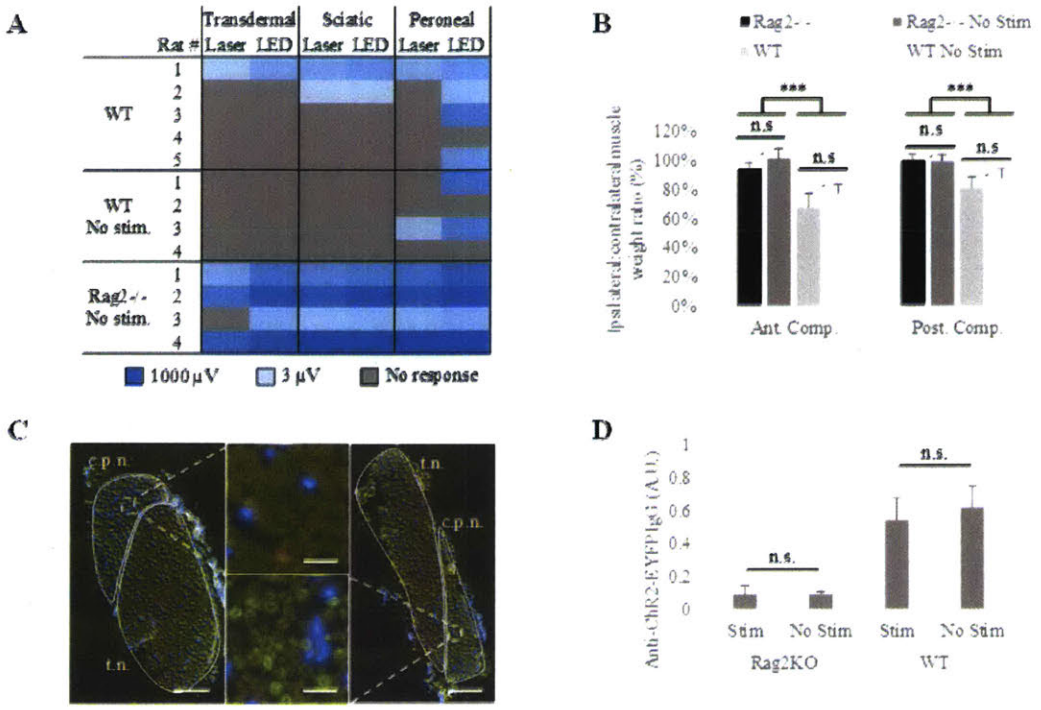


**Figure 6.12: Excitotoxicity controls reveal no difference from rats with regular stimulation**

*(A) Logarithmic $V_{RMS}$ amplitude of TA motor activity in response to 473 nm, 310 mW laser and 600 mW LED illumination of the proximal tibia (transdermal), the surgically exposed sciatic nerve (sciatic) and the surgically exposed peroneal nerve (peroneal) during terminal procedures. Illumination comprised 4 s at 5 Hz and 10 ms PW for both light sources. WT animals have been illuminated transdermal every 2 weeks from injection, whereas WT and Rag2$^{-/-}$ no stim are being illuminated for the first time during terminal procedures. (B) Ipsilateral to contralateral side of injection muscle weight ratio at the time of euthanasia between Rag2$^{-/-}$ (n = 5), Rag2$^{-/-}$ no stim (n = 4), WT (n = 5), and WT no stim (n = 4) rats for both anterior (A.C.) and posterior (P.C.) compartment muscle groups. $P_{Rag2A.C.}$ = .14, $P_{WTA.C.}$ = .10, $P_{Rag2P.C.}$ = .30, $P_{WTP.C.}$ = .21, $P_{Rag2WTA.C.}$ = 8E-6, $P_{Rag2WTP.C.}$ = 2E-4. (C) Sciatic nerve from WT (left) and Rag2$^{-/-}$ (right) no stimulation controls showing no ChR2-EYFP+ axons and many ChR2-EYFP+ axons respectively: scale bar = 150 µm and 20 µm. (D) Normalized ELISA comparing plasma antibodies against ChR2(H134R)-EYFP for Rag2$^{-/-}$ and WT animals, with and without transdermal stimulation 12 weeks post*

*injection (Rag2KO: n = 5 for Stim group, n = 3 for No Stim group; WT: n = 5 for Stim group, n = 3 for No Stim Group). Note: WT Animal 3 no stim excluded from ELISA because blood not properly collected.*

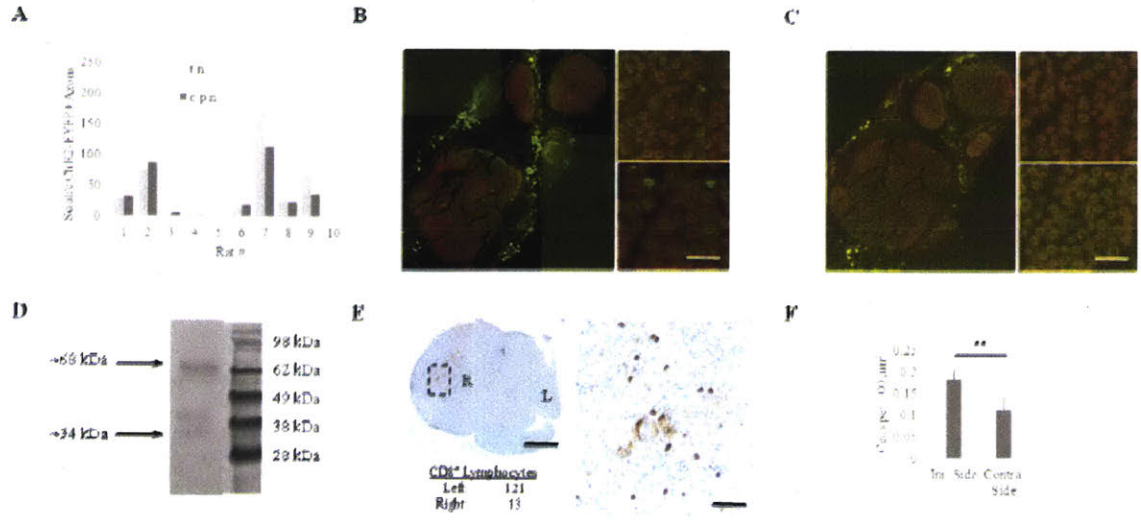


**Figure 6.13 ChR2-only virus still elicits immune response**

*(A) ChR2+ Axons as a percentage of total axons in tibial nerve (t.n.) and peroneal nerve (c.p.n.) for no reporter animals. No reporter rat #7 had maintained transdermal expression at time of euthanasia. (B) No reporter sciatic nerve stained for anti-ChR2 (green) along with c.p.n. (top, right) and t.n. (bottom, right) zoom-in sections: scale bar (left) = 150 μm; scale bar (right) = 15 μm. (C) No reporter sciatic nerve stained for anti-GFP (green) along with c.p.n. (top, right) and t.n. (bottom, right) zoom-in sections: scale bar (left) = 150 μm; scale bar (right) = 15 μm. (D) Western blot showing band for ChR2-only cell lysate. (E) Spinal cord cross-section of rat #2 showing CD8+ lymphocytes (brown) on ipsilateral side of AC injection: scale bar (left) = 1 mm. scale bar (right) = 20 μm. (F) Number of cells per 100 square microns within ventral horn gray matter (n=3) using Student's T test paired samples (P = .005).*

# 7 SCIENTIFIC AND CLINICAL IMPACT

Despite challenges in adaptive immunogenicity, optogenetic peripheral nerve stimulation still retains great potential for future clinical impact. The method is an anatomically targeted, molecularly precise tool that can be employed either to activate or inhibit targeted cellular activity locally or from a distance. Optogenetic peripheral nerve stimulation can largely be employed wherever an electrical peripheral nerve stimulator has been applied. These include treatments for chronic pain, bladder dysfunction, bowel dysfunction, depression, epilepsy, paraplegia and many others. Key benefits of optogenetics include that the treatment efficacy may be stronger than electrical stimulation due to activation of all of the targeted nerve fibers as opposed to a local subset, with fewer side effects. For example, VNS has a broad number of common side effects to electrical stimulation including cough, hoarseness, dyspnea, and headache. Severe side effects include paralysis or cardiac arrest. Theoretically, optogenetics can be employed to target a subset of vagal axons, which may have a direct effect on mitigating the depression or epilepsy without affecting axons to the heart, lungs, vocal cords or other organs. However, in order to achieve this clinical end, peripheral nerve optogenetics must overcome some key challenges to adoption.

## 7.1 Clinical optogenetic challenges

Other works have broadly described some of the key challenges to clinical adoption of optogenetic technologies in the peripheral nerve[138]. This thesis focuses on what we believe to be the most significant challenges for optogenetic peripheral nerve stimulation. These challenges listed in order include: the immune response to the opsin itself, the high dosages required for low levels of retrograde expression, and the difficulty in designing molecularly specific promoters for targeted expression. We believe that solving these challenges will enable the widespread adoption of optogenetics for clinical applications within the PNS. Briefly, we outline a set of strategies for addressing these challenges in future work.

### 7.1.1 Addressing immune challenges

We discover in this thesis that a key impediment to clinical application of optogenetic technologies is an adaptive immune response targeted directly at the opsin transgene. We conclude that ChR2-specific transduction in ventral horn motor neurons is eliciting an immune response. We also report evidence that other favourable opsins such as ReaChR, CoChR, CsChrimson, and JAWS are also likely undergoing immune-mediated neuronal destruction. We note that there is a variation in muscle atrophy among the opsin groups, indicating one of two findings: (1) some opsins may be naturally more immunogenic or (2) some opsins express better than others, and expression levels differentially affect the strength of the immune response. We know that viral dosage directly translates to the strength of the immune response because it directly correlates to the concentration of anti-ChR2 plasma antibody levels as measured by sandwich ELISA. Further, we know that expression is dependent on more than just the viral dosage, because ChrimsonR does not express in peripheral nerves despite having the same viral titer as CsChrimson. Therefore, there is transcription and translation variability for opsin expression, which affects the strength of the immune response. However, it is interesting to note that opsin engineering and site-directed mutagenesis, employed to endow favorable expression, wavelength, and kinetic properties, also are associated with greater muscle atrophy, a measure of immune responses.

There are two broad categories of strategies for evading the immune response. The first strategy for evading the immune response involves manipulation of the immune system itself. This comprises pharmacological interventions including immunosuppressive or haematological strategies such as targeted blockade of neutralizing antibodies. Within this thesis, we only test two specific types of immunosuppression: PS2, which did not prevent neuronal death, and tacrolimus, which did prevent neuronal death. It would be interesting to identify whether immunosuppression would be required long-term to maintain expression or whether immunosuppression only is needed at the early phases of transduction. It is possible that hSyn is mildly leaky so that certain leukocytes or dendritic cells express high levels of ChR2. These ChR2-expressing immune cells may exacerbate the strength of the immune response such that CTLs and activated macrophages break the BSCB and drive VH neuron death. If this were the case, transient immunosuppression may only be necessary to outlast the lifespan for these AAV-transduced leukocytes or dendritic cells. Evidence against this potential mechanism is the lack of ChR2 DNA in the ipsilateral lymph node in the biodistribution study. However, only the axillary lymph node was analysed in the biodistribution – the inguinal lymph node, the chief lymphatic drainage location for the lower limb, may have had higher levels of ChR2 DNA expression. Further, the amount of ChR2 DNA required to activate an immune response within a lymph node may be well below detection threshold in the biodistribution. Significant future study would be required to optimize the pharmaceutical, timing, and strength of immunosuppression for long-term optogenetic nerve fiber transduction.

The second strategy for evading the immune response involves "humanization" of the opsin to confer domains that are less susceptible to immune attack. One method of accomplishing this could be via the use of peptide pools as antigens within an ELISPOT or immunoprecipitation to identify the most immunogenic epitopes of the ChR2 protein. After identifying the problem epitopes, one could explore three unique strategies to design optimal opsins: (1) site-directed mutagenesis at these epitopes, (2) replacement of the epitope with a less-immunogenic epitope from another sequence-aligned algal opsin, or (3) replacement of the epitope with a sequence aligned epitope from a mammalian or human opsin. A preliminary sequence alignment using BLAST did not reveal significant overlap

between ChR2(H134R) and a few common human opsins such as OPN1SW and OPN5. However, there may be opsins to draw sequences from in other species that may have less immunogenicity within the human spinal cord as well as greater levels of sequence alignment.

In addition to immunosuppression, we learned from the outliers within the dosage, timing, & anatomy, WT and placebo groups that certain rats have significantly prolonged optogenetic expression. These three rats all had expression lasting at least 12 weeks, and one rat still expressed transdermal 72 weeks following injection. These rats are all within treatment groups that have lost expression, so it difficult to make definitive conclusions regarding maintenance of expression. However, one interesting potential mechanism underlying the continued expression is related to the significant anemia that two of these rats had at 6 weeks of age. Perhaps there is some other lurking variable that is resulting in both anemia and optogenetic longevity. One interesting future study would be to impose anemia in a subset of rats via regular bleeding while monitoring optogenetic expression levels. If expression levels over time are significantly improved, anemia can be determined as the cause of prolonged expression. Future work should focus on better understanding potential mechanisms behind the relationship between anemia and AAV mediated gene therapies. It is possible that this relationship may have profound implications even beyond peripheral nerve optogenetic gene therapy.

### 7.1.2 Addressing expression challenges

In addition to immune challenges, both viral leakage and low expression levels may remain a key challenge in the implementation of optogenetic technologies. In our work, we discover that injection of AAV within neonatal rats significantly increases the expression levels of opsin compared to adult rats. This phenomenon is likely due to synaptic pruning or axonal dieback from poly-innervated myocytes during the first two weeks of murine development, which increases the probability of successful retrograde transduction. For clinical applications of optogenetics, transduction in the adult is of key importance. For IM injections, synaptic pruning may confer a large difference between the adult and neonate. However, for intradermal or intra-nerve injections, synaptic pruning may not confer

significant benefits to the neonate, outside of that associated with the higher vp/kg dosage in neonates. One challenge with administration of even greater AAV titers is that they may introduce a large anti-AAV specific antibody response, which is not something we discovered specifically here in this work.

To our knowledge, we are using the highest concentration of viral vector as well as largest volumes of delivery of any study to this point in the peripheral nerve. We do this to promote the highest possible levels of opsin expression. Even considering these manipulations, $Rag2^{-/-}$ c.p.n. expression totaled, at most, ~150 axons with the hSyn promoter. Considering there are roughly 600 motor axons in the c.p.n.[56], and even if we liberally assume that transduction was limited to only c.p.n. motor axons as opposed to the ~1,300 myelinated afferents, the hSyn expression efficiency is, at most, 25% of axons. Further, within these 150 axons, there is significant variability between very highly expressing axons and very poorly expressing axons, which has a strong effect on the optogenetic recruitment order. The low efficiency represents a key challenge for the high expressions required in clinical implementations for motor control, cutaneous feedback or pain inhibition.

Several strategies may be employed to further increase transduction efficiency. Recent work has discovered that engineering of the AAV capsid can increase its ability to cross the BBB and BSCB from intravenous delivery[78]. Although these researchers employed manipulations on the capsid surface of AAV8, similar manipulations could be engineered for AAV6, which can assist in both retrograde trafficking as well as spinal cord expression. Another strategy may be promoter based. We notice that the CAG promoter resulted in higher transduction as measured by s.n. cross-sections. The c.p.n. of the CAG animals contained ~270 transduced axons, almost double the highest expressing hSyn c.p.n. While the promoter itself is unlikely to affect the number of DNA copies within target neurons, it is likely to affect the transcription and translation efficiency. This means there are likely some neurons, which have hSyn-ChR2 DNA at low MOIs that do not directly translate to axonal expression. The same neurons at the same MOI with CAG as the promoter would

produce sufficient opsin to be optogenetically excitable. A third strategy to promote expression involves further modulation of the dosage and location of the injection. Previous research has focused on the nerve-muscle end plate, which theoretically would encompass a greater density of myocytes[23]. We found that injecting the muscle directly compared to the muscle and nerve at 2 weeks resulted in slightly weaker EMG recordings, corresponding to fewer transduced axons. Other groups have reported the use of a needle that can be electrically stimulated for delivering AAV, such that the nerve-muscle end plate can be better identified during the injection procedure. Future study varying the injection location within the muscle will likely reveal significant insights into the improving the expression yield.

Lastly, AAV is not quite a passive protein. In targeting the anterior and posterior compartments with two different opsins, we identify some non-targeted CsChrimson+ axons in the t.n. and ChR2+ axons in the c.p.n. This is due to viral spread. When compared to the dye localization tests, viral spread appears to contribute more significantly to anatomical leakage in non-target tissues. Unlike the dye, which remains co-localized to the specific compartment of injection, the AAV can move quasi-lifelike through tissue, seeking to infect new host locations. As a result, non-target transfection can be a significant challenge. Serotype optimization and capsid engineering can help limit AAV spread, but future technologies, perhaps using viscous gels or nanomaterials to help contain AAV to specific injection locations may help prevent off-target effects.

### 7.1.3 Specificity challenges

Employing new promoters to specify molecular subsets of neurons can be tricky at best. It is one thing to use tools like RNAseq to identify molecular expression differences of subsets of neurons. However, there is a disconnect between understanding protein expression differences between neuronal subsets and tediously identifying the enhancers that contribute to the differential in protein expression. Further, employing those enhancers appropriately in episomal AAV constructs to drive selective expression can require further optimization. Several neuron-subtype specific enhancers are commonly used within the nervous system, and new enhancers are continuously being discovered. Three interesting

avenues of exploration within the somatic PNS include enhancers localized to a few proteins of key interest. The first is choline acetyl transferase (CHAT), a marker of motor neurons, which would drive selective efferent expression via an SV40 promoter. A second includes enhancers localized to the Piezo2 protein, which has been identified as a marker of cutaneous touch[174] and proprioception[175] for prosthetic feedback applications. Lastly, an enhancer localized to the Npy2r gene would be of significant value to the inhibition of chronic pain in nociceptors. Similar protein subsets exist for autonomic nerves and enhancer identification for these proteins can help drive selective virally mediated optogenetic expression within a nerve of interest.

Further molecular specificity can be employed via a gene circuit that requires two unique enhancers to be simultaneously activated to drive transcription. For example, the hSyn enhancer can be combined with an enhancer for Npy2r to verify that transcription only occurs in neurons and specifically those that are responsible for nociception. Without hSyn, transcription of the Npy2r gene is known to be active in other cell types, such as cardiac myocytes, which may result in unexpected off-target effects. It is critical that these complex mammalian gene circuits for conferring cell-type specificity are explored prior to the successful implementation of human peripheral nerve transduction, as they are the key to limit off-target effects. In an attempt to control motor tissue, for example, inadvertent activation of an individual's nociceptive fibers would be devastating. Conversely, inadvertent muscle paralysis during optogenetic pain inhibition may have significant consequences. Further study into peripheral nerve specific enhancers is critical.

## 7.2 Key advantages of FOS by Application

Assuming the above challenges have been appropriately addressed, there are several system-specific advantages of FOS for translatable applications. Within each biological system of interest, there are unique benefits of FOS over conventional electrical stimulation. Key applications discussed in detail here include VNS for epilepsy or depression, median or ulnar nerve stimulation for fine motor control of the hand, and c.p.n. stimulation for post-stroke foot drop. However, other applications are also presented including erectile dysfunction, gastrointestinal disorders, and chronic pain mitigation at the

level of the nerve trunk. Each of these FOS implementations can be employed in a closed-loop manner that uses a combination of sensor data to modulate the intensity or frequency of illumination. We describe several of these biological systems below as well as how FOS may be successfully employed in these systems.

### 7.2.1 Non-Stroke Paralysis:

FOS has been postulated as a strategy to stimulate muscle tissue targets because it can provide a natural order recruitment of muscle fibers. Current limitations of functional electrical stimulation (FES), used to restore muscle function to paralysis victims[14], include an early onset of muscle fatigue, because fast-fatiguing fibers are preferentially recruited by current-controlled electrical stimulation. Optogenetic control of muscle tissue has been shown to reduce this effect by recruiting fatigue-resistant fibers predominately[20]. These fibers also tend to be responsible for more fine motor control. Applications include, but are not limited to, the treatment of spinal cord injury, post-polio syndrome, ALS, or other type of CNS-mediated loss of motor function.

### 7.2.2 Chronic pain

Although transdermal stimulation of optogenetically active pain fibers has been shown previously[70], identified results have been limited to the cutaneous endings of nociceptive fibers in the skin. The aforementioned transdermal results indicate that it is possible to activate fibers at the nerve trunk level, which may have advantages, such as a broader anatomic area of neural inhibition. Applications include chronic pain from the spinal cord nerves, cranial nerves (such as trigeminal neuralgia), or other etiologies.

### 7.2.3 Neuroprostheses

Intra-nerve injections of high-concentration AAV into nerve stumps could produce optogenetically active nerve fibers; use of specific molecular promoters such as Npy2r, Vglut2, Piezo or others could define subsets of mechanoreceptors that may play a selective role in touch mechanotransduction. By targeting the molecularly defined subpopulations of these nerves such as low threshold mechanoreceptors (LTMRs) one could enable transdermal optogenetic delivery of light in a way that makes touch within the prosthetic

hand feel like touch from their true hand. This would greatly improve the functionality of current prosthetic devices by providing the much needed "sense of touch" feedback to amputees from their electromechanical devices.

### 7.2.4 Stroke

One major complication in stroke victims is foot-drop, a condition characterized by the inability of the patient to dorsiflex during swing phase resulting in the toes dragging along the ground; patients with foot-drop have a decreased quality of life and a higher risk of falls. The condition can occur with direct nerve damage to the brain center responsible for dorsiflexion, at the level of the spinal cord, or with damage to the s.n. or c.p.n. itself. In any of the above cases, the c.p.n., responsible for innervating the foot dorsiflexor muscles, no longer receives cortical input during voluntary gait. FES of the c.p.n. has been shown to assist in both rehabilitative and continuous applications for the foot-drop. As described in Chapter 1, these FES systems all suffer significant drawbacks. Use of transdermal FOS could eliminate fatigue due to the natural order recruitment. In addition, the common peroneal nerve traverses the knee less than 1 cm from the skin surface, placing it in range of potential transdermal FOS systems.

### 7.2.5 Vagus nerve stimulation for depression and epilepsy

VNS is an end-stage therapy for the treatment of depression and epilepsy. It involves placing implanted electrical leads adjacent to the vagus nerve, and routing leads to a device in the subcutaneous chest wall. It is not well understood why VNS helps improve both mood disorders and epilepsy. Side-effects of VNS are many including a chronic cough and difficulty breathing, both of which are related to the vagus nerve's other autonomic functions. Selective stimulation of molecularly unique genetically-defined axonal subsets could help alleviate this side effect by stimulating only the neurons responsible for alleviating the depression or epilepsy.

### 7.2.6 Obesity/diabetes/eating disorders/IBD:

In addition to mood, the vagus nerve is implicated in a variety of diseases as a master regulator of autonomic function. Recent research has identified molecularly-distinct vagus

nerve afferents that are differentially expressed in the gut, lungs, heart, allergy, and stomach[21,22]. Five unique subtypes of vagal nerve afferents have been discovered, which can be identified by specific distinctive molecular markers[21,22]. For example, selective optogenetic stimulation of GPR65-ires-cre mice crossed with lox-ChR2 caused a blockade of gastric contractions and decreased gastric pressure, whereas selective optogenetic stimulation of GLP1R-ires-cre mice crossed with lox-ChR2 caused an increase in gastric pressure. As these two subtypes comprised the majority of duodenal afferent vagal fibers, it was desired to assess the effect of opotgenetic stimulation on feeding behavior in an awake, freely moving mouse. Due to anatomical size and geometry limitations associated with the vagus nerve, it has yet proven to be impossible to fit an optical cuff around the vagus nerve without compromising the nerve health. As a result, a technique that can increase the nerve depth of optogenetic PNS could enable transdermal stimulation of the vagus nerve to study feeding behavior in these cre-dependent subtypes. One could imagine this type of research leading to new insights on eating disorders including obesity and diabetes as well as optimal pharmacological interventions to manage faulty neural sensors of gastric stretch and nutrients. It is reasonable to believe that these conditions may be alleviated via optogenetic stimulation of the selective subtypes responsible for afferent feedback, such as the gastric stretch receptors responsible for conveying satiety to the brain to treat obesity.

### 7.2.7 Erectile Dysfunction:

The cavernous nerve, which controls penile motility is commonly damaged during a prostatectomy, a surgical technique used widely to treat prostate cancer. Damage to the cavernous nerve has been linked to erectile dysfunction because the cavernous nerve can trigger arousal in response to neurochemical cues. Optogenetic control of penile erection via smooth muscle has been shown in animal models[84]. However, it has not yet been shown through direct transdermal stimulation of the cavernous nerve. One potential method to achieve this is to inject the retrograde AAV prior to prostate surgery allowing for full nerve expression in case the nerve is cut during the surgery.

## 7.3 Wearable designs for clinical optogenetics

For the above applications, there are several nerves, which run superficial enough to the skin to be appropriately targeted for transdermal peripheral nerve optogenetics. These include the nerves of the forearm, leg, neck, and perineum. Some major nerves, which run ~2 cm or less from the surface of the skin are listed in Table 7.1; also shown are disease applications for the specified target nerve.

**Table 7.1 Nerve targets for clinical transdermal optogenetic peripheral nerve stimulation**

| Nerve | Location | Innervates | Min distance from skin | Disease Application | Technology |
|---|---|---|---|---|---|
| Median N. | Wrist | Hand sensation and intrinsic muscles | 3.2 mm | Paralysis, amputation, pain | LED Wristband |
| Ulnar N. | Wrist | Hand sensation and intrinsic muscles | 2.1 mm | Paralysis, amputation, pain | LED Wristband |
| Radian N. | Elbow | Upper Limb Extensors | ~1 cm | Paralysis, amputation, pain | LED Elbow Brace |
| c.p.n. | Knee | Foot Dorsiflexors | ~1 cm | Paralysis, foot-drop for stroke victims, pain | LED knee brace |
| Cavernosal N. | Perineum | Corpus Spongiosum | ~1 cm | Erectile Dysfunction | LED underwear |
| Vagus N. | Neck | Gut, Stomach, Heart, Lungs, Brain | ~1.7 cm | Obesity, Anorexia, IBD, Diabetes, Depression, Epilepsy | LED patch |
| t.n. | Knee | Foot Plantarflexors and sensation | ~2 cm | Paralysis, amputation, pain | LED knee brace |

### 7.3.1 Generalized Control Architecture for Closed-Loop Transdermal Optogenetic Stimulation

Output physiology (e.g., position, velocity, pain, appetite, etc.) can be modulated in a closed-loop fashion through the transdermal approach. Prior optogenetic closed-loop control strategies have been described for scientific experiments, not for clinical applications[176]. Additionally, these control strategies do not account for transdermal activation of nerve tissue. The general control diagram describes a set of inputs and outputs for control of neural tissue using optogenetics. First, input sensors for measuring desired physiology such as sweat and movement sensors or neural signals, or a button press for

manual control with human emotional state as the closed-loop physiology change, along with wireless transmission capabilities is presented. Second, the input signal is fed into a microcontroller for processing of input sensors within a specific control strategy (some defined above, but others include reflexive, state-based or pattern recognition control) and outputting a desired signal (power, frequency, duty cycle, #LEDs) following mathematical operations of the input signal. Third, a current source is shown which may demultiplex the input signal into individual currents for each light source channel. Fourth, a light source such as a high-powered LED or a DPSS laser which optimally emit light a specific frequency through the skin is depicted. Fifth, the light drives a change in output physiology as described above which can include physical movement, pain relief, appetite changes, mood improvement, sexual arousal, or others. Sixth, a data acquisition capability is presented for measuring the output of the physiology sensors as well as the model and line-output from the microcontroller for further processing or to be saved for model. The specific control architecture can be tailored for the specific application employed.

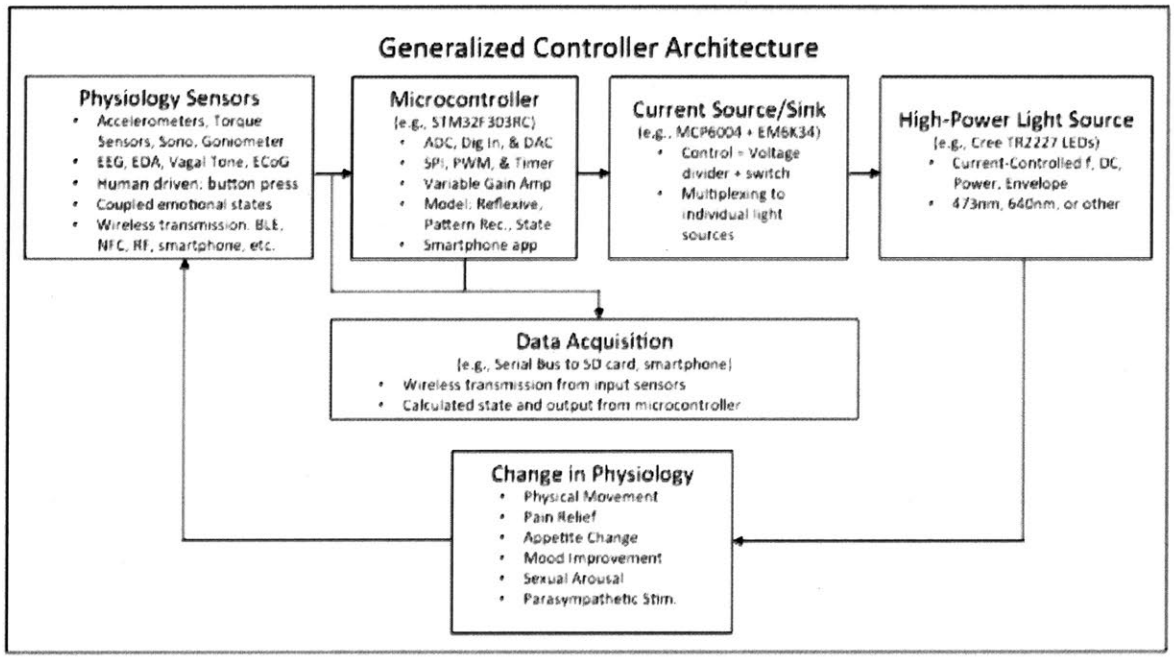


**Figure 7.1 General controller architecture for closed-loop optogenetics**

*The diagram outlines the general architecture for closed-loop feedback within one patient. However, it is possible that patients are coupled to one another, so that the input signal for*

*one patient is driven by an output change in physiology from another patient. These can be linked by several technologies including BLE, NFC, RF. In addition, use of smartphones as the processor and wireless communication device can be employed both for a single individual, and coupling two or more individuals together. In this way, appetite control, for example, can be socially reinforced, so that when one person at a table is satiated, other individuals also begin to feel full. Alternatively, emotional states can be coupled so that when one individual feels compassionate, as measured by certain sensors, that can stimulate empathy in another individual.*

### 7.3.2 Illuminated wristband or patch for optogenetic motor control in the hand

LEDs positioned in proximity to the median and ulnar nerves and a rechargeable battery may be encased in an ergonomic wristband (Fig 7.2). The wavelength can be tailored to the wavelength required for the specific opsin injected. Depending on anatomy and power requirements, the device may or may not have a cooling system comprising a heatsink or fluid system to prevent burns at the surface. Microcontrollers inside the device may control the frequency, power, and duty cycle of the delivered light. Optogenetic stimulation of the median and ulnar nerves at the wrist could provide fine motor control to intrinsic hand muscles including the lumbricals, the flexor pollicis brevis, the abductor pollicis, and others. In addition, targeted stimulation of sensory fibers could provide cutaneous or proprioceptive sensory feedback from touch sensors located on prosthetic fingers or hands. The form of the device could be either a wristband or an adhesive patch. The patch may be affixed to the skin through the use of biocompatible adhesives. The wristband may be mechanically stable around the outside of the wrist.

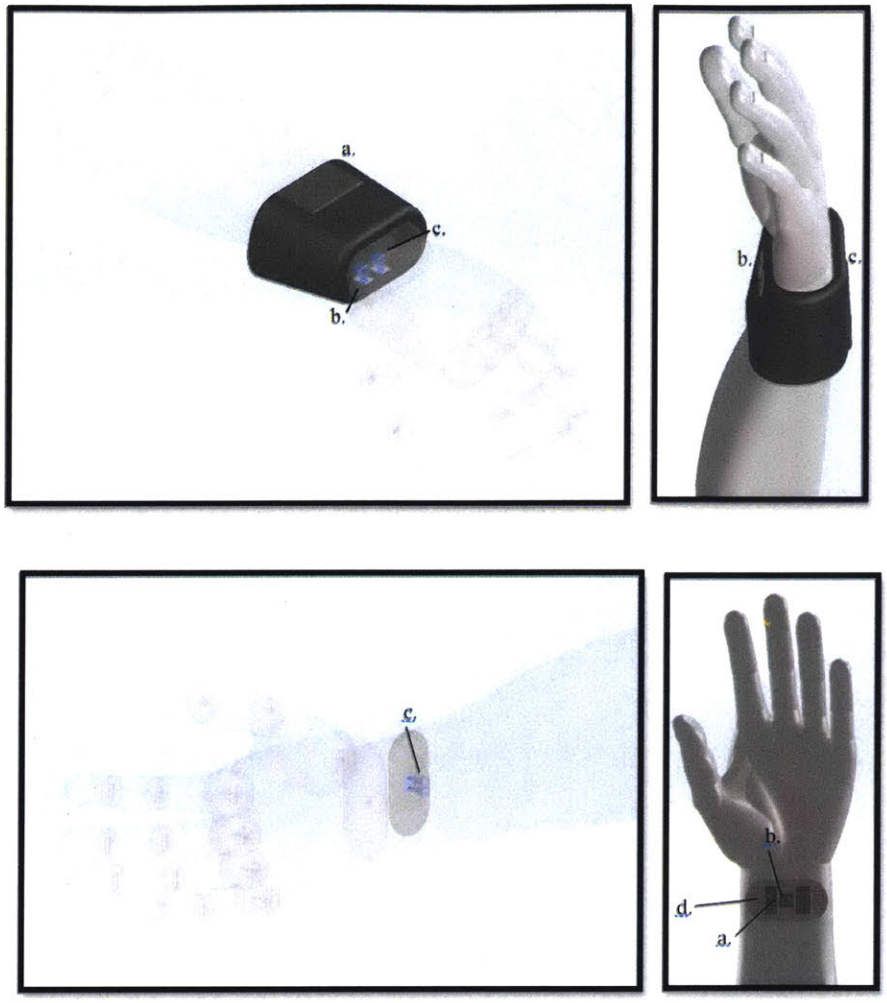


**Figure 7.2: Wearable designs as a wristband (top) or patch (bottom)**

*a. - rechargeable battery and microcontroller | b. – Light source (e.g., LED) casing | c. – transdermal light | d. – adhesive layer*

In a closed-loop fashion, the motor control architecture may take the form shown (Fig 7.3). For the case of hand position control, a change in muscle state, comprising position and velocity, can be used as the input to the microcontroller, which then implements a specific control architecture to drive current to the LEDs and initiate transdermal optogenetic closed-loop contraction.

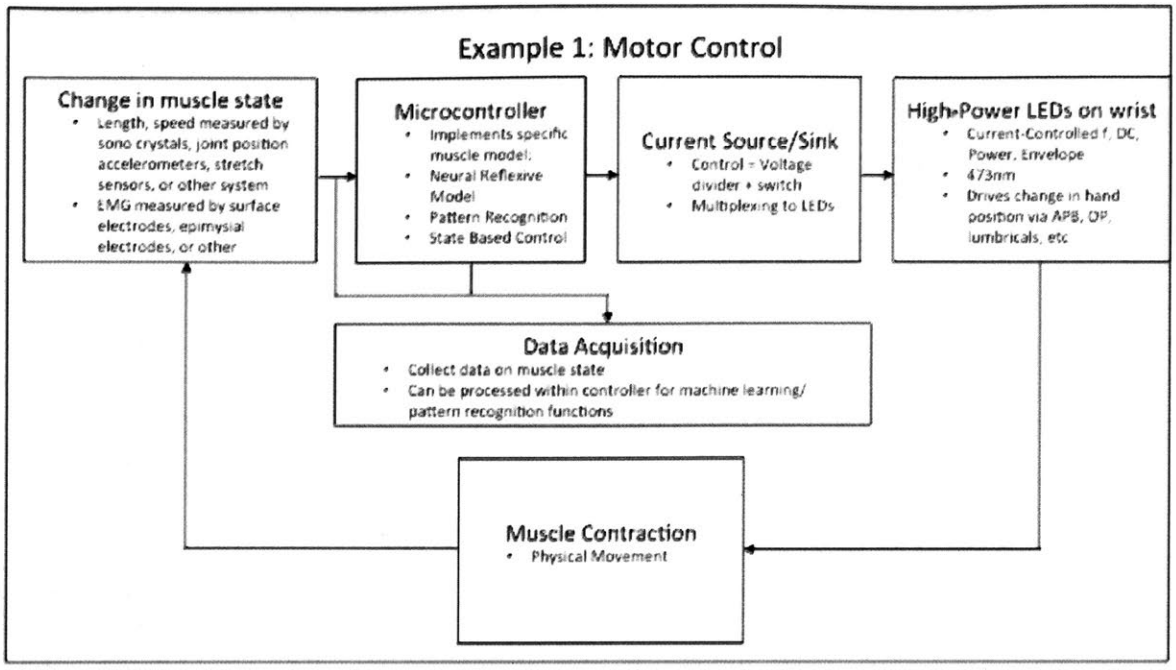


**Figure 7.3 Motor control architecture for position control using optogenetics**

In a specific implementation, the above architecture was implemented for performing closed-loop position control in a murine model to control the ankle joint using optogenetics (Fig 7.4). Muscle state was tracked using a distance sensor on the ankle joint. PI control gains were adjusted as well to the desired rise time and delay of the system. The system developed was called pseudo-SITO because it has a single input, position, which can control two independent outputs, the LED to the t.n. or the LED to the c.p.n. However, the system is designed so that only one LED is on at a given time, based on a 90° cutoff which switches the ankle from plantarflexion to dorsiflexion and vice versa.

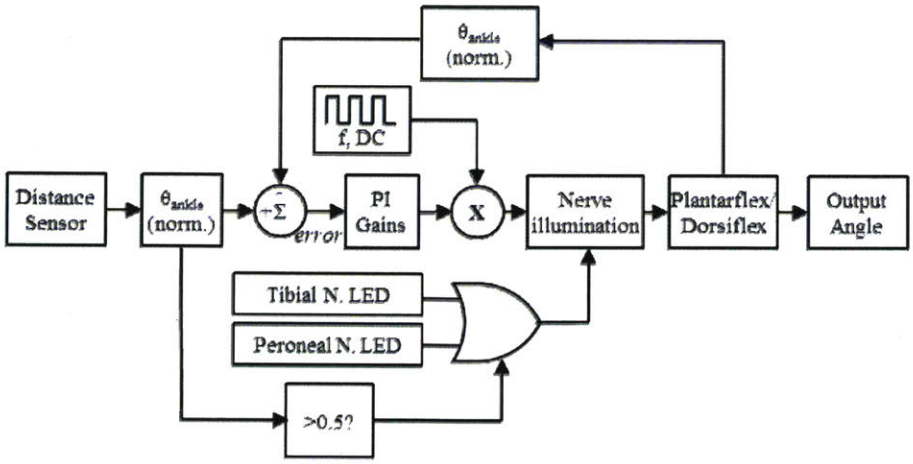


**Figure 7.4: Closed loop position control diagram of murine ankle**

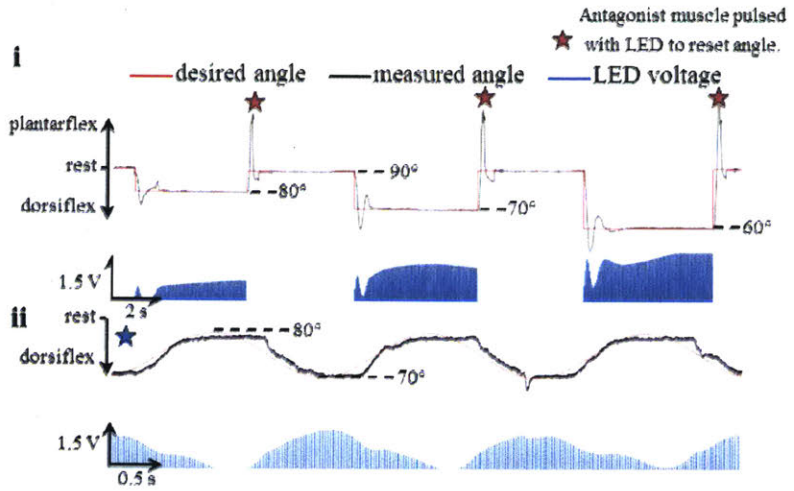


**Figure 7.5: Closed-loop position control of murine ankle**

Using the control structure outlined, closed-loop position control of the ankle can be achieved using optogenetics in real-time (Fig 7.5). In this diagram, the rat foot can achieve any desired ankle within a ~100 ms time frame. The system can be set up to optimize to minimize overshoot, but it comes at the expense of a slower rise time. Because the opsin is time-variant and non-linear, there is an extra position burst following initial stimulation. Further, the opsin requires an increasing illumination intensity to maintain the same position due to opsonal inactivation in the first few seconds. This process eventually reverses as the opsin reaches a steady state (Fig 3.2). In addition to a discrete state, the

position can also track a sinusoidal input, reflective of repetitive biophysical loops, such as the gait cycle (Fig 7.5ii). In this setup, illumination intensity increases to dorsiflex the ankle and decreases to return the angle to rest.

### 7.3.3 Illuminated knee brace or patch for optogenetic treatment of paralysis and foot-drop syndrome

LEDs positioned outside the c.p.n. as well as a rechargeable battery may be fitted to a stretchable knee brace. This allows the device to be secure while not restricting user motion. Although shown blue here, the wavelength can be tailored to the specific opsin injected. Microcontrollers inside the device may control the frequency, power, and duty cycle of the delivered light. Optogenetic stimulation of the c.p.n. could provide motor control via activation of AC dorsiflexors, such as the TA. In foot-drop or paralysis, this technology could allow muscles including the TA, Extensor Digitorum Longus, and others to fire based on sensors in the device that track the leg state including, but not limited to, accelerometers, position sensors, torque sensors, gyroscopes, etc. In addition, unique controller designs could be established for driving the illumination including reflexive controllers, state-based controllers, pattern-recognition controllers, and others. Optogenetic control of the t.n. as well as its innervating muscles is also possible, although the t.n. lies about twice as deep as the peroneal nerve at the knee. These could be used to assist gait by illuminating the opsin+ nerve at the proper time in the gait cycle. The design can take the form of a knee brace or a patch. The knee brace itself may be composed of an elastomer, fabric, silicone, or plastic material, with an exterior designed to remain aesthetically pleasing to the user. The patch may employ biocompatible adhesives such as acrylic or hydrocolloid; there can be a patch for each nerve, or a single patch with LEDs, targeted to each nerve.

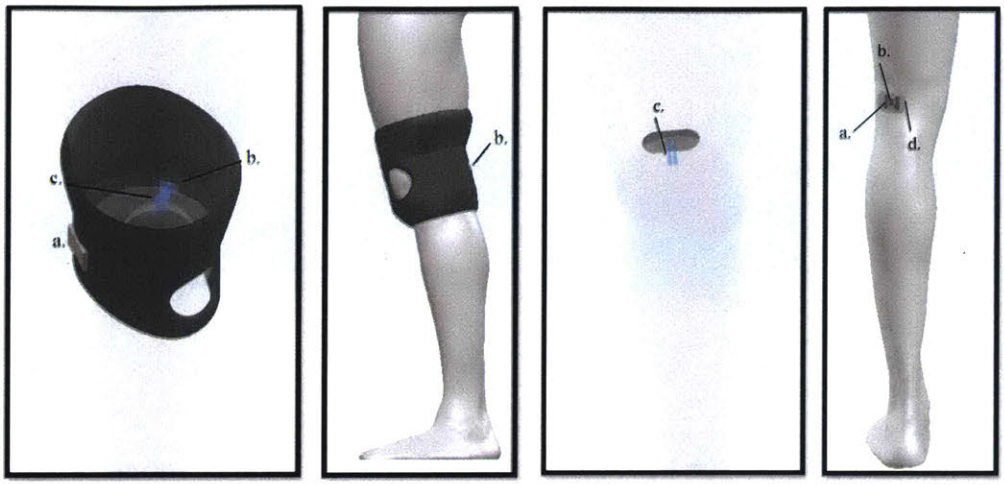


**Figure 7.6 LED knee brace or leg patch for optogenetic correction of foot-drop**

*a. - rechargeable battery and microcontroller | b. – Light source (e.g., LED) casing | c. – transdermal light | d. – adhesive layer*

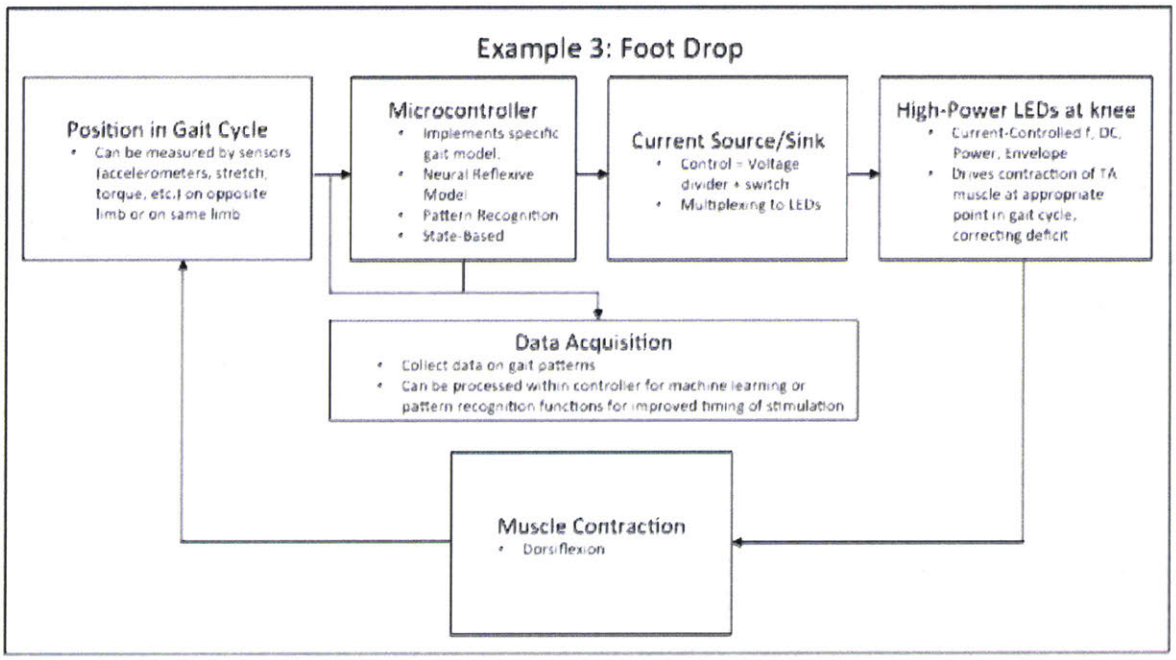


**Figure 7.7: Motor control architecture for foot-drop control using optogenetics**

### 7.3.4 Illuminated patch for optogenetic treatment of vagus nerve

LEDs and a rechargeable battery may be encased within a patch to be worn on the anterolateral surface of the neck (Fig 7.8). The exterior may be designed to remain aesthetically pleasing to the user. This allows the device to be secure while not restricting user motion. As with the other systems, the device may or may not have a cooling system comprising a heatsink or fluid system to prevent burns at the surface. Optogenetic stimulation of the vagus nerve (depicted here) could provide autonomic control and sensation from its fibers in the GI tract, heart, lungs, as well as the treatment of mood and seizures through downstream neurological and endocrine pathways. This technology may be employ ed for the treatment of several disorders defined by optogenetically targeting molecular-specific subtypes in the vagus nerve. Use of a patch design can be employed to customize the treatment to the individual. The body of the patch may be composed of an elastomer, fabric, silicone, or plastic material, with an exterior designed to remain aesthetically pleasing to the user. Closed loop inputs can include a change in diet, satiety, or emotional state (Fig 7.9).

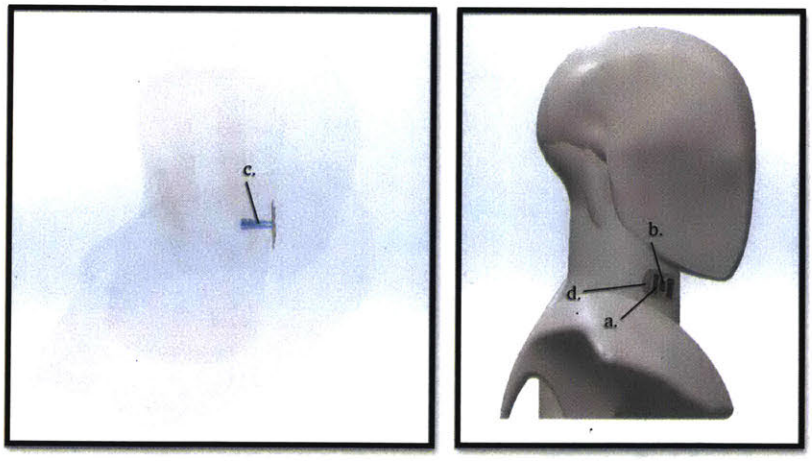


**Figure 7.8 Wearable patch for optogenetic vagus nerve stimulation**

*a. - rechargeable battery and microcontroller | b. – Light source (e.g., LED) casing | c. – transdermal light | d. – adhesive layer*

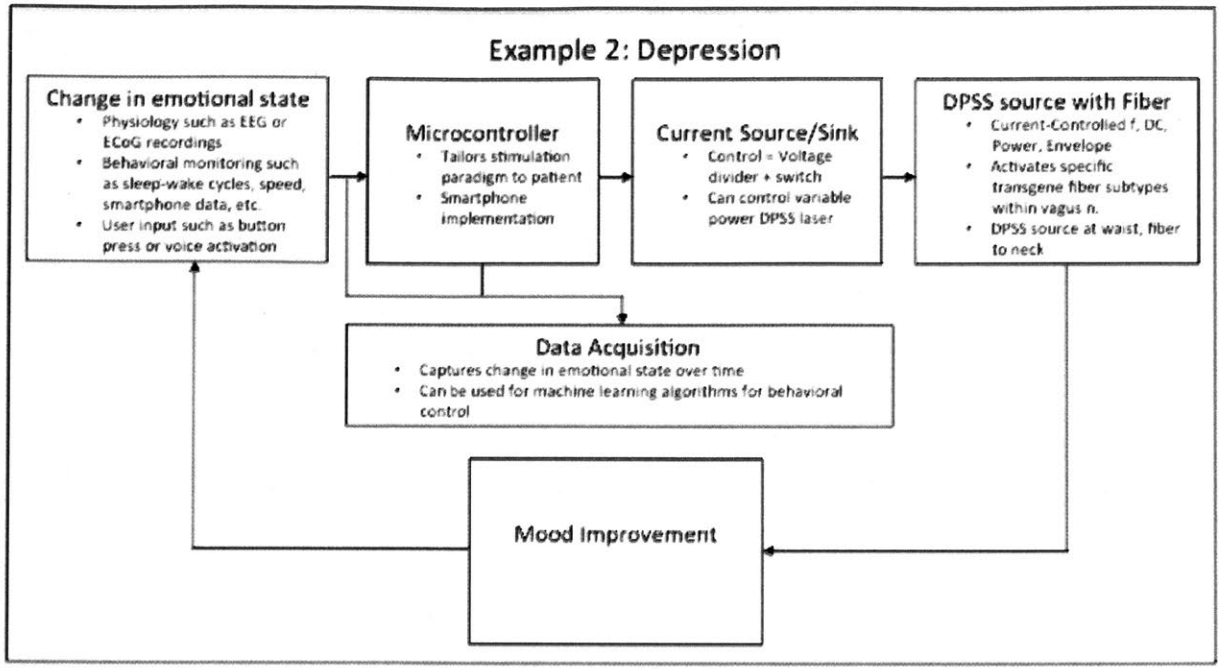


**Figure 7.9: Controller architecture for optogenetic VNS treatment of depression**

## 7.3.5 Conclusion

Potential clinical applications of deep tissue optogenetic peripheral nerve stimulation include new treatments for fine motor control, chronic pain treatment at the level of the nerve trunk, and other conditions outlined above. Inclusion of MC simulation results for the median n. and ulnar n. in the adult human suggests that FOS position control of hand gestures via selective transdermal stimulation at the level of the wrist following IM AAV6 injections in intrinsic hand muscles is a not-too-distant possibility. One could imagine an LED wristband restoring fine motor control for tasks such as handwriting to a paralyzed patient without requiring any implanted hardware. Another example involves optogenetically targeting the vagus nerve, a peripheral cranial nerve implicated in numerous ailments, including epilepsy, migraines, obesity, hypertension, fibromyalgia, Crohn's disease, asthma, depression and obsessive-compulsive disorder. An efficient method of stimulating the vagus nerve with minimal side effects and high target specificity, such as described here, may have profound implications to the study of various illnesses and disabilities. Significant work needs to be done, however, before these future technologies can be considered. For the long-term goal of transdermal optogenetic

peripheral nerve stimulation, the future optimization of immunogenicity, expression, and selectivity are of paramount importance.

# 8 REFERENCES


1. Tan, D. W. *et al.* A neural interface provides long-term stable natural touch perception. *Sci. Transl. Med.* **6,** 257ra138-257ra138 (2014).
2. Navarro, X. *et al.* A critical review of interfaces with the peripheral nervous system for the control of neuroprostheses and hybrid bionic systems. *J. Peripher. Nerv. Syst.* **10,** 229–58 (2005).
3. Bhadra, N. & Kilgore, K. L. High-frequency electrical conduction block of mammalian peripheral motor nerve. *Muscle Nerve* **32,** 782–790 (2005).
4. Deer, T. R., Pope, J. E. & Kaplan, M. A novel method of neurostimulation of the peripheral nervous system: The StimRouter implantable device. *Tech. Reg. Anesth. Pain Manag.* **16,** 113–117 (2012).
5. Strand, N. H., Trentman, T. L., Vargas, B. B. & Dodick, D. W. Occipital nerve stimulation with the Bion® microstimulator for the treatment of medically refractory chronic cluster headache. *Pain Physician* **14,** 435–40
6. Konstantin Slavin. Peripheral Nerve Stimulation. *International Neuromodulation Society* (2012). Available at: http://www.neuromodulation.com/PNS.
7. Birk, D. M., Yin, D. & Slavin, K. V. Regulation of Peripheral Nerve Stimulation Technology. *Prog. Neurol. Surg.* **29,** 225–37 (2015).
8. Heiduschka, P. & Thanos, S. Implantable bioelectric interfaces for lost nerve functions. *Prog. Neurobiol.* **55,** 433–461 (1998).
9. Navarro, X. *et al.* A critical review of interfaces with the peripheral nervous system for the control of neuroprostheses and hybrid bionic systems. *J. Peripher. Nerv. Syst.* **10,** 229–258 (2005).
10. Lefurge, T., Goodall, E., Horch, K., Stensaas, L. & Schoenberg, A. Chronically implanted intrafascicular recording electrodes. *Ann. Biomed. Eng.* **19,** 197–207 (1991).
11. Ceballos, D. *et al.* Morphologic and functional evaluation of peripheral nerve fibers regenerated through polyimide sieve electrodes over long-term implantation. *J. Biomed. Mater. Res.* **60,** 517–528 (2002).

12. Lundborg, G., Gelberman, R. H., Minteer-Convery, M., Lee, Y. F. & Hargens, A. R. Median nerve compression in the carpal tunnel--functional response to experimentally induced controlled pressure. *J. Hand Surg. Am.* **7,** 252–9 (1982).
13. Slavin, K. V. Peripheral nerve stimulation for neuropathic pain. *Neurotherapeutics* **5,** 100–106 (2008).
14. P950035 NeuroControl Freehand System.pdf.
15. Sator-Katzenschlager, S. *et al.* Subcutaneous Target Stimulation (STS) in Chronic Noncancer Pain: A Nationwide Retrospective Study. *Pain Pract.* **10,** 279–286 (2010).
16. Verrills, P., Vivian, D., Mitchell, B. & Barnard, A. Peripheral Nerve Field Stimulation for Chronic Pain: 100 Cases and Review of the Literature. *Pain Med.* **12,** 1395–1405 (2011).
17. Brazzelli, M., Murray, A. & Fraser, C. Efficacy and Safety of Sacral Nerve Stimulation for Urinary Urge Incontinence: A Systematic Review. *J. Urol.* **175,** 835–841 (2006).
18. Karceski, S. & Schacter, S. in *UpToDate* (ed. Ted. W. Post) (UpToDate, 2015).
19. Isakov, E., Mizrahi, J. & Najenson, T. Biomechanical and physiological evaluation of FES-activated paraplegic patients. *J. Rehabil. Res. Dev.* **23,** 9–19 (1986).
20. Llewellyn, M. E., Thompson, K. R., Deisseroth, K. & Delp, S. L. Orderly recruitment of motor units under optical control in vivo. *Nat. Med.* **16,** 1161–1165 (2010).
21. Williams, E. K. *et al.* Sensory Neurons that Detect Stretch and Nutrients in the Digestive System. *Cell* **166,** 209–221 (2016).
22. Chang, R. B., Strochlic, D. E., Williams, E. K., Umans, B. D. & Liberles, S. D. Vagal Sensory Neuron Subtypes that Differentially Control Breathing. *Cell* **161,** 622–33 (2015).
23. Towne, C., Montgomery, K. L., Iyer, S. M., Deisseroth, K. & Delp, S. L. Optogenetic control of targeted peripheral axons in freely moving animals. *PLoS One* **8,** e72691 (2013).
24. Hareendran, S. *et al.* Adeno-associated virus (AAV) vectors in gene therapy: immune challenges and strategies to circumvent them. *Rev. Med. Virol.* **23,** 399–413 (2013).
25. Mingozzi, F. *et al.* Immune responses to AAV vectors: overcoming barriers to successful gene therapy. *Blood* **122,** 23–36 (2013).
26. RetroSense Therapeutics Doses First Patient in Phase I/II Clinical Trial for Lead Compound RST-001 | Business Wire. Available at: http://www.businesswire.com/news/home/20160321005376/en/RetroSense-Therapeutics-Doses-Patient-Phase-III-Clinical.
27. Reardon, S. Light-controlled genes and neurons poised for clinical trials. *Nature* (2016). doi:10.1038/nature.2016.19886
28. GenSight Biologics receives Orphan Drug Designation and Advanced Therapy Medicinal Product classification in Europe for GS030 in Retinitis Pigmentosa | Business Wire. Available at: http://www.businesswire.com/news/home/20160831006523/en/GenSight-Biologics-receives-Orphan-Drug-Designation-Advanced.
29. Ye, H., Daoud-El Baba, M., Peng, R.-W. & Fussenegger, M. A synthetic

optogenetic transcription device enhances blood-glucose homeostasis in mice. *Science* **332,** 1565–1568 (2011).

30. Pasquina, P. F. *et al.* First-in-man demonstration of a fully implanted myoelectric sensors system to control an advanced electromechanical prosthetic hand. *J. Neurosci. Methods* **244,** 85–93 (2015).
31. Össur Introduces First Mind-Controlled Bionic Prosthetic Lower Limbs for Amputees. Available at: http://www.ossur.com/about-ossur/news-from-ossur/1396-ossur-introduces-first-mind-controlled-bionic-prosthetic-lower-limbs-for-amputees. (Accessed: 15th April 2016)
32. Dhillon, G. S., Lawrence, S. M., Hutchinson, D. T. & Horch, K. W. Residual function in peripheral nerve stumps of amputees: implications for neural control of artificial limbs. *J. Hand Surg. Am.* **29,** 605-15–8 (2004).
33. Badia, J., Pascual-Font, A., Vivó, M., Udina, E. & Navarro, X. Topographical distribution of motor fascicles in the sciatic-tibial nerve of the rat. *Muscle Nerve* **42,** 192–201 (2010).
34. Raspopovic, S. *et al.* Restoring Natural Sensory Feedback in Real-Time Bidirectional Hand Prostheses. *Sci. Transl. Med.* **6,** 222ra19-222ra19 (2014).
35. Branner, A. & Normann, R. A. A multielectrode array for intrafascicular recording and stimulation in sciatic nerve of cats. *Brain Res. Bull.* **51,** 293–306 (2000).
36. Musick, K. M., Chew, D. J., Fawcett, J. W. & Lacour, S. P. PDMS microchannel regenerative peripheral nerve interface. in *2013 6th International IEEE/EMBS Conference on Neural Engineering (NER)* 649–652 (2013). doi:10.1109/NER.2013.6696018
37. Lacour, S. P. *et al.* Long micro-channel electrode arrays: a novel type of regenerative peripheral nerve interface. *IEEE Trans. neural Syst. Rehabil. Eng. a Publ. IEEE Eng. Med. Biol. Soc.* **17,** 454–460 (2009).
38. Srinivasan, A., Guo, L. & Bellamkonda, R. V. Regenerative microchannel electrode array for peripheral nerve interfacing. in *2011 5th International IEEE/EMBS Conference on Neural Engineering* 253–256 (IEEE, 2011). doi:10.1109/NER.2011.5910535
39. Lancashire, H. T. *et al.* Microchannel neural interface manufacture by stacking silicone and metal foil laminae. *J. Neural Eng.* **13,** 34001 (2016).
40. Chamberlain, L. J., Yannas, I. V, Hsu, H. P. & Spector, M. Connective tissue response to tubular implants for peripheral nerve regeneration: the role of myofibroblasts. *J. Comp. Neurol.* **417,** 415–30 (2000).
41. Musick, K. M. *et al.* Chronic multichannel neural recordings from soft regenerative microchannel electrodes during gait. *Sci. Rep.* **5,** 14363 (2015).
42. Xiong, L., Chen, P. & Zhou, Q. Adhesion promotion between PDMS and glass by oxygen plasma pre-treatment. *J. Adhes. Sci. Technol.* **28,** 1046–1054 (2014).
43. Wang, C., Cho, S.-J. & Kim, N.-Y. SU-8-Based Structural Material for Microelectronic Processing Applications. *Mater. Manuf. Process.* **6914,** 130709115848005 (2013).
44. Vernekar, V. N. *et al.* SU-8 2000 rendered cytocompatible for neuronal bioMEMS applications. *J. Biomed. Mater. Res. - Part A* **89,** 138–151 (2009).
45. Hassler, C., Boretius, T. & Stieglitz, T. Polymers for neural implants. *Journal of Polymer Science, Part B: Polymer Physics* **49,** 18–33 (2011).

46. Ohsawa, I. & Inui, K. Use of tripolar electrodes for minimization of current spread in uncut peripheral nerve stimulation. *Neurosci. Res.* **64,** 63–66 (2009).
47. Franssila, S. *Introduction to Microfabrication. Introduction to Microfabrication* (2010). doi:10.1002/9781119990413
48. Cullinane, J. B. User's evaluation of pin grid array sockets. *Connect. Specif.* **6,** 39–44 (1990).
49. Yannas, I. V. *Tissue and Organ Regeneration in Adults*. (Springer New York, 2015). doi:10.1007/978-1-4939-1865-2
50. Borke, R. C., Curtis, M. & Ginsberg, C. Choline acetyltransferase and calcitonin gene-related peptide immunoreactivity in motoneurons after different types of nerve injury. *J. Neurocytol.* **22,** 141–153 (1993).
51. Yuan, Q., Su, H., Chiu, K., Lin, Z.-X. & Wu, W. Assessment of the rate of spinal motor axon regeneration by choline acetyltransferase immunohistochemistry following sciatic nerve crush injury in mice. *J. Neurosurg.* **120,** 502–8 (2014).
52. Behan, W. M. H., Cossar, D. W., Madden, H. A. & McKay, I. C. Validation of a simple, rapid, and economical technique for distinguishing type 1 and 2 fibres in fixed and frozen skeletal muscle. *J. Clin. Pathol.* **55,** 375–80 (2002).
53. Vinay Kumar, Abul Abbas, Nelson Fausto, J. A. *Robbins and Cotran Pathologic Basis of Disease*. (Saunders, Elsevier, 2010).
54. Navarro, X. E. T. M. Selective fascicular stimulation of the rat sciatic nerve with multipolar polyimide cuff electrodes. .
55. Chamberlain, L. J., Yannas, I. V, Hsu, H. P., Strichartz, G. & Spector, M. Collagen-GAG substrate enhances the quality of nerve regeneration through collagen tubes up to level of autograft. *Exp. Neurol.* **154,** 315–29 (1998).
56. Schmalbruch, H. Fiber composition of the rat sciatic nerve. *Anat. Rec.* **215,** 71–81 (1986).
57. Lowrie, M. B., Krishnan, S. & Vrbová, G. Permanent changes in muscle and motoneurones induced by nerve injury during a critical period of development of the rat. *Dev. Brain Res.* **31,** 91–101 (1987).
58. Lago, N. & Navarro, X. Correlation between target reinnervation and distribution of motor axons in the injured rat sciatic nerve. *J. Neurotrauma* **23,** 227–40 (2006).
59. da Silva, C. F., Madison, R., Dikkes, P., Chiu, T.-H. & Sidman, R. L. An in vivo model to quantify motor and sensory peripheral nerve regeneration using bioresorbable nerve guide tubes. *Brain Res.* **342,** 307–315 (1985).
60. Moldovan, M., Sørensen, J. & Krarup, C. Comparison of the fastest regenerating motor and sensory myelinated axons in the same peripheral nerve. *Brain* **129,** 2471–83 (2006).
61. Lago, N., Ceballos, D., Rodríguez, F. J., Stieglitz, T. & Navarro, X. Long term assessment of axonal regeneration through polyimide regenerative electrodes to interface the peripheral nerve. *Biomaterials* **26,** 2021–31 (2005).
62. Stieglitz, T., Beutel, H., Schuettler, M. & Meyer, J.-U. Micromachined, Polyimide-Based Devices for Flexible Neural Interfaces. *Biomed. Microdevices* **2,** 283–294
63. Boyden, E. S., Zhang, F., Bamberg, E., Nagel, G. & Deisseroth, K. Millisecond-timescale, genetically targeted optical control of neural activity. *Nat. Neurosci.* **8,** 1263–1268 (2005).
64. Lin, J. Y., Knutsen, P. M., Muller, A., Kleinfeld, D. & Tsien, R. Y. ReaChR: a red-

shifted variant of channelrhodopsin enables deep transcranial optogenetic excitation. *Nat. Neurosci.* **16,** 1499–508 (2013).

65. Alilain, W. J. *et al.* Light-Induced Rescue of Breathing after Spinal Cord Injury. *J. Neurosci.* **28,** 11862–11870 (2008).
66. Bryson, J. B. *et al.* Optical Control of Muscle Function by Transplantation of Stem Cell-Derived Motor Neurons in Mice. *Science (80-. ).* **344,** 94–97 (2014).
67. Wang, H. *et al.* Fatal Neurological Respiratory Insufficiency Is Common Among Viral Encephalitides. *J. Infect. Dis.* **208,** 573–583 (2013).
68. Caggiano, V., Sur, M. & Bizzi, E. Rostro-Caudal Inhibition of Hindlimb Movements in the Spinal Cord of Mice. *PLoS One* **9,** e100865 (2014).
69. Liske, H., Qian, X., Anikeeva, P., Deisseroth, K. & Delp, S. Optical control of neuronal excitation and inhibition using a single opsin protein, ChR2. *Sci. Rep.* **3,** 3110 (2013).
70. Iyer, S. M. *et al.* Virally mediated optogenetic excitation and inhibition of pain in freely moving nontransgenic mice. *Nat. Biotechnol.* **32,** 274–8 (2014).
71. Aravanis, A. M. *et al.* An optical neural interface: in vivo control of rodent motor cortex with integrated fiberoptic and optogenetic technology. *J. Neural Eng.* **4,** S143-56 (2007).
72. Park, S. Il *et al.* Soft, stretchable, fully implantable miniaturized optoelectronic systems for wireless optogenetics. *Nat. Biotechnol.* **33,** 1280–1286 (2015).
73. Arlow, R. L., Foutz, T. J. & McIntyre, C. C. Theoretical principles underlying optical stimulation of myelinated axons expressing channelrhodopsin-2. *Neuroscience* **248,** 541–551 (2013).
74. OMLC. Optical Properties Spectra.
75. Jacques, S. L. Optical properties of biological tissues: a review. *Phys. Med. Biol.* **58,** R37-61 (2013).
76. Mason, M. R. *et al.* Comparison of AAV Serotypes for Gene Delivery to Dorsal Root Ganglion Neurons. *Mol. Ther.* **18,** 715–724 (2010).
77. Zincarelli, C., Soltys, S., Rengo, G. & Rabinowitz, J. E. Analysis of AAV Serotypes 1–9 Mediated Gene Expression and Tropism in Mice After Systemic Injection. *Mol. Ther.* **16,** 1073–1080 (2008).
78. Chan, K. Y. *et al.* Engineered AAVs for efficient noninvasive gene delivery to the central and peripheral nervous systems. *Nat. Neurosci.* **20,** 1172–1179 (2017).
79. Richards, R. & Dempski, R. E. Adjacent channelrhodopsin-2 residues within transmembranes 2 and 7 regulate cation selectivity and distribution of the two open states. *J. Biol. Chem.* **292,** 7314–7326 (2017).
80. Ji, Z.-G. *et al.* Light-evoked Somatosensory Perception of Transgenic Rats That Express Channelrhodopsin-2 in Dorsal Root Ganglion Cells. *PLoS One* **7,** e32699 (2012).
81. Kapur, S., Richner, T., Brodnick, S., Williams, J. & Poore, S. Development of an Optogenetic Sensory Peripheral Nerve Interface. *Plast. Surg. Res. Counc.* (2014).
82. Ayling, O. G. S., Harrison, T. C., Boyd, J. D., Goroshkov, A. & Murphy, T. H. Automated light-based mapping of motor cortex by photoactivation of channelrhodopsin-2 transgenic mice. *Nat. Methods* **6,** 219–224 (2009).
83. Chuong, A. S. *et al.* Noninvasive optical inhibition with a red-shifted microbial rhodopsin. *Nat. Neurosci.* **17,** 1123–9 (2014).

84. Kim, T., Folcher, M., Baba, M. D.-E. & Fussenegger, M. A Synthetic Erectile Optogenetic Stimulator Enabling Blue-Light-Inducible Penile Erection. *Angew. Chemie Int. Ed.* **54,** 5933–5938 (2015).
85. Magown, P., Shettar, B., Zhang, Y. & Rafuse, V. F. Direct optical activation of skeletal muscle fibres efficiently controls muscle contraction and attenuates denervation atrophy. *Nat. Commun.* **6,** 8506 (2015).
86. Peterson, E. J. & Tyler, D. J. Motor neuron activation in peripheral nerves using infrared neural stimulation. *J. Neural Eng.* **11,** 16001 (2013).
87. Bashkatov, A. N. *et al.* In vivo and in vitro study of control of rat skin optical properties by acting of osmotical liquid.
88. Bashkatov, A. N., Genina, E. A. & Tuchin, V. V. Optical properties of skin, subcutaneous, and muscle tissues: A review. *J. Innov. Opt. Health Sci.* **4,** 9–38 (2011).
89. Islam, M. S. *et al.* Extracting structural features of rat sciatic nerve using polarization-sensitive spectral domain optical coherence tomography. *J. Biomed. Opt.* **17,** 56012 (2012).
90. Hendriks, B. H. W. *et al.* Nerve detection with optical spectroscopy for regional anesthesia procedures. *J. Transl. Med.* **13,** 380 (2015).
91. Yaroslavsky, A. N. *et al.* Optical properties of selected native and coagulated human brain tissues in vitro in the visible and near infrared spectral range. *Phys. Med. Biol.* **47,** 305 (2002).
92. Welch, A. J. & Van Gemert, M. J. C. *Optical-thermal response of laser-irradiated tissue. Optical-Thermal Response of Laser-Irradiated Tissue* (2011). doi:10.1007/978-90-481-8831-4
93. McCartney, C. J. L., Xu, D., Constantinescu, C., Abbas, S. & Chan, V. W. S. Ultrasound examination of peripheral nerves in the forearm. *Reg. Anesth. Pain Med.* **32,** 434–9
94. Stujenske, J. M., Spellman, T. & Gordon, J. A. Modeling the Spatiotemporal Dynamics of Light and Heat Propagation for In Vivo Optogenetics. *Cell Rep.* **12,** 525–34 (2015).
95. Pennes, H. H. Analysis of Tissue and Arterial Blood Temperatures in the Resting Human Forearm. *J. Appl. Physiol.* **1,** (1948).
96. Ward, S. R. & Lieber, R. L. *Density and hydration of fresh and fixed human skeletal muscle. Journal of Biomechanics* **38,** (2005).
97. Hasgall, P. *et al.* IT'IS Database for thermal and electromagnetic parameters of biological tissues. *Version 3.0, September 01st, 2015, DOI: 10.13099/VIP21000-03-0.*
98. Fagher, B. & Monti, M. Thermogenic effect of two β-adrenoceptor blocking drugs, propranolol and carvedilol, on skeletal muscle in rats. A microcalorimetric study. *Thermochim. Acta* **251,** 183–189 (1995).
99. Allen, J. T., Allen, J. T. & Bowman, H. F. The Simultaneous Measurement of Thermal Conductivity, Thermal Diffusivity, and Perfusion in Small Volumes of Tissue. *J. Biomech. Eng.* **106,** 192 (1984).
100. Rins, M., Diez, I., Calpena, A. C. & Obach, R. Skin density in the hairless rat. Evidence of regional differences. *Eur. J. Drug Metab. Pharmacokinet.* **Spec No 3,** 456–7 (1991).

101. Shoudai, K., Peters, J. H., McDougall, S. J., Fawley, J. A. & Andresen, M. C. Thermally Active TRPV1 Tonically Drives Central Spontaneous Glutamate Release. *J. Neurosci.* **30,** 14470–14475 (2010).
102. Glickman, R. D. Phototoxicity to the Retina: Mechanisms of Damage. *Int. J. Toxicol.* **21,** 473–490 (2002).
103. Stockley, J. H. *et al.* Surpassing light-induced cell damage in vitro with novel cell culture media. *Sci. Rep.* **7,** 849 (2017).
104. Khan, I., Tang, E. & Arany, P. Molecular pathway of near-infrared laser phototoxicity involves ATF-4 orchestrated ER stress. **5,** 10581 (2015).
105. Remington, S. J. Fluorescent proteins: maturation, photochemistry and photophysics. *Curr. Opin. Struct. Biol.* **16,** 714–721 (2006).
106. Tozburun, S., Cilip, C. M., Lagoda, G. A., Burnett, A. L. & Fried, N. M. Continuous-wave infrared optical nerve stimulation for potential diagnostic applications. *J. Biomed. Opt.* **15,** 55012
107. Cheever, T. R., Olson, E. A. & Ervasti, J. M. Axonal Regeneration and Neuronal Function Are Preserved in Motor Neurons Lacking ß-Actin In Vivo. *PLoS One* **6,** e17768 (2011).
108. Honjoh, T. *et al.* Optogenetic Patterning of Whisker-Barrel Cortical System in Transgenic Rat Expressing Channelrhodopsin-2. *PLoS One* **9,** e93706 (2014).
109. Wang, H. *et al.* High-speed mapping of synaptic connectivity using photostimulation in Channelrhodopsin-2 transgenic mice. *Proc. Natl. Acad. Sci. U. S. A.* **104,** 8143–8 (2007).
110. Stark, E., Roux, L., Eichler, R. & Buzsáki, G. Local generation of multineuronal spike sequences in the hippocampal CA1 region. *Proc. Natl. Acad. Sci. U. S. A.* **112,** 10521–6 (2015).
111. Klapoetke, N. C. *et al.* Independent optical excitation of distinct neural populations. *Nat. Methods* **11,** 338–46 (2014).
112. Montgomery, K. L. *et al.* Beyond the brain: Optogenetic control in the spinal cord and peripheral nervous system. *Sci. Transl. Med.* **8,** 337rv5 (2016).
113. Bainbridge, J. W. B. *et al.* Long-Term Effect of Gene Therapy on Leber's Congenital Amaurosis. *http://dx.doi.org/10.1056/NEJMoa1414221* (2015).
114. Sack, B. K. & Herzog, R. W. Evading the immune response upon in vivo gene therapy with viral vectors. *Curr. Opin. Mol. Ther.* **11,** 493–503 (2009).
115. Kohro, Y. *et al.* A new minimally-invasive method for microinjection into the mouse spinal dorsal horn. *Sci. Rep.* **5,** 14306 (2015).
116. Boretius, T. *et al.* A transverse intrafascicular multichannel electrode (TIME) to interface with the peripheral nerve. *Biosens. Bioelectron.* **26,** 62–69 (2010).
117. Maimon, B. *et al.* Assessment of Nerve Regeneration through a Novel Microchannel Array. *Int. J. Phys. Med. Rehabil.* **4,** (2016).
118. DYER, K. R. & DUNCAN, I. D. THE INTRANEURAL DISTRIBUTION OF MYELINATED FIBRES IN THE EQUINE RECURRENT LARYNGEAL NERVE. *Brain* **110,** 1531–1543 (1987).
119. Stewart, J. D. Peripheral nerve fascicles: Anatomy and clinical relevance. *Muscle Nerve* **28,** 525–541 (2003).
120. Thompson, A. C., Stoddart, P. R. & Jansen, E. D. Optical Stimulation of Neurons. *Curr. Mol. Imaging* **3,** 162–177 (2014).

121. Peterson, E. J. & Tyler, D. J. Motor neuron activation in peripheral nerves using infrared neural stimulation. *J. Neural Eng.* **11,** 16001 (2014).
122. Lin, J. Y. A User's Guide to Channelrhodopsin Variants: Features, Limitations and Future Developments. doi:10.1113/expphysiol.2009.051961
123. Maimon, B. *et al.* Transdermal optogenetic peripheral nerve stimulation. *J. Neural Eng.* (2017). doi:10.1088/1741-2552/aa5e20
124. Fenno, L., Yizhar, O. & Deisseroth, K. The Development and Application of Optogenetics. doi:10.1146/annurev-neuro-061010-113817
125. Prigge, M. *et al.* Color-tuned channelrhodopsins for multiwavelength optogenetics. *J. Biol. Chem.* **287,** 31804–12 (2012).
126. Lin, J. Y., Lin, M. Z., Steinbach, P. & Tsien, R. Y. Characterization of engineered channelrhodopsin variants with improved properties and kinetics. *Biophys. J.* **96,** 1803–14 (2009).
127. Zepetnek, J. E. T. de, Gordon, T., Stein, R. B. & Zung, H. V. Comparison of force and EMG measures in normal and reinnervated tibialis anterior muscles of the rat. *Can. J. Physiol. Pharmacol.* **69,** 1774–1783 (1991).
128. Mense, S. Muscle pain: mechanisms and clinical significance. *Dtsch. Arztebl. Int.* **105,** 214–9 (2008).
129. Mohan, R., Tosolini, A. P. & Morris, R. Targeting the motor end plates in the mouse hindlimb gives access to a greater number of spinal cord motor neurons: An approach to maximize retrograde transport. *Neuroscience* **274,** 318–330 (2014).
130. Gray, S. J. *et al.* Optimizing Promoters for Recombinant Adeno-Associated Virus-Mediated Gene Expression in the Peripheral and Central Nervous System Using Self-Complementary Vectors. *Hum. Gene Ther.* **22,** 1143–1153 (2011).
131. Hofherr, A., Fakler, B. & Klöcker, N. Selective Golgi export of Kir2.1 controls the stoichiometry of functional Kir2.x channel heteromers. *J. Cell Sci.* **118,** 1935–1943 (2005).
132. Gradinaru, V. *et al.* Molecular and cellular approaches for diversifying and extending optogenetics. *Cell* **141,** 154–65 (2010).
133. ALUSI, S., GLICKMAN, S. & AZIZ, Tz. Tremor in multiple sclerosis. *J. Neurol. Neurosurg. Psychiatry* **66,** 131–134 (1999).
134. O'Suilleabhain, P. E. & Matsumoto, J. Y. Time-frequency analysis of tremors. *Brain* 2127–34 (1998).
135. Harmaline induced tremors | Services | PsychoGenics. Available at: http://www.psychogenics.com/harmaline.html. (Accessed: 2nd June 2017)
136. McGie, S. C., Zariffa, J., Popovic, M. R. & Nagai, M. K. Short-Term Neuroplastic Effects of Brain-Controlled and Muscle-Controlled Electrical Stimulation. *Neuromodulation Technol. Neural Interface* **18,** 233–240 (2015).
137. Arcourt, A. *et al.* Touch Receptor-Derived Sensory Information Alleviates Acute Pain Signaling and Fine-Tunes Nociceptive Reflex Coordination. *Neuron* **93,** 179–193 (2017).
138. Montgomery, K. L. *et al.* Beyond the brain: Optogenetic control in the spinal cord and peripheral nervous system. *Sci. Transl. Med.* **8,** 337rv5 (2016).
139. Miyashita, T., Shao, Y. R., Chung, J., Pourzia, O. & Feldman, D. E. Long-term channelrhodopsin-2 (ChR2) expression can induce abnormal axonal morphology and targeting in cerebral cortex. *Front. Neural Circuits* **7,** 8 (2013).

140. Gradinaru, V., Thompson, K. R. & Deisseroth, K. eNpHR: a Natronomonas halorhodopsin enhanced for optogenetic applications. *Brain Cell Biol.* **36,** 129–139 (2008).
141. Zhao, S. *et al.* Improved expression of halorhodopsin for light-induced silencing of neuronal activity. *Brain Cell Biol.* **36,** 141–154 (2008).
142. Zimmerman, D. *et al.* Effects on capacitance by overexpression of membrane proteins. *Biochem. Biophys. Res. Commun.* **369,** 1022–1026 (2008).
143. Gradinaru, V. *et al.* Targeting and Readout Strategies for Fast Optical Neural Control In Vitro and In Vivo. *J. Neurosci.* **27,** (2007).
144. Beppu, K. *et al.* Optogenetic Countering of Glial Acidosis Suppresses Glial Glutamate Release and Ischemic Brain Damage. *Neuron* **81,** 314–320 (2014).
145. Perny, M., Muri, L., Dawson, H. & Kleinlogel, S. Chronic activation of the D156A point mutant of Channelrhodopsin-2 signals apoptotic cell death: the good and the bad. *Cell Death Dis.* **7,** e2447 (2016).
146. Ansari, A. M. *et al.* Cellular GFP Toxicity and Immunogenicity: Potential Confounders in in Vivo Cell Tracking Experiments. *Stem Cell Rev.* **12,** 553–559 (2016).
147. Stripecke, R. *et al.* Immune response to green fluorescent protein: implications for gene therapy. *Gene Ther.* **6,** 1305–1312 (1999).
148. Taghizadeh, R. R. & Sherley, J. L. CFP and YFP, but Not GFP, Provide Stable Fluorescent Marking of Rat Hepatic Adult Stem Cells. *J. Biomed. Biotechnol.* **2008,** 1–9 (2008).
149. Doroudchi, M. M. *et al.* Virally delivered Channelrhodopsin-2 Safely and Effectively Restores Visual Function in Multiple Mouse Models of Blindness. *Mol. Ther.* **19,** 1220–1229 (2011).
150. Ganesan, L. P. *et al.* Rapid and Efficient Clearance of Blood-borne Virus by Liver Sinusoidal Endothelium. *PLoS Pathog.* **7,** e1002281 (2011).
151. Chen, A. C.-H. *et al.* Low-Level Laser Therapy Activates NF-kB via Generation of Reactive Oxygen Species in Mouse Embryonic Fibroblasts. *PLoS One* **6,** e22453 (2011).
152. Lignani, G. *et al.* Long-term optical stimulation of channelrhodopsin-expressing neurons to study network plasticity. *Front. Mol. Neurosci.* **6,** 22 (2013).
153. Feldbauer, K. *et al.* Channelrhodopsin-2 is a leaky proton pump. *Proc. Natl. Acad. Sci. U. S. A.* **106,** 12317–22 (2009).
154. Li, Q. *et al.* Electrophysiological Properties and Viability of Neonatal Rat Ventricular Myocyte Cultures with Inducible ChR2 Expression. *Sci. Rep.* **7,** 1531 (2017).
155. McCarty, D. M., Young, S. M. & Samulski, R. J. Integration of Adeno-Associated Virus (AAV) and Recombinant AAV Vectors. *Annu. Rev. Genet.* **38,** 819–845 (2004).
156. Fisher, K. J. *et al.* Recombinant adeno-associated virus for muscle directed gene therapy. *Nat. Med.* **3,** 306–12 (1997).
157. Robertson, G., Garrick, D., Wilson, M., Martin, D. I. & Whitelaw, E. Age-dependent silencing of globin transgenes in the mouse. *Nucleic Acids Res.* **24,** 1465–71 (1996).
158. Okada, T. *et al.* A Histone Deacetylase Inhibitor Enhances Recombinant Adeno-

associated Virus-Mediated Gene Expression in Tumor Cells. *Mol. Ther.* **13,** 738–746 (2006).
159. Migliaccio, A. R. *et al.* Stable and unstable transgene integration sites in the human genome: extinction of the Green Fluorescent Protein transgene in K562 cells. *Gene* **256,** 197–214 (2000).
160. Kong, Q. *et al.* Transgene Expression Is Associated with Copy Number and Cytomegalovirus Promoter Methylation in Transgenic Pigs. *PLoS One* **4,** e6679 (2009).
161. Sevc, J. *et al.* Effective long-term immunosuppression in rats by subcutaneously implanted sustained-release tacrolimus pellet: Effect on spinally grafted human neural precursor survival. *Exp. Neurol.* **248,** (2013).
162. Yednock, T. A. *et al.* Prevention of experimental autoimmune encephalomyelitis by antibodies against α4βl integrin. *Nature* **356,** 63–66 (1992).
163. Badell, I. R. *et al.* Pathogen Stimulation History Impacts Donor-Specific CD8 $^{+}$ T Cell Susceptibility to Costimulation/Integrin Blockade-Based Therapy. *Am. J. Transplant.* **15,** 3081–3094 (2015).
164. Maimon, B. E., Sparks, K., Srinivasan, S., Zorzos, A. & Herr, H. M. Two Color Independent Optogenetic Peripheral Nerve Stimulation. *Nat. Biomed. Eng.*
165. Doroudchi, M. M. *et al.* Virally delivered Channelrhodopsin-2 Safely and Effectively Restores Visual Function in Multiple Mouse Models of Blindness. *Mol. Ther.* **19,** 1220–1229 (2011).
166. Bishop, D. L., Misgeld, T., Walsh, M. K., Gan, W.-B. & Lichtman, J. W. Axon Branch Removal at Developing Synapses by Axosome Shedding. *Neuron* **44,** 651–661 (2004).
167. Derelanko, M. J. Determination of erythrocyte life span in F-344, Wistar, and Sprague-Dawley rats using a modification of the [3H]diisopropylfluorophosphate ([3H]DFP) method. *Fundam. Appl. Toxicol.* **9,** 271–6 (1987).
168. Grant, S. M., Wiesinger, J. A., Beard, J. L. & Cantorna, M. T. Iron-deficient mice fail to develop autoimmune encephalomyelitis. *J. Nutr.* **133,** 2635–8 (2003).
169. Fülöp, T. *et al.* Relationship between the response to influenza vaccination and the nutritional status in institutionalized elderly subjects. *J. Gerontol. A. Biol. Sci. Med. Sci.* **54,** M59-64 (1999).
170. Akbas, S. H. *et al.* Effects of some hematological parameters on whole blood tacrolimus concentration measured by two immunoassay-based analytical methods. *Clin. Biochem.* **38,** 552–557 (2005).
171. Park, S. *et al.* Association between post-transplant red cell distribution width and prognosis of kidney transplant recipients. *Sci. Rep.* **7,** 13755 (2017).
172. Maimon, B. E. *et al.* Transdermal optogenetic peripheral nerve stimulation. *J. Neural Eng.* **14,** 34002 (2017).
173. Bartanusz, V., Jezova, D., Alajajian, B. & Digicaylioglu, M. The blood-spinal cord barrier: Morphology and Clinical Implications. *Ann. Neurol.* **70,** 194–206 (2011).
174. Ranade, S. S. *et al.* Piezo2 is the major transducer of mechanical forces for touch sensation in mice. *Nature* **516,** 121–125 (2014).
175. Woo, S.-H. *et al.* Piezo2 is the principal mechanotransduction channel for proprioception. *Nat. Neurosci.* **18,** 1756–1762 (2015).
176. Grosenick, L., Marshel, J. H. & Deisseroth, K. Closed-Loop and Activity-Guided